BENTHIC-PELAGIC OXYGEN AND NUTRIENT CYCLES IN A SEASONALLY HYPOXIC COASTAL BASIN

by

Subhadeep Rakshit

Submitted in partial fulfilment of the requirements
for the degree of Doctor of Philosophy

at

Dalhousie University
Halifax, Nova Scotia
September 2023

Dedication

To maa and baba for their endless love and support.

TABLE OF CONTENTS

LIST OF TABLES

LIST OF FIGURES

ABSTRACT

The biogeochemical cycling of nutrients and oxygen in the coastal ocean is of high importance given that anthropogenic nutrient inputs have doubled the preindustrial nutrient load to water bodies. In particular, excess nitrogen (N) causes eutrophication and hypoxia in the coastal ocean, which is further exacerbated by increased stratification due to global warming. Owing to relatively shallow waters in coastal regions, processes within the sediment and water column play equally important roles in key biogeochemical cycles. To understand the factors that regulate the nutrient and oxygen cycle in seasonally hypoxic coastal basins, this thesis employs high-resolution field observations conducted in Bedford Basin, coupled with numerical modeling, to investigate the impact of various geochemical, biological, and physical drivers. In Chapter 2, field observations of weekly CTD casts and measured benthic oxygen uptake were used to develop and parameterize a numerical model to understand the development of hypoxia in Bedford Basin and quantify different sources and sinks of oxygen in three contrasting years. Chapter 3 is focused on understanding the annual development of the nitrogen cycle based on weekly timeseries of geochemical parameters and phylogenetic marker genes in bottom waters over four consecutive years. Measured geochemical and biological parameters were incorporated into a box model to simulate the nitrification dynamics and identify the controlling factors. Through this approach, a novel mechanism of nitrification was identified whereby strong physical mixing dilutes the resident nitrifier biomass leading to delayed and decoupled nitrification. Weak physical mixing during winter may have the reverse effect. In Chapter 4, benthic biogeochemical processes were studied through seasonal measurements of organic matter remineralization rate, benthic fluxes, sediment geochemical profiles, along with reaction-transport modeling.

Overall, this thesis studied the development of hypoxia in a coastal basin, nutrient cycles in the water column and sediment, and the physical and biological drivers of coupled biogeochemical cycles.

LIST OF SYMBOLS AND ABBREVIATIONS USED

μM = micro molar (micromole/liter)

mM = millimolar (millimole/liter)

φ = Porosity

ρ = Density

1D = One dimensional

amoA = ammonium monooxygenase gene

AO = Ammonia Oxidation

AOA = Ammonia Oxidizing Archaea

AOB = Ammonia Oxidizing Bacteria

AOO = Ammonia Oxidizing Organism

ASV = Amplicon Sequence Variant

BB = Bedford Basin

BBMP = Bedford Basin Monitoring Program

BIO = Bedford Institute of Oceanography

BNF = Biological Nitrogen Fixation

C/*C*= Carbon/*generic concentration of a component “C”*

Chl-a = Chlorophyll-(a)

cm = centimeter

CTD = Conductivity-Temperature-Depth

D_0 = Diffusion coefficient

D_b = Bioturbation

D_s = Tortuosity corrected diffusion coefficient

DBL = Diffusive Boundary Layer

DNRA = Dissimilatory nitrate reduction to ammonium

DOU = Diffusive Oxygen Uptake

Fe = Iron

$Fe(OH)_3$ = iron oxides

FeS = Iron monosulfide

FeS_2 = Pyrite

g = gravitational acceleration

h = height

H_2S = Hydrogen sulfide

K = adsorption constant

k = rate constant

Ks = Half-saturation constant

Kz = eddy diffusivity

MEOPAR = Marine Environmental Observation, Prediction and Response Network

m = meter

mm = millimeter

mM = millimolar

Mn = Manganese

MnO_2= Manganese dioxide

N = Nitrogen

N_2O = Nitrous Oxide

NO_2^- = Nitrite

NO_3^- = Nitrate

nxr = Nitrite oxidoreductase gene

OC = Organic Carbon

OFI = Ocean Frontier Institute

OM = Organic Matter

OMZ = Oxygen Minimum Zone

Pb = Lead

POC = Particulate Organic Carbon

PON = Particulate Organic Nitrogen

PNM = Primary Nitrite Maximum

qPCR = Quantitative Polymerase Chain Reaction

rRNA = Ribosomal ribonucleic acid

RQ = Respiratory Quotient

RTM = Reaction Transport Model

S = Salinity

SO_4^{2-} = Sulfate

SST = Sea Surface Temperature

T = Temperature

t = time

TC = Total carbon

TEA = Terminal Electron Acceptor

TN = Total Nitrogen

TOC = Total Organic Carbon

TON = Total Organic Nitrogen

TOSST = Transatlantic Ocean System Science and Technology

TOU = Total Oxygen Uptake

TS = Temperature-salinity

z = depth

ACKNOWLEDGEMENT

First and foremost, I would like to thank my supervisor Chris Algar for his encouragement, scientific insights, and support both academically and personally. Thank you Chris for introducing me to the field of Oceanography, teaching me modelling, and giving me opportunity and freedom to work on various projects even it was not always directly related to the thesis. Thank you for guiding and maintaining positivity through the entire journey. You have been truly a great supervisor. I would also like to thank my co-supervisor Andy Dale for all of those insightful meetings and sharing your expertise which made the journey even smoother.

I am thankful to the immensely supportive and expert advisory committee members Doug Wallace, Carly Buchwald, Markus Kienast and Andy Dale. I always came out of the meetings with clearer perception on the project and with new motivations.

I would like to thank TOSST and NSGS for their financial support towards stipend. Additionally, I would like to thank TOSST for giving me the opportunity to participate in various international summer schools and make new friends which has been great for personal development and outlook for the world.

My thanks go to all the former and present lab members of Algar-Buchwald lab who has been good friends and supported thorough chat about research or life and keeping an enjoyable lab atmosphere. I would especially like to thank our lab manager Maria Armstrong who has been a great friend and helped and supported me a lot not only with research but also through our chats time to time about life in general.

Special mention goes to Bedford Institute of Oceanography for starting the Bedford Basin timeseries and giving access to the data which formed the base of the project. The boat captains of Connors Diving company, especially Jim deserves special mention for assisting us during several sampling campaigns to the basin.

The collaborations I formed remained a vital part of the current thesis. I would like to thank Sebastian Haas, Brent Robicheau, Doug Wallace, and Nicolaas Glock without whom this thesis would not have been at its present form.

I will forever be grateful to the Dalhousie Oceanography department, the entire faculty and stuff and DOSA for their profound support at the time of personal crisis.

I would like to thank many of my friends from school and university in India, and many new friends that I made here in Halifax for providing psychological support through chats and phone calls, with special thanks to Ricardo, Aly, Najeem, Haley, Katie, Maria, Lorenza, Francesco, Sebastian and many more that I probably missed.

Lastly, I thank my mother for her sacrifices and support without which I could not have completed the degree.

Chapter 1: INTRODUCTION

1.1 Coastal ocean and its role in nutrient cycling

Coastal regions are the transition boundary between terrestrial and marine ecosystems (Nixon et al. 1996). These regions are important from a human perspective as more than half the world population lives within 60 km of the coast (Small and Nicholls 2003). We depend on the coastal ocean for food, transportation, energy and recreational needs. Coastal oceans are amongst the most productive regions on the planet, driven by the high nutrient input from land due to natural and anthropogenic factors. Nutrient loading stimulates carbon dioxide (CO_2) uptake through photosynthesis, producing oxygen (O_2) as a waste product (Field et al. 1998). The opposite process of photosynthesis is respiration, where heterotrophic organisms harness energy by oxidizing organic matter (OM) using a terminal electron acceptor (TEA) (e.g., oxygen), releasing CO_2 along with inorganic nutrients. A fraction of the autotrophically-produced OM is respired heterotrophically in water column, with the remainder sinking to the seafloor to provide energy to the benthic ecosystem. This downward flux of organic carbon and associated nutrients is generally known as the biological carbon pump (Sanders et al. 2014).

Respiration of OM in water and sediment consumes oxygen, leading to net oxygen consumption below the euphotic zone. In regions with restricted circulation such as semi-enclosed bays, estuaries, coastal basin and fjords, this might lead to development of bottom water hypoxia (Fennel and Testa 2019). Whilst in the open ocean most of the sinking OM is respired in the water column, in shallow coastal waters a large fraction of the sinking OM is deposited on the seafloor. Coastal sediments are hence a significant player in global nutrient cycles. In very shallow waters, the sediment may be the dominant oxygen sink and an important driver of coastal hypoxia (Fennel and Testa 2019). Coastal and shelf sediments are sites of active organic carbon burial, accounting for up to 85% of the total organic matter burial in the global ocean (Smith et al. 2015). Driven by this high OM load, coastal and shelf sediments are further responsible nearly half of the total global denitrification (Middelburg et al. 1996; Devol 2015).

In the water column, OM respiration is usually dominated by aerobic processes whereas in oxygen deficit zones anaerobic processes such as denitrification can be important. Aerobic oxidation of organic matter by microbes consumes oxygen while releasing CO_2 and inorganic nutrients such as ammonium and phosphate. Ammonium, in the absence of light, is further aerobically oxidized to nitrite by ammonia oxidizing archaea or bacteria (AOA or AOB) and subsequently nitrite is oxidized to nitrate by nitrite oxidizing bacteria (NOB). This two-step conversion of ammonium to nitrate is known as nitrification and controls the speciation of dissolved inorganic nitrogen (DIN), which is the primary limiting nutrient for phytoplankton growth in coastal ocean.

In contrast to the water column, oxygen in fine-grained coastal sediment is usually depleted within the top few millimetres due to relatively high organic matter concentrations and OM respiration rates. OM is oxidized using TEAs in the following sequence according to their Gibb's free energy yield – O_2 > NOx (NO_2^- + NO_3^-)> Mn^{4+}-oxide > Fe^{3+}-oxide > SO_4^{2-} > CH_2O (Tromp et al. 1995). Following oxygen, when nitrate acts as the TEA, denitrification removes the bioavailable or fixed nitrogen by reducing it to dinitrogen gas, N_2. Fixed nitrogen can also be removed through anammox, whereby ammonium oxidized anaerobically by nitrite to N_2. This process could be responsible for nearly 10% of fixed N loss from estuarine sediment (Burdige 2011). Contrastingly, dissimilatory nitrate reduction to ammonium (DNRA), which also takes place anaerobically in sediment by some bacteria, retains fixed nitrogen in the system and may compete with denitrification for nitrate (Giblin et al. 2013; Hellemann et al. 2020). Therefore, these competing and coupled reactions in coastal sediments make the study of nitrogen cycle a complex task, especially where the oxidation-reduction (redox) processes occur in close succession such as in coastal sediments. These processes in the sediment are not only important for the macro elements of life such as C, N, O, but also for Fe, S. The sediment is major source of the dissolved micronutrient iron to the water column with shelf sediments (0-200 m depth) accounting for nearly half of the global benthic dissolved iron flux (Dale et al. 2015). In coastal and shelf sediment, a large portion of the OM is remineralized via sulfate reduction that produces hydrogen sulfide (H_2S). The iron cycle in sediment plays a crucial role in keeping H_2S locked up in sediment in the form of pyrite (FeS_2) and prevents the release of toxic H_2S gas to overlying water which can cause mass mortality in macrofaunal community (Van Cappellen and Wang 1996; Levin et al. 2009; Seitaj et al. 2015).

1.2 Significance of the study of coastal oxygen and nutrient cycle in a changing world

In a changing global environment, it is especially important to understand the biogeochemical C-O-N cycles and how they are controlled by the interaction with other environmental factors, particularly the physical environment that is subject to climate-driven changes. In the last few decades, due to global warning and increasing water column stratification, the global dissolved oxygen inventory in the ocean has decreased by more than 2% (Schmidtko et al. 2017). The effect is more severe in the coastal ocean, especially in areas with restricted water column circulation such estuaries, semi-enclosed bays, marginal seas and fjords (Breitburg et al. 2018a), where coastal hypoxia has increased by 5.5% per year in the last few decades (Vaquer-Sunyer and Duarte 2008). Moreover, the input of fixed nitrogen has doubled due to anthropogenic activity in the last few decades which is causing eutrophication in freshwater lakes and coastal oceans. In turn, the increased heterotrophic respiration of sinking OM in eutrophic water bodies is consuming oxygen thus creating hypoxia and even anoxia with detrimental effects on the coastal ocean especially in coastal basins with restricted circulation (Galloway et al. 2004).

Biogeochemical cycles are shaped by the interaction of physical, chemical, and biological processes and cannot be fully understood without consideration of the primary influencing factors. For example, inorganic nutrients (e.g. DIN) are transformed mainly through the actions of microbes, that in turn are controlled by temperature, light, and water column mixing (Chapter 3). The speciation of DIN and its availability also controls phytoplankton growth, which sequesters CO_2 from the atmosphere, provides oxygen and forms the base of the food chain. Human actions are causing enhanced nutrient loading to water bodies and greenhouse gases in the atmosphere, leading to eutrophication and global warming. This warming increases stratification, which restricts the oxygen distribution in the water column which can be exacerbated by eutrophication (Chapter 2). The biogeochemical processes in the sediment are driven by the input of OM from the surface ocean and controlled by physical (e.g. molecular diffusion, compaction), biological (actions of inhabiting biosphere) and chemical (redox chemistry) processes. These are also subject to changes in the water column for instance with decreasing oxygen condition, such as in hypoxia and anoxia. Faunal communities might be seriously impacted, resulting in reduced biological mixing of sediment and distribution of chemical species within the upper sediment. Also, long term shifts in oxygen concentration in bottom waters might lead to the emergence of low oxygen tolerant species (e.g., denitrifying foraminifera) in the sediment through ecosystem shifts, with consequences on benthic biogeochemistry (Chapter 4).

To gain understanding about these intertwined biogeochemical processes and their dynamics under environmental changes, multiparameter, temporally resolved long-term timeseries and observations play a crucial role. This thesis explores the biogeochemical processes occurring in the water column and sediment of a coastal basin to gain insights on the effects of the physical environment. With this aim, the thesis focused on Bedford Basin, a 70 m deep seasonally hypoxic fjord basin on the Northwest Atlantic that is connected to the Scotian Shelf through a 20 m deep sill. The site is the location of a long running timeseries of weekly measurements of various hydrological and geochemical properties of water over the last three decades (Bedford Basin Monitoring Program, BBMP). The basin water column mixes every winter and bottom water is re-oxygenated. As surface water temperature increases in summer, the increased stratification prevents surface water from mixing with deeper layers and leads to hypoxic bottom waters until re-ventilation during the following winter. Notably, bottom water hypoxia can also be terminated by intrusions of dense, oxygenated, Scotian Shelf water in summer-fall, although, these events are infrequent and do not occur each year. Besides oxygen, this cycle of mixing-stratification, creates annual cycle for other biogeochemical variables as well, for example dissolved inorganic nitrogen, dissolved inorganic carbon, microbial populations etc. Due to this relatively predictable natural cycle in Bedford Basin, and its easy accessibility for sampling, it can be considered as a “natural laboratory”, where different aspects of the biogeochemical cycle can be studied over consecutive years.

Although several studies have been conducted on the basin mostly on understanding general circulation, phytoplankton dynamics, geology, and to a lesser extent geochemistry, very few so far have focused on understanding the nutrient cycle in water column (Punshon and Moore 2004b) and sediments. This knowledge gap provides a unique opportunity to explore the coupled benthic-pelagic nutrient cycles in the context of the long running timeseries and the historical background established by the BBMP.

1.3 Thesis objectives and structure

This thesis aims to gain a holistic understanding of the biogeochemical processes occurring at the sediment-water continuum, especially focussing on the coupled C-O-N cycles, by incorporating multiparameter oceanographic observations, specific experiments, and numerical modeling. To begin with, Chapter 2 aims to quantify the sources and sinks of oxygen and the factors responsible for the development of hypoxia in the coastal basin. Field observations of weekly CTD casts and measured benthic oxygen uptake rates were used to develop and parameterize a numerical model to simulate oxygen dynamics in the basin for three study years. In Chapter 3, through a collaborative study, the nitrification cycle in bottom water of BB was investigated using weekly timeseries of physical, geochemical and microbiological parameters. More specifically, this chapter unifies the multiparameter observational dataset in a mathematical modeling framework. Using the model, the contrasting patterns of the nitrification cycle were simulated for four years, leading to the discovery of a general mechanism whereby dilution of the resident nitrifier biomass by winter water column mixing explains the decoupling and time lags of nitrification in different years. Chapter 4, studies the sediment early diagenetic processes in BB. Observational campaigns were conducted to measure seasonal benthic nutrient fluxes, solid and porewater geochemistry and OM remineralization rates, which were the first direct measurements of these parameters from the region. The data were used to design and parameterize a coupled sediment early diagenetic 1-D reaction transport model. Inspired by the initial results, the potential of benthic denitrification by foraminifera in BB was tested. Chapter 4 also presented the benthic nutrient budget, and identifies the major processes governing the sediment biogeochemistry.

Chapter 2: SOURCES AND SINKS OF BOTTOM WATER OXYGEN IN A SEASONALLY HYPOXIC FJORD[1]

2.1 Abstract

Deoxygenation of the ocean has been occurring over the last half century, particularly in poorly ventilated coastal waters. In coastal and estuarine environments, both the water column and sediments play key roles in controlling oxygen variability. In this study, we focus on controls of oxygen concentration in Bedford Basin (BB), a 70 m deep, seasonally hypoxic semi-enclosed fjord on the West Atlantic coast in Nova Scotia. The basin is connected to the Scotian Shelf via a narrow 20 m deep sill that restricts the resupply of bottom water. Hypoxia was recorded seasonally in 2018, 2019 and 2021with minimum oxygen concentration of 5, 6.7 and 2.7 µM, respectively. Using a 1-D benthic-pelagic coupled model we investigate oxygen consumption and resupply processes during these years. The model was constrained with weekly water column measurements of temperature, salinity, chlorophyll-a fluorescence and dissolved oxygen from a monitoring station in the central basin together with seasonal measurements of benthic diffusive oxygen uptake. Our model suggested that 29-81%, and up to 36% of bottom water re-oxygenation occurred during the winter mixing period and through summer/fall intrusions of Scotian Shelf water, respectively. Occasional shelf water intrusions occurred rapidly, on a timescale of a few hours, and delivered equivalent amounts of oxygen as winter mixing and were sufficient to end bottom water hypoxia. Collectively, these mechanisms supplied the majority of the oxygen delivered to the bottom water. Oxygen supply to bottom waters during periods of water column stratification accounted for 19-36% of the annual flux. The

---

[1] Rakshit, S., A. W. Dale, D. W. Wallace, and C. K. Algar. 2023. Sources and sinks of bottom water oxygen in a seasonally hypoxic fjord. Front. Mar. Sci. 10: 655. https://doi.org/10.3389/fmars.2023.1148091

Author contribution: SR and CA conceptualized the study; SR, CA collected samples; SR performed the research with supervision from AD and CA; SR, AD, DW and CA contributed to the detailed discussion of the results. SR wrote the manuscript with input from all authors.

mean benthic uptake was 12±8 mmol m^{-2} d^{-1} and contributed ~20% of the total oxygen consumption below the sill depth. In 2021, sea surface temperature (SST) was unusually high and likely resulted in 50% less bottom water oxygenation compared to 2018 and 2019 due to increased stratification; SST in BB was found to be increasing at a rate of 0.11±0.02 °C/year. Climate control on water column stratification are discussed and numerical experiments are used to compare the effects of different water column mixing scenarios on bottom water oxygenation.

2.2 Introduction

Declining dissolved oxygen in the ocean is of global concern. Several reports have identified an increase in the incidence of hypoxia (dissolved $O_2 < 63$ μM) over the last half century (Diaz and Rosenberg 2008; Gilbert et al. 2010; Schmidtko et al. 2017; Breitburg et al. 2018b). The extent, frequency, duration, and intensity of these events have increased globally (Diaz and Rosenberg 2008), with a 5.5% per year increase in reported coastal hypoxia in the last few decades (Vaquer-Sunyer and Duarte 2008). While this may partially be attributed to increased monitoring (Vaquer-Sunyer and Duarte 2008), the ultimate driving mechanisms are likely to be climate related shifts in ocean circulation, increased nutrient loading, and increased stratification of surface waters (Stramma et al. 2008; Diaz and Rosenberg 2008; Frölicher et al. 2009; Gilbert et al. 2010; Jutras et al. 2020).

The bottom waters of semi-enclosed, coastal basins, fjords, and estuaries may be particularly susceptible to hypoxia (Fennel and Testa 2019). Often, the presence of a sill restricts bottom water circulation which, combined with stratification during summer months, limits oxygen resupply. If loss due to respiration exceeds replenishment, hypoxic or even anoxic conditions may develop. In winter months, surface cooling and increased wind-driven mixing often reduces stratification and bottom waters may be reoxygenated. This natural seasonal cycle can be altered or exacerbated by anthropogenetic influences such as eutrophication or long-term trends of increased stratification and decreased oxygen solubility associated with climate warming.

To understand the sensitivity of a particular coastal area to seasonal hypoxia, it is necessary to quantify not only oxygen losses due to respiration in the water column and sediments, but also the various mechanisms of oxygen resupply, e.g., mixing with oxygenated surface waters. In coastal environments with shallow waters, processes within the sediment can be particularly important for oxygen budgets (e.g., Fennel and Testa, 2019). Under hypoxic conditions, bottom sediments can also become a major source of nutrients, in particular phosphorous, creating a positive feedback between eutrophication and oxygen depletion (Conley et al. 2002; Noffke et al. 2016; Song et al. 2021). On the other hand, sediment can remove fixed nitrogen through denitrification (Seitzinger et al. 2006; Fennel et al. 2009). Hypoxia, when it occurs, can also alter nitrogen cycling by promoting dissimilatory nitrate reduction to ammonium (DNRA) which retains bioavailable nitrogen in the environment (Jäntti and Hietanen 2012; Noffke et al. 2016).

In the present study, we quantify the sources and sinks of oxygen in a restricted coastal basin and demonstrate how long-term monitoring combined with biogeochemical modeling can unravel the mechanisms driving coastal hypoxia. The study is focused on Bedford Basin (BB) (Figure 2.1), a well-studied site (Petrie and Yeats 1990b; Shan et al. 2011b; Haas et al. 2021), which forms the inner portion of Halifax Harbour, an industrialized port surrounded by the city of Halifax (Canada), located on the Scotian Shelf in the northwest Atlantic Ocean. The basin itself is a 70 m deep, 17 km^2, fjord-type estuary. The Sackville River delivers freshwater into the head of the basin and at its seaward end the basin is connected to the outer Halifax Harbour and the Scotian Shelf via a 20 m deep sill. The freshwater input ($5.3 \ m^3 \ s^{-1}$) is small compared to the mean tidal volume ($2.5 \times 10^7 \ m^3$) and the total basin volume ($5.1 \times 10^8 \ m^3$) (Petrie and Yeats 1990b; Haas et al. 2022). The presence of the sill restricts the estuarine circulation to the upper 20 m and the bottom water can become isolated from the surface layer due to stratification, leading to development of seasonal hypoxia. The average flushing time previously estimated for the entire basin is 91 days but for bottom waters it can be upwards of 194 days (Shan and Sheng 2012; Burt et al. 2013a; Haas et al. 2021). The prevailing wind blows from the North-West direction from September to April; the wind direction varies more in summer, but is mostly from the South-West direction. Typically, hypoxia develops in late summer or fall and ends during the late winter when convective mixing oxygenates the bottom waters. Oxygen is also occasionally resupplied by intrusions of dense Scotian Shelf water that can replenish either the bottom or mid-depth waters (Shi and Wallace 2018a; Haas et al. 2021). These intrusions appear to be more common in the fall.

The regular occurrence of coastal hypoxia makes BB an ideal natural laboratory to study oxygen dynamics. In addition, since 1992 the Bedford Basin Monitoring Program (BBMP), which was initiated by the Bedford Institute of Oceanography (BIO) and expanded in the last decade by Marine Environmental Observation, Prediction and Response Network (MEOPAR) and the Ocean Frontier Institute (OFI), has carried out weekly measurements of hydrographic properties at the deepest point (70 m) in the basin (Compass Buoy Site, Figure 2.1). This includes weekly CTD casts for hydrographic (T, S) and several chemical properties in both the surface (1, 5, 10m) and bottom (60m) waters. Bedford Basin has been the focus of numerous studies examining geological (Miller et al. 1982; Buckley and Winters 1992; Fader and Miller 2008a), chemical (Shi and Wallace 2018a), climatological (Li and Harrison 2008a), biogeochemical (Conover 1975; Hargrave 1978a; Taguchi and Hargrave 1978; la Roche 1983; Azetsu-Scott and Johnson 1994; Punshon and Moore 2004b; Li et al. 2010; Burt et al. 2013a; Georges et al. 2014a; Haas et al. 2021, 2022; Robicheau et al. 2022) and environmental (Rao et al. 1993; Pan and Subba Rao 1997; Scott 2005; AMEC 2011; Lacasse et al. 2013; Vercaemer and Sephton 2014) aspects of the basin. Several of these studies have focussed on processes influenced by the transient hypoxic characteristics of the basin. However, to-date there has been no study focussed on the key processes responsible for controlling the oxygen budget of the basin.

To understand the benthic contribution to oxygen dynamics, seasonal changes in benthic oxygen uptake were measured in 2019 using microsensor profiling of collected sediment cores. These were used to develop a coupled benthic-water column reactive-transport model of oxygen dynamics in the basin. We used the model to examine three contrasting years: 2018, 2019 and 2021 that apparently displayed different mechanisms of oxygen supply to subsurface waters. The year 2019 had prolonged winter mixing, while in 2021 winter mixing was the weakest on record. Both 2019 and 2021 were without shelf water intrusions, whereas 2018 experienced two intrusions that replenished the bottom water. We used the model to examine the oxygen budget and mechanisms driving hypoxia including the sensitivity of oxygen levels to potential climate-induced changes, such as increased stratification or decreased winter mixing.

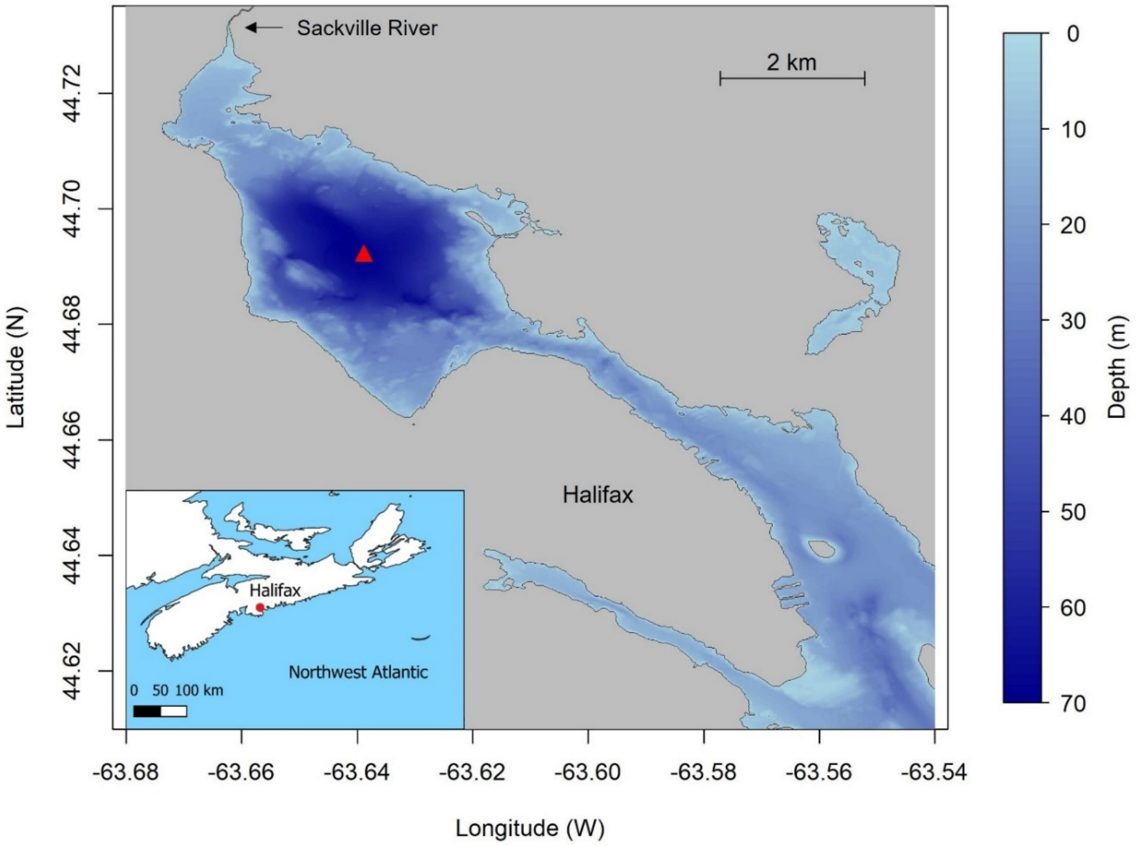

Figure 2.1. Bathymetric map of Bedford Basin and Halifax Harbour. The Compass Buoy station in Bedford Basin is shown by red triangle.

2.3 Materials and methods

2.3.1 Study area and sampling

Weekly CTD data of the water column were obtained from Bedford Institute of Oceanography website (BIO 2022) as part of a long term oceanographic monitoring program at the Compass Buoy site (Lat: 44.6937N, Lon: 63.6403W) (Li 2014a). In addition to temperature and salinity the CTD (Seabird SBE 25) was equipped with an oxygen sensor (SBE 43), and a fluorescence (chlorophyll-a) sensor. The monitoring program was interrupted in 2020 due to the Covid-19 pandemic and only a few weeks of data are available. Therefore, this study excludes the year 2020.

The sediments at the sampling station are described as fine-grained LaHave clay which dominates in BB at water depths >30 m (Fader and Miller 2008a). Shallower depths of the basin have coarser sediment, with some locations containing gravel and boulders (Fader and Miller, 2008). Sediment samples were obtained from the Compass Buoy sampling station during 2019 on 12th February, 7th May, 26th August and 7th November corresponding to distinct seasons, that is, mid winter, post-spring bloom, late summer, and fall, respectively. Sediment cores were collected using a multi-corer device (KC Denmark) that houses 60 cm-long polycarbonate liners with 10 cm internal diameter. Approximately 35 cm of sediment and 25 cm of water were recovered with an intact sediment-water interface (SWI). Cores were transferred to a cool room at Dalhousie University within 2-3 hours. The cores were extruded until ~6 cm of water was left above the SWI. Afterwards, the overlying water was bubbled with an air:N_2 gas mixture to maintain the oxygen concentration at *in-situ* levels and stored overnight in darkness. A single sediment core from each sampling date was used for oxygen microsensor profiling.

Oxygen profiling was conducted with a Clark-type microsensor (Unisense OX-100). The O_2 sensor was calibrated using a 2-point calibration of 100% saturation using aerated water, and 0% oxygen saturation using ascorbate-sodium hydroxide solution. Dissolved oxygen solubility was corrected for salinity and temperature using the Unisense software. The sensor was mounted on a Unisense micromanipulator approximately 2-5 mm above the SWI (determined by eye). Duplicate or triplicate profiles were recorded at 100 μm depth resolution until oxygen reached zero concentration. Sediment porosity was later determined from one of the sampling events after sectioning the sediment core at 1 cm intervals.

A benthic instrument pod was moored 5 m off the bottom (recorded data at 60 m water depth) over the period 20th August 2018 to 7th December 2018. The pod was equipped with a CTD sensor (Seabird SBE 37-SI S/N 2975) and an oxygen sensor (RBR coda Optical Dissolve Oxygen sensor S/N 93074). These sensors recorded measurements at ~1 minute intervals.

2.3.2 Stratification parameter

Density profiles derived from CTD data were used to calculate a water column stratification parameter, ϕ (J m^{-3}) that represents the energy required to fully homogenize the water column through vertical mixing (Simpson 1981):

$$\phi = \frac{1}{h}\int_{-h}^{0}(\rho_{av} - \rho_{w})gz\,dz \quad \text{with } \rho_{av} = \frac{1}{h}\int_{-h}^{0}\rho_{w}dz$$

where h is the total depth of water column (m), z is depth (m), g is gravitational acceleration (m s^{-2}), ρ_w (kg m^{-3}) is density at depth z and ρ_{av} (kg m^{-3}) is the depth-averaged water column density.

2.3.3 Calculation of diffusive oxygen uptake (DOU)

We largely followed the procedure of Glud (2008) for interpreting microsensor profiles to

$$DOU = -D_0 \frac{dO_2}{dz} \qquad (1)$$

calculate the diffusive oxygen uptake (DOU). It was determined from each microsensor profile using three different approaches. First, DOU was calculated from the linear oxygen gradient across the diffusive boundary layer (DBL). The DBL thickness was identified from the slight change in slope in linear oxygen profiles at the junction of the DBL and SWI. In Eq (1), D_0 is the diffusion coefficient of O_2 adjusted for the temperature and salinity of the overlying water (calculated using R-package “marelac” (Soetaert et al. 2010a)) and dO_2/dz is the O_2 concentration gradient within the DBL.

Second, since DOU calculated above may be subject to errors due to incorrectly estimating the ex-situ DBL thickness (Bryant et al. 2010), the DOU was also calculated using Fick’s first law of diffusion using the oxygen gradient just below the SWI:

$$DOU = -D_s\varphi \frac{dO_2}{dz} \qquad (2)$$

Where φ is porosity, Ds is the tortuosity-corrected diffusion coefficient for oxygen after Boudreau (1996); $D_s=D_0/(1-2ln(\varphi))$. The first three points below the SWI were used to calculate the oxygen gradient.

Finally, each profile was modeled using a 1D steady state reaction-transport model, assuming that the transport of oxygen into sediment was controlled by molecular diffusion and that oxygen consumption can be described using Michaelis-Menten kinetics (Soetaert et al. 1996a; Boudreau 1997),

$$D_s\varphi\frac{d^2O_2}{dz^2} = \varphi k_{O2.sedi}\cdot\frac{O_2}{O_2+K_{sO2}} \tag{3}$$

where $k_{O2.sedi}$ is a maximum rate of oxygen consumption and K_{sO2} is the half saturation constant. The solution of equation (3) was fit to each measured profile by adjusting $k_{O2.sedi}$ whereas K_{sO2} was set to a small value (K_{sO2} =1 µM) to prevent negative oxygen concentrations. DOU was then determined from the depth integrated rate of oxygen consumption. This approach allows the DOU to be quantified in addition to the O_2 consumption rate verses depth in the sediment.

In theory, all three approaches should give the same result. In reality this is not necessarily the case because accurate determination of the sediment water interface and the DBL thickness can be difficult with a microelectrode recording at 100 µm vertical resolution. The use of all three approaches provides a check on the consistency of each DOU calculation method.

2.3.4 Benthic pelagic coupled oxygen model

A dynamic 1-D (vertical) coupled model of the water column and sediment was used to reproduce the seasonal oxygen dynamics of BB bottom water at the Compass Buoy site. Equations 4 and 5 represent dissolved oxygen mass conservation for the water column and sediment, respectively.

$$\frac{dO_2}{dt} = K_z(t)\frac{d^2O_2}{dz^2} - k_{O2w}.chla(t).\frac{O_2}{O_2+K_{sO2}} \tag{4}$$

$$\varphi \frac{dO_2}{dt} = D_s \varphi \frac{d^2 O_2}{dz^2} - k_{O2.sedi} \cdot \varphi \cdot \frac{O_2}{O_2 + K_{sO2}} \qquad (5)$$

where K_z is the time-variable eddy diffusivity for parameterizing vertical mixing and *chla* is the depth-integrated chlorophyll-a content (see below). The formulation of equation 4 and 5 are conceptually similar to Burt et al. (2013) and Soetaert et al. (1996b). The model domain consists of a 50 m water column which extends from 20 m to 70 m water depth, and a domain comprising 1 cm of sediment at the bottom of the water column. The latter is justified since the oxygen penetration depth is only 1-2 mm (see Results). The water and sediment domains both consist of 100 equally spaced grid cells. We chose 20 m as the upper boundary to represent the water below the sill. The outflow of the Sackville River, tidal currents, and wind-induced mixing are generally restricted to the upper 20 m, leaving the otherwise stratified BB water below the sill relatively isolated from mixing in the surface layer (Shan et al. 2011b; Shan and Sheng 2012). This allows a 1-D approximation to be applied for the modeled water column below 20 m, where changes in solute concentration due to horizontal advection are usually negligible.

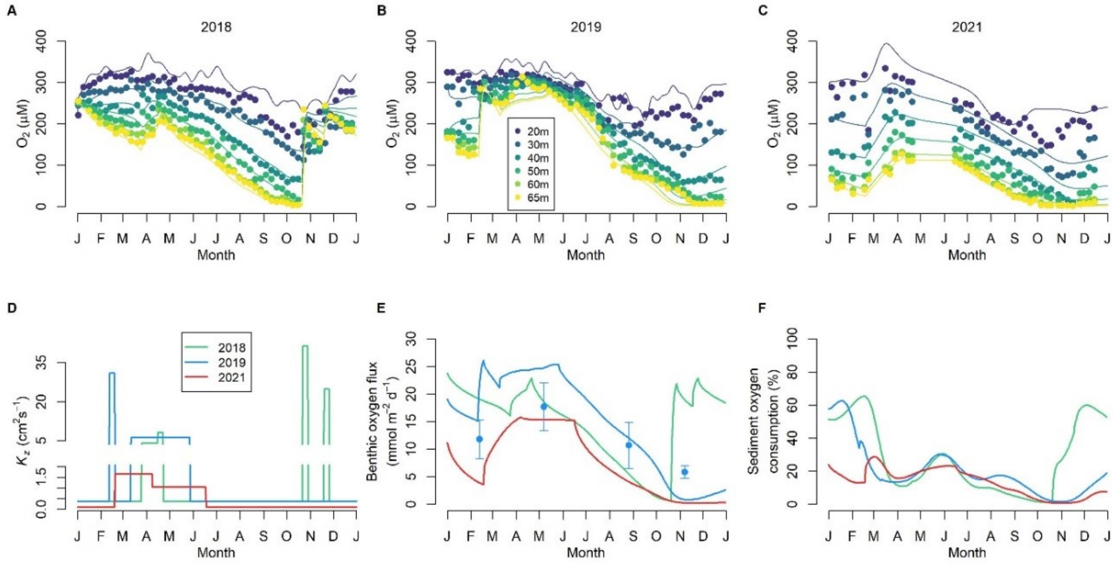

Figure 2.2. Benthic-pelagic model simulations. (A), (B) and (C) show the dissolved oxygen concentration at different water depths for 2018, 2019 and 2021 respectively. The filled circles and curves represents the observed and modeled oxygen concentration, respectively. (D) Modeled eddy diffusivity (Kz); note the vertical axis break. (E) Modeled benthic oxygen fluxes. The symbols show the observed mean DOU for 2019. (F) The contribution of sediment to total oxygen consumption as predicted by the model

Wintertime eddy diffusion is typically high due to reduced stratification and convective mixing results in oxygenation of the entire water column. This was determined empirically based on the observed oxygen concentration at 60 m. The non-conservative nature of dissolved oxygen makes it a useful indicator of active mixing, while conservative tracers such as temperature or salinity can only indicate that mixing has occurred. Spring mixing was defined as the period between the onset of a sustained increase in bottom water oxygen and the timepoint when bottom water oxygen began to decline.

The eddy diffusivity during winter was adjusted until modelled oxygen concentrations matched the observed rise in bottom water oxygen. During the stratified summer period, Kz was estimated by fitting the weekly BBMP temperature profiles (Figure A1). Shelf water intrusions were parameterized by increasing the K_z to match the observed rise in oxygen concentration in the bottom waters (Figure 2.2 **Error! Reference source not found.**D, Table A1).

The consumption of oxygen in the water column via respiration of organic matter is described by the last term in Eq. 4. The depth-integrated chlorophyll fluorescence from CTD casts (Figure 2.3F) was used as a proxy for total organic matter load in the water column. The model ignores the additional contribution of fluvial organic matter from the Sackville River due to a lack of data. However, we believe that this contribution would be a second order effect given that the fluvial discharge is small compared to the tidal volume and total volume of the basin. We use a depth-integrated approach rather than using vertically resolved chlorophyll data since depth-integrated chlorophyll better represents the primary production and respiration during particle sinking and, therefore, the organic matter inventory in the water column. It also avoids uncertainties arising from different particle sinking speeds. The aerobic respiration dependency on chlorophyll-a was set as first-order, and a Michaelis-Menten type dependency was chosen for oxygen; here we used $K_{sO2} = 20$ μM which gave a good model-data fit. The water column respiration rate constant, k_{O2w}, was constrained using the dissolved oxygen concentrations and assumed to be constant. It was obtained by fitting of the model to the observed water column oxygen data for the year 2019. This year was chosen because it was free of intrusions and displayed relatively normal winter mixing. The same value was then used for the simulations for 2018 and 2021. We reiterate that oxygen data was also used to constrain mixing during the winter period. However, this does not compromise the use of oxygen data to concurrently estimate k_{O2w} since the rapid increase in oxygen during winter mixing is much larger than the rate of oxygen decline due to respiration. For the stratified period, when the Kz is an order of magnitude lower, temperature was used instead to fit Kz independently.

Transport of oxygen into the sediment was determined solely by molecular diffusion (Eq. 5) and coupled to the oxygen dynamics in the water column (Eq. 4) through the flux across the sediment water interface. The rate of sediment oxygen consumption, $k_{O2.sedi}$, and the half-saturation constant, K_{sO2}, were assumed to be constant and taken as the mean values of the microsensor measurements performed in 2019.

The oxygen concentration measured weekly at 5 m water depth was assumed to be representative of the oxygen concentration of the surface layer (< 20m) and was imposed as the upper boundary condition for the water column domain. Oxygen continuity between the water column and sediment was achieved by setting the time-variable bottom water oxygen concentration as the upper boundary for the sediment domain. Benthic oxygen uptake represented a loss of oxygen from the lower water column. A zero-flux condition was applied for oxygen at the lower boundary of the sediment domain. Model parameter values are given in Table S1. The model was solved in the R programing environment using the R packages FME (Soetaert and Petzoldt 2010b), ReacTran (Soetaert and Meysman 2012) and deSolve (Soetaert et al. 2010c).

2.4 Results

2.4.1 Water column

The bottom water properties of years 2018, 2019 and 2021 show that the overall trends of these three years were generally consistent with the climatology and other long-term observational studies in the basin (Figure 2.3) (Li and Harrison 2008a; Haas et al. 2021). Contour plots of temperature, salinity, and oxygen (Figure A2) indicate that surface cooling during winter and spring reduces the stratification allowing a stronger vertical convection and ventilation of bottom waters. The stratification during this period was lowest in all three years, coinciding with lowest sea surface temperature (SST). Stratification was highest during the period July-September when SST was also highest, suggesting stratification was primarily controlled by SST. In 2021, the SST was generally higher than the climatology which led to the noticeably higher stratification throughout the year Figure 2.3D,E).

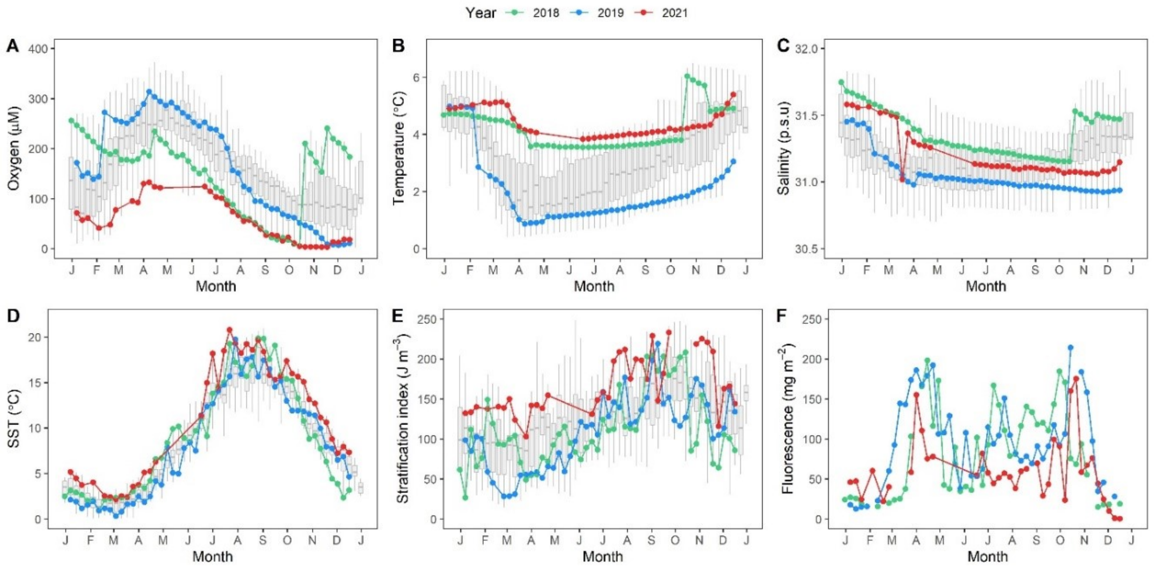

Figure 2.3. The boxplots represent the climatology of Bedford Basin (2000-2021) and the colored curves show the values for the indicated years derived from weekly CTD deployment at the Compass Buoy site. (A), (B), (C) Dissolved oxygen concentration, temperature, and salinity at 60 m water depth. (D) Sea surface temperature (SST) at 2 m depth. (E) Water column stratification index (see text for details). (F) Depth integrated chlorophyll fluorescence. Note that the climatology excludes 2020 data since the data collection was limited due to covid-19 restrictions.

At the start of 2018 bottom waters were oxygenated due to a shelf water intrusion at the end of 2017 (Haas et al. 2021). Winter mixing in 2018 was brief as can be seen in the rapid increase in oxygen concentration that occurred in April together with a decrease in salinity and temperature (Figure 2.3A,B,C). In the absence of further winter mixing, bottom water oxygen declined consistently in 2018 to near anoxic conditions until mid-October when an intrusion from the Scotian Shelf re-oxygenated the bottom water. This was followed by a second intrusion in November, marked by the sudden increase in oxygen and salinity primarily affecting the deeper layers of the basin (Figure 2.3A,C; Figure A2D,J).

The vertical winter mixing regime in 2019 was longer and persisted from mid-February to mid-April. The bottom water temperature was 0.8 °C at this time and the lowest of the three years considered here, whereas the winter oxygen concentration was the highest (314 µM). No intrusion occurred in 2019 and the bottom water oxygen concentration consistently declined to near anoxia.

The winter mixing was particularly weak in 2021. Oxygen increased only slowly from mid-February to May. The maximum bottom water oxygen concentration in winter reached only 132 μM, compared to >200 μM for 2018 and 2019. A steady decline in the bottom water oxygen across all three years was observed once the mixing phase ended and the surface water temperature increased, leading to stratification.

A phytoplankton spring bloom occurred every year following the cessation of water column mixing (Figure 2.3F, Figure A2M-O). Chlorophyll-a fluorescence maxima were observed between 5 and 10 m (Figure A2M-O). The 2021 spring bloom was the weakest (peak chlorophyll 11.1 mg m^{-3}) whereas 2018 and 2019 showed similar spring bloom intensities (peak chlorophyll concentration 21.5 mg m^{-3}). Primary production persisted throughout the stratified period and a prominent second phytoplankton bloom was observed during the fall months. Particularly, an intense fall bloom in 2019 followed shortly after Hurricane Dorian on 7th September 2019, and this was associated with the highest chlorophyll-a concentration (24.5 mg m^{-3}) measured over the entire study period. The maximum fall bloom intensity in 2018 and 2021 were similar at 15.2 and 15.4 mg m^{-3}, respectively.

Bottom waters experienced hypoxic conditions in all three study years. The onset of hypoxia occurred earliest in 2021 followed by 2018 and 2019. The total duration of hypoxia in the bottom water in 2018, 2019, and 2021 was 11, 12, and 28 weeks, respectively. The lowest oxygen concentrations at 60 m were 5.0, 6.7, and 2.7 μM for 2018, 2019, and 2021, respectively. In 2018 and 2019, hypoxia was restricted to the lower 30 m of the basin whereas in 2021 hypoxia extended over the lower 40 m (Figure A2J-L). The 2018 hypoxic event was, however, interrupted by an intrusion of relatively dense, warmer oxygenated water in mid-October and again in mid-November. The intrusion appeared to displace the low-oxygen water to mid depth, resulting in a mid-depth oxygen minimum (Figure A2J). Finally, assuming <0.2 mg/l O_2 (=6.25 μM) as the threshold for anoxia (Testa et al. 2017), the Bedford Basin bottom water experienced anoxia in 2018 and 2021 for periods of 1 and 6 weeks, respectively.

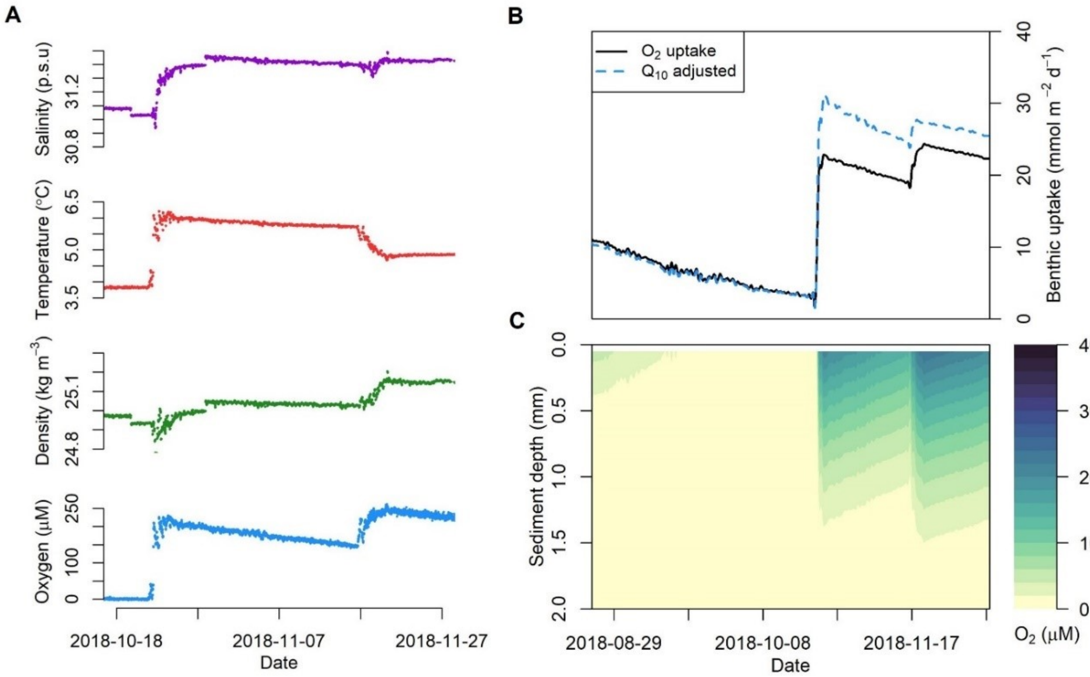

Figure 2.4 High resolution data recorded by the benthic instrument pod deployed at 60 m water depth in late 2018, showing the intrusions of Scotian Shelf water to Bedford Basin. (A) The panels (top-bottom) show bottom water salinity, temperature, density (-1000 kg/m^3) and dissolved oxygen concentration, respectively. (B) Benthic-pelagic model simulation of O_2 uptake suggests that the benthic flux increases rapidly following the first intrusion. The dashed curve represents a simulation with a Q_{10} value of 20, and the solid curve show a simulation without accounting for the temperature increase ($Q_{10} = 1$). (C) Change in oxygen penetration depth in the sediment following the intrusions.

The benthic instrument pod deployed at 60 m depth in 2018 recorded both intrusions at high temporal resolution (Figure 2.4A). The first intrusion took place on 22 October 2018 and within a few hours bottom water oxygen concentrations increased from ~10 to 200 µM, temperature increased by ~2.2 °C and salinity by ~0.4. The second intrusion on 16 November 2018 was more protracted and led to an increase in oxygen concentrations from 140 to 230 µM. Salinity increased marginally, and temperature decreased, presumably because the second intrusion occurred late in the year when air temperature was lower, resulting in an increase in density. The rapid change in bottom water after the intrusions is indicated by the temperature-salinity plots in Figure A3. A steady decline in oxygen concentrations was observed after each intrusion.

Table 2.1. Oxygen utilization rate in the water column as determined from the local decline rate in the specified periods at 60 m water.

	Period	**Oxygen utilization ($mmol\ m^{-3}\ d^{-1}$)**
2018	Stratified period [18/04/2018 – 17/10/2018]	1.31±0.03
	After 1st intrusion [24/10/2018 – 14/11/2018]	2.68±0.04
	After 2nd intrusion [21/11/2018 – 19/12/2018]	1.91±0.17
2019	Stratified period [10/04/2019 – 18/12/2019]	1.39±0.05
2021	Stratified period [16/06/2021 – 14/10/2021]	0.99±0.04

The summertime oxygen utilization rate estimated using the local decline rate, i.e. dO_2/dt, (Table 2.1) in 2018 and 2019, determined from the periods of steady oxygen depletion at 60 m water depth, were similar at 1.31±0.03 and 1.39±0.05 mmol m^{-3} d^{-1}, respectively. The rate was lower in 2021 at 0.99±0.04 mmol m^{-3} d^{-1}. However, oxygen utilization was significantly higher in 2018 following the first and second intrusions at 2.68±0.04 and 1.91±0.17 mmol m^{-3} d^{-1} (Table 2.1).

2.4.2 Benthic oxygen penetration depth and DOU

The seasonal benthic oxygen flux and oxygen penetration depth (OPD) in the sediment was determined from the oxygen profiles measured in sediment cores using microsensors. OPD was highest in May (1.7±0.1 mm) after the spring bloom when bottom water oxygen was also highest (Figure 2.5A, Table 2.2). At other times the OPD was <1 mm with no clear seasonal variation. The different methods of calculating DOU showed consistent patterns (Figure 2.5B). DOU calculated from the model (RTM) (Eq. 3) gave the highest DOU followed by the application of Fick's First Law below the SWI (Eq. 2) and in the DBL (Eq. 1). However, in most cases the DOU determined from the SWI and RTM approaches were similar, whereas the DBL approach gave noticeably lower estimates. This could be due to the use of the microsensor recording at 100 μm vertical resolution that might have been too low to determine accurately the DBL thickness. Mean DOU was the highest in May and lowest in fall, coincident with minimum oxygen concentrations in the bottom water.

DOU in winter and late summer showed intermediate values. Mean annual DOU based on all three methods ranged from 5.8 to 17.7 mmol m^{-2} d^{-1} with an average of 11.5±4.8 mmol m^{-2} d^{-1}.

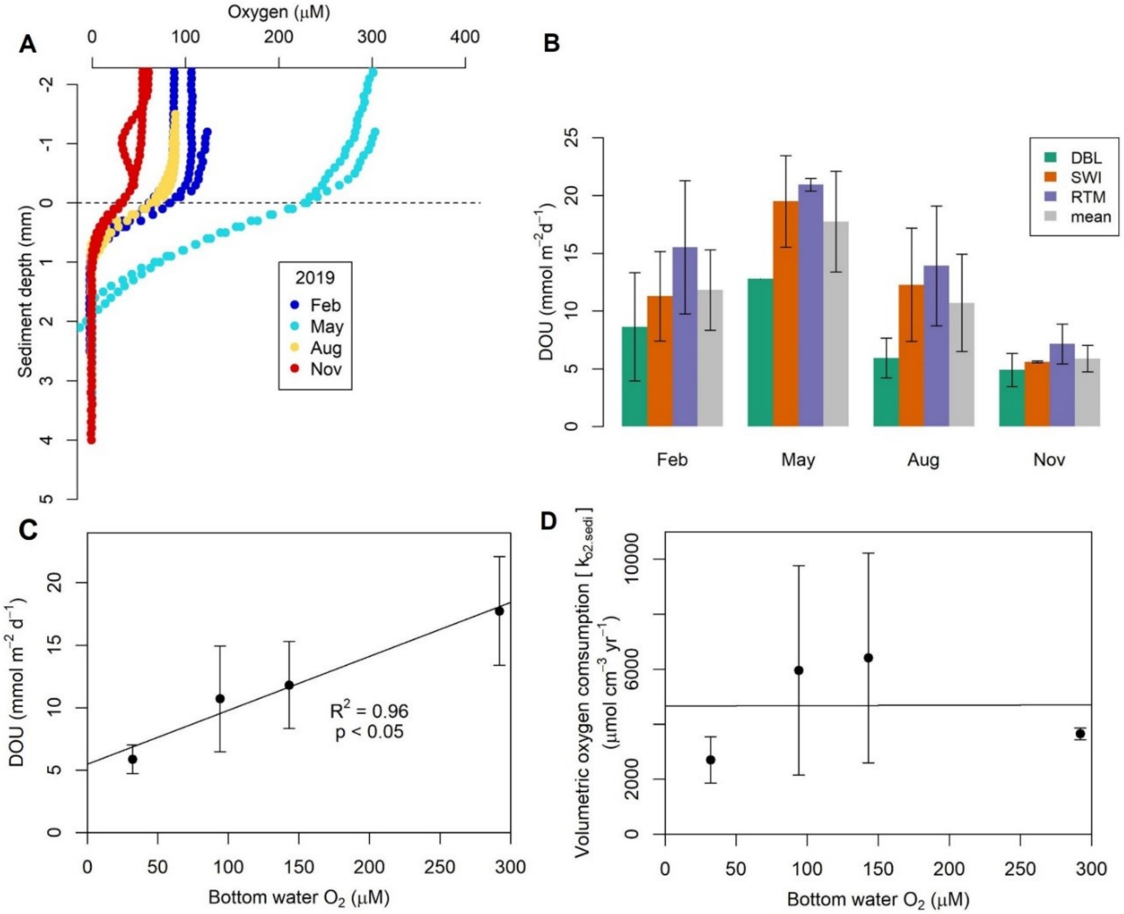

Figure 2.5. (A) Sediment oxygen microsensor profiles measured in sediment cores from Bedford Basin. The horizontal dashed line denotes the sediment-water interface. (B) Diffusive oxygen uptake determined from the oxygen microsensor profiles derived from three approaches; DBL (oxygen gradient in the diffusive boundary layer (DBL)), SWI (from the linear oxygen gradient just below the sediment water interface), RTM (model fit of oxygen data in (A)). (C) Mean DOU is significantly ($p<0.05$) correlated with bottom water oxygen concentration. (D) No significant correlation was observed between bottom water oxygen concentration and sediment oxygen consumption rate.

Table 2.2. Sediment microsensor measurement showing oxygen penetration depth in the sediment, benthic diffusive boundary layer thickness, and diffusive oxygen uptake (DOU) calculated from three different approaches – (i) oxygen concentration gradient at the benthic diffusive boundary layer (DBL), (ii) oxygen concentration gradient just below the sediment water interface (SWI) and (iii) steady-state reactive transport model (RTM), respectively. Volumetric sediment oxygen consumption rate constants as determined by the model are also reported.

2019	Bottom water O_2 (μM)	Oxygen Penetration Depth (mm)	Diffusive boundary layer thickness, δ_{DBL} (mm)	Diffusive oxygen uptake (DOU) (mmol m^{-2} d^{-1})	Oxygen consumption rate, ($k_{O2.sedi}$) (μmol cm^{-3} yr^{-1})
Feb (*n*=3)	143	0.8±0.1	0.4±0.2	(i) 8.5±4.7 (ii) 11.3±3.9 (iii) 15.5±5.8	6415±3810
May (*n*=2)	292	1.7±0.1	0.5	(i) 12.8 (ii) 19.5±4 (iii) 20.9±0.5	3656±216
Aug (*n*=2)	94	0.8±0.2	0.3±0.1	(i) 5.9±1.7 (ii) 12.3±4.9 (iii) 13.9±5.2	5959±3803
Nov (*n*=2)	32	0.9±0.1	0.3±0	(i) 4.9±1.5 (ii) 5.6±0.1 (iii) 7.2±1.7	2707±840

A one-way ANOVA test of DOU across the seasons showed significant differences in mean values (*p=0.02, F-value= 5.6*). However, no significant differences of mean DOU values were found among the three methods used (*p=0.2, F-value=1.6*), suggesting that DOU exhibited statistically significant intra annual variability.

The seasonal mean DOU correlated significantly with bottom water oxygen concentration (R^2=0.96, *p*=0.01, Figure 2.5C). The seasonal maximum sediment oxygen consumption rate ($k_{O2.sedi}$,) determined from microsensor profiles was 4700±1800 μmol (O_2) cm^{-3} yr^{-1} and did not show any significant pattern with bottom water oxygen concentrations (Figure 2.5D, Table A1). Therefore, we assumed that the sediment respiration rate constant was seasonally invariable in the coupled benthic-pelagic model.

2.4.3 Coupled benthic-pelagic model

Our coupled benthic-pelagic model was able to simulate the seasonal oxygen concentrations below the sill depth in the BB (20-70 m) for 2018, 2019 and 2021 (Figure 2.2). The wintertime *Kz* values estimated in this study (Table A1, Figure 2.2D) fell within the eddy diffusivity values (1-100 $cm^2 s^{-1}$) reported from an extensive study of UK coastal waters (Riddle and Lewis 2000). However, the stratified period *Kz* value (Figure 2.2D, Table A1) was lower than previously estimated for BB by Burt et al., (2013), yet similar to the eddy diffusion coefficient estimated for Saanich Inlet (Hamme et al. 2015); a similarly stratified coastal basin. Along with bottom water oxygen, this result indicates winter mixing in 2018 started slowly, immediately followed by a strong mixing. In 2019, winter mixing was stronger and longer, and occurred in two phases (Figure 2.2D). In 2021, the winter mixing was the weakest of the three years yet persisted for several months. During the summer stratified period with low *Kz* (Figure 2.2D, Table A1), net oxygen consumption occurred and oxygen in the bottom water declined steadily in all three years.

Modelled water column respiration ranged from 0.002 to 3.37 mmol O_2 m^{-3} d^{-1}. Mean water column respiration equalled 1.21±0.84, 1.43±0.87 and 0.84±0.42 mmol m^{-3} d^{-1}, respectively, for 2018, 2019 and 2021. Depth-integrated water column respiration ranged from 3.73 – 164.19 mmol m^{-2} d^{-1}, with annual mean values for 2018, 2019 and 2021 of 60.92±40.45, 71.61±42.41 and 42.42±19.36 mmol m^{-2} d^{-1}, respectively. Simulated benthic oxygen uptake for 2019 compared favorably with the DOU determined from microsensor profiles (Figure 2.2E). Mean benthic oxygen uptake was 14.9±6.7, 14.8±8.7 and 7.3±5.7 mmol m^{-2} d^{-1} for 2018, 2019 and 2021, respectively. Mean sediment uptake over all three years was 12.35±7.94 mmol m^{-2} d^{-1}. The seasonal variation of the sediment contribution to the total oxygen consumption is shown in Figure 2.2F. Overall, sediment oxygen uptake contributed approximately one fifth of total oxygen respiration below sill depth (>20 m), with mean benthic contributions of 28%, 20%, 14%, respectively, for 2018, 2019 and 2021.

2.5 Discussion

2.5.1 Pelagic and benthic oxygen respiration

Our model-derived mean BB water column respiration rate of 1.16±0.78 mmol O_2 m^{-3} d^{-1} is higher than previous estimates of 0.3 mmol O_2 m^{-3} d^{-1} (Burt et al. 2013a) and lies at the lower end of the global range of water-column respiration (0.02-75 mmol O_2 m^{-3} d^{-1}) (Robinson and Williams 2005). It is, however, similar to the rate of 1.2 mmol m^{-3} d^{-1} estimated for the Scotian Shelf (Thomas et al. 2012) and to the rate of 1.3 mmol O_2 m^{-3} d^{-1} determined in 2002 by Punshon and Moore (2004). The mean rate coincides with the oxygen utilization estimated from the rate of oxygen decline at 60 m during the stratified period (Table 2). The enhanced oxygen utilization following intrusions (Table 2) could be due to warmer water temperature elevating respiration rates (Haas et al. 2021).

In the organic-rich Bedford Basin sediment (Fader and Miller 2008a), DOU is proportional to bottom water oxygen concentration, implying that the benthic O_2 flux is diffusion limited. Similar observations have been made in other studies (Rasmussen and Jorgensen 1992; Rabouille et al. 2021). The annual mean DOU in 2019, based on four seasonal measurements in this study, was 11.5±4.8 mmol m^{-2} d^{-1}, and model derived mean benthic uptake was 12.6±7.9 mmol m^{-2} d^{-1}. The mean total benthic oxygen uptake (TOU) determined previously in BB using whole core incubations was 17.6±10 mmol m^{-2} d^{-1} (Hargrave 1978a), suggesting that non-diffusive transport processes such as bioirrigation and macrofaunal respiration could contribute ~30% to TOU in BB sediment. This is lower than that reported by Glud (2008) who argued that non-diffusive processes at water depths <100 m could be ~60% of TOU. A lower contribution of faunal-mediated respiration in BB is likely due to the seasonally hypoxic nature of the bottom water where macrofaunal abundances might be lower (Fader and Miller 2008a). Burt et al. (2013) estimated a benthic oxygen flux in BB using radium distributions of 29 to 59 mmol O_2 m^{-2} d^{-1}; a factor of 2 to 4 higher than our estimate. However, these measurements were made in 2010 within six weeks following an intrusion event.

To examine the influence of a sudden intrusion of warm oxygenated water on the sediment oxygen flux, we forced the sediment model with the high-resolution oxygen data from the benthic instrument pod as a sediment-water boundary condition. The results show that oxygen flux increased by a factor of seven from 3 to 22 mmol m^{-2} d^{-1} over a few hours synchronously with oxygen concentration (Figure 2.4B). The higher temperature of intruding water could also further increase the sediment oxygen respiration rate and benthic oxygen uptake. We utilized the Q_{10} formulation to evaluate the impact of increased water temperature following the intrusion. The Q_{10} formulation is used to describe the temperature dependence on rates of biological processes, where the value of Q_{10} denotes the ratio of reaction rates for a temperature difference of 10 °C (Tjoelker et al. 2001). It is described as

$$R_2 = R_1\, Q_{10}^{(T_2 - T_1)/10} \tag{6}$$

where R_1 and R_2 are the reaction rates at temperature T_1 and T_2 (Sasaki et al. 2012). Re-running the model with a Q_{10} factor 20, previously suggested for BB (Haas et al., 2021), increased the benthic oxygen flux (Figure 2.4B) to 31 mmol m^{-2} d^{-1}. These values are in good agreement with the post-intrusion benthic oxygen flux of 43.7±15.1 mmol m^{-2} d^{-1} determined by Burt et al., (2013). The intrusion also increased the modelled OPD in the sediment substantially (Figure 2.4C). Hence, intrusions may impact sediment biogeochemistry by, for instance, enhanced oxidation of reduced substances that accumulate during hypoxic periods, and through removal of bioavailable nitrogen through more efficient coupled nitrification-denitrification that functions only weakly under hypoxic conditions (Fennel et al. 2009; Middelburg and Levin 2009).

The benthic oxygen dynamics in BB are consistent with other similar and related oceanic settings. In Chesapeake Bay, seasonal sediment oxygen consumption was found to be between 1.5 and 26.8 mmol m^{-2} d^{-1} with the water temperature and bottom water oxygen concentrations being the main controlling factors (Cowan and Boynton 1996). In the nearby lower St. Lawrence Estuary, the TOU was lower at 6.4 mmol m^{-2} d^{-1} at >200 m depth (Katsev et al. 2007). However, in fine Scotian Shelf sediment, TOU ranges from 8 to 12.5 mmol m^{-2} d^{-1} (Grant et al. 1991), which is close to our estimates of DOU from BB. Nevertheless, a detailed measurement of TOU would be required to verify the proportion of DOU and TOU and determine any changes in oxygen flux which might have occurred due to, for example, changes in organic matter and nutrient loading with continuing urbanization of the surrounding area. For the remainder of the discussion, we assume that DOU is representative of the total benthic oxygen uptake.

2.5.2 Oxygen budget for Bedford Basin

In the following, our model was used to derive an oxygen budget for BB below the depth of the sill (Figure 2.6) for each of the three years. In 2018 and 2019, the model estimated that a total of 25.6 and 25.1 mol O_2 m^{-2} y^{-1} was delivered to subsurface waters, respectively, decreasing to 14.3 mol O_2 m^{-2} y^{-1} in 2021 (Figure 2.6A). In 2018 and 2019, winter mixing accounted for 28.5% and 70% of the oxygen supply, respectively. Intrusions in 2018 contributed 35.5% to deep water oxygen, equivalent to 9.1 mol O_2 m^{-2} y^{-1}, which is comparable to the supply during winter mixing. Owing to weak winter mixing in 2021, the absence of intrusions and anomalously high SST (Figure 2.3D,), the oxygen supply to deep waters was the lowest of the three study years, with the winter mixing period accounting for 81% of total oxygen input (Figure 2.6B) and the remaining 19% supplied during the stratified period. These results show that deep waters receive the majority of the oxygen during winter mixing, and hence the ventilation largely depends on the strength and duration of winter mixing and stratification. Intrusions, when they occur, can supply equivalent amounts of oxygen in discrete episodic events.

To further investigate the impact of intrusions, we performed a model experiment where we ran the model for 2018 without intrusions. The oxygen budget was then compared with the model output simulating the real 2018 condition with intrusions (Figure A4). The lack of intrusions resulted in 27% less oxygen supply to the bottom water and a 14% decline in the annual mean water column oxygen concentration (193 μM with intrusions vs 166 μM without intrusions). Integrated over the post intrusion time frame in 2018 (Julian day 295 to 365), total oxygen supply decreased substantially to 63% without the intrusion and mean bottom water oxygen concentration decreased to 80 μM versus 219 μM with intrusions. The absence of intrusions also prolongs hypoxia at 60 m depth for the remainder of the year (mean concentration of 11±5 μM and duration of 21 weeks). The model also predicted that the reduced oxygen supply to the bottom waters could have resulted in 1.3 mol m^{-2} yr^{-}

[1] less benthic oxygen uptake (discussed in next paragraph). However, we found little difference (~3%) in the total water column respiration with and without intrusions. This emphasizes that intrusions are important for ventilation of bottom waters, relieving hypoxic conditions, and for the coupling of sediment and water column processes.

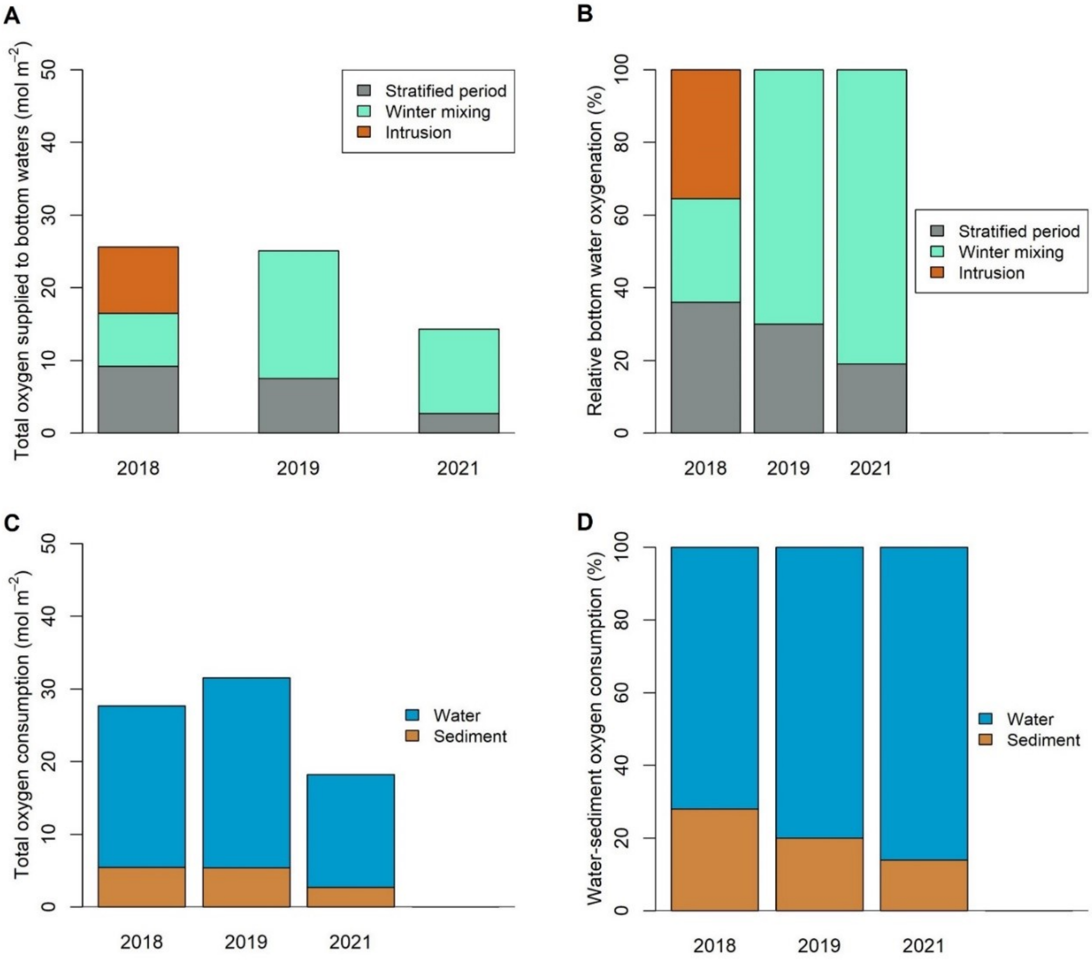

Figure 2.6. Model derived oxygen budget for Bedford Basin. (A) Annual oxygen supply to Bedford Basin bottom waters (>20 m) and (B) the relative contributions. (C) Annual oxygen consumption in the water column and sediment and (D) the relative contributions.

Benthic oxygen consumption was similar for 2018 and 2019 at 5.44 mol O_2 m^{-2} y^{-1}, respectively, whereas in 2021 it was 50% lower (2.7 mol m^{-2} y^{-1}) (Figure 2.6C). Since the DOU is proportional to bottom water oxygen concentration, it is likely that the weaker benthic respiration rates in 2021 were due to poor ventilation of bottom water during winter months. Our model suggests that total water column respiration was 22.2, 26.1 and 15.5 mol O_2 m^{-2} y^{-1} for 2018, 2019 and 2021, respectively. On average, water-column respiration accounted for ~80% of the total below sill depth oxygen consumption at the Compass Buoy site, whereas benthic uptake contributed ~20% (Figure 2.2F, Figure 2.6D). Consistent with our estimates, an oxygen budget for Chesapeake Bay suggested that water column respiration was the main driver of the oxygen demand with benthic respiration accounting for 26% (Li et al. 2015). However, in the St. Lawrence estuary, benthic oxygen demand was estimated to contribute 16-66% of total bottom water oxygen consumption (Lehmann et al. 2009; Bourgault et al. 2012).

Given that the oxygen respiration rate in sediment is 3-4 orders of magnitude higher than in the water column, the water depth plays a key role in the overall benthic contribution to total oxygen respiration (Fennel and Testa 2019). The model was used to derive a relationship between the benthic contribution and water depth, which was found to be best approximated by a logarithmic relation ($R^2=0.98$): $y = -21.46 \ln(x) + 103.58$, where y is the percent benthic oxygen consumption of total oxygen consumption, and x is the height

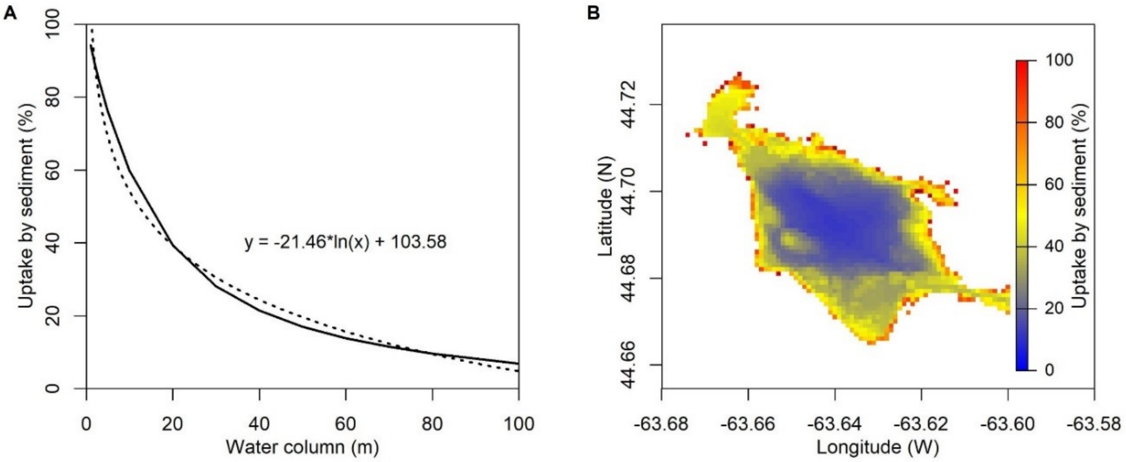

Figure 2.7. (A) Simulated proportion of sediment consumption versus water column depth (solid line). The dashed line shows a logarithmic function that describes the model data (R^2=0.98). This function was applied to Bedford Basin bathymetry to obtain the spatial contribution of benthic oxygen consumption (B).

of water column in meters (Figure 2.7A), similar to the findings by Kemp et al. (1992). A basin-wide estimate of sediment contribution to total oxygen respiration of ~35% was then obtained by applying the bathymetric data (Figure 2.7B). However, it should be remembered that sediment carbon content and grain size play a crucial role in determining the benthic oxygen uptake. The sediment is fine silt at our study site (Fader and Miller 2008a), whereas at shallower depths the sediment is coarser (Fader and Miller 2008a). This may significantly alter oxygen uptake (Huettel et al. 2014), as shown in Scotian Shelf sediments (Grant et al. 1991). Therefore, a more focused study on benthic oxygen uptake rates in different sediment types across the basin is required to accurately determine the overall role of sediment in the BB oxygen budget.

While a full three-dimensional model (Shan et al. 2011b; Shan and Sheng 2012) that fully captured the annual evolution of the surface layer due to changes in temperature, salinity, wind and tidal forcing, would be a more accurate representation of circulation and oxygen dynamics in the Basin, coupling it to a diagenetic sediment model would be computational challenging. The 1-D model used here however is simple enough to be fully coupled to a sediment diagenetic model while still representing the major features of the bottom waters (below 20 m) in the basin.

2.5.3 Sensitivity of hypoxia to variable mixing

Bottom water ventilation occurred in BB during each of our study years, but with variable intensity and duration. An oxygen increase in the bottom water was observed consistently during winters. Comparison of SST, stratification parameter and bottom water oxygen suggests that water column mixing begins when the SST is low resulting in diminished thermal stratification which facilitates convection, causing concomitant decreases in bottom water salinity and temperature along with an increase in oxygen (Figure 2.3, Figure A2). Besides winter mixing, the basin was also oxygenated through intrusions of Scotian Shelf water which occur often late in the year when the bottom water is hypoxic. Thus, intrusions effectively end hypoxia as observed in high latitude fjords and marginal seas (Cottier et al. 2005; Hamme et al. 2015; Holtermann et al. 2020). Noticeably, hurricane strength winds during summer-fall have little effects on water column mixing and bottom water oxygenation of BB unlike in some other coastal systems such as Chesapeake Bay (Testa et al. 2017). Temperature-salinity plots following Hurricane Dorian which passed over BB on 7th September 2019 (Scrosati 2020), showed that deeper layers below the pycnocline were unaffected by the storm (Figure A5). Similar observations were made following the category 2 Hurricane Juan in 2003 (Fogarty 2004) which also had no noticeable impact on the deeper basin (Figure A5).

The mean bottom water oxygen in 2021 was the lowest recorded in the BB timeseries, along with the highest SST and stratification (Figure 2.8A, C). We also found that throughout the timeseries, mean bottom water oxygen correlated weakly but significantly with mean stratification (Figure 2.8A) and that intra-annual stratification correlated strongly with SST (Figure 2.8B), but not with surface salinity. This indicates that surface water temperature plays key role in controlling seasonal stratification and could suggest warming induced deoxygenation in the future. Furthermore, the annual SST has increased in BB at a rate of 0.11±0.02 °C/year, with the strongest increase in the summer-fall months (Figure 2.8C, D). This is an order of magnitude higher than the global SST trend which ranges from 0.007-0.012 °C/year (Hausfather et al. 2017). However, despite this, we found no significant inter-annual correlation between annual SST and stratification from 2000 to 2021. This suggesting the situation is more complicated and other factors in addition to warming may play a role. These could include freshwater inflow and precipitation, storm intensity during winter months, timing, and intensity of shelf water intrusion in the preceding year which would stabilize bottom water by delivering denser water, and regional scale changes in the ocean-current circulation in the northwest Atlantic (Peterson et al. 2017; Jutras et al. 2020). Disentangling the effects of these different drivers on stratification and future oxygen levels would require further study.

Nevertheless, to further explore the sensitivity of future scenarios in terms of winter mixing variability and frequency of intrusions, we performed model experiments to explore how variations of oxygenation during mixing impact the oxygen budget in a system such as BB. Six scenarios were tested, each one over two consecutive years (Figure 2.9). We chose two consecutive years rather than one year because some of the considered scenarios (discussed later) might lead to a memory effect when transitioning from one scenario to another.

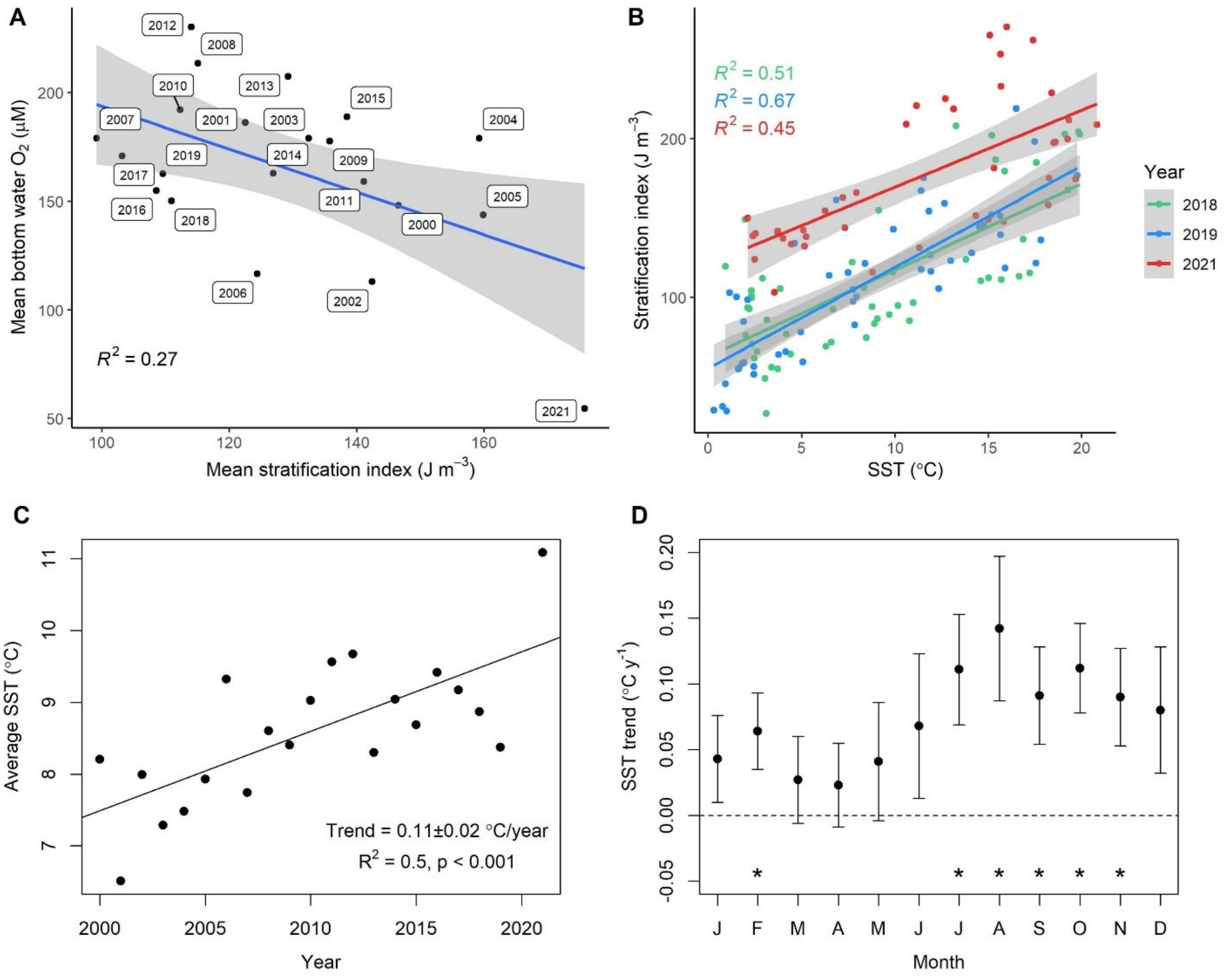

Figure 2.8. (A) Weak but significant ($p<0.05$) correlation between bottom water oxygen and water column stratification across the time-series data at Compass Buoy station. (B) Intra-annual stratification versus SST at 2 m depth ($p<0.05$). (C) Mean annual sea surface temperature (2 m depth) versus time shows a significant positive trend of increasing SST at a rate of 0.11± 0.02°C/year. (D) Monthly trend in increasing SST over the same time period (2000-2021). Asterisks denote the months where the SST increase is significant (*p<0.05*). Most warming takes place during summer-fall.

Therefore, a minimum of two years simulation is required to fully characterize the oxygen dynamics. We assumed that winter mixing occurs every year between mid February to mid March, when the average SST is at its lowest and the bottom water oxygen increases (Figure 2.3A, D). The upper boundary of the water column domain was set as long-term climatology of 5 m BB water. The water column conditions on 1 January 2019 were used as initial conditions.

In the first scenario, the baseline case, the winter mixing coefficient *Kz* was set to 31 cm^2 s^{-1} and the stratified *Kz* was set to 0.37 cm^2 s^{-1} based on the 2019 model result. The simulated baseline water column oxygen concentration and benthic flux are shown in Figure 2.9A, B. The oxygen budget of the other scenarios are compared with the baseline run (Figure 2.9C, Table A2). In the second scenario, the intensity of winter mixing was reduced by 50% by decreasing the wintertime *Kz*. Thirdly, we reduced the winter mixing by 90% to reflect even weaker mixing. In fourth case, 90% weaker winter mixing was tested in addition to a decrease in the stratified *Kz* by 70% (chosen to mimic the modeled 2021 case), reflecting higher-than-usual water column stratification in summer and fall. In the fifth case, based on the previous scenario #3, an intrusion was simulated in October of similar magnitude to the first intrusion of 2018. In sixth and final case, the baseline winter mixing was restored along with intrusions. The different mixing regimes throughout these case studies are summarized in Figure 2.9A.

In the baseline case, the basin was well-oxygenated and the maximum bottom water (60 m) oxygen concentration during winter mixing period was very close to the oxygen concentration at the surface boundary. The basin became hypoxic on week 24, and the total hypoxic period in the bottom water was 28 weeks/year (calculated from year 2). The mean oxygen at bottom water was 99 µM and the mean benthic oxygen flux was 10 mmol m^{-2} d^{-1}. In scenario #2, even though the winter mixing was 50% weaker, the highest winter-time oxygen at bottom water decreased only marginally and the oxygen dynamics were similar to the baseline run. This suggests that stronger mixing than the baseline case will have no noticeable impact in terms of bottom water oxygenation. A 50% reduction in winter mixing intensity also did not show any significant change in the oxygen budget. Yet, a drastic change in the oxygen levels and budget was observed with 90% lower mixing in scenario

#3 (Figure 2.9C). Here, the highest winter-time oxygen at bottom water was 145 μM (similar to 2021 level), which represents a 57% decrease from the baseline scenario.

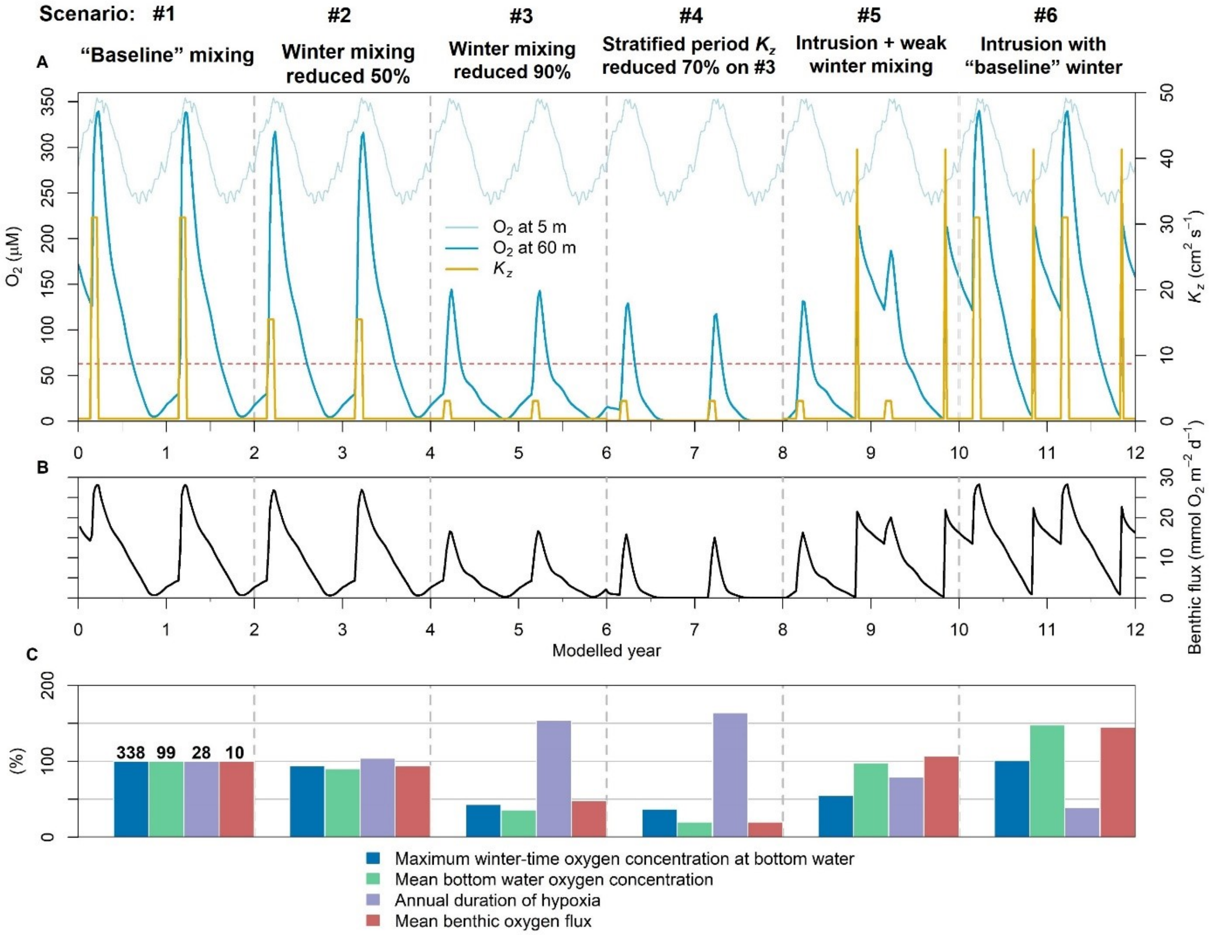

Figure 2.9. Model experiments simulating various mixing scenarios. Different mixing regimes are indicated at the top of (A) and separated by gray vertical dashed lines. (A) Oxygen concentration at simulated upper boundary (5 m) and in the bottom water (60 m). The red dashed line at 63 μM indicates the threshold for hypoxia. The yellow curve shows eddy diffusivity. (B) Benthic oxygen flux. (C) Comparison of the various mixing scenarios relative to "baseline" mixing (scenario #1). The numbers given on the top of the bars for baseline mixing represent maximum winter-time oxygen concentration (μM), mean annual oxygen concentration in the bottom water (μM), annual duration of hypoxia in the bottom water (weeks) and the mean annual benthic oxygen flux (mmol m^{-2} d^{-1}). The other scenarios are given as percentage relative this baseline case.

Consequently, bottom water hypoxia was more severe and prolonged, and the benthic oxygen flux decreased by almost 50%. In the fourth scenario, stronger water column stratification led to more intense hypoxia, and even anoxia, with a corresponding diminishment of the annual benthic oxygen flux. In the fifth case, the intrusion replenished the basin with oxygen ending the hypoxia. Following the intrusion at the end of year 8, the water column was more oxygenated in year 9. Finally, intrusions with baseline winter mixing significantly reduced hypoxia and substantially increased benthic oxygen flux. Thus, the model sensitivity analysis confirms our previous assertions that winter mixing and intrusions play an important role for oxygen turnover in the stratified BB. It remains an open question how their dynamic interplay will be impacted by ongoing changes in SST and oxygenation in the northwest Atlantic.

2.6 Conclusions

Three similar yet uniquely featured years were studied in combination with observations and numerical reactive transport modeling to understand the oxygen dynamics in Bedford Basin in the context of a long running water monitoring programme. Here, we report that the seasonally hypoxic Bedford Basin became seasonally anoxic as the bottom water was observed to have <0.2 mg/l O_2 for 1 and 6 weeks, respectively, in 2018 and 2021.

We conclude that majority of the bottom water oxygenation occurs during winter convective mixing period as a result of cooling of surface waters, and occasionally in summer-fall via rapid intrusions of oxygenated dense Scotian Shelf water. However, mixing during the stratified period also provides a non-negligible oxygen supply to the deeper layers. Oxygen supply during winter mixing and during the stratified period was found to be SST sensitive. We suggest that the potential exists to exacerbate hypoxia as a result of increasing SST, which has been observed in BB at rates that are an order of magnitude higher than for the global ocean. The majority of the oxygen is consumed through water column respiration at the study site, whereas sediment oxygen uptake accounts for one fifth of the total oxygen consumption.

The 1D numerical model was applied to the basin water column below the sill depth and was able to predict the oxygen dynamics over the three-year time-series, suggesting these types of models could be readily implemented in other coastal inlets and freshwater lakes to aid in monitoring and predicting the occurrence of hypoxia. The study shows the importance of maintaining high temporal resolution monitoring for being able to identify controlling factors of oxygen supply and consumption. The study suggests strong links between climate-sensitive physical forcing and biogeochemical cycling thresholds. The success of the oxygen model in simulating the time-series data motivates the use of such models in predicting complete nutrient cycles for similar systems.

Chapter 3: PHYSICAL MIXING IN COASTAL WATERS CONTROLS AND DECOUPLES NITRIFICATION VIA BIOMASS DILUTION[2]

3.1 Abstract

Nitrification is a central process of the aquatic nitrogen cycle that controls the supply of nitrate used in other key processes, such as phytoplankton growth and denitrification. Through time-series observation and modelling of a seasonally stratified, eutrophic coastal basin, we demonstrate that physical dilution of nitrifying microorganisms by water column mixing can delay and decouple nitrification. The findings are based on a four-year, weekly time-series in the subsurface water of Bedford Basin, Nova Scotia, Canada, that included measurement of functional (*amoA*) and phylogenetic (16S rRNA) marker genes. In years with colder winters, more intense winter mixing resulted in strong dilution of resident nitrifiers in subsurface water, delaying nitrification for weeks to months despite availability of ammonium and oxygen. Delayed regrowth of nitrifiers also led to transient accumulation of nitrite (3–8 μmol kg_{sw}^{-1}) due to decoupling of ammonia- and nitrite oxidation. Nitrite accumulation was enhanced by ammonia-oxidizing bacteria (*Nitrosomonadaceae*) with fast enzyme kinetics, which temporarily outcompeted the ammonia-oxidizing archaea

---

[2] Haas, S., Robicheau, B.M., Rakshit, S., Tolman, J., Algar, C.K., LaRoche, J. and Wallace, D.W., 2021. Physical mixing in coastal waters controls and decouples nitrification via biomass dilution. *Proceedings of the National Academy of Sciences*, *118*(18), p.e2004877118. https://doi.org/10.1073/pnas.2004877118

Author contribution: I joined the then ongoing study at an early stage which was initially conceived and started by the co-authors. Along with the first author, I studied the timeseries data. I came up with a numerical modeling scheme and eventually modeled the biogeochemical dynamics of DIN, oxygen and predicted the microbial gene abundances leading to the main take away point of the paper, i.e. physical dilution of microbial biomass controls the onset of nitrification and a strong winter mixing, which sufficiently dilutes resident microbial biomass, can decouple the 2 steps of nitrification – ammonium oxidation and nitrite oxidation, leading to accumulation of nitrite in water.
P.S.: This chapter contains several paragraphs on in-depth microbiology as the paper was a multidisciplinary work by collaboration of three PhD students, however, since I am mostly from chemical oceanography background, I have limited knowledge on the technical aspects of the microbial analysis.

(*Nitrosopumilus*) that dominated under more stable conditions. The study reveals how physical mixing can drive seasonal and interannual variations in nitrification through control of microbial biomass and diversity. Variable, mixing-induced effects on functionally specialized microbial communities are likely relevant to biogeochemical transformation rates in other seasonally stratified water columns. The detailed study reveals a complex mechanism through which weather- and climate-variability impacts nitrogen speciation, with implications for coastal ecosystem productivity. It also emphasizes the value of high-frequency, multi-parameter time series for identifying complex controls of biogeochemical processes in aquatic systems.

3.2 Introduction

Coastal waters worldwide are subject to inputs of anthropogenic nitrogen (N) which impact primary production and marine ecosystems through alteration of both the quantity and speciation (oxidized/reduced, inorganic/organic) of N (Peñuelas et al. 2013; Glibert et al. 2016). These are key controls on phytoplankton growth and community composition, altering patterns and magnitude of primary production, causing eutrophication and harmful algae blooms and impacting carbon flux (Yoshiyama and Sharp 2006; Domingues et al. 2011; Glibert et al. 2016). For example, relative increase in ammonium over nitrate supply can shift phytoplankton community compositions toward smaller species with the potential to cause harmful algal blooms and reduced productivity (Glibert et al. 2016). The speciation of N also exerts control on key microbial N-cycling pathways, including the fixed-N removal processes anammox and denitrification. These pathways depend on the availability of oxidized forms of N that can be converted to N_2 and thereby removed from the pool of readily bioavailable N within ocean waters.

It is therefore essential to understand the processes and environmental factors that control the speciation of dissolved inorganic nitrogen (DIN= $NO_3^- + NO_2^- + NH_3/NH_4^+$) between oxidized (nitrate and nitrite) and reduced (ammonium/ammonia) forms, as well as between organic and inorganic forms (LaRoche et al. 1997; Glibert et al. 2016). A central process controlling DIN-speciation is nitrification, the two-step oxidation of ammonia (NH_3) to nitrate (NO_3^-) via nitrite (NO_2^-). Ammonia-oxidizing organisms (AOO), either archaea (AOA) from the phylum *Thaumarchaeota* or bacteria (AOB), catalyze the oxidation of ammonia to nitrite:

$$\text{Ammonia oxidation (AO): } 2NH_3 + 3O_2 \rightarrow 2NO_2^- + 2H^+ + 2H_2O \quad (1)$$

AO kinetics differ between the two AOO groups, with higher maximum reaction velocities (V_{max}) and ammonium half-saturation constants (K_m) in AOB (Suzuki et al. 1974; Ward 1987; Bollmann et al. 2005) compared to AOA (Martens-Habbena et al. 2009; Horak et al. 2013; Peng et al. 2016). Nitrite-oxidizing bacteria (NOB) are responsible for the second step from nitrite to nitrate:

$$\text{Nitrite oxidation (NO): } 2NO_2^- + O_2 \rightarrow 2NO_3 \quad (2)$$

Recently, an exception to the two-organism nitrification paradigm (Daims et al. 2015; van Kessel et al. 2015) has been recognized through the discovery of complete ammonia oxidation to nitrate (“comammox”) by individual *Nitrospirae* bacteria (Daims et al. 2015; van Kessel et al. 2015). This could play a role in coastal marine waters under some conditions (Xia et al. 2018).

In the ocean, nitrification maxima typically occur at or below the base of the euphotic zone, spatially separated from photosynthetic primary production (Horak et al. 2013; Santoro et al. 2013; Peng et al. 2016). However, vertical transport can supply products of nitrification to the euphotic zone (Yool et al. 2007; Johnson et al. 2010). Incomplete nitrification may therefore affect phototrophic communities, since the speciation of externally-supplied N (e.g. ammonium vs. nitrate) can significantly impact both the structure and productivity of phytoplankton (Glibert et al. 2016).

Accumulation of the intermediate product of nitrification, nitrite, has been documented in a wide range of marine systems, including at the base of the oceanic euphotic zone (Lomas and Lipschultz 2006) and transiently in coastal bights, bays and estuaries (Horrigan et al. 1990; Beman et al. 2010; Heiss and Fulweiler 2016; Schaefer and Hollibaugh 2017; Laperriere et al. 2019). In many cases, the presence of nitrite can be attributed to decoupling of AO and NO, which are usually tightly coupled despite ecophysiological differences between AOA and NOB (Kitzinger et al. 2020). A large variety of environmental factors, including temperature and oxygen, have been associated with the decoupling of nitrification in marine systems (Philips et al. 2002; Bristow et al. 2015; Heiss and Fulweiler 2016; Schaefer and Hollibaugh 2017). Here we describe nitrite accumulation arising from nitrifier regrowth following physical dilution, which might point to a role for nitrifier biomass in a more general mechanism for decoupling nitrification in seasonally stratified water columns.

Physical transport is widely recognized to control phytoplankton growth in aquatic systems, for example through supply of nutrients to the euphotic zone from below (Dutkiewicz et al. 2001; Johnson et al. 2010). Mixing also plays a role in the initiation of spring blooms according to the "dilution-recoupling" hypothesis (Behrenfeld 2010), which posits that dilution of both phytoplankton and grazer biomass leads to fewer grazer-phytoplankton encounters. It has been shown that nitrification can be enhanced by the mixing of ammonium-rich waters into well-oxygenated waters (McCarthy et al. 1984; Laperriere et al. 2019), whereas the mixing-induced transport of NOB biomass away from the depth of optimal growth at the base of the euphotic zone has recently been implicated as a factor explaining local nitrite accumulation (Zakem et al. 2018). Here, we describe a different way in which mixing controls nitrification, whereby seasonal and interannual variations in mixing lead to temporally variable rates of nitrification as a consequence of nitrifier biomass dilution.

High-frequency, long-term measurements of the physical and chemical environment along with the associated microorganisms have been shown to be a valuable tool set for determining environmental controls on microbial processes (Punshon and Moore 2004a; Li and Harrison 2008b; Johnson et al. 2010; Robidart et al. 2012; El-Swais et al. 2015; Ma et al. 2019). However, such time series are rare because of the sustained, multi-disciplinary effort and teamwork they require.

Here, we present results of such a time-series based study of nitrification within the bottom water (60 m) of Bedford Basin (BB), a eutrophic, anthropogenically impacted, fjord-like embayment located within the Halifax Regional Municipality on the Atlantic coast of Nova Scotia, Canada (see SI Appendix, SI Materials and Methods for more details). Restricted water exchange with the open ocean and annual cycles of stratification and winter mixing make BB a useful natural laboratory to study the relationship between microbial growth phases, geochemistry and physical processes. Based on four years of weekly observations of ammonia monooxygenase subunit A (*amoA*) gene copy numbers (via quantitative PCR; qPCR), microbial community composition (16S rRNA gene amplicon sequencing), nutrient concentrations, and a biogeochemical model enhanced by functional gene modeling, we observed variable dilution of the nitrifier population following winter mixing events. We propose that intense winter mixing during cold winters flushes the resident nitrifier population from the basin bottom waters, resulting in a delay in nitrification and decoupling of AO and NO until the nitrifier community can reestablish. During warmer winters, when mixing is less intense, growth can keep pace with mixing and effectively prevent dilution.

3.3 Study setting and time series context

The 4-year time series of molecular and chemical data from BB bottom water presented here (SI Appendix, SI Materials and Methods) was collected between January 2014 and December 2017, at the center of the basin (44°41’37”N, 63°38’25”W). Our study was conducted in the context of a longer, weekly oceanographic time series established in 1992 (Li and Harrison 2008b; Li 2014b). BB (70 m maximum depth) experiences annual cycles of turbulent winter mixing and seasonal stratification. Water above the sill depth (20 m) is subject to circulation and tidal exchange with the Atlantic Ocean (Scotian Shelf) throughout the year (Petrie and Yeats 1990a; Fader and Miller 2008b; Shan et al. 2011a), while the bottom water is effectively disconnected from this circulation during stratified periods. Stratification is established in spring (~April) and persists into winter (November–February), when it breaks down due to intense cooling (Shan et al. 2011a; Li 2014b). In some years, the stratified period is interrupted by the intrusion of relatively warm and saline water from the Scotian Shelf into the bottom water of the basin (Platt et al. 1972; Punshon and Moore 2004a; Burt et al. 2013b). Unlike the more extended periods of convective mixing during winter, these intrusions are short-lived and do not break down the vertical stratification, but they do ventilate the bottom water and modify its biogeochemistry (Punshon and Moore 2004a; Burt et al. 2013b). The fate of “older” bottom water that is displaced following an intrusion is not well-characterized but presumably involves upwelling and mixing into near-surface layers followed by exchange with continental shelf-water. The euphotic zone (>1% surface irradiation) depth in Bedford Basin is ≤25 m year-round so that the conditions in the bottom water (60 m) are permanently dark (Taguchi and Platt 1977; Li 2014b).

AOA peptides and the presence of *Nitrospina*-type NOB have previously been detected in BB bottom water (Georges et al. 2014b), which has a microbial community that is distinct from that in the near-surface waters (El-Swais et al. 2015). Despite continuous availability of ammonium (mostly >1 µmol kg_{sw}^{-1}), AO rates are highly variable (Punshon and Moore 2004a).

3.4 Results

3.4.1 Physical mixing and nutrient cycling in Bedford-Basin, 2014-2017

The mixing regime within BB between 2014 and 2017 displayed a sequence of full water column winter/spring mixing followed by stratification throughout summer and fall (Figure 3.1) that was consistent with longer-term observations (SI Appendix, Figure B1). During stratified periods the bottom water was relatively isolated from near-surface water as indicated by consistently cold temperatures (~1–4°C) despite strong near-surface temperature variability (1–18°C). Dissolved oxygen was an especially clear indicator of active mixing due to its non-conservative nature and near-surface source: periods of stratification were marked by a steady decline in bottom water oxygen and were clearly distinguishable from periods of mixing when oxygen was delivered to the bottom water (Figure 3.2A).

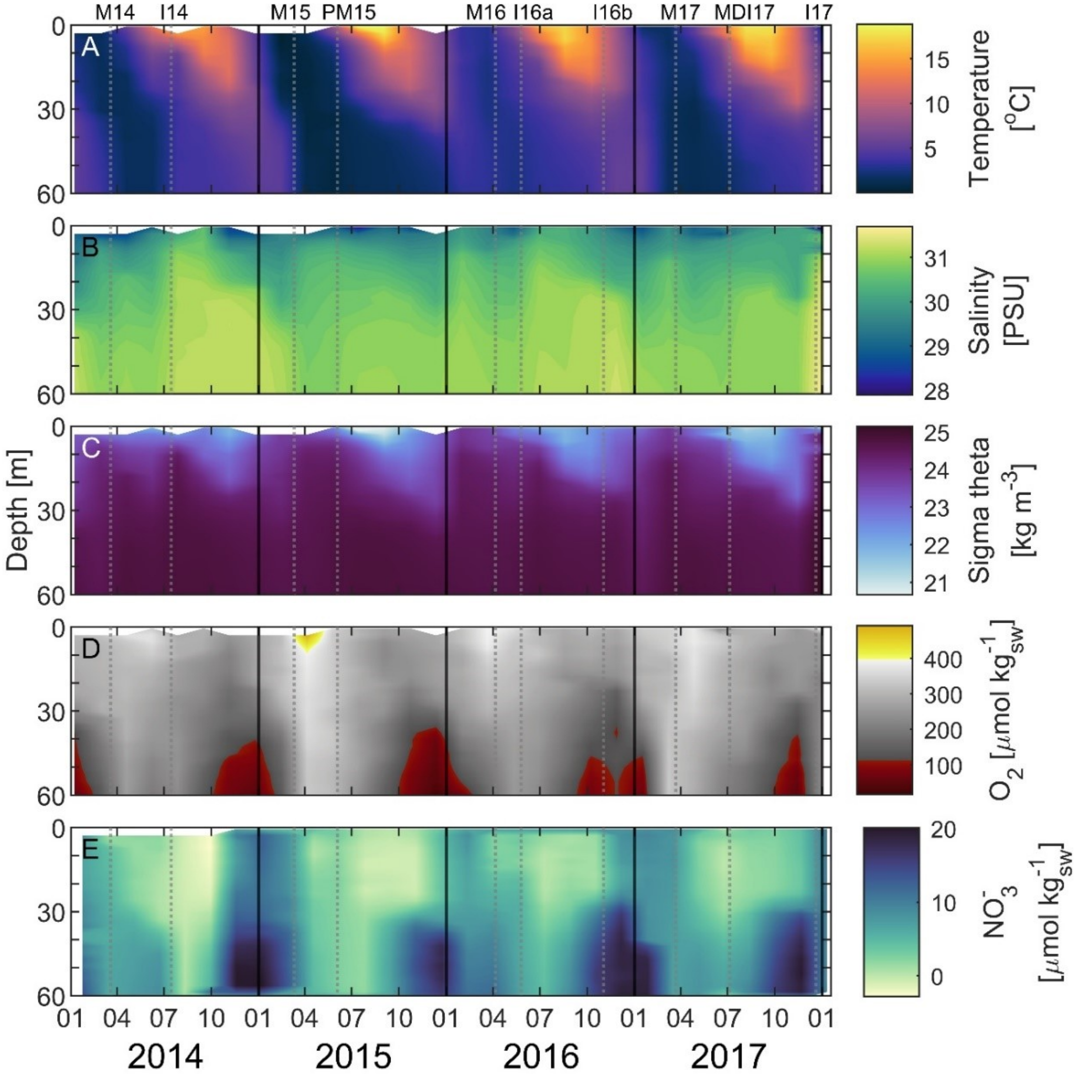

Figure 3.1. Time series of weekly vertical profiles of temperature (A), salinity (B), sigma theta (potential density) (C), dissolved oxygen (D), nitrate (E) in Bedford Basin between January 2014 and December 2017. Event numbers indicate winter mixing ("M") or intrusion events ("I"). "MDI17" is an intrusion to mid-depth waters of BB. PM15 indicates the prolonged phase of winter mixing in 2015.

The event markers M14, PM15, M16 and M17 in Figure 3.2A show the end of winter mixing and onset of stratification each year around April as indicated by the beginning of steady oxygen decrease. The stratified periods were interrupted by occasional shelf-water intrusions into the bottom water (Events I14, I16a, I16b and I17: Figure 3.1, Figure 3.2A). In July 2017, there was an intrusion of shelf water to mid-depth layers (~30 m) of BB (Shi and Wallace 2018b). Some of this intruding water was entrained into the bottom layers during the subsequent weeks, as indicated by nitrate decrease and a transient delay in oxygen decrease at 60 m (Event MDI17: Figure 3.2A,B).

The intrusion events delivered warmer (0.5–2.3°C temperature increase) and saltier (0.2–0.6 PSU salinity increase) offshore water to the bottom of BB, whereas winter mixing decreased both the temperature and salinity of the bottom water (Figure 3.1A,B). The cooling and freshening effect of winter mixing and the contrasting effect of intrusions on BB bottom water are reflected in the "spiciness" of the water. Spiciness is a derived parameter that is proportional to both temperature and salinity and can be used to distinguish water types that share the same density (Flament 2002). Sudden increases in spiciness occurred with each intrusion event (Events I14, I16a, I16b, I17).

In contrast, rapid decreases in spiciness associated with winter mixing adding relatively cold and fresh water to the bottom layer occurred in early 2014, 2015 and 2017 (Events M14, M15, M17; Figure 3.2A). They co-occurred with rapid increases in oxygen concentration indicating intense winter mixing (Figure 3.2A). The spiciness decrease in winter 2016 was much less pronounced (M16), whereas lowest spiciness was observed in late April 2015 (Figure 3.2A), suggesting winter mixing was strongest in 2015 and weakest in 2016.

This is consistent with lower air temperatures during winter 2015 compared to winter 2016. Low temperatures drive winter mixing in BB through cooling of surface water (Li and Harrison 2008b; Shan et al. 2011a), and average January–March atmospheric temperatures recorded at Environment and Climate Change Canada's Bedford Basin station were lowest in 2015 (-4.4°C) and highest in 2016 (-0.5°C), with intermediate values observed in 2014 (-2.7°C) and 2017 (-1.6°C). The average January–March temperatures since 2008, when data became available at this station, have been -1.5°C (standard deviation: 1.3°C) and the winter temperatures in 2015 were the coldest on record for this station.

Additionally, higher values of buoyancy frequency (N^2, a measure of water parcel stability) in winter 2016 indicated stronger stratification than in other years (Figure 3.2A). Taken together, these observations indicate that winter mixing was weakest in 2016 and strongest in 2015, whereas 2014 and 2017 represented intermediate cases.

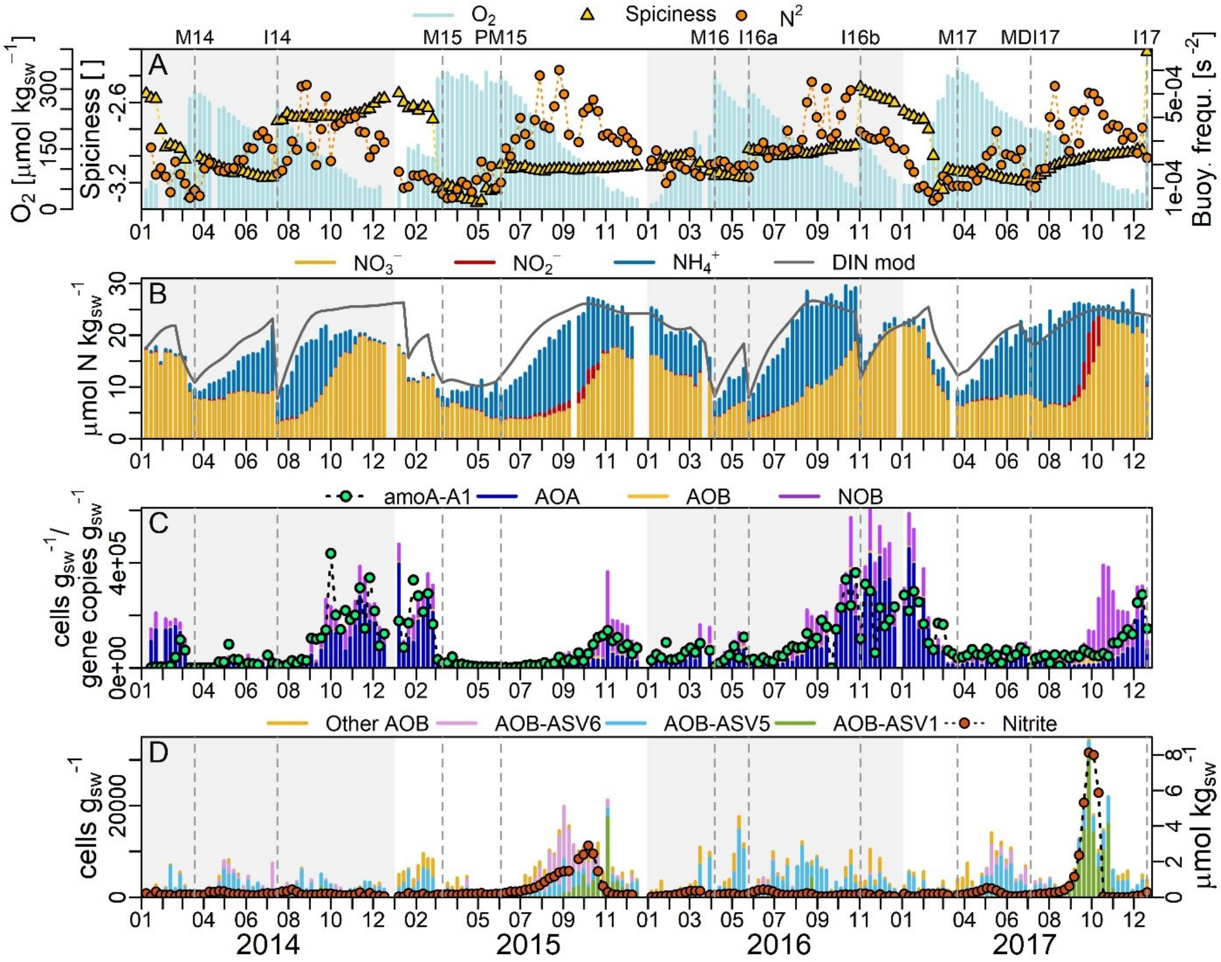

Figure 3.2. Time series of biogeochemical parameters observed at 60 m in Bedford Basin, 2014–2017. A) Buoyancy frequency (N^2), spiciness and oxygen concentration. B) Ammonium, nitrite and nitrate concentration along with modeled DIN concentrations. C) Abun Abundance of Thaumarchaeota (AOA), Nitrospinaceae (NOB) and Nitrosomonadaceae (AOB) affiliated ASVs, as well as amoA-A1. D) Nitrite concentration and the abundance (based on % total 16S rRNA amplicon sequences scaled to total cell counts) of ASVs affiliated with Nitrosomonadaceae (NOB). Event numbers (“M”, “I”, “PM”, “MDI”) as in Figure 3.1.

Both winter mixing and intrusions led to increased dissolved oxygen and decreased DIN concentrations in the bottom water (Figure 3.2A,B). In all four years, ammonium concentrations increased with the onset of stratification (~April) due to remineralization of organic N, reaching maxima of 13–18 µmol kg_{sw}^{-1} during the stratified period (Figure 3.2B). The proportion of nitrate in DIN increased in late summer, indicating that nitrification exceeded the rate of N remineralization. Continuous water column profiles measured by a nitrate sensor (SI Appendix, SI Materials and Methods) showed that the vertical nitrate maximum in each year was located close to our standard sampling depth of

60 m (Figure 3.1E). At the end of the stratified periods, ammonium typically decreased to relatively low concentrations ≤2.0 µmol kg_{sw}^{-1}. However, in 2015, ammonium remained above ~6 µmol kg_{sw}^{-1} (Figure 3.2B).

Despite these repeating patterns of physical mixing and ammonium accumulation, the timing of nitrate accumulation differed between years. The derivative of nitrate with respect to time (Figure 3.3D), which can be used to assess the addition and removal of nitrate as a function of time, indicates that in 2016, nitrate began to increase immediately after the onset of stratification, whereas a delay in accumulation was observed following winter mixing in 2014 and 2015 (Figure 3.2B).

3.4.2 Diversity of 16S rRNA genes affiliated with nitrifiers

To examine the diversity of nitrifiers during the time series period, we analyzed the abundance of amplicon sequence variants (ASV) affiliated with the known nitrifiers *Thaumarchaeota* (AOA), *Nitrosomonadaceae* (AOB) and *Nitrospinaceae* (NOB). Relative abundances of nitrifier-affiliated ASVs were scaled to total microbial cell counts (Figure 3.2C,D; SI Appendix, SI Materials and Methods). The relative abundance of ASVs affiliated with nitrifiers (sum of *Thaumarchaeota*, *Nitrosomonadaceae*, *Nitrospinaceae*) in the microbial community ranged from <0.1% to 38%, which corresponded to 2.1×10^2 – 6.1×10^5 cells g_{sw}^{-1} after scaling to microbial cell counts (Figure 3.2C). AOA abundance (max. 4.5×10^5 cells g_{sw}^{-1}) was similar to other coastal systems (Pitcher et al. 2011; Robidart et al. 2012).

The abundance of beta-AOB was low compared to AOA (Figure 3.2C), but the larger cell sizes of AOB compared to AOA may entail higher biogeochemical impact per cell (Martens-Habbena et al. 2009). The two most abundant *Thaumarchaeota*-affiliated ASVs in the BB bottom water, AOA-BB-ASV2 and AOA-BB-ASV3, were closely related and formed a distinct clade within the genus *Nitrosopumilus* (SI Appendix, Figure B2B). AOA-BB-ASV3 was most abundant in 2015, while AOA-BB-ASV2 dominated in the remaining years.

AOB were affiliated with the betaproteobacterial family *Nitrosomonadaceae* (beta-AOB; SI Appendix, Figure B2A). Beta-AOB-BB-ASV6, which formed a clade independent of the *Nitrosomonas* and *Nitrosospira* clades (bootstrap support >80%), showed a distinct maximum in fall 2015 (SI Appendix, Figure B2A, D). Beta-AOB-BB-ASV1, which fell into a cluster of *Nitrosomonas*-like BB sequences, had a maximum in fall 2017 and a smaller amplitude maximum in late fall 2015.

NOB were affiliated with the genus *Nitrospina* (SI Appendix, Figure B2A). The three most abundant *Nitrospina*-affiliated ASVs showed minima in summer and maxima in fall/winter. *Nitrospirae*-affiliated 16S rRNA genes were present in only a few samples at very small percentage (<0.1%) and did not fall within the genus *Nitrospira* (SI Appendix, Figure B2A), suggesting no role for comammox in BB bottom water during the study period (Xia et al. 2018).

3.4.3 Controls on the temporal distribution of *amoA* and nitrifier-affiliated 16S rRNA ASVs

To investigate how the timing of nitrification may be controlled by variations in nitrifier biomass and diversity, we further characterized the AOA by quantifying six marine phylotypes of the functional gene for ammonia oxidation, *amoA*. The most abundant archaeal phylotype was amoA-A1 (up to 4.4×10^{5} *amoA* copies g_{sw}^{-1}), which has been found primarily in ocean surface waters (Sintes et al. 2016). Strong correlation between *Thaumarchaeota*-affiliated ASV and amoA-A1 abundance (Spearman's rho: $R^2 = 0.66$, $p<1\times10^{-47}$; Figure 3.2C) suggested that amoA-A1 variations tracked AOA abundance. The much lower abundance of the other phylotypes ($\leq1.1\times10^{4}$ copies g_{sw}^{-1}) and their association with mixing events rather than nitrate concentration (SI Appendix, Figure B3; Table B1), suggest that these rarer phylotypes were transient populations, which were transported from near-surface or shelf waters but were unable to establish themselves in the bottom water of BB (SI Appendix, SI Discussion 1).

Only phylotype amoA-A1 correlated with nitrate (Spearman's rho: $R^2 = 0.42$; $p<1\times10^{-24}$) and its abundance decreased during both winter mixing and intrusion events (Figure 3.2C), which explains its inverse correlation with oxygen (Table 3.1; SI Appendix, Figure B4, Table B1). This suggests that amoA-A1 was active and the dominant phylotype. However, in 2017, amoA-A1 abundance did not increase until after the period of rapid nitrite and nitrate increase (September/October; Figure 3.2B,C). A peak in the abundance of *Nitrosomonadaceae*-affiliated ASVs coinciding with this period of steep nitrite and nitrate increase in 2017, suggests a significant role for beta-AOB (Figure 3.2B,C,D).

Table 3.1. Results from Spearman's Rho correlation tests between oxygen concentration, spiciness, nitrifier abundances and their time derivatives (dx/dt) using 2014–2017 BB bottom water data.

Parameter pair		n	r	p
O_2	amoA-A1	196	-0.59	3.9E-20
	AOA	197	-0.60	6.2E-21
	NOB	197	-0.76	6.2E-39
$d(O_2)/dt$	d(amoA-A1)/dt	188	-0.19	0.0105
	d(AOA)/dt	190	-0.28	0.0001
	d(NOB)/dt	190	-0.27	0.0002
d(spiciness)/dt	d(amoA-A1)/dt	193	-0.18	0.0106
	d(AOA)/dt	195	-0.27	0.0001
	d(NOB)/dt	195	-0.14	0.0460

A statistically significant correlation was identified between oxygen increases and decreases in the nitrifier proxies amoA-A1 as well as in the AOA and NOB cell densities (Table 3.1). This is suggestive of mixing-associated decreases that can be explained by dilution with BB near-surface water, which was depleted in AOA and NOB (SI Appendix, Figure B5) and flushed by the near-surface estuarine circulation and tidal exchange with offshore waters (Petrie and Yeats 1990a; Fader and Miller 2008b; Shan et al. 2011a). Thus, physical mixing with the near-surface water can act as a net sink for nitrifier biomass, diluting it within the bottom water. Winter mixing coincided with more pronounced nitrifier decreases than the intrusion events of 2014 and 2016 (I14, I16a, I16b; Figure 3.2C). The degree of amoA-A1 dilution within the bottom water due to winter mixing varied between years, with stronger amoA-A1 decrease in 2014 (minimum: 11 copies g_{sw}^{-1}, dilution factor ≈ 10^3) and 2015 (min: 1.0×10^3 copies g_{sw}^{-1}, dilution factor ≈ 10^2)

compared to 2016 (5.6×10^3 copies g_{sw}^{-1}, dilution factor ≈ 10) and 2017 (4.1×10^4 copies g_{sw}^{-1}, dilution factor ≈ 10).

After the strong dilution following winter mixing in 2014 and 2015 (Events M14, M15: Figure 3.2C), delayed regrowth of the nitrifier population was observed, which coincided with delayed nitrate accumulation during the same periods. Conversely, nitrate increased immediately following cessation of winter mixing in 2016 and 2017 (Events M16, M17: Figure 3.2C), when amoA-A1 winter-time minima were less pronounced. The increase in nitrate and amoA-A1 at the beginning of the 2017 stratified period was interrupted by the mid-depth intrusion of July 2017 (Event MDI17: Figure 3.2C).

3.4.4 A biogeochemical model of nitrogen cycle in BB bottom water

To gain mechanistic insight into the influence of winter mixing on nitrifier growth dynamics and nitrification rates, a simple N-cycling box model was constructed for the BB bottom water (SI Appendix, Figure B6, Table B2, Table B3, Table B4). Conceptually this model is analogous to a bioreactor, where a resident population of nitrifiers actively grows below the pycnocline but can be diluted through time-varying exchange with BB near-surface water (by winter mixing) or Scotian Shelf water (by intrusions; SI Appendix, Figure B6). During the stratified period, the nitrifiers remain relatively isolated from the near-surface water and dilution is negligible. During winter mixing or intrusion events, the population is subjected to dilution as the exchange term increases. If the dilution rate is much faster than the growth rate, then washout of the "bioreactor" can occur. At the low dilution rate applied during stratified periods, net population growth can occur.

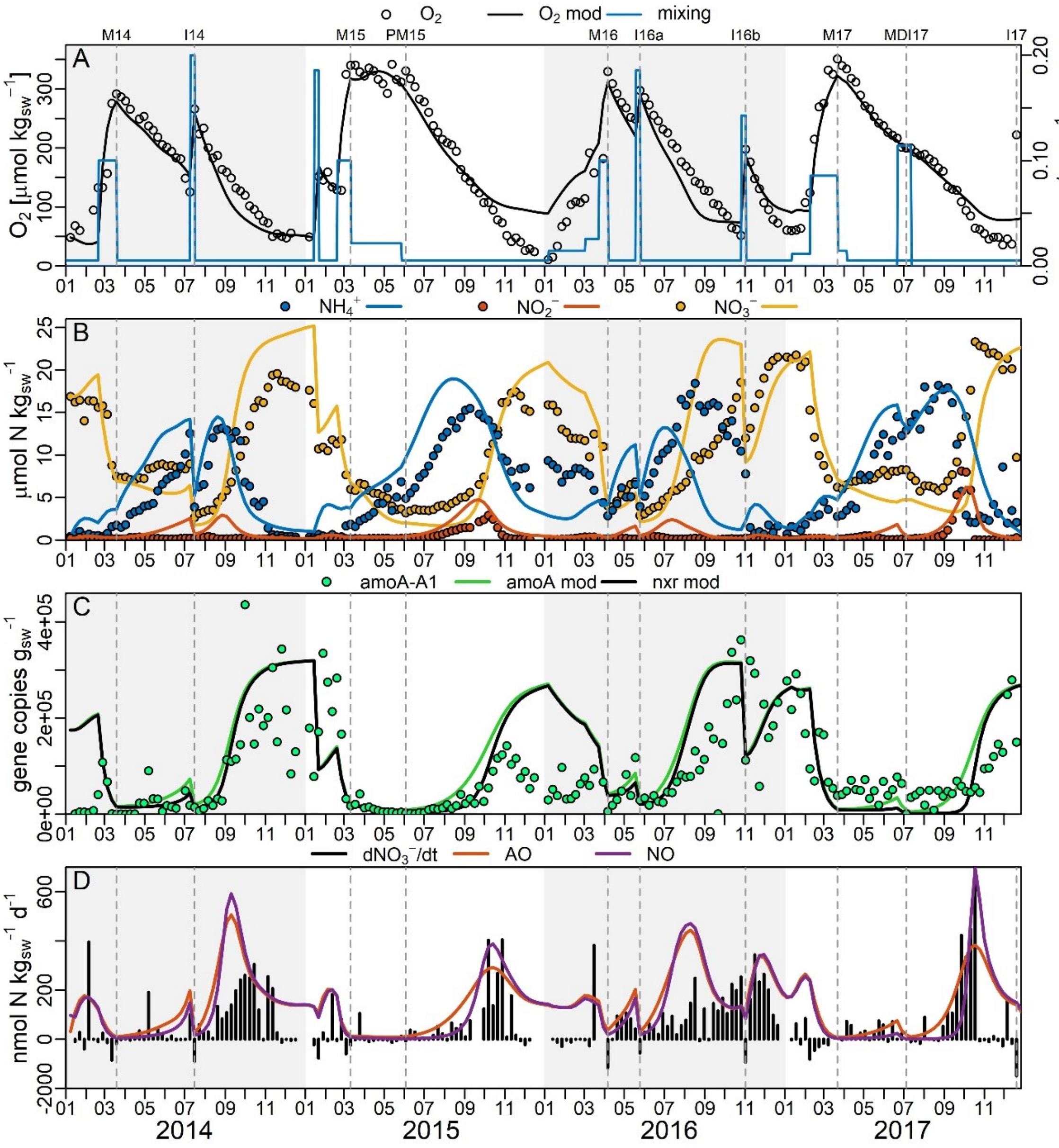

Figure 3.3. Time series of observed (scatter or bar) and modeled (lines: "mod") biogeochemical parameters at 60 m in Bedford Basin, 2014–2017. A) Oxygen concentrations (modeled and observed) and the inverse of residence time t, describing the timescale of exchange of Bedford Basin bottom water with water from the basin surface or the shelf. B) Observed and modeled ammonium, nitrite and nitrate concentrations. C) AmoA-A1 (modeled and observed) and nxr (modeled) gene abundance. D) Modeled rates of ammonia oxidation and nitrite oxidation as well as time derivative of observed nitrate concentration, dNO3- /dt (note the less detailed scale for negative values). Event numbers ("M", "I", "PM", "MDI") as in Figure 3.1.

Use, in the model, of a single set of rate constants for N remineralization, AO and NO (SI Appendix, Table B4) was sufficient to reproduce the overall seasonal trends in DIN and *amoA* copies observed at 60 m from 2014–2017 (Figure 3.3). Much of the observed inter- and intra-annual variability was resolved by this simple modeling approach, including the delayed nitrate production observed in 2014 (pre-intrusion) and 2015, as well as the immediate nitrate increases observed following 2015/16 winter mixing and the intrusion events in 2014 and 2016 (Figure 3.3). A Q_{10}-type temperature dependence for the rate constants of AO, NO and N remineralization was required to represent the increased ammonium and nitrate production rates observed following intrusion events, which delivered warmer water (Figure 3.1B; SI Appendix, Table B4, SI Discussion 2). Some observations, such as the decrease in amoA-A1 abundance and the stop of nitrate accumulation in November 2015 despite ~6 µmol kg_{sw}^{-1} ammonium still being present (Figure 3.3B,C) were not captured by the model. These mismatches are discussed in SI Appendix, SI Discussion 3.

3.4.5 Variability in modeled nitrification rates was caused mainly by the dilution of nitrifier biomass by physical mixing

The modeled representation of AOO population density approximated the observed time series of amoA-A1 abundance (Figure 3.3). After the long and intense winter mixing period of 2015 (Events M15, PM15: Figure 3.3A), which reduced the nitrifier population to very low levels (Figure 3.2C), the modeled AO rate took several months to increase substantially (Figure 3.3D) despite the presence of >5 µmol kg_{sw}^{-1} ammonium during this period of delayed nitrification. In 2016, when shorter and less intense winter mixing resulted in less dilution of the nitrifier population, nitrification rates increased immediately after mixing ceased.

Experiments with the model were consistent with the observation that dilution of the AOO population during winter delayed nitrification: manipulation of the diluting effect of 2015 winter mixing on *amoA* gene copy numbers, while holding its effect on all other parameters constant, resulted in extended (increased influence of mixing on nitrifiers) or shortened (decreased influence) delay in both nitrifier growth and nitrate production (Figure 3.4).

Results from a statistical evaluation of physical and geochemical parameters from the full-length BB time series (>10 years; SI Appendix, Table B1, Table B5, SI Discussion 4) were also consistent with a role of winter mixing in delaying nitrification. Spiciness during the years 2014–2017 was lowest in March of 2015 (Event M15: Figure 3.2A). Using data from the full-length time series, we observed that the magnitude of the annual spiciness minimum during winter (January–April) as well as the annual average oxygen concentration correlated with both the annual average nitrate concentration and the annual average value of the nitrate/ammonium ratio (SI Appendix, Table B5). The minimum spiciness and annual average oxygen concentration parameters may represent empirical indices of winter mixing intensity (minimum spiciness) and mixing intensity in general (average oxygen) so that these correlations are consistent with an overall negative effect of mixing on nitrification in BB.

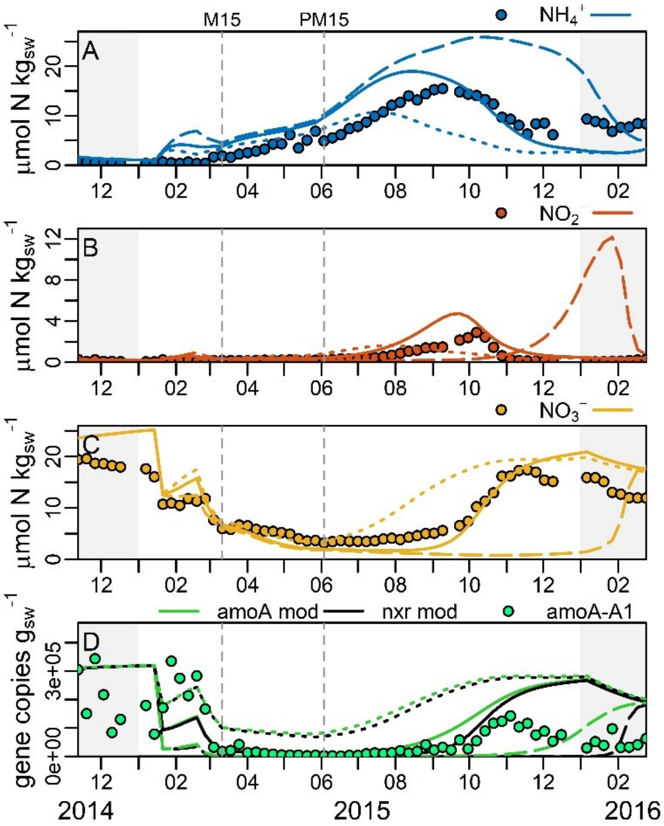

Figure 3.4. Observations and model output as in Figure 3.3, but focused on the year 2015 and showing the output from experimental model runs for which the effect of winter mixing on amoA and nxr was manipulated during winter mixing of 2015 (January 14th – May 27th). For this manipulation, the diluting effect of mixing on the nitrifier marker gene populations was multiplied by 2 (dashed lines) or divided by 2 (dotted lines) compared to the standard model (solid lines). A) Ammonium concentrations; B) nitrite concentrations; C) nitrate concentrations; D) nxr (modeled only) and amoA concentrations. Event numbers ("M", "I", "PM", "MDI") as in Figure 3.1.

3.4.6 Nitrite accumulation as another consequence of nitrifier biomass dilution

The model reproduced the nitrite peaks observed in September/October 2015 and 2017 (Figure 3.3B). They appeared when modeled *amoA* exceeded *nxr* (the modeled functional gene for NO) during periods of regrowth following dilution of these populations (Figure 3.3B,C). This implies that nitrite accumulated due to decoupled regrowth of the two nitrifier populations after their dilution. Experiments with the model additionally demonstrated that increased dilution of nitrifier populations by mixing could have increased (and delayed) the accumulation of nitrite (Figure 3.4). An additional influence of beta-AOB suggested by the observed coincidence of beta-AOB maxima with the 2015 and 2017 nitrite maxima (Figure 3.2D) will be discussed below.

3.5 Discussion

Our analyses of the time series revealed that winter mixing controls nitrate production via its effect on nitrifier biomass and diversity (Figure 3.2, Table 3.1). During winter, surface-water cooling drives convective mixing, which mixes the bottom waters with nitrifier-depleted near-surface water (SI Appendix, Figure B5). The estuarine circulation and tidal exchange with offshore waters in the near-surface layers can then remove the nitrifiers from Bedford Basin (Petrie and Yeats 1990a; Fader and Miller 2008b; Shan et al. 2011a). Colder winters with stronger mixing were associated with stronger nitrifier biomass dilution that delayed nitrification by weeks to months and caused transient nitrite accumulation coinciding with beta-AOB growth (Figure 3.2). The role of mixing is corroborated by statistical analyses of the long-term time series (SI Appendix, Table B5, Table B6, SI Discussion 4). Additionally, a simple mechanistic model of microbial growth was able to reproduce observed interannual differences in nitrifier regrowth and the timing of nitrate accumulation based on variations in mixing intensity (Figure 3.3, Figure 3.4).

On this basis, we propose a mechanism by which mixing dilutes nitrifier biomass, leading to both delay and decoupling of nitrification due to delays in nitrifier regrowth. This mechanism adds to a variety of environmental factors including light, copper and temperature, which are known to potentially inhibit, limit or decouple nitrification (Groeneweg et al. 1994; Joye and Hollibaugh 1995; Philips et al. 2002; Merbt et al. 2012; Amin et al. 2013; Schaefer and Hollibaugh 2017). As observed, ammonium that accumulated during periods of AO delay can eventually fuel fast AOO growth. Temporarily, this can outpace the regrowth of the NOB, which require time to adjust their population size once increased amounts of nitrite become available (Figure 3.4). The resulting high AO rates temporarily exceed NO rates, which drives nitrite accumulation. As discussed in the following section, an additional effect of mixing on nitrifier community composition favored beta-AOB in their competition with AOA, which enhanced the nitrite accumulation.

3.5.1 Transient beta-AOB growth is associated with nitrite accumulation and suggests mixing-induced shifts ammonia oxidizer dominance

Nitrosopumilus-like *Thaumarchaeota* (AOA) of the amoA-A1 phylotype were consistently present in BB bottom water and were overall the most abundant ammonia oxidizers during the 4-year period. However, we also observed short-lived peaks in beta-AOB-affiliated ASVs that coincided with the largest nitrite accumulations and were followed by steep increases of nitrate (Figure 3.2B,D). These AOB peaks appeared when high ammonium concentration coincided with strong dilution of the nitrifier community in 2015 and after the mid-depth intrusion of July 2017, which suggests that opportunistic, fast-growing AOB temporarily outcompeted slower-growing AOA and were involved in creating the relatively large (>1 μmol kg_{sw}^{-1}) nitrite accumulations. As these AOB eventually became substrate-limited by depleting ammonium to levels below their K_m, the AOA population re-established its dominance (Figure 3.2C,D). In 2016, relatively weak winter mixing allowed the resident AOA population to persist through the winter so that it was ready to utilize ammonium as it became available following the onset of stratification (Figure 3.2A,B,C). Even when ammonium accumulated to high concentrations later that year, the AOA were established in a stable environment, which allowed them to outcompete AOB. Hence, we suggest that mixing created temporary niches for the beta-AOB, which have higher V_{max} and K_m compared to AOA (Suzuki et al. 1974; Ward 1987; Bollmann et al.

2005; Martens-Habbena et al. 2009; Horak et al. 2013; Peng et al. 2016). The fast enzyme kinetics of beta-AOB likely enhanced nitrite accumulation by promoting decoupling from NOB growth and further translated into steep increases of nitrate once the NOB population was large enough to decrease the initially accumulated nitrite.

We note that the slow and steady nitrate increase of the 2016 stratified period, when AOB played a negligible role, was overestimated by the model, whereas the steep nitrate increase in September/October 2017, which was associated with the highest abundance of AOB-affiliated ASVs (Figure 3.2C,D), was reproduced more closely (Figure 3.3C). This suggests that the fixed set of rate constants employed in the model are more representative of faster "AOB-type" AO (2015, 2017) than slower "AOA-type" AO (2014, 2016). This may also explain the "false" nitrite peaks generated by the model during the AOA-dominated years 2014 and 2016 (Figure 3.3B).

A model version adjusted to "AOA-type" AO would therefore be expected to improve the fit to the observations made in 2016. Indeed, use of a different AO parameterization in an otherwise identical model better represented the absence of strong nitrite accumulation and the steady nitrate increase observed in 2016, but strongly overestimated the delay in nitrate accumulation in 2015 and 2017 (SI Appendix, Figure B7). For the purpose of this study, the simple model with a single AOO population (Figure 3.3) was valuable in demonstrating that the interannual differences in nitrite and nitrate accumulation were independent of variable AO kinetics. Yet, the model adjusted to 2016 observations (SI Appendix, Figure B7) provided insights on a more granular level and showed that slower AOA kinetics could better simulate the conditions of 2016 (steady nitrate increase, absence of even a small nitrite maximum). In the future, a more complex model with at least two kinetically distinct AOO populations would be required to further explore the competition based on the kinetic differences between AOB and AOA. The observations presented here demonstrate how mixing can affect not only the biomass of nitrifiers but also their community composition, both having consequences for the transformation of N species. This, in turn, suggests that explicit modeling of nitrifier biomass and its diversity is important for understanding N cycling in dynamic coastal systems and projecting its response to variable climate forcing.

3.5.2 Controls by physical mixing explains seasonal changes in AO rates

Similar ranges and variability in AO rates as described here were observed in BB bottom water by Punshon and Moore (Punshon and Moore 2004a), who measured AO rates using isotopic labelling experiments throughout 2002, but did not have supporting data describing the nitrifier community. Notably, they found no correlation of AO rates with either temperature or ammonium concentration but instead an association of low rates with winter mixing, which led them to speculate about an influence of nitrifier biomass on AO rates.

Here we are able to show that this lack of correlation as well as variable AO rates are indeed consequences of variable nitrifier biomass, which masks the effect of ammonium and temperature on AO rates. Our model, which includes nitrifier biomass, temperature and ammonium concentration on AO rates (SI Appendix, Table B3), was able to reproduce the trends observed in BB bottom water during 2002 following adjustment of mixing and surface boundary conditions to reflect the conditions of that year (SI Appendix, Figure B8). That is, using model parameterizations that had been tuned to represent the 2014–2017 time series (Figure 3.3), it was possible to reproduce the independently collected nitrate and ammonium concentration data and AO rates measured in 2002 (SI Appendix, Figure B8). This suggests that dilution of ammonia oxidizer biomass by winter mixing was the reason for the low rates of AO measured in March 2002 (Punshon and Moore 2004a).

An alternative hypothesis to biomass dilution for an effect of mixing on AO rates, could be "cold shock" associated with a sudden decrease in temperature upon the initiation of convective mixing. Cold shock might inhibit nitrification to an extent greater than the Q_{10} temperature dependency included in the model. However, laboratory studies suggest that such effects are relatively small and short-lived (order of a few days) in nitrifiers shocked by a sudden 10°C temperature decrease (Hwang and Oleszkiewicz 2007). By contrast, the largest observed temperature decrease in BB bottom water between 2014 and 2017 was 3.4°C week^{-1} (in February 2015).

3.5.3 Broader significance of mixing-induced dilution and shifting of nitrifier communities

Any water column subject to intermittent stratification may, in principle, be susceptible to the identified control of mixing on nitrification. If water supplied by mixing or advection is relatively poor in viable nitrifier biomass but contains ammonium or organic N, ammonium and nitrite may consequently accumulate due to delayed nitrification and associated temporal decoupling of nitrification. This could apply to subsurface waters of seasonally mixed lakes where climatic variations can affect the extent of spring mixing (Salmaso 2005) as well as fjord-like basins and estuaries similar to BB with seasonal stratification-mixing cycles and/or irregular intrusion events (Horrigan et al. 1990; Ma et al. 2019; Kelly et al. 2020). The mechanism might even operate in shelf ecosystems subject to seasonal blooms and sinking of organic matter, periodic upwelling or seasonal changes in shelf-slope exchange (Mordy et al. 2010; Santoro et al. 2013; White et al. 2019).

Hence, similar mixing-related control mechanisms on nitrification may be widespread, but high-frequency time series of long duration that include microbiological markers to trace biomass variations may be required to recognize and elucidate their global distribution. The sparsity of such time series datasets, especially those with high temporal resolution, might explain why such a mechanism has not been described previously.

There are, however, some indications in the literature for its occurrence. For example, higher *Thaumarchaeota* numbers were observed in near-surface waters of Monterey Bay during stratification in fall compared to relatively unstratified waters in spring (Robidart et al. 2012). Hollibaugh et al. (Hollibaugh et al. 2014) made similar observations using seasonal sampling in coastal near-surface waters off Georgia (USA): the highest copy numbers of thaumarchaeal *amoA* and 16S rRNA genes were found at the end of the stratified period, while much lower numbers were found earlier in the stratified period and prior to the onset of stratification. A follow-up study on the same system suggested that accelerated growth of AOA under high summer temperatures might have been responsible for the decoupling of nitrification and nitrite accumulation (Schaefer and Hollibaugh 2017). However, the observed increase of AOA during the stratified period are also consistent with the mechanism presented here, whereby physical mixing dilutes the nitrifier community, causing nitrite peaks upon AOA regrowth.

Seasonal variations in nitrification and nitrifier biomass as well as transient nitrite accumulation have been observed in many other marine coastal and shelf systems and the causal mechanisms are often poorly understood (Horrigan and Springer 1990; Mordy et al. 2010; Robidart et al. 2012; Hollibaugh et al. 2014; Schaefer and Hollibaugh 2017; Laperriere et al. 2019). Schaefer and Hollibaugh (Schaefer and Hollibaugh 2017) suggested that high temperature may decouple nitrification by promoting rapid AOO growth. Decoupling by rapid AOO growth may also underlie observations of nitrification decoupling associated with sudden availability of ammonium (Pitcher et al. 2011; Ma et al. 2019). The mechanism involving physical dilution described here relies on a similar principle to decouple nitrification by eventual fast AOO growth (following delayed AOO regrowth), leading to AO>NO and nitrite accumulation (Figure 3.4B,D). This suggests that, rather than NOB inhibition or limitation, AOO growth variations that cannot be immediately matched by NOB growth may be a common driver of transient nitrite accumulation in many aquatic systems.

3.5.4 Nitrifier biomass dilution as a link between climate, nitrification and phytoplankton ecology

Our study reveals how mixing can affect functional microbial communities with biogeochemical consequences on seasonal and interannual timescales. The timing of nitrification in BB bottom water varies with the degree of “washout” (via mixing) of nitrifier populations which develop during the previous year. This demonstrates an interannual “memory” of biogeochemical conditions in this coastal ecosystem that can be conveyed by the over-wintering of microbial communities, but that can also be erased by periods of strong mixing. Effects of mixing on microbial biomass have been described previously (Behrenfeld 2010; Zakem et al. 2018), but our analyses also demonstrate how physical mixing can lead to alterations in functional microbial community composition by creating conditions under which AOB can outcompete AOA.

The variable nitrifier biomass dilution might therefore control the speciation of DIN in subsurface waters. This can influence phytoplankton growth upon resupply of subsurface DIN by destratification or upward transport mechanisms to sunlit waters (Johnson et al. 2010). Within BB, for example, intrusion-driven upwelling could affect phytoplankton ecology by delivering DIN to the euphotic zone, which tends to be N-limited (SI Appendix, Figure B9) and low in ammonium and nitrate during summer (Li 2014b). The variable speciation of supplied DIN can impact phytoplankton ecology and the health of aquatic ecosystems. For example, a high share of ammonium in DIN supply has been linked to lower primary productivity and selection against diatoms and towards smaller algal species with higher potential to form harmful algae blooms (Yoshiyama and Sharp 2006; Domingues et al. 2011; Glibert et al. 2016).

The link between mixing and nitrification can control not only the speciation, but also the quantity of fixed N available to primary producers, since oxidized forms of nitrogen are the substrate for denitrification. Low oxygen coastal environments are responsible for a significant fraction of global N-removal (Voss et al. 2013; Sokoll et al. 2016). Therefore, alterations in the balance between fixed-N retention and removal in such systems due to variable nitrification may have larger-scale consequences for N cycling.

Moreover, all these effects are linked to weather and climate, since atmospheric forcing plays an important role for stratification-mixing patterns of ocean waters (Capotondi et al. 2012). For example, infrequent deep water renewal events in a coastal basin have been linked to variations in freshwater run-off and other atmospherically controlled variables (Kelly et al. 2020). In BB, winter mixing is largely driven by heat loss to the atmosphere (Li and Harrison 2008b; Shan et al. 2011a). Since strong winter mixing can delay nitrification, air temperatures and heat loss during winter can influence the timing and extent of nitrification over the remainder of the year. Our findings provide a new example of how weather- and climate-variability can drive variations in DIN speciation with biogeochemical implications for phytoplankton ecology and fixed-N budgets. Previous examples of climate-ecosystem connections involving nitrogen speciation have focused on variations in external nitrogen supply to coastal bays, such as the relative supply of inorganic vs organic forms of N (LaRoche et al. 1997). Here, however, the link is made via physical controls on microbial community composition.

For Atlantic Canada, as for many other temperate regions, the increase in winter temperatures and changes in storm patterns observed over the past decades are projected to continue as a consequence of climate change (Greenan et al. 2019; Zhang et al. 2019). It is tempting to speculate that climate change will result in reduced wintertime convective mixing in Bedford Basin as a result of strengthened haline stratification in winter due to increased freshwater input (increased precipitation or decreased freshwater retention in snow cover) and/or milder winter temperatures (reduced heat loss). However, climate-related changes of mixing intensity in other coastal systems may be very different. Assuming a scenario of decreased winter mixing and notwithstanding any secondary effects such as lower oxygen concentration due to decreased ventilation, our findings would suggest a strengthening of the interannual memory of the system and therefore less delay in nitrate production.

The high (weekly) resolution of the Bedford Basin time-series was an essential pre-requisite to identify and understand the complex patterns of nitrifier diversity and N speciation and their connection to physical forcing. This emphasizes the importance of multi-parameter, high-frequency oceanographic time series in combination with biogeochemical models for elucidating the complicated interactions between microbial communities and the physical conditions they are subjected to. Such approaches are needed to understand and project the impacts of variable forcing and climate change on microbial communities and biogeochemical processes in dynamic coastal environments.

3.6 Materials and methods

3.6.1 Bedford Basin study site, sampling and time series context

Descriptions of the study site, the long-term time series context, sampling procedures and the source of atmospheric data are detailed in SI Appendix, SI Materials and Methods.

3.6.2 Analysis of bulk nutrient, particulate and chlorophyll *a* concentrations

Nutrients, particulates and chlorophyll *a* were analyzed by standard methodology, as detailed in SI Appendix, SI Materials and Methods.

3.6.3 Numerical modeling

A time-resolved box model was used to simulate annual N cycling in the bottom water of BB and investigate possible mechanisms for temporal decoupling of N remineralization, AO and NO (SI Appendix, Figure B6). The use of a box model was motivated by a lack of spatial resolution in our data set, and the philosophy of not making the model more complicated than the resolution of the data we are seeking to understand. The model equations (SI Appendix, Table B2) compute the change in state variable concentration *(dC/dt)* with time. These include chemical concentrations (O_2, NH_3/NH_4^+, NO_2^-, NO_3^-), and two microbial populations, represented by the marker genes for ammonia (*amoA*) and nitrite oxidation (*nxr*). A complete list of differential equations, reactions and rate parameters are presented in SI Appendix, Table B2, Table B3 and Table B4. The initial remineralization reaction was forced by weekly particulate organic carbon (POC) data from 60 m and accounted for seasonal variability in remineralization (e.g. the spring bloom), which was not explicitly represented in the model. Remineralization consumes POC and O_2, producing NH_3/NH_4^+ according to the Redfield ratio (SI Appendix, Table B3). Nitrification was modelled as a two-step process: AO ($NH_3/NH_4^+ \rightarrow NO_2^-$) facilitated by ammonia oxidizers (*amoA*) and NO ($NO_2^- \rightarrow NO_3^-$) facilitated by nitrite oxidizers (*nxr*), both also consuming O_2. A Q_{10} formulation was used to represent the influence of temperature on the rate constants for remineralization and nitrification (SI Appendix, Table B3). A loss term for NO_3^- (a first-order function of nitrate concentration: SI Appendix, Table B3) was included, representing the loss of NO_3^- to N assimilation by chemoautotrophs as well as denitrification, both in the sediment and potentially the anoxic micro-zones associated with particles (Bianchi et al. 2018). Empirically, it accounts for the fact that remineralization with Redfield stoichiometry over-predicts DIN concentrations in the latter half of each year when DIN:P ratios decline at 60 m in BB (SI Appendix, Figure B9). A loss term for O_2 represents sediment uptake and was based on measured O_2 uptake by BB sediments (Hargrave 1978b).

The model assumes that the bottom water of BB is one stable box that only marginally interacts with the near-surface water (5 m) during the stratified period which prevails for most of the year. During mixing periods (winter/spring), the water column overturns, mixing the bottom water with near-surface water. Additionally, short-lived, randomly timed intrusions introduce shelf-water into the bottom water. Mixing was implemented with the following mathematical relationship:

$$\left.\frac{\partial C_i}{\partial t}\right|_{mix} = \frac{1}{\tau} \cdot \left(C_i^{5m} - C_i\right) \tag{3}$$

Where C_i is the concentration at 60 m of the state variable in question, C_i^{5m} is its concentration in the near-surface water (5 m) and τ is the exchange timescale of bottom water with near-surface water from within the basin or the Scotian Shelf. For the stratified period, this timescale was chosen based on the eddy diffusivity values from Bedford Basin determined by Burt et al. (Burt et al. 2013b) and a length scale from the depth of the sill to the bottom of basin (~50 m) according to the relation h^2/K_z. During the intrusion events, τ was decreased to a small value to recreate the sudden step-like O_2 concentration changes observed in our weekly timeseries. During winter, when convective cooling and storms homogenize the basin water, τ was decreased to reproduce the specifically observed increase in bottom water O_2 during this time. O_2 was used as tracer of mixing, because its non-conservative nature makes it a particularly sensitive tracer of active mixing. Since the surface was the only source of O_2 to the bottom water, active mixing at a rate exceeding O_2 consumption was needed to increase or maintain O_2 concentrations. Conservative tracers (e.g. salinity), once equalized between bottom and near-surface water can become insensitive to further mixing in the following weeks, whereas biological O_2 consumption quickly resets O_2 as a tracer sensitive to further mixing. It is assumed that the timeseries of weekly measurements at 5 m depth for O_2, NO_3^-, NO_2^-, NH_3/NH_4^+, are representative of the near-surface water that is exchanged with the basin bottom water and are used as the top boundary condition. The concentrations of *amoA* and *nxr* were taken to be 0 in the near-surface water (SI Appendix, Figure B5). Unlike the remaining intrusion and winter mixing events, the 2017 mid-depth intrusion was modeled as an exchange of 60-meter water with a water mass representing BB mid-depth water (200 µmol O_2 kg_{sw}^{-1}, 12 µmol NH_4^+ kg_{sw}^{-1}, 5 µmol NO_3^- kg_{sw}^{-1}, 0 µmol NO_2^- kg_{sw}^{-1}, 0 gene populations).

To constrain the kinetic parameters, the O_2-half saturation constants for AO and NO were chosen from literature values (SI Appendix, Table B4). The rate constants for remineralization (*k.remin*), AO (*k.AO*) and NO (*k.NO*) were fit to the four year times series by minimizing the cost function:

$$\sum_j \sum_i \left(\frac{y_{ij}^{mod} - y_{ij}^{obs}}{\bar{y}_i}\right)^2$$

4

where y_{ij}^{mod} and y_{ij}^{obs} are the modelled and observed concentrations of i (= O_2, NO_3^-, NO_2^-, NH_3/NH_4^+) at time *j,* and $\overline{y}_i$ is the average concentration of each in the time series. The model was coded in the programing language R, using the package ‘deSolve’ to solve differential equations (Soetaert et al. 2010b) and the package ‘FME’ for least-square fitting (Soetaert and Petzoldt 2010a).

3.6.4 Microbial cell counts

Total microbial cells <35 µm were stained with SYBR™ Green I (Invitrogen) and quantified by flow cytometry, as detailed in SI Appendix, SI Materials and Methods.

3.6.5 DNA extraction, 16S rRNA amplicon sequencing, sequence analysis and deposition

DNA extractions of 0.2–160 µm fractionated seawater were completed as previously described (Haas et al. 2019) and amplicon sequencing of the V4-V5 variable region of the16S rRNA gene of bacteria and archaea was conducted at the Integrated Microbiome Resource, Dalhousie University (ref. (Comeau et al. 2017) and methodology therein). Illumina sequences of the 16S rRNA gene were processed using a QIIME-2 based workflow (Bolyen et al. 2019) as described in SI Appendix, SI Materials and Methods. Phylogenetic trees were built as described in SI Appendix, SI Materials and Methods.

3.6.6 Quantitative PCRs (qPCR)

Six oceanic archaeal phylotypes of the archaeal *amoA* gene (amoA-A1, -A2, -A3, -A4, -A5 and -A6) as defined by Sintes et al. (Sintes et al. 2016) were quantified by qPCR. Details of the assays used to quantify the different phylotypes can be found in SI Appendix, SI Materials and Methods and in SI Appendix, Table B7 and Table B8.

3.6.7 Deposition of DNA sequences, data and model code

The subset of ASV sequences used in this study (i.e. affiliated with potential nitrifiers) was deposited in GenBank under the accession numbers MT175443-MT175495. Other data as well as model code related to this work was submitted to the Pangaea database: https://doi.pangaea.de/10.1594/PANGAEA.914705. The subset of data produced by the Bedford Institute of Oceanography can additionally be accessed under this link: http://www.bio.gc.ca/science/monitoring-monitorage/bbmp-pobb/bbmp-pobb-en.php.

Chapter 4: BENTHIC FORAMINIFERA AND TUBEWORMS PLAY KEY ROLES IN SEDIMENT EARLY DIAGENESIS IN A SEASONALLY HYPOXIC FJORD[3]

4.1 Abstract

Coastal regions, especially semi-enclosed bays, estuaries, and fjords are among some of the most vulnerable areas of the planet facing the impact of environmental changes due to eutrophication and deoxygenation. Due to their relatively shallow water column, the benthic processes in coastal oceans play important roles in nutrient cycles. Here we studied the sediment early diagenetic processes of Bedford Basin, a 70 m deep seasonally hypoxic fjord on the West Atlantic coast in Nova Scotia, Canada. We measured seasonal benthic fluxes and porewater profiles of oxygen, dissolved inorganic carbon (DIC) and nutrients, solid profiles of organic carbon, nitrogen and iron, anoxic reaction rates, and benthic foraminiferal assemblage and intra-cellular nitrate concentration. These data were used to constrain a coupled reaction transport model for early diagenesis. The model suggests that inverse porewater concentration profiles observed for DIC and ammonium were due to deep bioirrigation activity of the tubeworm *Spiochaetopterus sp.* which along with intense iron diagenetic cycle prevented accumulation of free sulfide in the top 25 cm of sediment despite the oxygen penetration depths of only ~1 mm. Modeling suggested organic carbon and nitrogen deposition was 25.2 and 2.9 mmol m^{-2} d^{-1} with burial efficiency of 23% and 17% respectively. Low oxygen tolerant and denitrification capable benthic foraminifera *Stainforthia fusiformis* dominated (>90%) the foraminiferal assemblage. The study

---

[3] Rakshit, S., N. Glock, M. Armstrong, F. Scholz, A. W. Dale, C. K. Algar. Benthic foraminifera and tubeworms play key roles in sediment early diagenesis in a seasonally hypoxic fjord. (*In prep*)

Author contribution: SR and CA conceived the study. SR, MA, CA collected the samples and conducted the experiments. SR, MA, FS analyzed the samples, NG performed the foraminifera experiments with the help from SR. SR developed and parameterized the numerical model and performed the research with supervision from AD and CA. SR wrote the manuscript with contribution from all authors.

indicated that total denitrification rate was 1.6 mmol N m^{-2} d^{-1} where foraminiferal denitrification could contribute up to 75%. Ecological importance of tubeworms and denitrifying foraminifera are discussed.

4.2 Introduction

Coastal oceans are amongst the most productive regions of the planet, driven by the high nutrient input from land due to natural and anthropogenic factors (Field et al. 1998). The high load of organic matter is subsequently remineralized in the water column and sediment, consuming oxygen and releasing inorganic nutrients that can be subsequently utilized by autotrophs. Due to a relatively shallow water column, coastal and shelf sediments receive a large portion of the sinking organic matter where it drives a cascade of redox sensitive reactions (Jahnke et al. 1990). Regenerated nutrients can be returned to the water column, stored in the sediment or, in the case of nitrogen, be removed from the ecosystem through denitrification. Coastal and shelf sediments account for more than half of the total N loss from the marine system (Middelburg et al., 1996; Bohlen et al., 2012). Denitrification coupled to organic matter degradation using nitrate as the terminal electron acceptor (TEA) is usually referred to as canonical/bacterial denitrification. However, this classic conception has been challenged with the discovery of certain benthic foraminifera (unicellular eukaryotes) which can store nitrate intra-cellularly at high concentrations and capable of performing complete denitrification (Risgaard-Petersen et al. 2006). Since the discovery of denitrifying foraminifera in a hypoxic Swedish fjord basin, they have been identified in various places and account for 2-100% of total denitrification in the sediments where they have been observed (Pina-Ochoa et al. 2010; This study). Bioavailable N can also be removed by some chemoautotrophic bacteria performing anammox, where ammonium is oxidized to N_2 gas by nitrite. This process could account for up to 10% of total denitrification in estuarine sediment (Burdige 2011). On the contrary, dissimilatory nitrate reduction to ammonium (DNRA) by some bacteria retains bioavailable N in the ecosystem (Giblin et al. 2013; Hardison et al. 2015).

The degradation of organic matter in sediments also plays a crucial role in the C, O, Mn, Fe, and S cycles (Berner 1980). TEAs are consumed in the following sequence according to their Gibbs free energy yield – O_2 > NO_3^- > Mn^{4+}-oxide > Fe^{3+}-oxide > SO_4^{2-} > CH_2O (Tromp et al. 1995). In organic rich sediments, such as in coastal and estuarine sediments, the oxygen is consumed within the top few millimetres and numerous other tightly coupled redox-sensitive reactions occur in short succession within the uppermost centimeters (Seitaj et al. 2017). Reaction-transport models (RTM) have been used to simulate benthic fluxes and the rates and mechanism of these tightly coupled reactions (Boudreau 1997; Soetaert et al. 2000; Lessin et al. 2018). These models are also useful in testing hypotheses and understanding the benthic response to changes in the environment.

In this study, we focus on Bedford Basin (BB) (Figure 4.1), a semi-enclosed estuarine fjord on the coast of the Northwest Atlantic. It is 70 m deep and connected to the Scotian Shelf through a 20 m deep sill that restricts circulation in the water masses below the sill depth (Petrie and Yeats 1990b; Shan et al. 2011b). Bottom water of BB is usually oxygenated every year due to winter mixing and infrequently in summer-fall due to shelf water intrusions (Rakshit et al., 2023). It is a eutrophic basin, where distinct phytoplankton bloom occurs in spring and fall. Primary productivity is usually sustained throughout the year except in winter via supply of nutrients from sewage outfalls, the Sackville River or from deep water. Net oxygen consumption occurs in the bottom water and sediments when the water column is stratified, leading to the onset of hypoxic conditions in late summer and fall. This repetitive cycle makes BB an ideal system to study the development of coastal hypoxia and the corresponding biogeochemical impacts on the coupled cycles of carbon, oxygen, and nitrogen. In addition, a long-term oceanographic monitoring station has been maintained at the Compass Buoy site in the deepest part of the basin by the Bedford Institute of Oceanography (BIO) (Li et al. 1998, 2010; Li and Harrison 2008a). BB bottom water features annual nitrification cycles that have been studied recently (Haas et al. 2021, 2022). Although the many aspects of basin's oceanography have been documented, the coupled benthic-pelagic oxygen and nutrient cycles have yet to be investigated in detail.

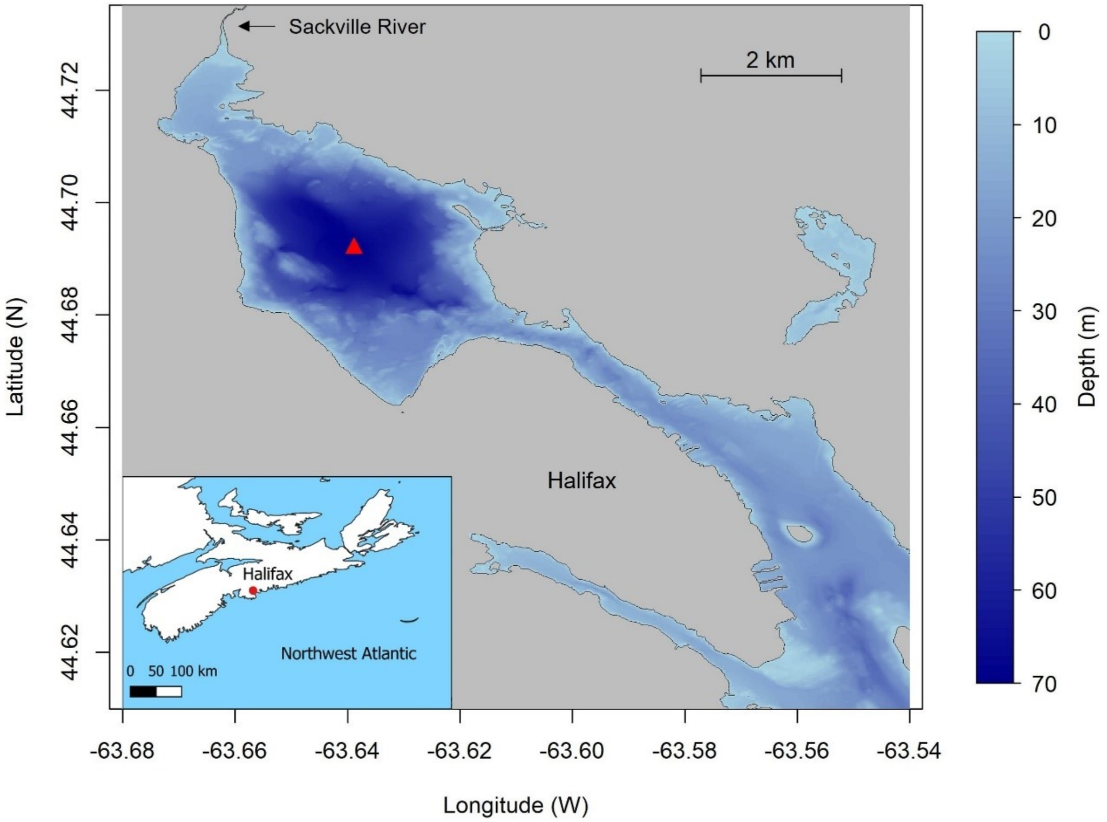

Figure 4.1. Bathymetric map of Bedford Basin and Halifax Harbour. The red triangle indicates the Compass Buoy site. The inset shows its location in Nova Scotia adjacent to the city of Halifax.

The sediment below 30 m water depth is dominated by silty clay and rich in organic matter (Fader and Miller 2008a). Underwater camera surveys revealed that the seafloor is inhabited by long tubeworms (*Spiochaetopterus*) (Hargrave 1989; Fader and Miller 2008a). Some patches of bacterial mats, probably *Beggiatoa* spp., have also been identified (Fader and Miller 2008a). Scott (2005) studied the distribution of benthic foraminifera in BB and reported the presence *Fursenkoina fusiformis* (*Stainforthia fusiformis* according to (Hayward et al. 2023)) in the deep basin. Certain foram species from the genus *Stainforthia* have been shown to denitrify (Piña-Ochoa et al. 2010). Although denitrification rates of *S. fusiformis* have not been measured, it clusters in the phylogenetic tree with the other denitrifying foraminifera (Woehle et al. 2022). Their existence in BB raises immediate curiosity in understanding their role in benthic nutrient cycling and adds to the motivations for this study. Hence, we measured the seasonal sediment-water fluxes and concentrations of nutrients and solids in BB sediment. Additionally, we performed sediment incubations to determine how the organic carbon remineralization rate change with depth. We quantified the abundance of living *S. fusiformis* and measured its intracellular nitrate storage to assess its role in benthic N-cycling in BB. We used these data to constrain a benthic RTM and identify the major early diagenetic processes involving C, N, O, Fe, and S cycling in BB.

4.3 Materials and methods

4.3.1 Study area and sampling

Sediment cores were collected from Bedford Basin Compass Buoy station (Lat: 44.6937N, Lon: 63.6403W) using a multi-corer (KC Denmark) in February, May, August, November-2019, November-2020 and May, November-2021 (Table 4.1). The core barrels were 60 cm long with 10 cm internal diameter, made of polycarbonate, and collected approx. 35 cm of sediment and 25 cm of water, keeping the sediment water interface intact. Recovered cores were transported on ice to a temperature-controlled lab (~4 °C) within 3 hours of collection. Since Nov-2020, the cores were additionally submerged in a larger core barrel filled with bottom water to minimize oxygen contamination while transporting. The number of cores collected on each day varied from 8-12. Depending upon the number of cores collected, duplicate or triplicate cores were used to extract porewater through a Rhizon sampler (0.2 micron), and/or sectioning and centrifuging 15 min at 5000 rpm. For the latter case, the supernatant was filtered through a 0.45-micron filter. Porewater was analyzed for ammonium, nitrate, nitrite, ferrous iron (II), hydrogen sulfide. From Nov-2020, DIC was also measured. Ammonium (Solórzano 1969), hydrogen sulfide (Cline 1969) and Fe (II) (Viollier et al. 2000) were measured spectrophotometrically. Nitrite+nitrate (NOx) was measured using chemiluminescence method (Hendrix and Braman 1995) in Thermalox-NOx instrument. DIC was measured using Apollo SciTech DIC analyzer. It was calibrated with certified reference material (CRM, Scripts Institution of Oceanography). The precision was within 0.4% of the final concentration. One core from each sampling date was extruded until a 6 cm water headspace remained, after which duplicate or triplicate oxygen micro profiles were recorded using Unisense™ microelectrodes at 100 µm vertical resolution. The diffusive oxygen uptake (DOU) was calculated from these oxygen profiles by fitting a 1D steady state reactive transport model of sediment oxygen consumption (Rakshit et al. 2023) (Chapter 2). Duplicate or triplicate cores were used for determining benthic nutrient fluxes ex-situ by whole core incubation. Sampled water nutrients were measured using an autoanalyzer (Skalar San++ autoanalyzer) following standard laboratory protocols (McGrath et al. 2019). For November 2020 and May 2021, one core was used to perform anoxic sediment incubations to determine vertical remineralization rates as described below.

For sampling events in 2019, one sediment core was sectioned in 1-2 cm intervals. Porosity was measured in these samples by taking wet and dry weight of the sediment, assuming dry sediment density of 2.65 g cm^{-3} and porewater salinity 31. Porosity variation with depth was described by the equation,

$$y = y_{inf} + (y_0 - y_{inf}).exp(-z/a) \tag{1}$$

here y is porosity at depth z, y_0 and y_{inf} is porosity at surface and at depth respectively, and a is porosity attenuation with depth. The sectioned sediment was also used to determine total carbon and total nitrogen using Elemental Analyzer (Costech ECS4010). Additionally, dried sediment samples were analyzed for excess ^{210}Pb for determining the sedimentation and bioturbation rate (Black et al. 2023). In May 2019, dried sediments were also analyzed for solid iron to measure pyrite (Fe_{py}) and total reactive iron (Fe_{rectv}) (Scholz and Neumann 2007). Porosity, radioisotope concentrations, TC, TN, C/N, iron depth profiles were assumed to be invariable across seasons. These analyses were not repeated at other sampling dates.

Table 4.1. Sampling dates, corresponding bottom water conditions (60 m depth) and measured ex-situ fluxes. Uncertainties on fluxes are corresponds to multiple measurements (duplicate or triplicate core incubation). For DOU it is multiple porewater microsensor profiles. Negative sign implies the direction of the flux is from bottom water into the sediment.

Sampling date	**BW temp °C**	**BW salinity p.s.u.**	**BW O_2 µM**	**BW NH_4^+ µM**	**BW NO_3^- µM**	**DOU flux mmol m^{-2} d^{-1}**	**DIC flux mmol m^{-2} d^{-1}**	**NH_4^+ flux mmol m^{-2} d^{-1}**	**NO_3^- flux mmol m^{-2} d^{-1}**
12-Feb-2019	4.9	31.39	144	1.04	9.48	-15.5±5.7	n/a	1.4±0.1	-1.2±0.01
07-May-2019	1.1	31.03	292	3.72	4.64	-20.9±0.5	n/a	0.6	-0.27
26-Aug-2019	1.5	30.97	94	16.62	6.89	-13.9±5.1	n/a	1.3±0.4	-0.05±0.17
07-Nov-2019	2.0	30.93	32	16.80	13.50	-7.1±1.7	n/a	6	-2
04-Nov-2020	5.1	31.67	186	1.64	12.53	-15.1±1.3	22±8.5	2.3±0.5	-0.8±0.02
04-May-2021	4	31.25	124	1.51	20.40	-11.5±0.9	3.8±1.7	1.2±0.1	-1±0.1
02-Nov-2021	4.3	31.06	3	5.22	18.38	n/a	21.1±6.2	2.7±0.2	-1.3±0.04
Mean	3.3±1.7	31.19±0.27	125±97	6.7±7	12.3±5.8	-14±4.6	15.6±10.2	2.2±1.8	-0.9±0.7
Model	4*	31*	170*	7.2*	12.2*	-12.3†	19.6	2.2	-1.4

*Imposed boundary condition to the model, calculated from BBM. †Total oxygen flux.

4.3.2 Whole core incubation

For ex-situ whole core incubations, duplicate or triplicate cores were kept in a cold room (~4 °C). Core tops were fitted with caps as airtight as possible. Caps were fitted with a port for inserting an oxygen probe (Hatch LDO probe), which recorded the oxygen concentration in the bottom water every 15 minutes. This data was not reported because in most cases it showed inconsistent trend plausibly due to air leakage from core caps, and therefore, we assumed DOU was representative of total oxygen uptake. The cap also has two ports for sampling the bottom water and a port for bubbling with gas. An air-N_2 gas mixture was bubbled for three hours to maintain the bottom water at *in-situ* oxygen level. The later port was then closed, and the core left to settle for two hours before beginning the experiment. The cores were incubated for 24 hours, during which water samples were collected at four equally spaced time points (~8 hours). The water samples were collected using a syringe from one sampling port, while the other sampling port was connected to a water head containing bottom water in order to replace the extracted water with bottom water. The collected water samples were filtered through a 0.45 micron filter and stored frozen at -20°C until further analysis. The concentration data were used to determine benthic fluxes of ammonium and nitrate using the following equation:

$$Flux = dC/dt \times h \tag{2}$$

Where dC/dt is the change in concentration of solute in the overlying water during the incubation and h is the height of the water. Fluxes are reported in the unit of mmol m^{-2} d^{-1}.

From November 2020, a water sample was additionally collected at the beginning and at the end of the experiment (two timepoints) to determine the DIC flux. These samples were collected in 12 ml Labco Exetainer glass vials, filled from bottom, and overflowed to ensure that no air-bubbles were formed or trapped in the vials while sampling. Samples were fixed with 10 µl saturated $HgCl_2$, capped and stored at 4 °C until analysis. Additional samples were collected from the bottom water reservoir at the beginning and at the end of all the flux experiment and analyzed for any change in concentration, thus acting as pseudo control of our experiment. Note that no attempt was made to prevent air contact in the bottom water bottle other than keeping the lid closed. During the experiment, the core top water was stirred continuously with cap fitted magnetic stirrer at 60 rpm to prevent the development of concentrations gradients in the water column without disturbing the surface sediment surface.

4.3.3 Anoxic incubation method

Anoxic incubations were used to determine organic carbon remineralization rates vertically through the sediment. Cores were sliced at 0-2, 2-4, 8-10, 16-18 cm intervals into Ziploc bags and moved to a N_2-atmosphere glove box with rapid handling to minimize oxygen exposure. Inside the glove box, samples were homogenized within the bag. A small cut was made on the bottom corner of the Ziploc bag and the sediment was squeezed into eight 15 ml falcon tubes leaving no headspace. The caps were further wrapped with parafilm. Four bottles of 1000 ml ascorbic acid solution (i.e. anoxic solution) were prepared. The tubes belonging to each depth were kept submerged in the solution. These bottles were incubated in darkness at *in-situ* (4 ºC) temperature. Two sediment tubes from each depth were sacrificed at 0, 1, 3 and 7 week intervals. The dissolved oxygen (DO) concentration of the bottled ascorbic acid was measured during sampling with a handheld Hach DO probe. It was <1% air saturation for all timepoints. Sacrificed tubes were centrifuged at 5000 rpm for 15 minutes. The tubes were opened inside a glove box under N_2 atmosphere and extracted porewater was analysed for DIC, NH_4^+, Fe^{2+}, H_2S. Carbon and nitrogen remineralization rates were determined from the linear slope of the change in concentrations over time.

The sedimentary organic carbon remineralization rate was determined from the production of DIC over time. Similarly, organic nitrogen remineralization (ammonification) was also determined from the production of NH_4^+ after accounting for the adsorption on particle as

$$NH_{4\,total}^{+} = NH_{4\,pw}^{+}\{\varphi + (1-\varphi)K_{ads}\} \tag{3}$$

Where $NH_{4\,total}^{+}$ and $NH_{4\,pw}^{+}$ are total and dissolved NH_4^+ concentration, respectively, φ is porosity and K_{ads} (=1.6 $cm^3\ g^{-1}$) is the adsorption coefficient (Berg et al. 2003). The calculation assumes that nitrification or anammox rates were zero, which is reasonable since the incubations were conducted under anoxic conditions.

4.3.4 Sampling for foraminifera

In November 2020 and May 2021, one core was sectioned at 1 cm intervals over the top 5 cm. Sectioned sediment was collected in 500 ml glass jars. Rose Bengal was added to stain the cytoplasm in living foraminifera. Rose Bengal (2 g) was dissolved in 1 litre ethanol in a separate conical flask, from which 200 ml was added to each glass jar to provide a sediment - ethanol slurry of 30%-70% v/v. The slurry was gently stirred and uniformly mixed. The jars were capped and wrapped with parafilm. The height of the sediment in each jar was marked for later determination of the sediment volume (next section) and the jars were stored (>14 days) at room temperature until further analysis. Additionally, in March 2022, we performed benthic foraminiferal sampling with the aim of recovering live foraminifera samples and determining their intra-cellular nitrate content.

4.3.4.1 Determination of living abundances

The samples, stained with Rose Bengal were wet sieved over a 125-µm and a 63-µm mesh. The >125-µm and the 63-125-µm fractions were collected separately and dried at ~40°C. Afterwards, the sample jars were filled with water up to the sediment fill mark level. The volume of the water that represents the bulk sediment volume was measured in a graduate cylinder (accuracy ~ ± 5 cm^3). The level mark was not recognizable any more on the sample vials of the top cm of the samples from November 2020 and, thus, could not be determined. For the following analyzes we assumed the same sample volume as in the top cm from May 2021. Subsequently, samples were split and specimens of *Stainforthia fusiformis* that were stained in a vital raspberry red color were counted under the microscope. Living stained foraminifera were fixed in plummer cells.

4.3.4.2 Preparation of living specimens for intracellular nutrient analyses

To collect living foraminifera specimens for the intracellular NO_3^- analyses, samples from March 2022 were directly wet sieved within two days after sampling using filtered seawater from Bedford Basin. Three samples of 9 to 70 living *Stainforthia fusiformis* specimens and two additional samples of 8 and 11 living *Elphidium albiumbilicatum* specimens were picked since these were the most abundant benthic foraminifera species in the deep basin. All samples were photographed with a stereomicroscope camera for the later determination of foraminiferal biovolume. Afterwards, foraminifera were cleaned and the NO_3^- extracted following the methodology of Glock et al., (2020). Specimens were rinsed with NO_3^--free artificial seawater prepared from Red Sea salt. Subsequently, they were transferred into centrifuge tubes with a small amount of artificial seawater. Then, 3 mL of reverse osmosis water (conductivity 0.055 $\mu S\ cm^{-1}$) was added to the samples. Within the water, foraminiferal specimens were broken, using a clean pipette tip. A procedural blank was carried through the same procedure without foraminiferal specimens for blank corrections of the NO_3^- analyses (five blanks in total). All samples were frozen at – 20 °C for at least two hours and thawed afterwards. This procedure was repeated three times to destroy plasma membranes and release intra-cellular NO_3^- analyses (Burke et al. 1976; Dowgert and Steponkus 1984). Subsequently, samples were filtered through sterile 0.2 µm cellulose-acetate filters and stored frozen for later analysis of nitrate concentration. Foraminiferal abundances were not calculated for March 2022 campaign.

4.3.4.3 Biovolume determination of living foraminifera

The total foraminiferal cell volume of each species was estimated following Geslin et al. (2011). We assumed that the internal test volume corresponds to 75% of the total test volume and was completely filled with cytoplasm (Hannah et al. 1994). Methodology and equations for exact biovolume estimation for several benthic foraminifera species are given by de Freitas et al. (2021). Neither *S. fusiformis* nor *E. albiumbilicatum* are listed in de Freitas et al. (2021) so we use the best resembling geometric shape for the biovolume estimation (i.e., cone for *S. fusiformis* and prolate spheroid for *E. albiumbilicatum*).

4.3.5 Numerical model

A one-dimensional, steady state, reactive transport model was used to simulate the sediment early diagenetic processes in Bedford Basin. The model is conceptually similar to previously developed models (Soetaert et al., 1996; Wang and van Cappellen, 1996; Boudreau, 1997; Bohlen et al., 20112; Dale et al., 2016). The model includes 11 solutes, namely O_2, DIC, NH_4^+, NO_3^-, Fe^{2+}, Mn^{2+}, SO_4^{2-}, H_2S, and CH_4, and intracellularly stored NO_3^- (in foraminifera cell, and other bacteria; NO_{3for}^- and NO_{3bac}^- respectively) (Table C1). We also considered 10 solid species including three pools of organic matter – highly, medium and poorly reactive (OM1, OM2, OM3), three pools of iron (III) oxides – highly, medium and poorly reactive fraction ($Fe(OH)_3$, $Fe(OH)_3$.MR, $Fe(OH)_3$.LR respectively), two pools of MnO_2 (MnO_2 and MnO_2.MR), iron monosulfide (FeS) and pyrite (FeS_2). Solutes were modeled in μmol cm^{-3} of porewater, and solid species were expressed in wt% of dry sediment (Table C1). The top 50 cm of sediment was simulated over 100 grid layers of increasing thickness with depth. The stoichiometric reaction network and rate expressions are descried in Table C2, C3, C4 and the corresponding model parameters are given in Table C5. The modelled species were transported in the sediment column by advection and compaction due to sedimentation, molecular diffusion, faunal bioturbation and bioirrigation. The following equations were used to express the change in concentration of solutes and solids:

$$\varphi \frac{\partial C_i}{\partial t} = \frac{\partial}{\partial z}\left(\varphi (D_b + D_s) \frac{\partial C_i}{\partial z}\right) - \frac{\partial}{\partial z}(\varphi u C_i) + \varphi \alpha_i (C_{i(0)} - C_i) + \varphi \sum R_i \qquad (4)$$

$$(1-\varphi) \frac{\partial C_j}{\partial t} = \frac{\partial}{\partial z}\left((1-\varphi) D_b \frac{\partial C_j}{\partial z}\right) - \frac{\partial}{\partial z}((1-\varphi) v C_j) + (1-\varphi) \sum R_j \qquad (5)$$

$$\varphi \frac{\partial C_{cNO3}}{\partial t} = \varphi \gamma_{cNO3} (C_{cNO3(0)} - C_{cNO3}) + \varphi \sum R_{cNO3} \qquad (6)$$

where t is time, z is sediment depth, C_i and C_j represent concentration of solutes and solids respectively, C_{cNO3} stands for intracellular nitrate stored in either benthic foraminifera or large bacteria. The nitrate uptake by these organisms can be assumed as non-local transport and therefore diffusive and advective transport terms are zero in equation 6. φ is porosity, and $(1-\varphi)$ is the solid volume fraction of the sediment. D_s is the tortuosity corrected diffusion coefficient for solutes after Boudreau (1996), $D_s = D_0/(1-2\ln(\varphi))$, where D_0 is temperature and salinity corrected diffusion coefficient of the solute. u and v denote advective velocity for solutes and solids, respectively. D_b is a bioturbation coefficient (cm^2 yr^{-1}) determined from excess ^{210}Pb profiles (Figure C1). α_i (year^{-1}) is the bioirrigation coefficient and $C_{i(0)}$ is concentrations of solute in the bottom water. γ_{cNO3} (year^{-1}) is a coefficient for non-local transport by foraminifera and other large vacuolated bacteria, and $C_{cNO3(0)}$ is the intracellular nitrate in equivalent porewater concentrations. In this study we considered intracellular nitrate storage in foraminifera, and the $C_{cNO3(0)}$ was taken from Dale et al. (2016) who studied a similar system. The bioirrigation coefficient for Fe^{2+} was set to one-fourth value of the other solutes for its high tendency to be oxidized in presence of oxygen near the sediment water interface (Dale et al. 2015). The non-local exchange processes where modeled using the equation,

$$y = y_{max} \,.\, (exp(z_L - z))/(1 + exp(z_L - z)) \qquad (7)$$

where y is either α in case of bioirrigation or γ for intracellular storage at depth z, y_{max} is the maximum value of y which is constant for the upper z_L cm of sediment, beyond this depth y decreases exponentially to zero.

The bioirrigation coefficient, α, was determining by fitting the model to the observed ammonium and DIC depth profile. Stored nitrate was transported actively by the organisms, such that diffusive and advective transport was neglected (see below). $\sum R$ denotes the sum of all the coupled reactions involving the chemical species. The coupled biogeochemical reactions considered in the model (Table C2) are driven by organic matter (OM) degradation. OM was degraded sequentially by aerobic respiration, denitrification, manganese (IV) oxide reduction, iron (III) oxide reduction, sulfate reduction and methanogenesis according to Gibbs free energy yield during respiration via different electron acceptors (O_2 > NO_3^- > MnO_2 > $Fe(OH)_3$ > SO_4^{2-} > CH_2O) (Tromp et al. 1995). The organic matter degradation rates were determined using Michaelis-Menten kinetics in which the preferable electron acceptor solely oxides OM until its concentrations reaches a limiting concentration defined by half-saturation concentration when the next preferable electron acceptor starts oxidizing OM and so on. Additionally, another inhibition by foraminiferal denitrification was implemented on OM degradation by other TEAs using the formulation $K_{s.for}/(K_{s.for} + NO_3^-{}_{for})$, here $K_{s.for}$ is half saturation constant for denitrification by foraminifera (Dale et al. 2016). This formulation was used because it was assumed that foraminifera, being motile, have an advantage over non-motile bacteria, and can actively look for fresh organic matter and refill their intracellular nitrate storage from bottom water or surface sediment using their pseudopodal network. Their abundance in BB was distributed throughout the top 5 cm and therefore it is safe to assume they survive by performing denitrification using internally stored nitrate at these depths whereas bacterial respiration takes place alongside sequentially using TEAs (see results and discussion). Degradation of one mole of organic matter produces rNC mole of NH_4^+, where rNC is the molar ratio of N:C in OM. Secondary redox reactions (Table C2) were expressed using bimolecular rate laws (Wang and van Van Cappellen, 1996).

4.3.6 Boundary conditions and model constraints

Upper and lower boundary conditions for all the species (Table C1Table C5) are required to solve the differential equations. For solutes, the upper boundary was defined as fixed concentration. These concentrations were obtained by averaging the bottom water concentration of ammonium, nitrate, and oxygen that was recorded at 60 m by the Bedford Basin Time Series (Li 2014a; Haas et al. 2021). The sulfate concentration was assumed to be 28.5 mM since bottom water has seawater salinity. DIC concentrations were determined from bottled water collected during sampling of this study. Hydrogen sulfide, dissolved iron and manganese were assumed to be absent in bottom water. The upper boundary of solids was defined as fixed fluxes. The OM and iron oxide fluxes were constrained with the model (Table C1). Zero gradient boundary conditions were applied to all species at the lower boundary. The parameters related to bioturbation were determined from measured excess ^{210}Pb profile (Figure C1). The bioirrigation parameters were constrained with measured porewater profiles of DIC and ammonium. The model was further constrained with benthic fluxes of oxygen, DIC, nitrate, ammonium, porewater profiles of oxygen, ammonium, DIC, dissolved iron, hydrogen sulfide and sediment remineralization rate measured by the anoxic incubations. A finite difference scheme and method of lines was applied to solve the coupled differential equations. The uneven grided model was constructed using R package "ReacTran" (Soetaert and Meysman 2012), and was solved using R package "deSolve" (Soetaert et al. 2010c). The model was run to steady state, that is $\frac{\partial C}{\partial t} = 0$, to explore the annually averaged carbon and nutrient turnover rates.

4.4 Results

4.4.1 Sediment appearance

The sediment was very soft, with a surface porosity >0.95 and decreasing to 0.90 at the bottom. The sediment surface appeared to have a thin (~1 cm) yellowish oxidized layer. There was an abundance of 2-4 mm long rice grain shaped particles in the uppermost 1-2 cm, which appeared to be fecal pellets (Figure C2). The sediment below the surface layer was black in color. A sulfide smell was seldom detected during sediment core handing and sectioning. Populations of the tubeworm *Spiochaetopterus sp.* were abundant during sampling, with long tubes in most sediment cores up to >30 cm length. On occasions, live worms were found in some tubes at depths >20 cm during core sectioning.

4.4.2 Sediment geochemistry

The surface TOC content was 5-7 wt% and decreased with depth. The C/N ratio of organic matter was ~10 (Figure 4.2 A,B). The total reactive iron fraction at the surface sediment was ~4 wt% and showed a marginal decrease with depth, whereas pyrite content increased with depth reaching ~2 wt% (Figure 4.2C, Figure C4). The Fe_{py} : Fe_{rectv} ratio increased consistently with depth and remained below 0.6 until 23 cm depth (Figure C4).

The oxygen penetration depth was consistently ~1 mm (Figure 4.2D). The porewater concentrations of NH_4^+ and DIC increased with depth in all seasons until ~5 cm depth with some seasonal variability. With the exception of winter 2019, the concentrations decreased consistently below this depth to the bottom of the sediment cores. The maximum concentration at ~5 cm measured in fall season for both NH_4^+ and DIC was 290 µM and 5800 µM, respectively, and a minimum concentration at 5 cm was recorded in May with a concentration of 150 and 3200 µM, respectively. At depth, no seasonality was detected and the average concentration at ~25 cm was 120 µM and 3500 µM, respectively, for NH_4^+ and DIC. This phenomenon of a reversal of concentration gradients will be referred to as an ‘inverse porewater profile’ (Figure 4.2E,F,Figure C3).

Porewater H_2S concentrations were negligible down to 25 cm depth in most seasons except for winter 2019. Dissolved iron was highest at the surface and then decreased with depth. The maximum measured concentration was ~200 µM at ~2.5 cm. NO_x (NO_3^-+NO_2^-) concentrations were generally (10-20 µM) close to the surface, although on occasions very high NO_x concentrations were observed within the top 5 cm of sediment, with a maximum measured concentration of >60 µM at 5 cm depth that may have been released from foraminifera vacuoles during sample handling (Bernhard et al. 2012). In deeper layers NO_x concentrations were negligible (Figure 4.2,Figure C3).

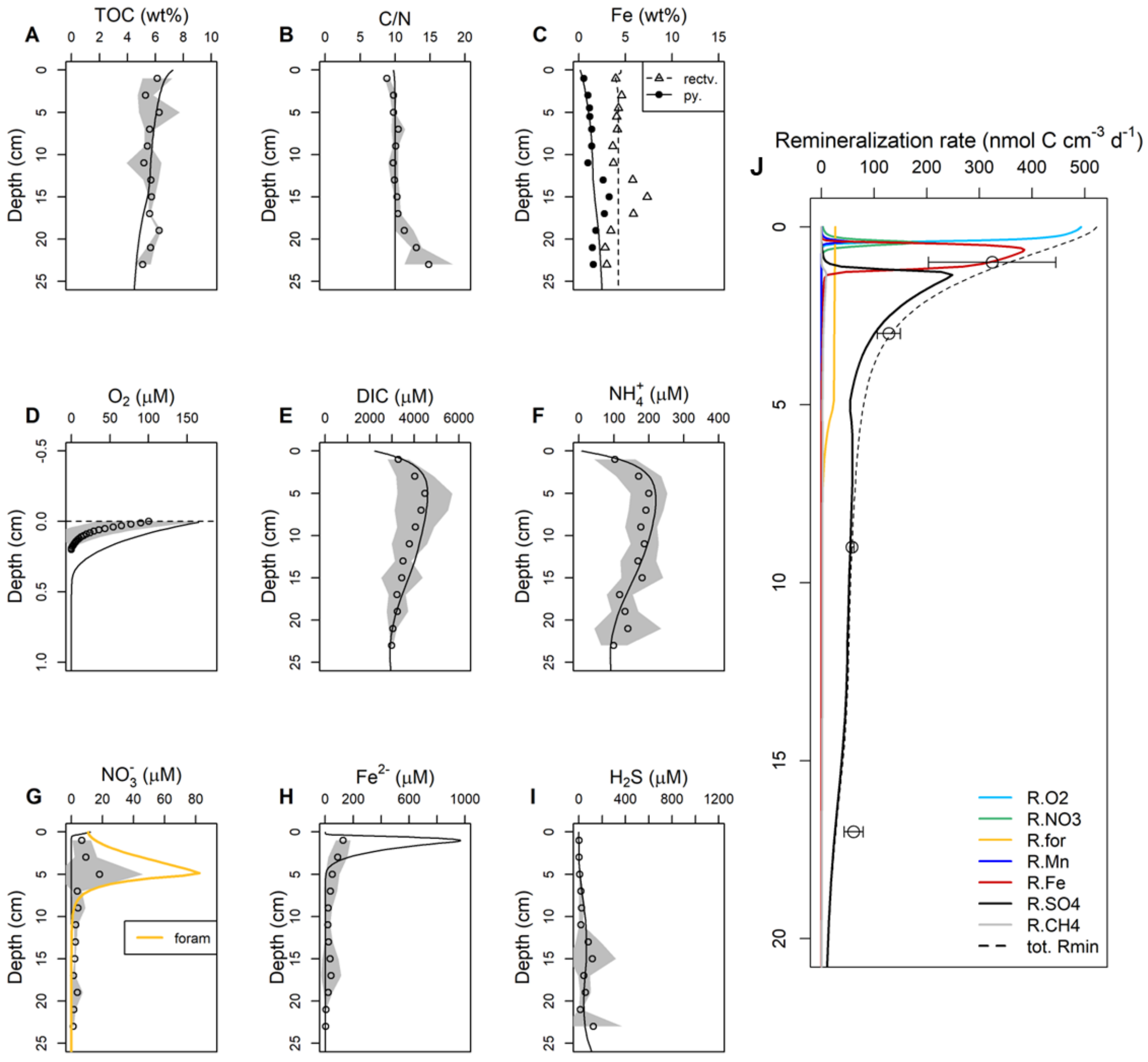

Figure 4.2. (A-I) Sediment solid phase and porewater distributions in Bedford Basin. The symbols denote the interannual average by taking mean of all sampling campaigns. The gray area around the symbol denotes the standard deviations (seasonal variation) of the mean. The lines denote the steady state model simulation. The yellow line in (G) is the modeled intracellular nitrate in equivalent porewater concentration. (J) Model simulated organic matter oxidation rates through sequential use of electron acceptors. The dashed line denotes the sum of all the remineralizations pathways. The open circle denotes the measured organic carbon remineralization rate determined from anoxic incubations.

4.4.3 Benthic solute fluxes

The benthic fluxes determined in this study are summarized in Table 4.1, Figure 4.3. The diffusive oxygen uptake (DOU) calculated from the microsensor oxygen gradients (Rakshit et al. 2023, Chapter 2) were linearly correlated with bottom water oxygen concentration (O_{2BW}). The maximum DOU was measured in summer when the water was well oxygenated, and the lowest DOU was measured in fall when the bottom water was hypoxic. Seasonality in the DIC efflux could not be determined due to the limited number of measurements. However, the summer DIC efflux appeared to be significantly lower than in fall. The sediment was a source of NH_4^+ year-round. Although a clear seasonality could not be identified, NH_4^+ efflux appeared to be highest in fall, and weakest in early summer. The NO_3^- flux was directed into the sediment in all seasons and the influx was highest in fall. BB sediment was a weak net source of DIN, except during the fall months (Table 4.1).

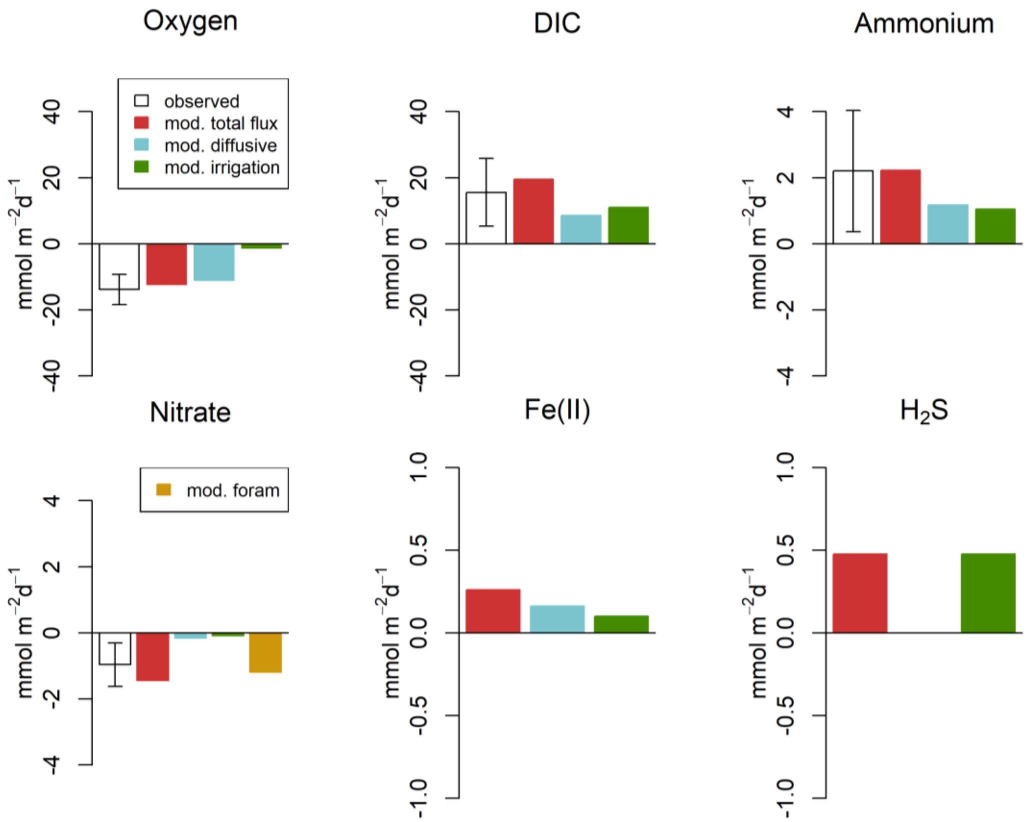

Figure 4.3. Modeled and measured benthic solute fluxes. Measured mean benthic flux is shown by the white bars. The red bars represent the model predicted steady state flux, which is the sum of diffusive (blue) and irrigation (green) fluxes. The nitrate flux shows additional contribution from foraminiferal uptake. Fe(II) and H_2S fluxes were not measured.

4.4.4 Anoxic incubation and organic matter remineralization rate

The carbon and nitrogen remineralization rates are summarized in Table 4.2, Figure 4.2J. Both rates decreased with depth in the sediment. Seasonal variability was noticed in the surface layers and became less evident with depth. The remineralization rate was higher in fall compared to early summer. The C/N ratio of remineralization rate were generally close to Redfield (7.1-11.5) with no clear trend with depth (Table 4.2). A linear increase in Fe^{2+} concentration was noticed at depths 0-2 and 2-4 cm, but not for 8-10 and 16-18 cm sediment, indicating that dissimilatory iron reduction plays a role in organic matter remineralization in the top 4 cm (Figure C5). Interestingly, the linear increase of Fe^{2+} stopped after 25 and 10 days of incubation in fall and early summer, respectively, and remained constant or decreased partially through the remaining duration of incubation. H_2S did not accumulate in the upper 4 cm for the entire duration of incubation in fall, and only accumulated at the final sampling point in summer. However, for sediment sections 8-10 and 16-18 cm, H_2S increased with time during both incubations (Figure C5).

Table 4.2. Organic carbon and nitrogen mineralization rate (nmol cm^{-3} d^{-1}) determined from anoxic incubation.

Depth	November 2020			May 2021		
(cm)	C_{min}	N_{min}	C_{min}:N_{min}	C_{min}	N_{min}	C_{min}:N_{min}
0-2	409.1±42.4	39.4±5.5	10.4	237.9±25.4	28.4±4.9	8.4
2-4	143.9±19.1	18.9±1.1	7.6	112.4±15	14.1±1.4	8
8-10	61.3±8.4	5.4±0.1	11.5	54.5±7.2	7.7±0.7	7.1
16-18	73.2±28.7	3.7±0.5	19.6	48±20	6.6±1	7.3

4.4.5 Results from foraminifera experiment

Living foraminiferal abundances in the top 5 cm of the sediment from the deep Bedford Basin varied from 233 ind. cm^{-2} in May 2021 to 496 ind. cm^{-2} in November 2020 (Table 4.3, Table C6). The two most abundant species were *S. fusiformis* (between 86 and 96% of the total assemblages) and *E. albiumbilicatum* (between 4 and 13%). Other living species that were present included *Eggerella advena*, *Spiroplectamina biformis*, *Globobulimina* sp. and *Labrospira crassimarga* yet accounted for only a minor part of the assemblages (0.2 - 0.6%).

The NO_3^- analyses in the living foraminifera revealed that *E. albiumbilicatum* does not have a significant NO_3^- storage, which is in good agreement with previous studies that did not detect a capacity of denitrification in *Elphidium* spp. (Piña-Ochoa et al. 2010; Glock 2023 and references therein). The intracellular NO_3^- concentration in *S. fusiformis* was 106.5 ± 43.0 mM (n = 3), equivalent to an intracellular NO_3^- content of 75.1 ± 23.8 pmol ind^{-1} (n = 3). It has been shown already that *Stainforthia* sp. can denitrify (Piña-Ochoa et al. 2010). Therefore, we use the published denitrification rate for *Stainforthia* sp. of 70 pmol ind^{-1} day^{-1} (Piña-Ochoa et al. 2010) to estimate total benthic foraminiferal denitrification rates in the deep Bedford Basin. Equations to estimate total benthic denitrification rates and total nutrient concentrations stored in foraminifera from living abundances, population densities and individual rates and nutrient content are available (Glock et al. 2019, 2020). Since *E. albiumbilicatum* showed no NO_3^- storage and the other species comprised a negligible part of the community, we only used the abundances and population densities of *S. fusiformis* to estimate foraminiferal denitrification and NO_3^- storage. The upscaled total benthic foraminiferal denitrification rates ranged from 0.16 mmol m^{-2} day^{-1} in May 2021 to 0.35 mmol m^{-2} day^{-1} in November 2020. Intracellular nitrate storage in the foraminifera ranged between 1.7 and 23.9 µmol l^{-1} of sediment in November 2020 and 1.3 and 5.9 µmol l^{-1} of sediment in May 2021 (Table 4.3, Table C6), thus occasionally exceeding the ambient NO_3^- concentration in the pore water.

Table 4.3. Foraminifera abundances for the dominant species present in the 0-5 cm sediment at Bedford Basin Compass Buoy station. See the text for calculation of total foraminiferal denitrification.

	Abundance (ind cm^{-2})	Intracellular concentration (mM)	Total denitrification rate (mmol N m^{-2} d^{-1})
November 2020			
Stainforthia fusiformis	473.6	n/a	0.35
Elphidium albiumbilicatum	21.0	n/a	n/a
Other species	0.9	n/a	n/a
May 2021			
Stainforthia fusiformis	201.0	n/a	0.16
Elphidium albiumbilicatum	30.8	n/a	n/a
Other species	1.5	n/a	n/a
March 2022			
Stainforthia fusiformis	n/a	107±43	n/a

4.4.6 Model results

The main goal of using the modeling approach here is to gain mechanistic understanding of the early diagenetic processes in the sediments and identify the dominant biogeochemical drivers of benthic biogeochemistry at Bedford Basin. Therefore, the model was used to represent yearly averages rather than intra-annual dynamics. Rather than trying to fit individual field conditions, we used a steady state modeling approach and constrained it with the measured average benthic fluxes, porewater and solid profiles, and OM mineralization rates.

To constrain this model with observations, we first adjusted the rain rate of the three pools of organic matter and their reactivity so that the observed DIC efflux, TOC% and C-mineralization rate at different depths agreed well with model simulation. Then, the bioirrigation coefficients were adjusted to obtain the observed porewater profiles of NH_4^+ and DIC. The results suggested that the inverse porewater profiles could be attributed to deep bioirrigation down to 30 cm by tubeworms. The iron oxide fluxes, reactivities and transformation to iron sulfide were then adjusted to obtain the best visible fit with the observed contents of reactive iron, pyrite as well as dissolved Fe^{2+} and H_2S. At this point, most of observed data and all benthic fluxes except nitrate could be simulated by the model. The nitrate influx observed in the whole core incubation experiments could not be simulated with the model in its current configuration. Therefore, non-local uptake by benthic microorganisms was incorporated. We ruled out the possibility of nitrate uptake by large sulfur bacteria and subsequent DNRA because the ammonium data could be simulated without it. Besides, no filamentous bacterial mats were observed on the recovered sediment cores. Therefore, we assigned the entire non-local transport of nitrate to foraminiferal uptake performing benthic denitrification. At this point the model could successfully simulate all the observed fluxes, depth profiles and remineralization rates observed from the experiments (Figure 4.2, Figure 4.3). The model-predicted foraminiferal nitrate uptake and denitrification was 3 to 8 times higher than the estimated foraminiferal denitrification rates (Section 4.4.5).

4.5 Discussion

The steady state sediment early-diagenetic model presented here was well constrained with the observations from Bedford Basin and can be assumed to represent the annually averaged sediment biogeochemistry of Bedford Basin with reasonable confidence. In the following, we discuss the observed and model results in context of previous studies in the basin, other similar ecosystems, and the recent understanding of the N cycle.

4.5.1 Organic matter turnover and benthic fluxes

The depositional organic carbon flux measured in the 1970s ranged from 17.2 to 21 mmol C m^{-2} d^{-1} (Hargrave and Taguchi 1976, 1978b). This is close to, but lower than, our model estimate of 25.2 mmol C m^{-2} d^{-1}. More data are required to determine whether this apparent 20-40% increase forms part of a longer term trend or else represents normal variation around the annual mean. The model suggests that the organic C burial efficiency in BB sediment is 23% i.e., the rate of C-sequestration at the bottom of the sediment core is 5.6 mmol C m^{-2} d^{-1}. The deposition flux of organic carbon in BB sediment is higher than some Norwegian fjords (Lalande et al. 2020), while similar to others (Wassmann 1984) and lower than turbid river-fed fjords (Hage et al. 2022). The organic carbon burial efficiency in BB is greater than some high arctic and temperate fjord and shelf areas (Kuliński et al. 2014), whereas in consensus with other fjord system (Faust and Knies 2019), BB acts as a hotspot of organic carbon burial (Smith et al. 2015).

Organic carbon mineralization in BB was dominated by sulfate reduction (Figure 4.4A) in consistent with other fine-grained coastal sediments, e.g., shallow depths of Skagerrak (Kristensen et al. 2018), seasonally hypoxic shallow shelf sediments of Gulf of Mexico (Owings et al. 2021) etc. Iron oxide reduction was estimated to be second most important pathway for OM degradation in BB (13%). Bacterial denitrification accounted for 2.5% whereas foraminiferal denitrification accounted for 9% of total organic matter degradation. Aerobic respiration accounted for <10% of the total respiration. The simulated benthic DIC and NH_4^+ flux was 19.6 and 2.2 mmol m^{-2} d^{-1}, respectively, with bioirrigation accounting for ~50% of the total flux (Figure 4.3). However, bioirrigation contributed only ~10% of total benthic oxygen uptake (Figure 4.3) indicating total oxygen uptake (TOU) is dominated by diffusion in BB. The respiration quotient (RQ) (DIC efflux: oxygen influx) was estimated to be 1.6 from the model.

The model calculated nitrogen budget for BB sediment (Figure 4.4B) indicates that majority (96%) of NH_4^+ produced by ammonification is fluxed out of the sediment while a minor portion undergoes nitrification. The calculated burial efficiency of the deposited organic nitrogen was 17% leading to 0.5 mmol N m^{-2} d^{-1} burial, which is within the rate of global N burial rate of 0.002-1.8 mmol N m^{-2} d^{-1} compiled from various ecosystems (Koziorowska et al. 2018). On the other hand, the total nitrate influx was 1.4 mmol m^{-2} d^{-1}, suggesting small efflux of DIN from the sediment. Considering the total N budget, the BB sediment acts as a net sink of N, removing (denitrification + burial) 2.1 mmol m^{-2} d^{-1} of fixed N. The model suggest that the total denitrification is 1.6 mmol N m^{-2} d^{-1}, where 1.2 mmol m^{-2} d^{-1} (75%) was carried out via foraminiferal denitrification, while canonical denitrification accounted for 25% of total denitrification. The nitrate influx observed in BB sediment was higher than similar seasonally hypoxic Eckernforde Bay (Dale et al. 2011) where a nitrate influx of 0.35±0.12 mmol m^{-2} d^{-1} was measured in winter, out of which 75% was ascribed to DNRA while 25% underwent canonical denitrification. However, the NH_4^+ efflux of 1.74±0.15 mmol m^{-2} d^{-1} at this site was similar to BB.

The foraminiferal denitrification that has been calculated from the living abundances of *S. fusiformis* (Table 4.3) and the individual denitrification rate of *Stainforthia* sp. (Piña-Ochoa et al. 2010) is 0.14 – 0.33 mmol m^{-2} d^{-1}, is lower than the modeled foraminiferal denitrification rate. One possibility for this discrepancy is related to the lack of measurements for denitrification rates for *S. fusiformis*. The denitrification rate published for *Stainforthia* sp. (Pina-Ochoa et al., 2010) is amongst the lowest species-specific denitrification rates for foraminifera that has yet been measured (Glock 2023). Thus, it is likely that the average denitrification rate for *S. fusiformis* might be a bit higher. Another factor is that in the model, we did not differentiate between foraminiferal nitrate uptake and denitrification rates, whereas the NO_3^- uptake rates of benthic foraminifera can be up to five times higher than their denitrification rates (Koho et al. 2011). Our measurements of the intracellular NO_3^- storage in *S. fusiformi*s reveal that there is a rich reservoir of NO_3^- stored in foraminifera that sometimes even can exceed the pore water NO_3^- content. If we account for the probable higher uptake rates, the foraminiferal NO_3^- uptake becomes similar to the total foraminiferal denitrification that has been predicted by the model. This, however, creates inconsistency from the steady state point of view. The high nitrate uptake must be denitrified at some time and the foraminifera can not keep on taking more nitrate than they can utilize. This consideration indicates that the rate estimated from foraminiferal abundance is probably the lowest denitrification rate in the BB sediment and the model estimated rate is towards the upper limit of the possible rate. The seasonal denitrification rates could probably lie in between this range.

Our modeled dissolved iron flux of 0.26 mmol Fe m^{-2} d^{-1} from the sediment to the overlying water is within the similar order of magnitude of the measured *in-situ* dissolved iron flux from BB sediment under hypoxic condition (*unpublished*). This indicates that the rate of dissolved iron release from BB sediment could be amongst the highest reported (Dale et al. 2015). In the BB water column, particulate iron concentrations and Fe/Al ratios increase with water depth (Hargrave 1989) which could be due to the reoxidation of benthic-derived dissolved iron in the water column. We found that H_2S barely accumulates in the upper 20 cm of the sediment even though sulfate reduction accounts for 64% of OM degradation and becomes the dominant OM remineralization pathway below 1.2 cm according to the model (Figure 4.2J). Interestingly, our model calculated oxygen budget (Figure 4.4) indicates that majority of the oxygen consumption in sediment can be attributed to the iron cycle, while sulfide oxidation plays a negligible part. This is probably expected as OPD in sediment is ~1 mm. H_2S produced in the sediment through sulfate oxidation below 1.2 cm is quickly incorporated in iron-sulfide minerals before diffusing to the oxic layer, pointing towards an active iron cycle. Although our model predicts a small H_2S efflux, this is entirely due to bioirrigation, and likely H_2S reoxidizes in contact with the oxic tube water. Indeed, consideration of the total Fe(III) deposition flux and Fe(III) required to support remineralization of 2.6 mmol orgC m^{-2} d^{-1} suggest that deposited iron must go through 6 cycles of oxidation-reduction before its ultimate burial as pyrite.

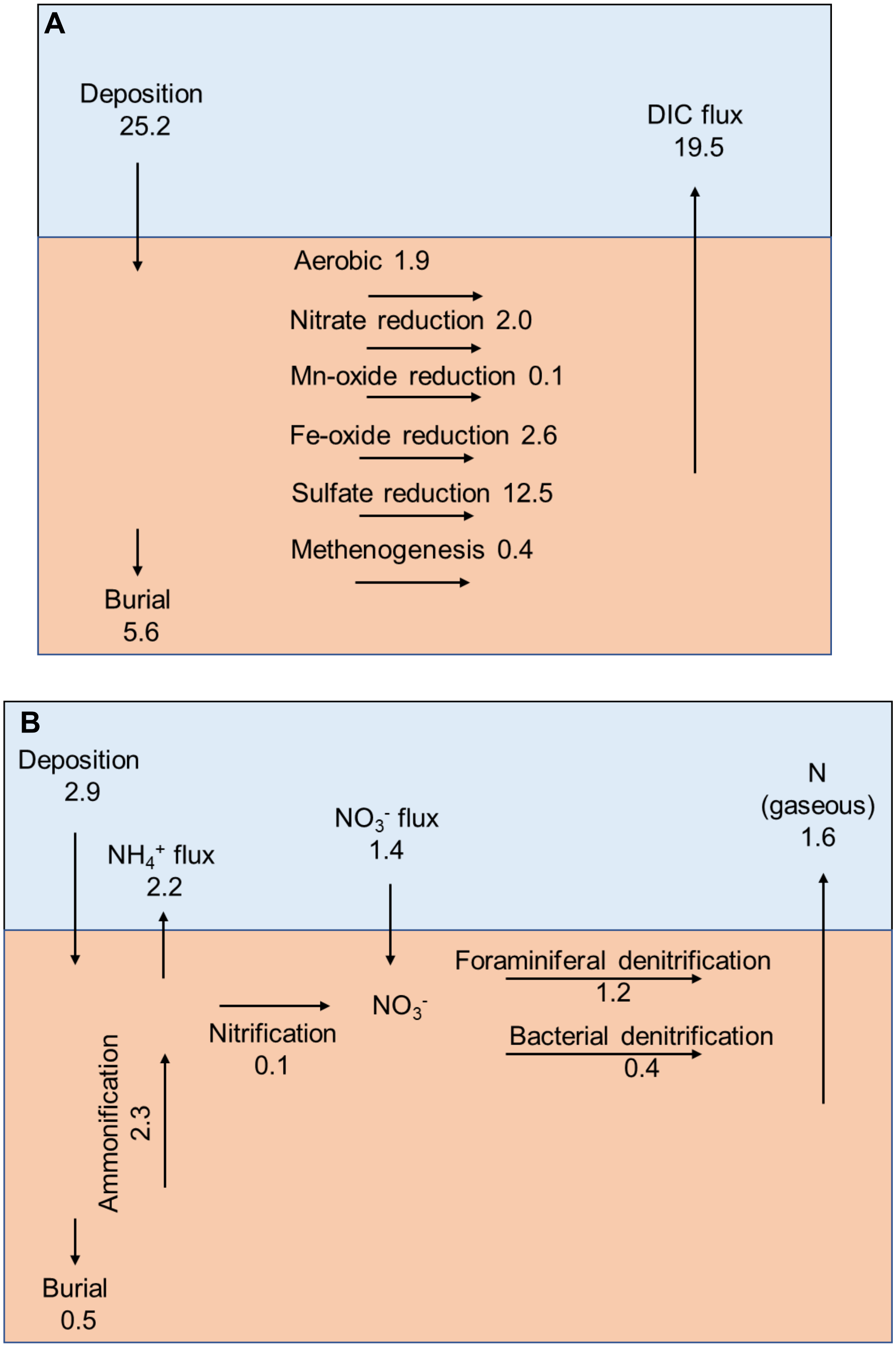

Figure 4.4. Benthic (A) carbon and (B) nitrogen budget of Bedford Basin. Values are given in the unit of mmol C m^{-2} d^{-1} and mmol N m^{-2} d^{-1} for carbon and nitrogen respectively. (C) Relative contribution of different biogeochemical reactions in total sediment oxygen consumption.

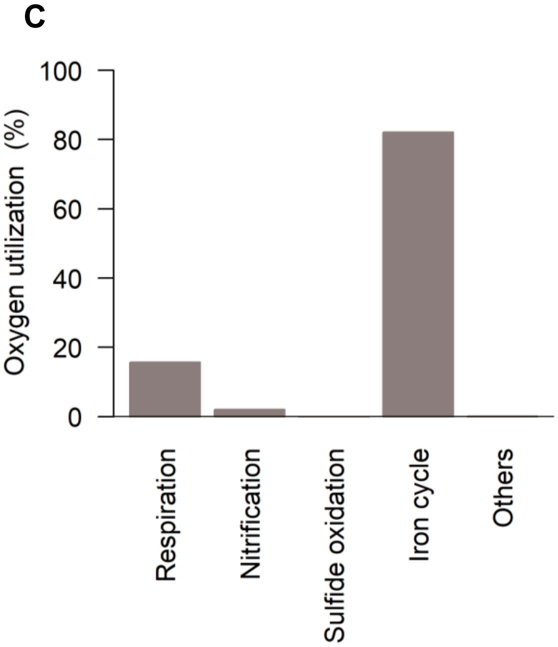

Figure 4.4. Continued from last page.

4.5.2 The impact of tubeworms on sediment geochemistry

The tubeworms, *Spiochaetopterus sp.*, predominant in BB sediment (Hargrave 1989; Fader and Miller 2008; This study) are tube forming polychaetes of the family Chaetopteridae and are a common species along the North Atlantic coast (Barnes 1964). They are typically 3-6 cm in length and construct vertical tubes up to 30 to 50 cm by secreting chitin-like material (Barnes 1964, this study). Under high flow regimes in the bottom water, they carry out suspension feeding, whereas deposit feeding predominates at lower flow regimes (Turner and Miller 1991). They egest waste as elongated fecal pellets shaped like a grain of rice and eject through the upper opening of the tube (Barnes 1964). This probably explains the plethora of fecal pellets that we observed on the collected sediment cores. The worms move vertically through the tubes frequently for the purpose of feeding, cleaning or constructing new segments to their tube. Their membranelles beat continually ensuring non-stop water circulation in the tube which is essential for their survival (Barnes 1964). Moreover, relict tubes of *Spiochaetopterus sp.* can induce passive flushing of the tubes in the presence of ambient bottom currents (Munksby et al. 2002). Therefore, the activity of tube-induced bioirrigation can have a major influence on the biogeochemistry of the sediment (Figure 4.6).

The bioirrigation rate is traditionally measured from incubated sediment cores using an inert tracer such as bromide. However, this technique has called into question, especially for ex-situ measurements where potential bioirrigators are likely to be affected during sediment core handling such as here in the case of the tubeworms (Kristensen et al. 2018). Therefore, alternative techniques, such as using porewater profiles of NH_4^+ or DIC have been suggested to be used to constrain bioirrigation profiles, as we have used in this study (Kristensen et al. 2018). We found that constant deep bioirrigation extending up to 30 cm best explained our data. However, we do not rule out even deeper depths of active bioirrigation as we lack data showing a gradual increase in porewater concentration of NH_4^+ and DIC at the base of bioirrigation zone (Aller 1980).

To understand the controls of bioirrigation on the subsurface geochemical distribution at BB we performed a number of model experiments (Figure 4.5). In the model experiments we – i) reduced the bioirrigation coefficient by a factor of 2, ii) along with reduced bioirrigation coefficient we reduced the depth of active bioirrigation by a factor of 2 (now the bioirrigation zone is till 15 cm below sea floor), iii) completely turned off bioirrigation, and, iv) turned off bioirrigation and lowered the bottom water oxygen to 10 μM to represent oxygen deficit condition.

We found that lowering the bioirrigation coefficient by a factor of 2 retained the typical shape of the depth profiles for DIC, NH_4^+ in BB however their concentration increased, and H_2S started to accumulate towards the bottom of the profile. When we farther reduced the depth of constant bioirrigation to 15 cm below sea floor, we noticed DIC and NH_4^+ concentration deviated significantly from the measured mean porewater profiles and resulted in increasing concentrations with depth. H_2S in this case started to accumulate in the porewater near 8 cm depth. When we turned off the bioirrigation, the DIC and NH_4^+ increased rapidly with depth, whereas H_2S accumulated near 8 cm, similar to the former case. While in addition, we lowered the bottom water oxygen to 10 μM, the DIC and NH_4^+

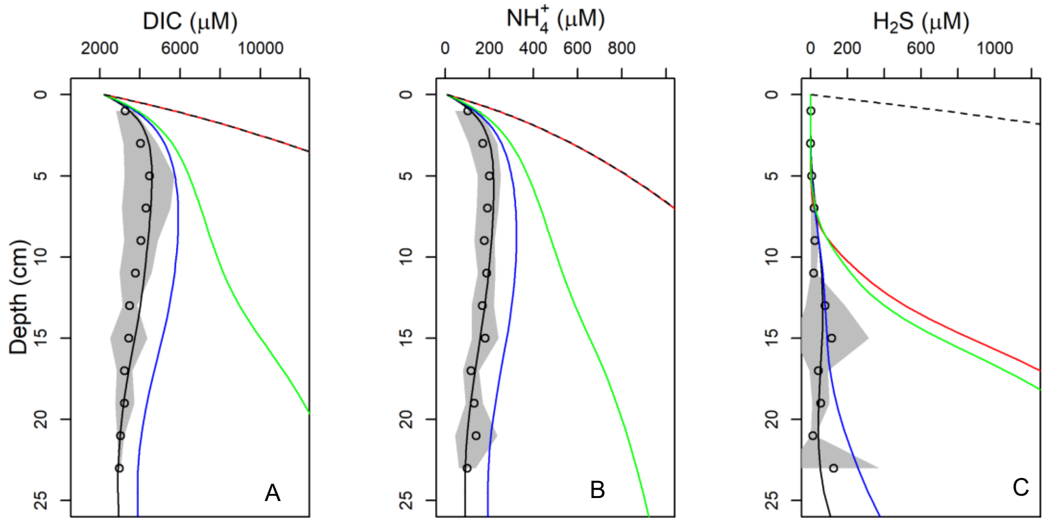

Figure 4.5 Model experiment with varying bioirrigation. The symbols, gray area and solid black lines are identical to figure 4.2. The solid blue, green, red and dashed black line correspond to the model conditions (i), (ii), (iii) and (iv) respectively as indicated in the text in section 4.5.2.

behaved similar to the previous case, however, the H_2S started to accumulate near the surface sediment and H_2S diffused out to the bottom water. The model experiments indicate that bioirrigation exerts strong control on the distribution of porewater solutes in BB, however for H_2S it has most control on the concentration below 8 cm. The top 8 cm of BB sediment remains H_2S free irrespective of bioirrigation. This is likely due to a combination of active iron redox cycling and bioturbation. In low oxygen regime however, when the redox cycling is not sufficiently active, the H_2S starts accumulating near the surface.

Therefore, the results indicated that the deep bioirrigation along with active iron redox cycling and bioturbation were responsible for the minimal H_2S accumulation in BB sediments at least up to 25 cm depth. The tubeworm mortality or disappearance due to ecosystem shift would likely result in shallowing of the suboxic zone, but other factor would keep free sulfide well below the surface sediments. These interpretations should be treated with caution as it is based on steady state scenario, whereas there is seasonal cycle of hypoxia in BB, and changes in bottom boundary conditions could impact the results. Our model suggests that unless the basin becomes permanently anoxic in future or bottom water oxygenation reduces substantially (Rakshit et al., 2023), the coupled biogeochemical processes will continue to prevent sulfide release from BB sediment. Nevertheless, the reason that the tubeworms construct upwards of 30 cm long tubes as seen BB, was not immediately clear. Findings of the living worms down to 30 cm during sectioning indicate that they spend considerable amount of time towards the bottom end of the tube. The likelihood of obtaining fresh organic matter is expected to be high towards the upper end of the tube, therefore, the apparent indication of them spending time at the bottom indicates some form of benefit they receive being down there. While not yet discovered for *Spiochaetopterus sp.* to the best of our knowledge, mutualism in tubeworm with symbiont sulfide oxidizing bacteria has been documented in variety of habitats including hydrothermal vents, cold seeps and fjords (Stewart et al. 2005). Thus, it is worth investigating if there exists any possible symbiosis between microbial consortium and tubeworm *Spiochaetopterus sp.* which might contribute to sulfide oxidation at depths of the sediments (Cordes et al. 2005; Sato and Sasaki 2021). Therefore, future studies should focus on quantitative estimates of benthic macrofauna and their spatiotemporal abundance, identification, combined with genomics and modeling to better understand their ecological role.

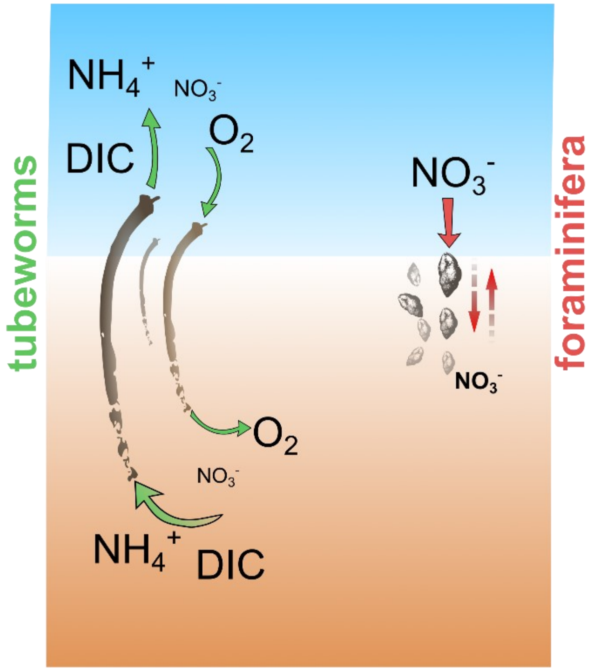

Figure 4.6. Schematic diagram of the actions of tubeworms and foraminifera relevant to Bedford Basin sediment. The tubeworms actively pump water into their inhabiting tube facilitating porewater-bottom water exchange. This process introduce oxygen deeper into the sediment layers where diffusive oxygen penetration depth is only a few millimeters. On the other hand, as the concentration of NH_4^+ and DIC is higher in porewater, this exchange process leads to efflux of these solutes from sediment and dilution of the solutes with bottom water at depths of the sediment. Benthic denitrifying foraminifera are motile and can stores nitrate in their cellular vacuole at high concentrations. The move vertically in the sediment to look for fresh organic matter or to escape predation and can perform denitrification at depths below porewater nitrate maximum.

4.5.3 Significance of foraminiferal denitrification

Denitrifying foraminifera probably acquired the genes necessary for denitrification from bacteria and has an ancient origin (Woehle et al. 2022). The foraminifera are motile and use their pseudopodal network to access nitrate from surface sediment and can migrate to deeper layer to escape predation or actively seek out for fresh organic matter, thus, they have competitive advantage over non-motile bacteria (Figure 4.6) (Dale et al. 2016). The benthic foraminifer, *S. fusiformis*, contributing to foraminiferal denitrification in BB appears to be a relatively recent inhabitant of the basin as their abundance has increased largely after 1970s (Scott 2005). It is a low oxygen tolerant species indicating the basin condition perhaps have deteriorated since last few decades. The model estimated rate of foraminiferal denitrification in BB lies towards the upper end of the global reports of foraminiferal denitrification (Table 4.4), suggesting they may increase denitrification in places with increased hypoxia and contribute significantly to N-loss from the system.

However, this observation may not be exclusively true as non-indigenous species of denitrifying foraminifera in Gullmar fjord were recently found to dominate benthic denitrification under oxic sediment, whereas in sediments below hypoxic water they contributed <5% to denitrification (Choquel et al. 2021). Prolonged hypoxia or anoxia could cause their activity to reduce as it has been suggested that the denitrifying foraminifera are probably facultative anaerobes and respire nitrate to maintain basic survival functions in the absence of oxygen, but require oxygen for energy intensive functions such as growth or reproduction (Piña-Ochoa et al. 2010). Interestingly, laboratory experiments found that while most denitrifying foraminifera can perform complete denitrification to N_2 gas, some foraminifera such as *Bolivina plicata, Stainforthia sp*. etc. could lack nitrous oxide reductase and produce nitrous oxide (N_2O) as the end product which makes them a source of this potent greenhouse gas (Piña-Ochoa et al. 2010). Therefore, the colonization of species such as *Stainforthia fusiformis* in low oxygen environments like BB as studied here, or in other fjords e.g. Gullmar fjord (Nordberg 2000; Polovodova Asteman and Nordberg 2013), generates concerns on its probable impact on global warming with changing environmental conditions. Further study is nonetheless needed to ascertain their roles in the marine greenhouse gas budget.

Table 4.4. Literature data on benthic foraminiferal denitrification from other sites (OMZ = oxygen minimum zone) compared to BB.

Study area	**Rate of foraminiferal denitrification (mmol N m^{-2} d^{-1})**	**% total denitrification**	**Method**[*]	**Reference**
Bedford Basin	1.2	75%	m,e	*This study*
Peruvian OMZ	1.4-1.5	87-90%	m,e	(Dale et al. 2016)
Skagerrak	0.72	70%	e	(Piña-Ochoa et al. 2010)
Bay of Biscay canyon	0.064	84%	e	(Piña-Ochoa et al. 2010)
Chilean OMZ	0.173	70%	e	(Piña-Ochoa et al. 2010)
Arabian Sea OMZ	0.078	9-15%	e	(Piña-Ochoa et al. 2010)
Tagus prodelta, estuary	0.072-240	8-50%	e	(Piña-Ochoa et al. 2010)
Sagamy Bay	0.05	4%	e,l	(Glud et al. 2009)
Peruvian OMZ	0.013-1.32	2-100%	e	(Glock et al. 2013)
Yellow Sea and East China Sea	0.016-0.088	24-61%	e	(Xu et al. 2017)
Gullmar Fjord	0.062-0.133	50-100%	e,l	(Choquel et al. 2021)

[*] : m= modeling, e=empirical, l=measured in lab

4.6 Conclusion

In this work, for the first time we studied the sediment early diagenesis in the seasonally hypoxic Bedford Basin, a natural laboratory for studying oxygen sensitive biogeochemical processes in coastal ocean. We employed direct measurements of benthic fluxes and porewater profiles of oxygen, DIC and nutrients and an empirical reaction transport model. We observed seasonality in the benthic fluxes of oxygen and DIN species. We conclude that long tubeworms, *Spiochaetopterus sp.*, led to inverse porewater profile of ammonium and DIC and contributed to nearly half of their efflux from BB sediment. Together with intense iron turnover and bioturbation, they help to prevent accumulation of hydrogen sulfide in at least top 25 cm of the sediment where the oxygen penetration depth is only a few millimeters. Experiments and modeling indicated that the foraminiferal denitrification rate in BB is among the highest globally, and could contribute up to 75% of the total denitrification in BB. In low oxygen environments, the presence and growing dominance of the foraminifera *Stainforthia fusiformis*, which could lack nitrous oxide reductase enzyme, might have major implication on N_2O gas budget in the changing world which needs further study. The present study was based on understanding the annually averaged early diagenetic processes. Future studies should focus on studying the seasonal evolution of the diagenetic processes and the potential impact of long-term changes in the redox conditions in the basin.

Chapter 5: CONCLUSIONS

This thesis uses Bedford Basin as a natural laboratory to explore biogeochemical cycles in the coastal ocean. The study is complemented by the long high-resolution time series maintained by BIO and MEOPAR, which gives the perspective of historical changes occurring due to climate and environmental changes. The thesis takes a multidisciplinary approach to further our understanding on coastal ocean biogeochemical dynamics. For example, recent advances in numerical models linking gene-centric information in environmental modeling to enhance prediction efficacy (Reed et al. 2014), has been farther progressed in this thesis by the incorporation of such ideas in reaction transport modeling to integrate "bio-geo-chemistry" in its literal true sense to uncover novel mechanisms of the N cycle (Chapter 3). In light of new discoveries in the nitrogen cycle, such as eukaryotic denitrification (Risgaard-Petersen et al. 2006), this study adds to the growing number regions where such evidence has been identified (Chapter 4). Additionally, using a benthic-pelagic coupled model, the development of hypoxia in the basin is studied exploring various mechanisms of oxygen resupply and consumption processes in coastal basins (Chapter 2).

5.1 Summary and main findings

In Chapter 2, the oxygen cycle in the seasonally hypoxic Bedford Basin was studied in conjunction with three years of weekly timeseries of high-resolution hydrographic data and seasonal benthic oxygen consumption. A simple numerical model was developed capable of simulating annual oxygen dynamics, which helped in quantifying different mechanisms of oxygen supply and consumption and their roles in development of hypoxia in the coastal ocean. The model showed that annual winter mixing periodically supplies the majority of the oxygen to the bottom water, although shelf water intrusions can supply equivalent amount of oxygen through rapid but infrequent events. The calculated oxygen budget indicated that although these two events supplied most of the oxygen to bottom waters of the fjord basin, slow mixing during the stratified period can add up to one third of the total annual oxygen supply. Both of the sources of bottom water oxygen (winter mixing and weak mixing during stratification) were found to be sensitive to the SST. Using historical data from the BBMP, it was shown that SST in BB is increasing at an order of magnitude higher rate than the global ocean. Consequently, recent years recorded the lowest annual bottom water oxygen in the basin, with seasonal anoxia for short periods. The work also quantified the sinks of oxygen for deeper parts of the basin. It was found that the majority of oxygen was consumed in the water column, with sediments accounting for one fifth of the total consumption. The model further suggested that the contribution of sediment in total oxygen loss increases logarithmically with increasing water depth, indicating that at shallow depths the sediments would be the dominant oxygen sink. While many studies have previously quantified the consumption of oxygen in the sediment and water column, the novelty of Chapter 2 lies in the simultaneous quantification the sources of oxygen in a coastal system.

In Chapter 3, the thesis took a multidisciplinary collaborative approach to delve into the mechanistic understanding of nitrification in the bottom waters of the basin by exploiting four years of weekly geochemical, hydrological and microbial data from BB bottom water. This work demonstrated an annual cycle of nitrification, and a decoupling between the processes of ammonification/remineralization and nitrification. To understand the mechanism responsible for this, a numerical box model was developed that incorporated geochemical, physical and biological processes into a single framework. This model identified a novel mechanism of nitrification whereby strong dilution of nitrifier biomass via physical mixing delays the onset of nitrification and decouples the two steps of nitrification by affecting regrowth of the AOA, AOB, NOB communities leading to accumulation of nitrite in the water column.

In Chapter 4, the nutrient cycle in the BB sediment was studied comprehensively for the first time. Seasonal measurements of nutrient flux, porewater profiles along with a numerical model opens the floor for further studies on the basin. The study identified that foraminiferal denitrification dominates the N loss from the sediment. This may have increased in importance in the last half century as the basin has faced progressive deoxygenation due to natural and anthropogenic factors. It is the first evidence of foraminiferal denitrification from the east coast of North America. The study also found that long tubeworms inhabiting BB sediment play key roles in the distribution of redox species, and together with active iron cycle, are responsible for maintaining a decimeter-scale suboxic zone in the BB sediment.

5.2 Significance, outlook, and future direction

The thesis has provided important insights into understanding the development of coastal hypoxia and intertwined nutrient cycles and designed easily implementable mathematical tools that can be used in monitoring and policy development. The trends found in SST increase in BB could serve as a proxy for the changing Scotian Shelf (Bill Li *per. comm.*), which is witnessing warming due to changes in ocean current in North Atlantic (Jutras et al. 2020). Similar to the relevance of phytoplankton dynamics of BB and Scotian Shelf (Robicheau et al. 2022), the process in the BB sediment could also provide an accessible avenue to study sediment processes under a changing environment which could be relevant in broader geographical regions.

Future research on BB should take on the findings of the thesis and make progress in a number of directions. To start with, the causes of SST increase should be identified with the help of regional 3D ocean circulation models to disentangle the contributing factors such as changes in ocean currents, global warming and quantify the warming trends in natural and anthropogenic components. As the basin may be on the cusp of transitioning from seasonally hypoxic to seasonally anoxic, the risk of a euxinic bottom water is increasing. Therefore, monitoring programs should include H_2S in their list of routine measurements.

This work presents the first detailed work on benthic nutrient cycles in the basin and was focused primarily on interactions of the nitrogen and oxygen cycles. Further insights could be gained by incorporating the study of stable N isotopes and isotope labeling studies to directly measure different rates of N transformation. The diagenetic model presented in the thesis was solved for steady state, however, in next step a transient model should be applied to predict the seasonal nutrient dynamics of benthic processes. The benthic model could be coupled with processes in the water column (e.g. in Chapter 2 and 3), to provide a 1D biogeochemical model of water and sediment. With the help of such a model, some of the complex processes could be scaled down with the goal of implementing diagenetic formulations in 3D regional models with more accuracy, unlike in present times when many regional models include sediment processes through simple approximations (Soetaert et al. 2000; Lessin et al. 2018). Such endeavour could be feasible based on BB because of the relatively predictable annual dynamics of the basin and availability of highly resolved timeseries. This could potentially allow developing machine learning algorithms, which could be extended to regional models.

Owing to the expertise available in ocean science and technology sector around Halifax, several ocean tech industries have developed in recent decades that uses BB as a trial ground for product development. These companies may benefit from the new knowledge on the underlying biogeochemical processes in BB water and sediment established in this thesis, potentially leading to accelerated R&D. Perhaps one of the most important companies in this sector is Planetary Tech, whose venture to carbon dioxide removal (CDR) from atmosphere by adding alkalinity to the seawater (ocean alkalinity enhancement (OAE)), has received worldwide attention. The test bed for this technology is Bedford Basin. To quantify the impact of this technology in nature, it is important to establish the natural sources of alkalinity in water where sediment is a key contributor. Understanding the benthic biogeochemistry is the first step which has been provided by the thesis. It also paved the way for university and private company partnerships and with an international collaboration, a basin scale drive to quantify benthic carbonate chemistry by measuring in-situ fluxes of DIC, alkalinity along with inorganic nutrients has recently been undertaken (Algar, Kononets, Rakshit, Wallace et al. *unpublished*).

The numerical tools developed in this thesis by studying the BB are in fact a set of general tools that can be applied to a wide variety of natural systems. The reaction-transport model developed are written in open-source R programming language, which researchers can easily adapt, and make full use of the codes to apply to specific requirements. For example, the modeling schemes developed in Chapter 2, have recently been applied to study the iodine dynamics in Bedford Basin (Shi, Rakshit et al. *unpublished*) and in stratified

Whycocomagh Bay in Canada (Chambers, Rakshit et al. *unpublished*) (Vandeplas 2023). Likewise, besides oxygen, dynamics of other biogeochemically relevant species can be studied, not only for BB, but for other coastal bays, fjords and freshwater lakes.

Similarly, a slight variation in the modeling approach in Chapter 3 was able to untangle the nitrogen isotope dynamics in BB rather well (Haas, Rakshit et al. 2022), and it enabled an alternative way to determine in-situ isotopic fractionation factor during nitrification, even when the system is not in steady state. This has classically been a prerequisite in determining isotopic fractionation factors (Mariotti et al. 1981).

This thesis has addressed a long outstanding task of quantifying the benthic nutrient cycle in BB and links to the timeseries of pelagic processes. The BB timeseries remained contributory in the entire study and demonstrated the immense worth of maintaining such high temporal resolution observations, which are only one a handful in the world. These types of records could be crucial in deciphering intrinsic mechanisms of biogeochemical cycles as shown in Chapter 3, and as such many could remain obscure till date where unobtainability of such timeseries in various geographic locations could be a bottleneck.

BIBLIOGRAPHY

Aller, R. C. 1980. Quantifying solute distributions in the bioturbated zone of marine sediments by defining an average microenvironment. Geochim Cosmochim Acta **44**: 1955–1965. doi:10.1016/0016-7037(80)90195-7

AMEC. 2011. Halifax Harbour Water Quality Monitoring Program Final Summary Report.

Amin, S. A., J. W. Moffett, W. Martens-Habbena, and others. 2013. Copper requirements of the ammonia-oxidizing archaeon *Nitrosopumilus maritimus* SCM1 and implications for nitrification in the marine environment. Limnol Oceanogr **58**: 2037–2045. doi:10.4319/lo.2013.58.6.2037

Amir, A., D. McDonald, J. A. Navas-Molina, and others. 2017. Deblur Rapidly Resolves Single-Nucleotide Community Sequence Patterns. mSystems **2**: e00191-16. doi:10.1128/msystems.00191-16

Anderson, R., C. Winter, and K. Jürgens. 2012. Protist grazing and viral lysis as prokaryotic mortality factors at Baltic Sea oxic−anoxic interfaces. Mar Ecol Prog Ser **467**: 1–14. doi:10.3354/meps10001

Azetsu-Scott, K., and B. D. Johnson. 1994. Time series of the vertical distribution of particles during and after a spring phytoplankton bloom in a coastal basin. Cont Shelf Res **14**: 687–705. doi:10.1016/0278-4343(94)90113-9

Baer, S. E., T. L. Connelly, R. E. Sipler, P. L. Yager, and D. A. Bronk. 2014. Effect of temperature on rates of ammonium uptake and nitrification in the western coastal Arctic during winter, spring, and summer. Global Biogeochem Cycles **28**: 1455–1466. doi:10.1002/2013GB004765

Barnes, R. D. 1964. TUBE-BUILDING AND FEEDING IN THE CHAETOPTERID POLYCHAETE, SPIOCHAETOPTERUS OCULATUS. Biol Bull **127**: 397–412. doi:10.2307/1539244

Behrenfeld, M. J. 2010. Abandoning Sverdrup's Critical Depth Hypothesis on phytoplankton blooms. Ecology **91**: 977–989. doi:10.1890/09-1207.1

Beman, J. M., R. Sachdeva, and J. A. Fuhrman. 2010. Population ecology of nitrifying *Archaea* and *Bacteria* in the Southern California Bight. Environ Microbiol **12**: 1282–1292. doi:10.1111/j.1462-2920.2010.02172.x

Berg, P., S. Rysgaard, and B. Thamdrup. 2003. Dynamic Modeling of Early Diagenesis and Nutrient Cycling. A Case Study in an Artic Marine Sediment. Am J Sci **303**: 905–955. doi:10.2475/ajs.303.10.905

Berner, R. A. 1980. Early Diagenesis: A Theoretical Approach, Princeton University Press.

Bernhard, J. M., K. L. Casciotti, M. R. McIlvin, D. J. Beaudoin, P. T. Visscher, and V. P. Edgcomb. 2012. Potential importance of physiologically diverse benthic foraminifera in sedimentary nitrate storage and respiration. J Geophys Res Biogeosci **117**: n/a-n/a. doi:10.1029/2012JG001949

Berounsky, V. M., and S. W. Nixon. 1990. Temperature and annual cycle of nitrification in waters of Narragansett Bay. Limnol Oceanogr **35**: 1610–1617. doi:10.4319/lo.1990.35.7.1610

Bianchi, D., T. S. Weber, R. Kiko, and C. Deutsch. 2018. Global niche of marine anaerobic metabolisms expanded by particle microenvironments. Nat Geosci **11**: 263–268. doi:10.1038/s41561-018-0081-0

BIO. 2022. Bedford Basin Monitoring Program.

Black, E. E., C. K. Algar, M. Armstrong, and S. S. Kienast. 2023. Insights into constraining coastal carbon export from radioisotopes. Front Mar Sci **10**: 1–20. doi:10.3389/fmars.2023.1254316

Bohlen, L., A. W. Dale, and K. Wallmann. 2012. Simple transfer functions for calculating benthic fixed nitrogen losses and C:N:P regeneration ratios in global biogeochemical models. Global Biogeochem Cycles **26**: 2011GB004198. doi:10.1029/2011GB004198

Bollmann, A., I. Schmidt, A. M. Saunders, and M. H. Nicolaisen. 2005. Influence of starvation on potential ammonia-oxidizing activity and *amoA* mRNA levels of *Nitrosospira briensis*. Appl Environ Microbiol **71**: 1276–1282. doi:10.1128/AEM.71.3.1276-1282.2005

Bolyen, E., J. R. Rideout, M. R. Dillon, and others. 2019. Reproducible, interactive, scalable and extensible microbiome data science using QIIME 2. Nat Biotechnol **37**: 852–857. doi:10.1038/s41587-019-0209-9

Boudreau, B. P. 1996. The diffusive tortuosity of fine-grained unlithified sediments. Geochim Cosmochim Acta **60**: 3139–3142. doi:10.1016/0016-7037(96)00158-5

Boudreau, B. P. 1997. Diagenetic Models and Their Implementation, Springer Berlin Heidelberg.

Bourgault, D., F. Cyr, P. S. Galbraith, and E. Pelletier. 2012. Relative importance of pelagic and sediment respiration in causing hypoxia in a deep estuary. J Geophys Res Oceans **117**: n/a-n/a. doi:10.1029/2012JC007902

Breitburg, D., L. A. Levin, A. Oschlies, and others. 2018a. Declining oxygen in the global ocean and coastal waters. Science (1979) **359**: eaam7240. doi:10.1126/science.aam7240

Breitburg, D., L. A. Levin, A. Oschlies, and others. 2018b. Declining oxygen in the global ocean and coastal waters. Science (1979) **359**: eaam7240. doi:10.1126/science.aam7240

Bristow, L. A., N. Sarode, J. Cartee, A. Caro-Quintero, B. Thamdrup, and F. J. Stewart. 2015. Biogeochemical and metagenomic analysis of nitrite accumulation in the Gulf of Mexico hypoxic zone. Limnol Oceanogr **60**: 1733–1750. doi:10.1002/lno.10130

Bryant, L. D., D. F. McGinnis, C. Lorrai, A. Brand, J. C. Little, and A. Wüest. 2010. Evaluating oxygen fluxes using microprofiles from both sides of the sediment-water interface. Limnol Oceanogr Methods **8**: 610–627. doi:10.4319/lom.2010.8.0610

Buckley, D. E., and G. v. Winters. 1992. Geochemical characteristics of contaminated surficial sediments in Halifax Harbour: impact of waste discharge. Can J Earth Sci **29**: 2617–2639. doi:10.1139/e92-208

Burdige, D. J. 2011. Estuarine and Coastal Sediments – Coupled Biogeochemical Cycling, p. 279–316. *In* Treatise on Estuarine and Coastal Science. Elsevier.

Burke, M. J., L. V Gusta, H. A. Quamme, C. J. Weiser, and P. H. Li. 1976. Freezing and Injury in Plants. Annu Rev Plant Physiol **27**: 507–528. doi:10.1146/annurev.pp.27.060176.002451

Burt, W. J., H. Thomas, K. Fennel, and E. Horne. 2013a. Sediment-water column fluxes of carbon, oxygen and nutrients in Bedford Basin, Nova Scotia, inferred from 224 Ra measurements. Biogeosciences **10**: 53–66. doi:10.5194/bg-10-53-2013

Burt, W. J., H. Thomas, K. Fennel, and E. Horne. 2013b. Sediment-water column fluxes of carbon, oxygen and nutrients in Bedford Basin, Nova Scotia, inferred from ^{224}Ra measurements. Biogeosciences **10**: 53–66. doi:10.5194/bg-10-53-2013

Canfield, Donald. E., R. Raiswell, and S. H. Bottrell. 1992. The reactivity of sedimentary iron minerals toward sulfide. Am J Sci **292**: 659–683. doi:10.2475/ajs.292.9.659

Capotondi, A., M. A. Alexander, N. A. Bond, E. N. Curchitser, and J. D. Scott. 2012. Enhanced upper ocean stratification with climate change in the CMIP3 models. J Geophys Res Oceans **117**. doi:10.1029/2011JC007409

Van Cappellen, P., and Y. Wang. 1996. Cycling of iron and manganese in surface sediments; a general theory for the coupled transport and reaction of carbon, oxygen, nitrogen, sulfur, iron, and manganese. Am J Sci **296**: 197–243. doi:10.2475/ajs.296.3.197

Choquel, C., E. Geslin, E. Metzger, and others. 2021. Denitrification by benthic foraminifera and their contribution to N-loss from a fjord environment. Biogeosciences **18**: 327–341. doi:10.5194/bg-18-327-2021

Cline, J. D. 1969. SPECTROPHOTOMETRIC DETERMINATION OF HYDROGEN SULFIDE IN NATURAL WATERS1. Limnol Oceanogr **14**: 454–458. doi:10.4319/lo.1969.14.3.0454

Comeau, A. M., G. M. Douglas, and M. G. I. Langille. 2017. Microbiome Helper: a Custom and Streamlined Workflow for Microbiome Research J. Eisen [ed.]. mSystems **2**: e00127-16. doi:10.1128/mSystems.00127-16

Conley, D. J., C. Humborg, L. Rahm, O. P. Savchuk, and F. Wulff. 2002. Hypoxia in the Baltic Sea and Basin-Scale Changes in Phosphorus Biogeochemistry. Environ Sci Technol **36**: 5315–5320. doi:10.1021/es025763w

Conover, S. A. M. 1975. Nitrogen utilization during spring blooms of marine phytoplankton in Bedford Basin, Nova Scotia, Canada. Mar Biol **32**: 247–261. doi:10.1007/BF00399204

Cordes, E. E., M. A. Arthur, K. Shea, R. S. Arvidson, and C. R. Fisher. 2005. Modeling the Mutualistic Interactions between Tubeworms and Microbial Consortia R.C. Vrijenhoek [ed.]. PLoS Biol **3**: e77. doi:10.1371/journal.pbio.0030077

Cottier, F., V. Tverberg, M. Inall, H. Svendsen, F. Nilsen, and C. Griffiths. 2005. Water mass modification in an Arctic fjord through cross-shelf exchange: The seasonal hydrography of Kongsfjorden, Svalbard. J Geophys Res Oceans **110**: 1–18. doi:10.1029/2004JC002757

Cowan, J. L. W., and W. R. Boynton. 1996. Sediment-Water Oxygen and Nutrient Exchanges along the Longitudinal Axis of Chesapeake Bay: Seasonal Patterns, Controlling Factors and Ecological Significance. Estuaries **19**: 562. doi:10.2307/1352518

Daims, H., E. V Lebedeva, P. Pjevac, and others. 2015. Complete nitrification by *Nitrospira* bacteria. Nature **528**: 504–509. doi:10.1038/nature16461

Dale, A. W., V. Brüchert, M. Alperin, and P. Regnier. 2009. An integrated sulfur isotope model for Namibian shelf sediments. Geochim Cosmochim Acta **73**: 1924–1944. doi:10.1016/j.gca.2008.12.015

Dale, A. W., L. Nickelsen, F. Scholz, C. Hensen, A. Oschlies, and K. Wallmann. 2015. A revised global estimate of dissolved iron fluxes from marine sediments. Global Biogeochem Cycles **29**: 691–707. doi:10.1002/2014GB005017

Dale, A. W., S. Sommer, L. Bohlen, and others. 2011. Rates and regulation of nitrogen cycling in seasonally hypoxic sediments during winter (Boknis Eck, SW Baltic Sea): Sensitivity to environmental variables. Estuar Coast Shelf Sci **95**: 14–28. doi:10.1016/j.ecss.2011.05.016

Dale, A. W., S. Sommer, U. Lomnitz, A. Bourbonnais, and K. Wallmann. 2016. Biological nitrate transport in sediments on the Peruvian margin mitigates benthic sulfide emissions and drives pelagic N loss during stagnation events. Deep Sea Res 1 Oceanogr Res Pap **112**: 123–136. doi:10.1016/j.dsr.2016.02.013

Devol, A. H. 2015. Denitrification, Anammox, and N 2 Production in Marine Sediments. Ann Rev Mar Sci **7**: 403–423. doi:10.1146/annurev-marine-010213-135040

Dhakar, S. P., and D. J. Burdige. 1996. A coupled, non-linear, steady-state model for early diagenetic processes in pelagic sediments. Am J Sci **296**: 296–330. doi:10.2475/ajs.296.3.296

Diaz, R. J., and R. Rosenberg. 2008. Spreading Dead Zones and Consequences for Marine Ecosystems. Science (1979) **321**: 926–929. doi:10.1126/science.1156401

Domingues, R. B., A. B. Barbosa, U. Sommer, and H. M. Galvão. 2011. Ammonium, nitrate and phytoplankton interactions in a freshwater tidal estuarine zone: potential effects of cultural eutrophication. Aquat Sci **73**: 331–343. doi:10.1007/s00027-011-0180-0

Dowgert, M. F., and P. L. Steponkus. 1984. Behavior of the Plasma Membrane of Isolated Protoplasts during a Freeze-Thaw Cycle. Plant Physiol **75**: 1139–1151. doi:10.1104/pp.75.4.1139

Dutkiewicz, S., M. Follows, J. Marshall, and W. W. Gregg. 2001. Interannual variability of phytoplankton abundances in the North Atlantic. Deep Sea Res 2 Top Stud Oceanogr **48**: 2323–2344. doi:10.1016/S0967-0645(00)00178-8

Edgar, R. C. 2004. MUSCLE: a multiple sequence alignment method with reduced time and space complexity. BMC Bioinformatics **5**: 113. doi:10.1186/1471-2105-5-113

El-Swais, H., K. A. Dunn, J. P. Bielawski, W. K. W. Li, and D. A. Walsh. 2015. Seasonal assemblages and short-lived blooms in coastal north-west Atlantic Ocean bacterioplankton. Environ Microbiol **17**: 3642–3661. doi:10.1111/1462-2920.12629

Fader, G. B. J., and R. O. Miller. 2008a. Surficial geology, Halifax harbour, Nova Scotia,.

Fader, G., and R. Miller. 2008b. Surficial geology, Halifax Harbour, Nova Scotia. Geological Survey of Canada Bulletin **590**: 1–165.

Faust, J. C., and J. Knies. 2019. Organic Matter Sources in North Atlantic Fjord Sediments. Geochemistry, Geophysics, Geosystems **20**: 2872–2885. doi:10.1029/2019GC008382

Fennel, K., D. Brady, D. DiToro, and others. 2009. Modeling denitrification in aquatic sediments. Biogeochemistry **93**: 159–178. doi:10.1007/s10533-008-9270-z

Fennel, K., and J. M. Testa. 2019. Biogeochemical Controls on Coastal Hypoxia. Ann Rev Mar Sci **11**: 105–130. doi:10.1146/annurev-marine-010318-095138

Field, C. B., M. J. Behrenfeld, J. T. Randerson, and P. Falkowski. 1998. Primary Production of the Biosphere: Integrating Terrestrial and Oceanic Components. Science (1979) **281**: 237–240. doi:10.1126/science.281.5374.237

Flament, P. 2002. A state variable for characterizing water masses and their diffusive stability: spiciness. Prog Oceanogr **54**: 493–501. doi:10.1016/S0079-6611(02)00065-4

Fogarty, C. 2004. Hurricane Juan Storm Summary. Canadian Hurricane Centre.

de Freitas, T. R., E. T. Bacalhau, and S. T. Disaró. 2021. Biovolume Method for Foraminiferal Biomass Assessment: Evaluation of Geometric Models and Incorporation of Species Mean Cell Occupancy. J Foraminifer Res **51**: 249–266. doi:10.2113/gsjfr.51.4.249

Frölicher, T. L., F. Joos, G.-K. Plattner, M. Steinacher, and S. C. Doney. 2009. Natural variability and anthropogenic trends in oceanic oxygen in a coupled carbon cycle–climate model ensemble. Global Biogeochem Cycles **23**: n/a-n/a. doi:10.1029/2008GB003316

Galloway, J. N., F. J. Dentener, D. G. Capone, and others. 2004. Nitrogen Cycles: Past, Present, and Future. Biogeochemistry **70**: 153–226. doi:10.1007/s10533-004-0370-0

Georges, A. A., H. El-Swais, S. E. Craig, W. K. W. Li, and D. A. Walsh. 2014a. Metaproteomic analysis of a winter to spring succession in coastal northwest Atlantic Ocean microbial plankton. ISME J **8**: 1301–1313. doi:10.1038/ismej.2013.234

Georges, A. A., H. El-Swais, S. E. Craig, W. K. Li, and D. A. Walsh. 2014b. Metaproteomic analysis of a winter to spring succession in coastal northwest Atlantic Ocean microbial plankton. ISME J **8**: 1301–1313. doi:10.1038/ismej.2013.234

Geslin, E., N. Risgaard-Petersen, F. Lombard, E. Metzger, D. Langlet, and F. Jorissen. 2011. Oxygen respiration rates of benthic foraminifera as measured with oxygen microsensors. J Exp Mar Biol Ecol **396**: 108–114. doi:10.1016/j.jembe.2010.10.011

Giblin, A., C. Tobias, B. Song, N. Weston, G. Banta, and V. Rivera-Monroy. 2013. The Importance of Dissimilatory Nitrate Reduction to Ammonium (DNRA) in the Nitrogen Cycle of Coastal Ecosystems. Oceanography **26**: 124–131. doi:10.5670/oceanog.2013.54

Gilbert, D., N. N. Rabalais, R. J. Díaz, and J. Zhang. 2010. Evidence for greater oxygen decline rates in the coastal ocean than in the open ocean. Biogeosciences **7**: 2283–2296. doi:10.5194/bg-7-2283-2010

Glibert, P. M., F. P. Wilkerson, R. C. Dugdale, and others. 2016. Pluses and minuses of ammonium and nitrate uptake and assimilation by phytoplankton and implications for productivity and community composition, with emphasis on nitrogen-enriched conditions. Limnol Oceanogr **61**: 165–197. doi:10.1002/LNO.10203

Glock, N. 2023. Reviews and syntheses : Foraminifera from anaerobic environments - Survival strategies , biogeochemistry , ecology and applications for paleoceanography. Biogeosciences Discussions 1–29. doi:10.5194/bg-2023-49

Glock, N., D. Romero, A. S. Roy, and others. 2020. A hidden sedimentary phosphate pool inside benthic foraminifera from the Peruvian upwelling region might nucleate phosphogenesis. Geochim Cosmochim Acta **289**: 14–32. doi:10.1016/j.gca.2020.08.002

Glock, N., A.-S. Roy, D. Romero, and others. 2019. Metabolic preference of nitrate over oxygen as an electron acceptor in foraminifera from the Peruvian oxygen minimum zone. Proceedings of the National Academy of Sciences **116**: 2860–2865. doi:10.1073/pnas.1813887116

Glock, N., J. Schönfeld, A. Eisenhauer, C. Hensen, J. Mallon, and S. Sommer. 2013. The role of benthic foraminifera in the benthic nitrogen cycle of the Peruvian oxygen minimum zone. Biogeosciences **10**: 4767–4783. doi:10.5194/bg-10-4767-2013

Glud, R. N. 2008. Oxygen dynamics of marine sediments. Marine Biology Research **4**: 243–289. doi:10.1080/17451000801888726

Glud, R. N., B. Thamdrup, H. Stahl, and others. 2009. Nitrogen cycling in a deep ocean margin sediment (Sagami Bay, Japan). Limnol Oceanogr **54**: 723–734. doi:10.4319/lo.2009.54.3.0723

Grant, J., C. W. Emerson, B. T. Hargrave, and J. L. Shortle. 1991. Benthic oxygen consumption on continental shelves off eastern Canada. Cont Shelf Res **11**: 1083–1097. doi:10.1016/0278-4343(91)90092-K

Greenan, B. J. W., T. S. James, J. W. Loder, and others. 2019. Changes in Oceans Surrounding Canada, p. 343–423. *In* E. Bush and D. Lemmen [eds.], Canada's Changing Climate Report. Government of Canada.

Gregory, D. 1993. Oceanographic, geographic and hydrological parameters of Scotia-Fundy and southern Gulf of St. Lawrence inlets. Canadian Technical Report of Hydrography and Ocean Sciences **143**: 1–248.

Groeneweg, J., B. Sellner, and W. Tappe. 1994. Ammonia Oxidation in Nitrosomonas at NH_3 Concentrations Near K_m: Effects of pH and Temperature. Water Res **28**: 2561–2566.

Haas, S., D. K. Desai, J. LaRoche, R. Pawlowicz, and D. W. R. Wallace. 2019. Geomicrobiology of the carbon, nitrogen and sulphur cycles in Powell Lake: a permanently stratified water column containing ancient seawater. Environ Microbiol **21**: 3927–3952. doi:10.1111/1462-2920.14743

Haas, S., S. Rakshit, T. Kalvelage, C. Buchwald, C. K. Algar, and D. W. R. Wallace. 2022. Characterization of nitrogen isotope fractionation during nitrification based on a coastal time series. Limnol Oceanogr **67**: 1714–1731. doi:10.1002/lno.12161

Haas, S., B. M. Robicheau, S. Rakshit, J. Tolman, C. K. Algar, J. LaRoche, and D. W. R. Wallace. 2021. Physical mixing in coastal waters controls and decouples nitrification via biomass dilution. Proceedings of the National Academy of Sciences **118**: e2004877118. doi:10.1073/pnas.2004877118

Hage, S., V. V. Galy, M. J. B. Cartigny, and others. 2022. Turbidity Currents Can Dictate Organic Carbon Fluxes Across River-Fed Fjords: An Example From Bute Inlet (BC, Canada). J Geophys Res Biogeosci **127**: 1–16. doi:10.1029/2022JG006824

Hamme, R. C., J. E. Berry, J. M. Klymak, and K. L. Denman. 2015. In situ O2 and N2 measurements detect deep-water renewal dynamics in seasonally-anoxic Saanich Inlet. Cont Shelf Res **106**: 107–117. doi:10.1016/j.csr.2015.06.012

Hannah, F., R. Rogerson, and J. Laybourn-Parry. 1994. Respiration rates and biovolumes of common benthic Foraminifera (Protozoa). Journal of the Marine Biological Association of the United Kingdom **74**: 301–312. doi:10.1017/S0025315400039345

Hansen, H. P., and F. Koroleff. 1999. Determination of nutrients, p. 159–228. *In* K. Grasshoff, K. Kremling, and M. Erhardt [eds.], Methods of Seawater Analysis. Wiley-VCH Verlag GmbH.

Hardison, A. K., C. K. Algar, A. E. Giblin, and J. J. Rich. 2015. Influence of organic carbon and nitrate loading on partitioning between dissimilatory nitrate reduction to ammonium (DNRA) and N2 production. Geochim Cosmochim Acta **164**: 146–160. doi:10.1016/j.gca.2015.04.049

Hargrave, B. T. 1978a. Seasonal Changes in Oxygen Uptake by Settled Particulate Matter and Sediments in a Marine Bay. Journal of the Fisheries Research Board of Canada **35**: 1621–1628. doi:10.1139/f78-252

Hargrave, B. T. 1978b. Seasonal Changes in Oxygen Uptake by Settled Particulate Matter and Sediments in a Marine Bay. Journal of the Fisheries Research Board of Canada **35**: 1621–1628. doi:10.1139/f78-252

Hargrave, B. T. 1989. Investigations of marine environmental quality in Halifax Harbour / Edited by H.B. Nicholls. H.B. Nicholls [ed.]. Can Tech Rep Fish Aquat Sci **1693**: 1–83.

Hargrave, B. T., and S. Taguchi. 1976. Sedimentation measurements in Bedford Basin, 1973-74. Technical report of Fisheries and Marine Service and Environment **608**: 1–129. doi:10.13140/2.1.2815.3125

Hargrave, B. T., and S. Taguchi. 1978a. Origin of Deposited Material Sedimented in a Marine Bay. Journal of the Fisheries Research Board of Canada **35**: 1604–1613. doi:10.1139/f78-250

Hargrave, B. T., and S. Taguchi. 1978b. Origin of Deposited Material Sedimented in a Marine Bay. Journal of the Fisheries Research Board of Canada **35**: 1604–1613. doi:10.1139/f78-250

Hausfather, Z., K. Cowtan, D. C. Clarke, P. Jacobs, M. Richardson, and R. Rohde. 2017. Assessing recent warming using instrumentally homogeneous sea surface temperature records. Sci Adv **3**. doi:10.1126/sciadv.1601207

Hayward, B. W., F. Le Coze, D. Vachard, and O. Gross. 2023. World Foraminifera Database. Stainforthia fusiformis (Williamson, 1858). Accessed through: World Register of Marine Species at: https://www.marinespecies.org/aphia.php?p=taxdetails&id=113070 on 2023-04-04.

Heiss, E. M., and R. W. Fulweiler. 2016. Coastal water column ammonium and nitrite oxidation are decoupled in summer. Estuar Coast Shelf Sci **178**: 110–119. doi:10.1016/j.ecss.2016.06.002

Hellemann, D., P. Tallberg, S. Aalto, M. Bartoli, and S. Hietanen. 2020. Seasonal cycle of benthic denitrification and DNRA in the aphotic coastal zone, northern Baltic Sea. Mar Ecol Prog Ser **637**: 15–28. doi:10.3354/meps13259

Hendrix, S. A., and R. S. Braman. 1995. Determination of Nitrite and Nitrate by Vanadium(III) Reduction with Chemiluminescence Detection. Methods **7**: 91–97. doi:10.1006/meth.1995.1013

Hollibaugh, J. T., S. M. Gifford, M. A. Moran, M. J. Ross, S. Sharma, and B. B. Tolar. 2014. Seasonal variation in the metatranscriptomes of a Thaumarchaeota population from SE USA coastal waters. ISME J **8**: 685–698. doi:10.1038/ismej.2013.171

Holtermann, P., R. Prien, M. Naumann, and L. Umlauf. 2020. Interleaving of oxygenized intrusions into the Baltic Sea redoxcline. Limnol Oceanogr **65**: 482–503. doi:10.1002/lno.11317

Horak, R. E. A., W. Qin, A. D. Bertagnolli, and others. 2018. Relative impacts of light, temperature, and reactive oxygen on thaumarchaeal ammonia oxidation in the North Pacific Ocean. Limnol Oceanogr **63**: 741–757. doi:10.1002/lno.10665

Horak, R. E. A., W. Qin, A. J. Schauer, E. V. Armbrust, A. E. Ingalls, J. W. Moffett, D. A. Stahl, and A. H. Devol. 2013. Ammonia oxidation kinetics and temperature sensitivity of a natural marine community dominated by Archaea. ISME J **7**: 2023–33. doi:10.1038/ismej.2013.75

Horrigan, S. G., J. P. Montoya, J. L. Nevins, J. J. McCarthy, H. Ducklow, R. Goericke, and T. Malone. 1990. Nitrogenous nutrient transformations in the spring and fall in the Chesapeake Bay. Estuar Coast Shelf Sci **30**: 369–391. doi:10.1016/0272-7714(90)90004-B

Horrigan, S. G., and A. L. Springer. 1990. Oceanic and estuarine ammonium oxidation: Effects of light. Limnol Oceanogr **35**: 479–482. doi:10.4319/lo.1990.35.2.0479

Huettel, M., P. Berg, and J. E. Kostka. 2014. Benthic Exchange and Biogeochemical Cycling in Permeable Sediments. Ann Rev Mar Sci **6**: 23–51. doi:10.1146/annurev-marine-051413-012706

Huntsman, A. G. 1924. Circulation and Pollution of Water In and Near Halifax Harbour. Contributions to Canadian Biology and Fisheries **2**: 71–81. doi:10.1139/f24-003

Hwang, J. H., and J. A. Oleszkiewicz. 2007. Effect of Cold-Temperature Shock on Nitrification. Water Environment Research **79**: 964–968. doi:10.2175/106143007x176022

Jahnke, R. A., Clare. E. Reimers, and D. B. Craven. 1990. Intensification of recycling of organic matter at the sea floor near ocean margins. Nature **348**: 50–54. doi:10.1038/348050a0

Jäntti, H., and S. Hietanen. 2012. The Effects of Hypoxia on Sediment Nitrogen Cycling in the Baltic Sea. Ambio **41**: 161–169. doi:10.1007/s13280-011-0233-6

Johnson, K. S., S. C. Riser, and D. M. Karl. 2010. Nitrate supply from deep to near-surface waters of the North Pacific subtropical gyre. Nature **465**: 1062–1065. doi:10.1038/nature09170

Joye, S. B., and J. T. Hollibaugh. 1995. Influence of Sulfide Inhibition of Nitrification on Nitrogen Regeneration in Sediments. Science (1979) **270**: 623–625. doi:10.1126/science.270.5236.623

Jutras, M., C. O. Dufour, A. Mucci, F. Cyr, and D. Gilbert. 2020. Temporal Changes in the Causes of the Observed Oxygen Decline in the St. Lawrence Estuary. J Geophys Res Oceans **125**: e2020JC016577. doi:10.1029/2020JC016577

Katsev, S., G. Chaillou, B. Sundby, and A. Mucci. 2007. Effects of progressive oxygen depletion on sediment diagenesis and fluxes: A model for the lower St. Lawrence River Estuary. Limnol Oceanogr **52**: 2555–2568. doi:10.4319/lo.2007.52.6.2555

Kelley, D. E. 2018. The OCE Package, p. 91–101. *In* Oceanographic Analysis with R. Springer.

Kelly, S., E. Eyto, M. Dillane, R. Poole, and M. White. 2020. Characterizing ventilation events in an anoxic coastal basin: Observed dynamics and the role of climatic drivers. Limnol Oceanogr **9999**: 1–23. doi:10.1002/lno.11462

Kemp, W., P. Sampou, J. Garber, J. Turtle, and W. Boynton. 1992. Seasonal depletion of oxygen from bottom waters of Chesapeake Bay: roles of benthic and planktonic respiration and physical exchange processes. Mar Ecol Prog Ser **85**: 137–152. doi:10.3354/meps085137

Kérouel, R., and A. Aminot. 1997. Fluorometric determination of ammonia in sea and estuarine waters by direct segmented flow analysis. Mar Chem **57**: 265–275. doi:10.1016/S0304-4203(97)00040-6

Kerrigan, E. A., M. Kienast, H. Thomas, and D. W. R. Wallace. 2017. Using oxygen isotopes to establish freshwater sources in Bedford Basin, Nova Scotia, a Northwestern Atlantic fjord. Estuar Coast Shelf Sci **199**: 96–104. doi:10.1016/j.ecss.2017.09.003

van Kessel, M. A. H. J., D. R. Speth, M. Albertsen, P. H. Nielsen, H. J. M. Op den Camp, B. Kartal, M. S. M. Jetten, and S. Lücker. 2015. Complete nitrification by a single microorganism. Nature **528**: 555–559. doi:10.1038/nature16459

Kitzinger, K., H. K. Marchant, L. A. Bristow, and others. 2020. Single cell analyses reveal contrasting life strategies of the two main nitrifiers in the ocean. Nat Commun **11**: 767. doi:10.1038/s41467-020-14542-3

Kitzinger, K., C. C. Padilla, H. K. Marchant, and others. 2019. Cyanate and urea are substrates for nitrification by *Thaumarchaeota* in the marine environment. Nat Microbiol **4**: 234–243. doi:10.1038/s41564-018-0316-2

Koho, K. A., E. Piña-Ochoa, E. Geslin, and N. Risgaard-Petersen. 2011. Vertical migration, nitrate uptake and denitrification: survival mechanisms of foraminifers (Globobulimina turgida) under low oxygen conditions. FEMS Microbiol Ecol **75**: 273–283. doi:10.1111/j.1574-6941.2010.01010.x

Koziorowska, K., K. Kuliński, and J. Pempkowiak. 2018. Deposition, return flux, and burial rates of nitrogen and phosphorus in the sediments of two high-Arctic fjords. Oceanologia **60**: 431–445. doi:10.1016/j.oceano.2018.05.001

Kristensen, E., H. Røy, K. Debrabant, and T. Valdemarsen. 2018. Carbon oxidation and bioirrigation in sediments along a Skagerrak-Kattegat-Belt Sea depth transect. Mar Ecol Prog Ser **604**: 33–50. doi:10.3354/meps12734

Kuliński, K., M. Kędra, J. Legeżyńska, M. Gluchowska, and A. Zaborska. 2014. Particulate organic matter sinks and sources in high Arctic fjord. Journal of Marine Systems **139**: 27–37. doi:10.1016/j.jmarsys.2014.04.018

Kumar, S., G. Stecher, and K. Tamura. 2016. MEGA7: Molecular Evolutionary Genetics Analysis Version 7.0 for Bigger Datasets. Mol Biol Evol **33**: 1870–1874. doi:10.1093/molbev/msw054

Laanbroek, H. J., and S. Gerards. 1993. Competition for limiting amounts of oxygen between *Nitrosomonas europaea* and *Nitrobacter winogradskyi* grown in mixed continuous cultures. Arch Microbiol **159**: 453–459. doi:10.1007/BF00288593

Lacasse, O., A. Rochon, and S. Roy. 2013. High cyst concentrations of the potentially toxic dinoflagellate Alexandrium tamarense species complex in Bedford Basin, Halifax, Nova Scotia, Canada. Mar Pollut Bull **66**: 230–233. doi:10.1016/j.marpolbul.2012.10.016

Lalande, C., K. Dunlop, P. E. Renaud, G. Nadaï, and A. K. Sweetman. 2020. Seasonal variations in downward particle fluxes in Norwegian fjords. Estuar Coast Shelf Sci **241**: 106811. doi:10.1016/j.ecss.2020.106811

Laperriere, S. M., N. J. Nidzieko, R. J. Fox, A. W. Fisher, and A. E. Santoro. 2019. Observations of Variable Ammonia Oxidation and Nitrous Oxide Flux in a Eutrophic Estuary. Estuaries and Coasts **42**: 33–44. doi:10.1007/s12237-018-0441-4

LaRoche, J., R. Nuzzi, R. Waters, K. Wyman, P. Falkowski, and D. Wallace. 1997. Brown Tide blooms in Long Island's coastal waters linked to interannual variability in groundwater flow. Glob Chang Biol **3**: 397–410. doi:10.1046/j.1365-2486.1997.00117.x

Lehmann, M. F., B. Barnett, Y. Gélinas, D. Gilbert, R. J. Maranger, A. Mucci, B. Sundby, and B. Thibodeau. 2009. Aerobic respiration and hypoxia in the Lower St. Lawrence Estuary: Stable isotope ratios of dissolved oxygen constrain oxygen sink partitioning. Limnol Oceanogr **54**: 2157–2169. doi:10.4319/lo.2009.54.6.2157

Lessin, G., Y. Artioli, E. Almroth-Rosell, and others. 2018. Modelling Marine Sediment Biogeochemistry: Current Knowledge Gaps, Challenges, and Some Methodological Advice for Advancement. Front Mar Sci **5**: 1–8. doi:10.3389/fmars.2018.00019

Letunic, I., and P. Bork. 2016. Interactive tree of life (iTOL) v3: an online tool for the display and annotation of phylogenetic and other trees. Nucleic Acids Res **44**: W242–W245. doi:10.1093/nar/gkw290

Levin, L. A., W. Ekau, A. J. Gooday, and others. 2009. Effects of natural and human-induced hypoxia on coastal benthos. Biogeosciences **6**: 2063–2098. doi:10.5194/bg-6-2063-2009

Li, W. K. W. 2014a. The state of phytoplankton and bacterioplankton at the Compass Buoy Station: Bedford Basin Monitoring Program 1992-2013. Canadian Technical Report of Hydrography and Ocean Sciences **304**: xiv + 122.

Li, W. K. W. 2014b. The state of phytoplankton and bacterioplankton at the Compass Buoy Station: Bedford Basin Monitoring Program 1992-2013. Canadian Technical Report of Hydrography and Ocean Sciences **304**: 1–122.

Li, W. K. W., and P. M. Dickie. 2001. Monitoring phytoplankton, bacterioplankton, and virioplankton in a coastal inlet (Bedford Basin) by flow cytometry. Cytometry **44**: 236–246. doi:10.1002/1097-0320(20010701)44:3<236::AID-CYTO1116>3.0.CO;2-5

Li, W. K. W., P. M. Dickie, and J. A. Spry. 1998. Plankton Monitoring Programme in the Bedford Basin, 1991- 1997. Canadian Data Report of Fisheries and Aquatic Sciences **1036**: vii + 342.

Li, W. K. W., and W. G. Harrison. 2008a. Propagation of an atmospheric climate signal to phytoplankton in a small marine basin. Limnol Oceanogr **53**: 1734–1745. doi:10.4319/lo.2008.53.5.1734

Li, W. K. W., and W. G. Harrison. 2008b. Propagation of an atmospheric climate signal to phytoplankton in a small marine basin. Limnol Oceanogr **53**: 1734–1745. doi:10.4319/lo.2008.53.5.1734

Li, W. K. W., M. R. Lewis, and W. G. Harrison. 2010. Multiscalarity of the nutrient-chlorophyll relationship in coastal phytoplankton. Estuaries and Coasts **33**: 440–447. doi:10.1007/s12237-008-9119-7

Li, Y., M. Li, and W. M. Kemp. 2015. A Budget Analysis of Bottom-Water Dissolved Oxygen in Chesapeake Bay. Estuaries and Coasts **38**: 2132–2148. doi:10.1007/s12237-014-9928-9

Lomas, M. W., and F. Lipschultz. 2006. Forming the primary nitrite maximum: Nitrifiers or phytoplankton? Limnol Oceanogr **51**: 2453–2467. doi:10.4319/lo.2006.51.5.2453

Lorenzen, C. J. 1966. A method for the continuous measurement of *in vivo* chlorophyll concentration. Deep Sea Research and Oceanographic Abstracts **13**: 223–227. doi:10.1016/0011-7471(66)91102-8

Ma, X., S. T. Lennartz, and H. W. Bange. 2019. A multi-year observation of nitrous oxide at the Boknis Eck Time Series Station in the Eckernförde Bay (southwestern Baltic Sea). Biogeosciences **16**: 4097–4111. doi:10.5194/bg-16-4097-2019

Mariotti, A., J. C. Germon, P. Hubert, P. Kaiser, R. Letolle, A. Tardieux, and P. Tardieux. 1981. Experimental determination of nitrogen kinetic isotope fractionation: Some principles; illustration for the denitrification and nitrification processes. Plant Soil **62**: 413–430. doi:10.1007/BF02374138

Martens-Habbena, W., P. M. Berube, H. Urakawa, J. R. de la Torre, and D. A. Stahl. 2009. Ammonia oxidation kinetics determine niche separation of nitrifying Archaea and Bacteria. Nature **461**: 976–979. doi:10.1038/nature08465

McCarthy, J. J., W. Kaplan, and J. L. Nevins. 1984. Chesapeake Bay nutrient and plankton dynamics. 2. Sources and sinks of nitrite. Limnol Oceanogr **29**: 84–98. doi:10.4319/lo.1984.29.1.0084

McDougall, T. J., and O. A. Krzysik. 2015. Spiciness. J Mar Res **73**: 141–152. doi:10.1357/002224015816665589

McGrath, T., M. Cronin, E. Kerrigan, D. Wallace, C. Gregory, C. Normandeau, and E. McGovern. 2019. A rare intercomparison of nutrient analysis at sea: lessons learned and recommendations to enhance comparability of open-ocean nutrient data. Earth Syst Sci Data **11**: 355–374. doi:10.5194/essd-11-355-2019

Merbt, S. N., D. A. Stahl, E. O. Casamayor, E. Martí, G. W. Nicol, and J. I. Prosser. 2012. Differential photoinhibition of bacterial and archaeal ammonia oxidation. FEMS Microbiol Lett **327**: 41–46. doi:10.1111/j.1574-6968.2011.02457.x

Middelburg, J. J., and L. A. Levin. 2009. Coastal hypoxia and sediment biogeochemistry. Biogeosciences **6**: 1273–1293. doi:10.5194/bg-6-1273-2009

Middelburg, J. J., K. Soetaert, P. M. J. Herman, and C. H. R. Heip. 1996. Denitrification in marine sediments: A model study. Global Biogeochem Cycles **10**: 661–673. doi:10.1029/96GB02562

Miller, A. A. L., P. J. Mudie, and D. B. Scott. 1982. Holocene history of Bedford Basin, Nova Scotia: foraminifera, dinoflagellate, and pollen records. Can J Earth Sci **19**: 2342–2367. doi:10.1139/e82-205

Mitchell, M., G. Harrison, K. Pauley, A. Gagné, G. Maillet, and P. Strain. 2002. Atlantic Zonal Monitoring Program Sampling Protocol. Canadian Technical Report of Hydrography and Ocean Sciences **223**: 1–23.

Mordy, C. W., L. B. Eisner, P. Proctor, P. Stabeno, A. H. Devol, D. H. Shull, J. M. Napp, and T. Whitledge. 2010. Temporary uncoupling of the marine nitrogen cycle: Accumulation of nitrite on the Bering Sea shelf. Mar Chem **121**: 157–166. doi:10.1016/j.marchem.2010.04.004

Munksby, N., M. Benthien, and R. N. Glud. 2002. Flow-induced flushing of relict tube structures in the central Skagerrak (Norway). Mar Biol **141**: 939–945. doi:10.1007/s00227-002-0874-x

Murphy, J., and J. P. Riley. 1962. A modified single solution method for the determination of phosphate in natural waters. Anal Chim Acta **27**: 31–36. doi:10.1016/S0003-2670(00)88444-5

Nixon, S. W., J. W. Ammerman, L. P. Atkinson, M. E. Q. Pilson, and S. P. Seitzinger. 1996. The fate of nitrogen and phosphorus at the land-sea margin of the North Atlantic Ocean Five major rivers with an average water flow exceeding 3000 m 3 s-l discharge. Biogeochemistry **35**: 141–180.

Noffke, A., S. Sommer, A. W. Dale, P. O. J. Hall, and O. Pfannkuche. 2016. Benthic nutrient fluxes in the Eastern Gotland Basin (Baltic Sea) with particular focus on microbial mat ecosystems. Journal of Marine Systems **158**: 1–12. doi:10.1016/j.jmarsys.2016.01.007

Nordberg, K. 2000. Decreasing oxygen concentrations in the Gullmar Fjord, Sweden, as confirmed by benthic foraminifera, and the possible association with NAO. Journal of Marine Systems **23**: 303–316. doi:10.1016/S0924-7963(99)00067-6

Owings, S. M., L. Bréthous, E. M. Eitel, and others. 2021. Differential manganese and iron recycling and transport in continental margin sediments of the Northern Gulf of Mexico. Mar Chem **229**: 103908. doi:10.1016/j.marchem.2020.103908

Pan, Y., and D. V. Subba Rao. 1997. Impacts of domestic sewage effluent on phytoplankton from Bedford Basin, eastern Canada. Mar Pollut Bull **34**: 1001–1005. doi:10.1016/S0025-326X(97)00115-X

Peng, X., C. A. Fuchsman, A. Jayakumar, M. J. Warner, A. H. Devol, and B. B. Ward. 2016. Revisiting nitrification in the Eastern Tropical South Pacific : A focus on controls. J Geophys Res Oceans **121**: 1667–1684. doi:10.1002/2015JC011455.Received

Peñuelas, J., B. Poulter, J. Sardans, and others. 2013. Human-induced nitrogen-phosphorus imbalances alter natural and managed ecosystems across the globe. Nat Commun **4**: 2934. doi:10.1038/ncomms3934

Peterson, I., B. Greenan, D. Gilbert, and D. Hebert. 2017. Variability and wind forcing of ocean temperature and thermal fronts in the Slope Water region of the Northwest Atlantic. J Geophys Res Oceans **122**: 7325–7343. doi:10.1002/2017JC012788

Petrie, B., and P. Yeats. 1990a. Simple models of the circulation, dissolved metals, suspended solids and nutrients in Halifax Harbour. Water Quality Research Journal of Canada **25**: 325–349.

Petrie, B., and P. Yeats. 1990b. Simple Models of the Circulation, Dissolved Metals, Suspended Solids and Nutrients in Halifax Harbour. Water Quality Research Journal **25**: 325–350. doi:10.2166/wqrj.1990.017

Philips, S., H. Laanbroek, and W. Verstraete. 2002. Origin, causes and effects of increased nitrite concentrations in aquatic environments. Reviews in environmental **1**: 115–141.

Pina-Ochoa, E., S. Hogslund, E. Geslin, and others. 2010. Widespread occurrence of nitrate storage and denitrification among Foraminifera and Gromiida. Proceedings of the National Academy of Sciences **107**: 1148–1153. doi:10.1073/pnas.0908440107

Piña-Ochoa, E., S. Høgslund, E. Geslin, and others. 2010. Widespread occurrence of nitrate storage and denitrification among Foraminifera and Gromiida. Proc Natl Acad Sci U S A **107**: 1148–1153. doi:10.1073/pnas.0908440107

Pitcher, A., C. Wuchter, K. Siedenberg, S. Schouten, and J. S. Sinninghe Damsté. 2011. Crenarchaeol tracks winter blooms of ammonia-oxidizing Thaumarchaeota in the coastal North Sea. Limnol Oceanogr **56**: 2308–2318. doi:10.4319/lo.2011.56.6.2308

Platt, T., A. Prakash, and B. Irwin. 1972. Phytoplankton nutrients and flushing of inlets on the coast of Nova Scotia. Le Naturaliste Canadien **99**: 253–261.

Polovodova Asteman, I., and K. Nordberg. 2013. Foraminiferal fauna from a deep basin in Gullmar Fjord: The influence of seasonal hypoxia and North Atlantic Oscillation. J Sea Res **79**: 40–49. doi:10.1016/j.seares.2013.02.001

Pruitt, K. D., T. Tatusova, and D. R. Maglott. 2007. NCBI reference sequences (RefSeq): a curated non-redundant sequence database of genomes, transcripts and proteins. Nucleic Acids Res **35**: D61–D65. doi:10.1093/nar/gkl842

Punshon, S., and R. M. Moore. 2004a. Nitrous oxide production and consumption in a eutrophic coastal embayment. Mar Chem **91**: 37–51. doi:10.1016/j.marchem.2004.04.003

Punshon, S., and R. M. Moore. 2004b. Nitrous oxide production and consumption in a eutrophic coastal embayment. Mar Chem **91**: 37–51. doi:10.1016/j.marchem.2004.04.003

Qin, W., S. A. Amin, W. Martens-Habbena, and others. 2014. Marine ammonia-oxidizing archaeal isolates display obligate mixotrophy and wide ecotypic variation. Proc Natl Acad Sci U S A **111**: 12504–12509. doi:10.1073/pnas.1324115111

Qin, W., K. A. Meinhardt, J. W. Moffett, A. H. Devol, E. Virginia Armbrust, A. E. Ingalls, and D. A. Stahl. 2017. Influence of oxygen availability on the activities of ammonia-oxidizing archaea. Environ Microbiol Rep **9**: 250–256. doi:10.1111/1758-2229.12525

Rabouille, C., B. Lansard, S. M. Owings, and others. 2021. Early Diagenesis in the Hypoxic and Acidified Zone of the Northern Gulf of Mexico: Is Organic Matter Recycling in Sediments Disconnected From the Water Column? Front Mar Sci **8**: 1–18. doi:10.3389/fmars.2021.604330

Rakshit, S., A. W. Dale, D. W. Wallace, and C. K. Algar. 2023. Sources and sinks of bottom water oxygen in a seasonally hypoxic fjord. Front Mar Sci **10**: 655. doi:10.3389/fmars.2023.1148091

Rao, D., Y. Pan, V. Zitko, G. Bugden, and K. Mackeigan. 1993. Diarrhetic shellfish poisoning (DSP) associated with a subsurface bloom of Dinophysis norvegica in Bedford Basin, eastern Canada. Mar Ecol Prog Ser **97**: 117–126.

Rasmussen, H., and B. B. Jorgensen. 1992. Microelectrode studies of seasonal oxygen uptake in a coastal sediment: role of molecular diffusion. Mar Ecol Prog Ser **81**: 289–303. doi:10.3354/meps081289

Reed, D. C., C. K. Algar, J. A. Huber, and G. J. Dick. 2014. Gene-centric approach to integrating environmental genomics and biogeochemical models. Proceedings of the National Academy of Sciences **111**: 1879–1884. doi:10.1073/pnas.1313713111

Riddle, A. M., and R. E. Lewis. 2000. Dispersion Experiments in U.K. Coastal Waters. Estuar Coast Shelf Sci **51**: 243–254. doi:10.1006/ecss.2000.0661

Risgaard-Petersen, N., A. M. Langezaal, S. Ingvardsen, and others. 2006. Evidence for complete denitrification in a benthic foraminifer. Nature **443**: 93–96. doi:10.1038/nature05070

Robicheau, B. M., J. Tolman, E. M. Bertrand, and J. LaRoche. 2022. Highly-resolved interannual phytoplankton community dynamics of the coastal Northwest Atlantic. ISME Communications **2**: 38. doi:10.1038/s43705-022-00119-2

Robidart, J. C., C. M. Preston, R. W. Paerl, K. A. Turk, A. C. Mosier, C. A. Francis, C. A. Scholin, and J. P. Zehr. 2012. Seasonal *Synechococcus* and *Thaumarchaeal* population dynamics examined with high resolution with remote *in situ* instrumentation. ISME J **6**: 513–523. doi:10.1038/ismej.2011.127

Robinson, C., and P. J. le B. Williams. 2005. Respiration and its measurement in surface marine waters, p. 147–180. *In* Respiration in Aquatic Ecosystems. Oxford University Press.

la Roche, J. 1983. Ammonium regeneration: its contribution to phytoplankton nitrogen requirements in a eutrophic environment. Mar Biol **75**: 231–240. doi:10.1007/BF00406007

Rognes, T., T. Flouri, B. Nichols, C. Quince, and F. Mahé. 2016. VSEARCH: a versatile open source tool for metagenomics. PeerJ **4**: e2584. doi:10.7717/peerj.2584

Ruijter, J. M., C. Ramakers, W. M. H. Hoogaars, Y. Karlen, O. Bakker, M. J. B. van den Hoff, and A. F. M. Moorman. 2009. Amplification efficiency: linking baseline and bias in the analysis of quantitative PCR data. Nucleic Acids Res **37**: e45. doi:10.1093/nar/gkp045

Sakamoto, C. M., K. S. Johnson, and L. J. Coletti. 2009. Improved algorithm for the computation of nitrate concentrations in seawater using an in situ ultraviolet spectrophotometer. Limnol Oceanogr Methods **7**: 132–143. doi:10.4319/lom.2009.7.132

Salmaso, N. 2005. Effects of climatic fluctuations and vertical mixing on the interannual trophic variability of Lake Garda, Italy. Limnol Oceanogr **50**: 553–565. doi:10.4319/lo.2005.50.2.0553

Sanders, R., S. A. Henson, M. Koski, and others. 2014. The Biological Carbon Pump in the North Atlantic. Prog Oceanogr **129**: 200–218. doi:10.1016/j.pocean.2014.05.005

Santoro, A. E., C. M. Sakamoto, J. M. Smith, and others. 2013. Measurements of nitrite production in and around the primary nitrite maximum in the central California Current. Biogeosciences **10**: 7395–7410. doi:10.5194/bg-10-7395-2013

Sasaki, A., Y. Hagimori, I. Yuasa, and T. Nakatsubo. 2012. Annual sediment respiration in estuarine sandy intertidal flats in the Seto Inland Sea, Japan. Landscape and Ecological Engineering **8**: 107–114. doi:10.1007/s11355-011-0157-0

Sato, M., and A. Sasaki. 2021. Evolution and Maintenance of Mutualism between Tubeworms and Sulfur-Oxidizing Bacteria. Am Nat **197**: 351–365. doi:10.1086/712780

Schaefer, S. C., and J. T. Hollibaugh. 2017. Temperature Decouples Ammonium and Nitrite Oxidation in Coastal Waters. Environ Sci Technol **51**: 3157–3164. doi:10.1021/acs.est.6b03483

Schmidtko, S., L. Stramma, and M. Visbeck. 2017. Decline in global oceanic oxygen content during the past five decades. Nature **542**: 335–339. doi:10.1038/nature21399

Scholz, F., and T. Neumann. 2007. Trace element diagenesis in pyrite-rich sediments of the Achterwasser lagoon, SW Baltic Sea. Mar Chem **107**: 516–532. doi:10.1016/j.marchem.2007.08.005

Scott, D. B. 2005. Pollution Monitoring in Two North American Estuaries: Historical Reconstructions Using Benthic Foraminifera. The Journal of Foraminiferal Research **35**: 65–82. doi:10.2113/35.1.65

Scrosati, R. A. 2020. Upwelling spike and marked SST drop after the arrival of cyclone Dorian to the Atlantic Canadian coast. J Sea Res **159**: 101888. doi:10.1016/j.seares.2020.101888

Seitaj, D., R. Schauer, F. Sulu-Gambari, S. Hidalgo-Martinez, S. Y. Malkin, L. D. W. Burdorf, C. P. Slomp, and F. J. R. Meysman. 2015. Cable bacteria generate a firewall against euxinia in seasonally hypoxic basins. Proceedings of the National Academy of Sciences **112**: 13278–13283. doi:10.1073/pnas.1510152112

Seitaj, D., F. Sulu-Gambari, L. D. W. Burdorf, A. Romero-Ramirez, O. Maire, S. Y. Malkin, C. P. Slomp, and F. J. R. Meysman. 2017. Sedimentary oxygen dynamics in a seasonally hypoxic basin. Limnol Oceanogr **62**: 452–473. doi:10.1002/lno.10434

Seitzinger, S., J. A. Harrison, J. K. Böhlke, A. F. Bouwman, R. Lowrance, B. Peterson, C. Tobias, and G. van Drecht. 2006. Denitrification across landscapes and waterscapes: A synthesis. Ecological Applications **16**: 2064–2090. doi:10.1890/1051-0761(2006)016[2064:DALAWA]2.0.CO;2

Shan, S., and J. Sheng. 2012. Examination of circulation, flushing time and dispersion in Halifax Harbour of Nova Scotia. Water Quality Research Journal **47**: 353–374. doi:10.2166/wqrjc.2012.041

Shan, S., J. Sheng, K. R. Thompson, and D. A. Greenberg. 2011a. Simulating the three-dimensional circulation and hydrography of Halifax Harbour using a multi-nested coastal ocean circulation model. Ocean Dyn **61**: 951–976. doi:10.1007/s10236-011-0398-3

Shan, S., J. Sheng, K. R. Thompson, and D. A. Greenberg. 2011b. Simulating the three-dimensional circulation and hydrography of Halifax Harbour using a multi-nested coastal ocean circulation model. Ocean Dyn **61**: 951–976. doi:10.1007/s10236-011-0398-3

Shi, Q., and D. Wallace. 2018a. A 3-year time series of volatile organic iodocarbons in Bedford Basin, Nova Scotia: a northwestern Atlantic fjord. Ocean Science **14**: 1385–1403. doi:10.5194/os-14-1385-2018

Shi, Q., and D. Wallace. 2018b. A 3-year time series of volatile organic iodocarbons in Bedford Basin, Nova Scotia: a northwestern Atlantic fjord. Ocean Science **14**: 1385–1403. doi:10.5194/os-14-1385-2018

Simpson, J. H. 1981. The shelf-sea fronts: implications of their existence and behaviour. Philosophical Transactions of the Royal Society of London. Series A, Mathematical and Physical Sciences **302**: 531–546. doi:10.1098/rsta.1981.0181

Sintes, E., D. De Corte, E. Haberleitner, and G. J. Herndl. 2016. Geographic Distribution of Archaeal Ammonia Oxidizing Ecotypes in the Atlantic Ocean. Front Microbiol **7**: 77. doi:10.3389/fmicb.2016.00077

Small, C., and R. J. Nicholls. 2003. A global analysis of human settlement in coastal zones. J Coast Res **19**: 584–599.

Smith, R. W., T. S. Bianchi, M. Allison, C. Savage, and V. Galy. 2015. High rates of organic carbon burial in fjord sediments globally. Nat Geosci **8**: 450–453. doi:10.1038/ngeo2421

Soetaert, K., P. M. J. Herman, and J. J. Middelburg. 1996a. A model of early diagenetic processes from the shelf to abyssal depths. Geochim Cosmochim Acta **60**: 1019–1040. doi:10.1016/0016-7037(96)00013-0

Soetaert, K., P. M. J. Herman, and J. J. Middelburg. 1996b. Dynamic response of deep-sea sediments to seasonal variations: A model. Limnol Oceanogr **41**: 1651–1668. doi:10.4319/lo.1996.41.8.1651

Soetaert, K., and F. Meysman. 2012. Reactive transport in aquatic ecosystems: Rapid model prototyping in the open source software R. Environmental Modelling & Software **32**: 49–60. doi:10.1016/j.envsoft.2011.08.011

Soetaert, K., J. J. Middelburg, P. M. J. Herman, and K. Buis. 2000. On the coupling of benthic and pelagic biogeochemical models. Earth Sci Rev **51**: 173–201. doi:10.1016/S0012-8252(00)00004-0

Soetaert, K., and T. Petzoldt. 2010a. Inverse modelling, sensitivity and monte carlo analysis in R using package FME. J Stat Softw **33**: 1–28. doi:10.18637/jss.v033.i03

Soetaert, K., and T. Petzoldt. 2010b. Inverse Modelling, Sensitivity and Monte Carlo Analysis in R Using Package FME. J Stat Softw **33**: 1–28. doi:10.18637/jss.v033.i03

Soetaert, K., T. Petzoldt, and F. J. R. Meysman. 2010a. marelac: Tools for Aquatic Sciences v2.1.3. R package.

Soetaert, K., T. Petzoldt, and R. W. Setzer. 2010b. Solving differential equations in R: Package deSolve. J Stat Softw **33**: 1–25. doi:10.18637/jss.v033.i09

Soetaert, K., T. Petzoldt, and R. W. Setzer. 2010c. Solving Differential Equations in R : Package deSolve. J Stat Softw **33**: 1–25. doi:10.18637/jss.v033.i09

Sokoll, S., G. Lavik, S. Sommer, T. Goldhammer, M. M. M. Kuypers, and M. Holtappels. 2016. Extensive nitrogen loss from permeable sediments off North-West Africa. J Geophys Res Biogeosci **121**: 1144–1157. doi:10.1002/2015JG003298

Solórzano, L. 1969. DETERMINATION OF AMMONIA IN NATURAL WATERS BY THE PHENOLHYPOCHLORITE METHOD 1 1 This research was fully supported by U.S. Atomic Energy Commission Contract No. ATS (11-1) GEN 10, P.A. 20. Limnol Oceanogr **14**: 799–801. doi:10.4319/lo.1969.14.5.0799

Song, G., S. Liu, J. Zhang, Z. Zhu, G. Zhang, H. K. Marchant, M. M. M. Kuypers, and G. Lavik. 2021. Response of benthic nitrogen cycling to estuarine hypoxia. Limnol Oceanogr **66**: 652–666. doi:10.1002/lno.11630

Stewart, F. J., I. L. G. Newton, and C. M. Cavanaugh. 2005. Chemosynthetic endosymbioses: adaptations to oxic–anoxic interfaces. Trends Microbiol **13**: 439–448. doi:10.1016/j.tim.2005.07.007

Stramma, L., G. C. Johnson, J. Sprintall, and V. Mohrholz. 2008. Expanding oxygen-minimum zones in the tropical oceans. Science (1979) **320**: 655–658. doi:10.1126/science.1153847

Suzuki, I., U. Dular, and S. C. Kwok. 1974. Ammonia or ammonium ion as substrate for oxidation by *Nitrosomonas europaea* cells and extracts. J Bacteriol **120**: 556–558.

Taguchi, S., and B. T. Hargrave. 1978. Loss Rates of Suspended Material Sedimented in a Marine Bay. Journal of the Fisheries Research Board of Canada **35**: 1614–1620. doi:10.1139/f78-251

Taguchi, S., and T. Platt. 1977. Assimilation of $^{14}CO_2$ in the dark compared to phytoplankton production in a small coastal inlet. Estuarine and Coastal Marine Science **5**: 679–684. doi:10.1016/0302-3524(77)90092-5

Testa, J. M., J. B. Clark, W. C. Dennison, and others. 2017. Ecological Forecasting and the Science of Hypoxia in Chesapeake Bay. Bioscience **67**: 614–626. doi:10.1093/biosci/bix048

Thomas, H., S. E. Craig, B. J. W. Greenan, and others. 2012. Direct observations of diel biological CO&lt;sub&gt;2&lt;/sub&gt; fixation on the Scotian Shelf, northwestern Atlantic Ocean. Biogeosciences **9**: 2301–2309. doi:10.5194/bg-9-2301-2012

Tjoelker, M. G., J. Oleksyn, and P. B. Reich. 2001. Modelling respiration of vegetation: evidence for a general temperature-dependent Q 10. Glob Chang Biol **7**: 223–230. doi:10.1046/j.1365-2486.2001.00397.x

Tromp, T. K., P. Van Cappellen, and R. M. Key. 1995. A global model for the early diagenesis of organic carbon and organic phosphorus in marine sediments. Geochim Cosmochim Acta **59**: 1259–1284. doi:10.1016/0016-7037(95)00042-X

Turner, E. J., and D. C. Miller. 1991. Behavior of a passive suspension-feeder (Spiochaetopterus oculatus (Webster)) under oscillatory flow. J Exp Mar Biol Ecol **149**: 123–137. doi:10.1016/0022-0981(91)90120-L

Vandeplas, S. 2023. Effects of an aquaculture fish farm on the sediment geochemistry of a naturally anoxic basin. Master’s Thesis. Dalhousie University. http://hdl.handle.net/10222/82749

Vaquer-Sunyer, R., and C. M. Duarte. 2008. Thresholds of hypoxia for marine biodiversity. Proceedings of the National Academy of Sciences **105**: 15452–15457. doi:10.1073/pnas.0803833105

Vercaemer, B., and D. Sephton. 2014. Rapid assessment and biofouling monitoring of Halifax Harbour and Bedford Basin following the detection of three new invasive ascidians in Nova Scotia. Can Tech Rep Fish Aquat Sci **3063**: v + 28.

Verhagen, F. J., and H. J. Laanbroek. 1992. Effects of Grazing by Flagellates on Competition for Ammonium between Nitrifying and Heterotrophic Bacteria in Chemostats. Appl Environ Microbiol **58**: 1962–1969.

Viollier, E., P. W. Inglett, K. Hunter, A. N. Roychoudhury, and P. Van Cappellen. 2000. The ferrozine method revisited: Fe(II)/Fe(III) determination in natural waters. Applied Geochemistry **15**: 785–790. doi:10.1016/S0883-2927(99)00097-9

Voss, M., H. W. Bange, J. W. Dippner, J. J. Middelburg, J. P. Montoya, and B. Ward. 2013. The marine nitrogen cycle: Recent discoveries, uncertaintiesand the potential relevance of climate change. Philosophical Transactions of the Royal Society B: Biological Sciences **368**: 20130121. doi:10.1098/rstb.2013.0121

Walker, C. B., J. R. de la Torre, M. G. Klotz, and others. 2010. *Nitrosopumilus maritimus* genome reveals unique mechanisms for nitrification and autotrophy in globally distributed marine crenarchaea. Proc Natl Acad Sci U S A **107**: 8818–8823. doi:10.1073/pnas.0913533107

Wang, Y., and P. van Cappellen. 1996. A multicomponent reactive transport model of early diagenesis: Application to redox cycling in coastal marine sediments. Geochim Cosmochim Acta **60**: 2993–3014. doi:10.1016/0016-7037(96)00140-8

Ward, B. B. 1987. Kinetic studies on ammonia and methane oxidation by *Nitrosococcus oceanus*. Arch Microbiol **147**: 126–133. doi:10.1007/BF00415273

Wassmann, P. 1984. Sedimentation and benthic mineralization of organic detritus in a Norwegian fjord. Mar Biol **83**: 83–94. doi:10.1007/BF00393088

White, M. E., P. A. Rafter, B. M. Stephens, S. D. Wankel, and L. I. Aluwihare. 2019. Recent Increases in Water Column Denitrification in the Seasonally Suboxic Bottom Waters of the Santa Barbara Basin. Geophys Res Lett **46**: 6786–6795. doi:10.1029/2019GL082075

Woehle, C., A.-S. Roy, N. Glock, and others. 2022. Denitrification in foraminifera has an ancient origin and is complemented by associated bacteria. Proceedings of the National Academy of Sciences **119**: e2200198119. doi:10.1073/pnas.2200198119

Xia, F., J. G. Wang, T. Zhu, B. Zou, S. K. Rhee, and Z. X. Quan. 2018. Ubiquity and Diversity of Complete Ammonia Oxidizers (Comammox). Appl Environ Microbiol **84**: e01390-18. doi:10.1128/AEM.01390-18

Xu, Z., S. Liu, R. Xiang, and G. Song. 2017. Live benthic foraminifera in the Yellow Sea and the East China Sea: vertical distribution, nitrate storage, and potential denitrification. Mar Ecol Prog Ser **571**: 65–81. doi:10.3354/meps12135

Yilmaz, P., L. W. Parfrey, P. Yarza, and others. 2014. The SILVA and "All-species Living Tree Project (LTP)" taxonomic frameworks. Nucleic Acids Res **42**: D643–D648. doi:10.1093/nar/gkt1209

Yool, A., A. P. Martin, C. Fernández, and D. R. Clark. 2007. The significance of nitrification for oceanic new production. Nature **447**: 999–1002. doi:10.1038/nature05885

Yoshiyama, K., and J. H. Sharp. 2006. Phytoplankton response to nutrient enrichment in an urbanized estuary: Apparent inhibition of primary production by overeutrophication. Limnol Oceanogr **51**: 424–434. doi:10.4319/lo.2006.51.1_part_2.0424

Zakem, E. J., A. Al-Haj, M. J. Church, and others. 2018. Ecological control of nitrite in the upper ocean. Nat Commun **9**: 1206. doi:10.1038/s41467-018-03553-w

Zhang, X., G. Flato, M. Kirchmeier-Young, and others. 2019. Changes in Temperature and Precipitation Across Canada, p. 112–193. *In* E. Bush and D. Lemmen [eds.], Canada's Changing Climate Report. Government of Canada.

APPENDIX A: SUPPORTING INFORMATION TO CHAPTER 2

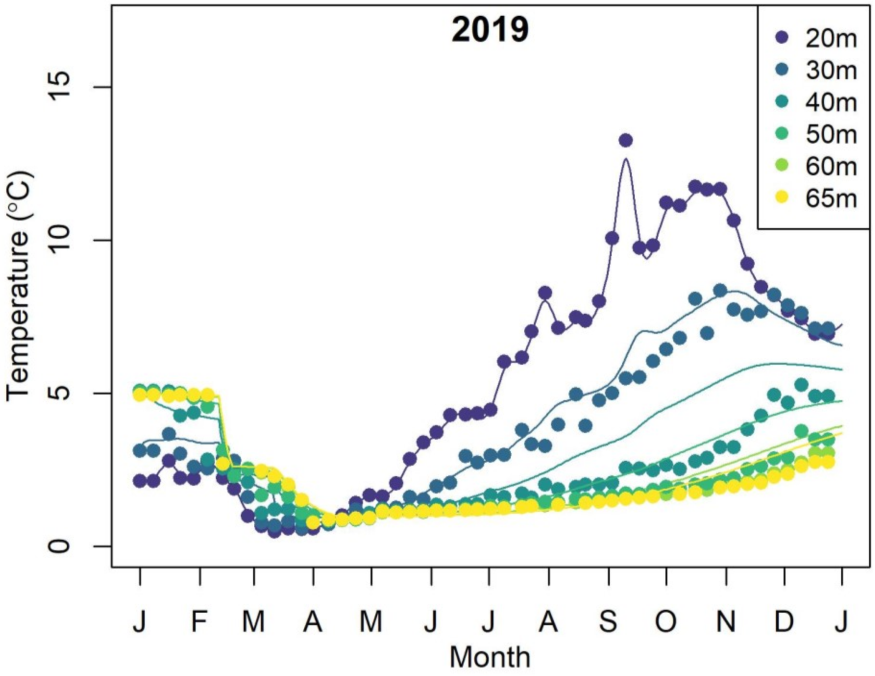

Figure A1. Model simulation of temperature (T) for 2019. Winter mixing was obtained by observed oxygen concentrations in the bottom water as described in section 2.4 of the main manuscript. Whereas stratified time Kz was obtained by fitting it to the observed temperature at different water depths, especially focusing on the deeper layers. The resulting plot shows a reasonable model fit to the temperature data. The model equation used here is $\frac{dT}{dt} = K_z \frac{d^2T}{dt^2}$.

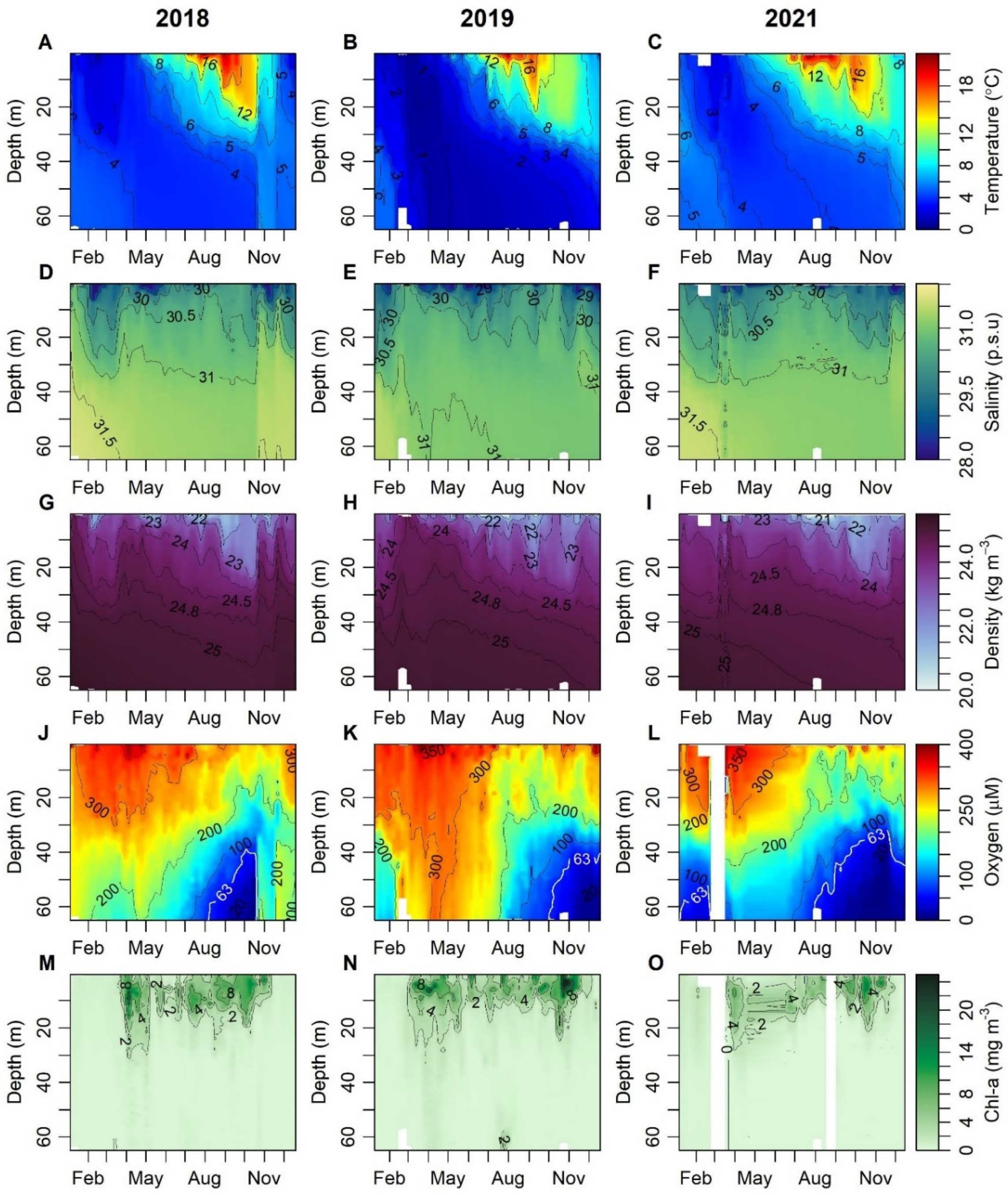

Figure A2. Measured depth-time plots of temperature, salinity, density, dissolved oxygen and chlorophyll fluorescence for 2018, 2019 and 2021 obtained from the weekly CTD deployments.

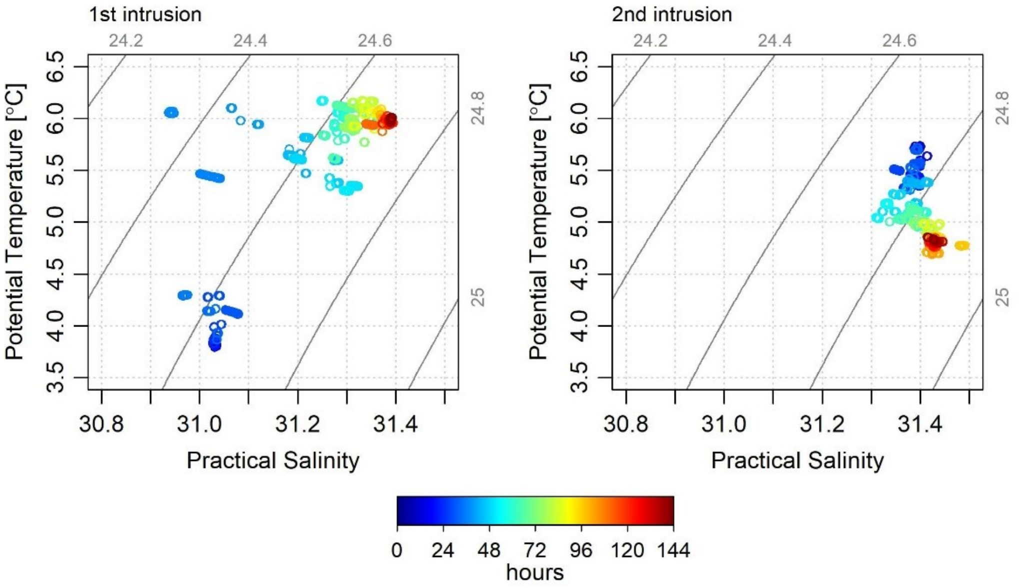

Figure A3. T-S plots showing the evolution of the water mass at 60 m during the 1st and 2nd intrusion of 2018 as captured by the benthic instrument pod. Six days (144 hours) of data around each intrusion are shown to demonstrate the rapid changes in T and S during intrusions. See Figure 3 in the main manuscript for more details. The contour lines on the plots are isopycnals (-1000 kg/m3).

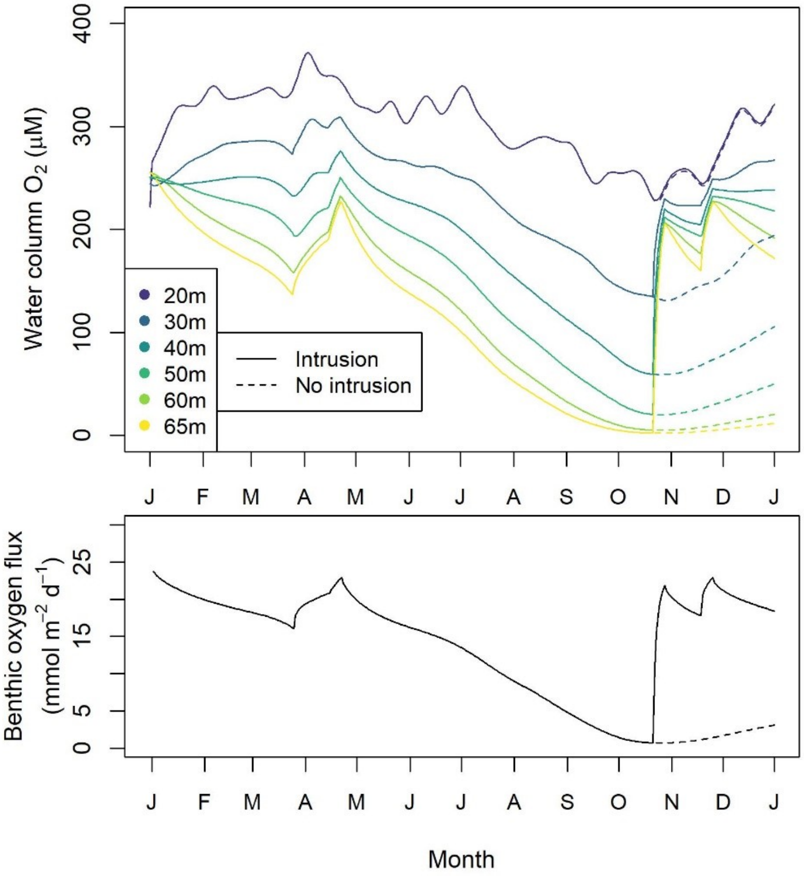

Figure A4. Model experiment showing comparison of oxygen dynamics in 2018 (solid curve) with model run without intrusion (dashed curve).

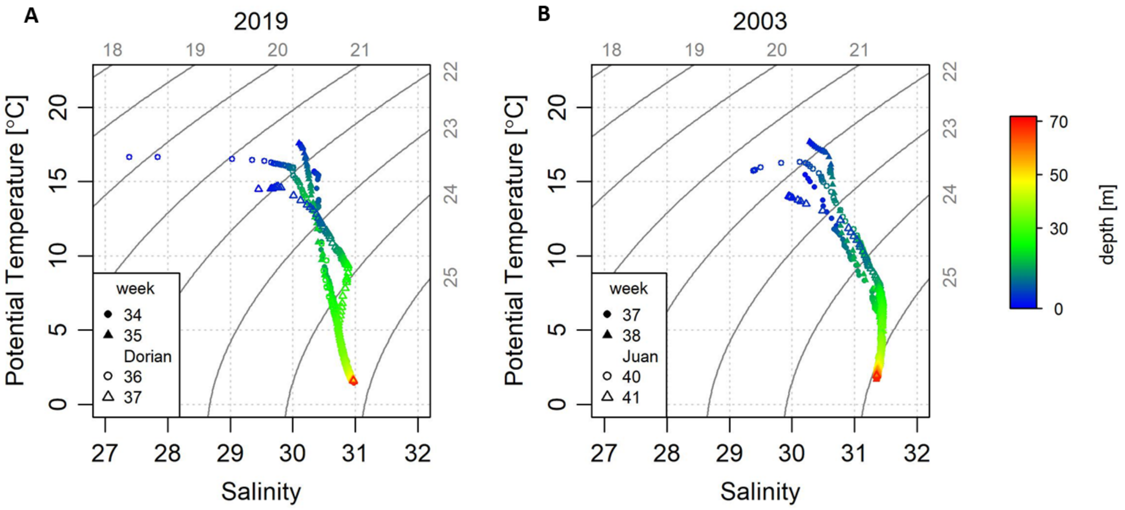

Figure A5. T-S plots showing the evolution of the water mass of the whole water column (0-70 m) two weeks before and after hurricane (A) Dorian (2019) and (B) Juan (2003).

Table A1. Parameters used in the benthic-pelagic coupled model.

Model parameters	**Description**	**2018**	**2019**	**2021**
K_z winter (cm^2 s^{-1}) [a†]	Eddy diffusivity during winter mixing	4.1, 8.3	31, 6.2	1.4, 1.2
K_z intrusion (cm^2 s^{-1}) [a†]	Eddy diffusivity during intrusions	41.3, 24.8	n/a	n/a
K_z stratified period (cm^2 s^{-1}) [a†]	Eddy diffusivity during the stratified period	0.37	0.37	0.11
$k_{O2.w}$ (cm^{-1} yr^{-1}) [a]	Water column respiration rate constant	7.5 x 10^{-7}	7.5 x 10^{-7}	7.5 x 10^{-7}
$k_{O2.sedi}$ (μmol cm^{-3} yr^{-1}) [a]	Maximum sediment oxygen consumption rate	4700	4700	4700
Ks.$_{O2}$ (μM) [a] in sediment	Half-saturation constant for oxygen	1	1	1
Ks.$_{O2}$ (μM) [a] in water	Half-saturation constant for oxygen	20	20	20

[a] Model constrained

[†]these values should be read together with Figure 2.2D to obtain the time period correspond to different values.

Table A2. Bottom water conditions and benthic oxygen flux at different model experiment scenarios. Here the 60 m water is referred as bottom water. Values in parenthesis denote percent change from the "baseline" (scenario#1).

Condition	**Maximum winter-time bottom water O_2 (μM)**	**Mean bottom water O_2 (μM)**	**Duration of annual hypoxia (weeks)**	**Mean benthic flux (mmol O_2 m^{-2} d^{-1})**
Scenario 1: Baseline mixing	338	99	28	10
Scenario 2: Winter mixing reduced by 50%	318 (-6)	90 (-10)	29 (+4)	9.4 (-6)
Scenario 3: Winter mixing reduced by 90%	145 (-57)	36 (-64)	43 (+54)	4.8 (-52)
Scenario 4: 90% weaker winter mixing + 70% lower stratified period *Kz*	125 (-63)	20 (-80)	46 (+64)	2.1 (-79)
Scenario 5: 90% weaker winter mixing + intrusion	186 (-45)	97 (-2)	22 (-21)	10.7 (+7)
Scenario 6: Baseline winter + intrusion	341 (+1)	147 (+48)	11 (-61)	14.6 (+46)

APPENDIX B: SUPPORTING INFORMATION TO CHAPTER 3

Bedford Basin: Study site

The BB is a fjord-like embayment within the Halifax Regional Municipality (Nova Scotia), the largest urban center in Atlantic Canada. The 17 km^2 basin is connected to the Halifax Harbour and ultimately the Scotian Shelf (North Atlantic) via a narrow channel, forming a ~20 m deep sill. The main freshwater inflow is from the Sackville River, which is small in volume (5.3 m^3 s^{-1}) compared to the mean tidal volume entering the basin (2.5×10^7 m^3) and the total basin volume of 5.1×10^8 m^3 (Petrie and Yeats 1990a; Gregory 1993). BB has a 2-layer estuarine type circulation, with relatively fresh water leaving the basin toward the harbor near-surface and relatively saline water entering the basin in the deeper layer (Huntsman 1924; Petrie and Yeats 1990a; Fader and Miller 2008b; Shan et al. 2011a). The basin and adjacent harbor are subject to intense anthropogenic use, most importantly a municipal wastewater treatment plant drains into the BB and four additional ones can be found in the extended harbor area (Kerrigan et al. 2017).

Sensor measurements, water sampling and atmospheric data

Sampling for this study was conducted within the framework of the BB Monitoring Program led by the Bedford Institute of Oceanography (BIO), which has conducted a weekly oceanographic monitoring (1992 to present) at the Compass Buoy Station, (44°41’37”N, 63°38’25”W), situated at the central deep point of the basin (~70 m; (Li 2014). From this time series, data from weekly CTD measurements with a Seabird SBE-25 CTD (including SBE-43 O_2 sensor) as well as particulate organic carbon (POC), particulate organic nitrogen (PON), chlorophyll *a* and nutrient data from four discrete depths (5 m, 60 m) were used in the present study. As of March 2015, the O_2 sensor data were cross-calibrated against discrete water samples analyzed by Winkler titration. Starting in 2014, the BIO monitoring has been augmented with additional measurements used in this study. Nitrate sensor (SUNA, Seabird Scientific; accuracy range: 2 µmol L^{-1}, manufacturer information) water column profiles were taken almost weekly, corrected for salinity and dissolved organic matter as previously described (Sakamoto et al. 2009), and calibrated against nitrate concentrations analyzed in discrete water samples (see below).

Beginning in January 2014, weekly water samples for molecular analyses were transported to the laboratory in cooled, dark bottles. Samples for DNA extraction were pre-filtered through 160 µm nylon mesh and concentrated on polycarbonate filters (0.2 µm, 47 mm; Isopore, Millipore) by a peristaltic pump. Filters were flash-frozen in liquid N_2 and stored at -80°C until DNA extraction. Samples for cell counts were analyzed on the same day or fixed in 1% paraformaldehyde for 10 minutes, flash-frozen in liquid N_2 and stored at -80°C for later analysis. Atmospheric data (temperature and wind speed) were retrieved from the Environment and Climate Change Canada database (https://climate.weather.gc.ca/historical_data/search_historic_data_e.html, Bedford Basin station, 44°42'36"N, 63°37'48"W).

Analysis of bulk nutrient, particulate and chlorophyll-a concentrations

DIN concentrations were analyzed using standard analytical methods for total ammonium (NH_3+NH_4^+; (Kérouel and Aminot 1997), nitrite (NO_2^-) and nitrate (NO_3^-; (Hansen and Koroleff 1999) with a precision (determined as the average standard deviation of all duplicate sample measurements) of 0.11 µmol kg_{sw}^{-1} (ammonium), 0.13 µmol kg_{sw}^{-1} (nitrate) and 0.01 µmol kg_{sw}^{-1} (nitrite). For the years 2016–2017, DIN concentrations were analyzed in the Canada Excellence Research Chair for Ocean Science and Technology (CERC.OCEAN) laboratory at Dalhousie University on a continuous flow auto-analyzer (San++, Skalar). For the years 2014–2015, mostly publicly available data from BIO were used, which were produced on similar instruments (Technicon II, Alpkem RFA300 or Seal Analytical AA3). Additional data from produced by BIO according to standard methods (phosphate and silicate (Murphy and Riley 1962; Hansen and Koroleff 1999; Mitchell et al. 2002), chlorophyll *a* (Lorenzen 1966; Li and Dickie 2001), POC and PON (Perkin Elmer Series II CHNS/O Analyzer 2400; (Li and Harrison 2008; Li 2014) were used for statistical evaluation of the long-term dataset.

Statistical analysis

Annual mean values as well as weekly standard anomalies, the weekly anomaly of a given parameter compared to the inter-annual weekly average of this parameter, standardized by the week-appropriate standard deviation (Li and Harrison 2008b), were calculated for various parameters from the BB time series, 1994 to 2018 (Li 2014b). Years for which a parameter was incompletely monitored (i.e. several consecutive weeks without measurements) were excluded from annual averaging but not from the standard anomalies. As a mixing proxy, the water spiciness was calculated from salinity, temperature and pressure, using the command ‘swSPICE’ from the R package OCE (Kelley 2018). The minimum spiciness during the winter mixing period (January–April) for each year was then used as a proxy for winter mixing intensity. Since winter mixing decreases temperature and salinity in BB bottom water (Figure 3.1A; (Shan et al. 2011; Li 2014), spiciness represents a more relevant proxy than density. Sackville River water discharge data (at Bedford station: 44°43'53"N, 63°39'37"W) were retrieved from the Environment and Climate Change Canada website (https://wateroffice.ec.gc.ca/mainmenu/historical_data_index_e.html). Statistical tests were implemented in R software, using the command ‘shapiro.test’ for the Shapiro-Wilk normality test, ‘corr.test’ from the ‘psych’ package for Pearson, Spearman’s rho and Kendall’s tau correlation tests, and the command ‘lm’ for multiple regressions.

Microbial cell counts

For cell counting, water was filtered through a 35 μm mesh and stained with 1× SYBR^{TM} Green I (Invitrogen) for 10 min in the dark at room temperature. Cells were enumerated on an Accuri C6 (BD) flow cytometer with excitation at 488nm and detection using FL1 (533/30) and FL3 (670LP).

Analysis of 16S rRNA amplicon sequences

16S rRNA amplicon sequences were processed using a QIIME-2 based workflow (Bolyen et al. 2019). Paired-end sequences were joined using VSEARCH (Rognes et al. 2016) and low-quality reads were filtered out using the Demux command and its default parameters. Deblur (Amir et al. 2017) was applied, with a trim-length of 354 bp, to correct reads and assign amplicon sequence variants (ASVs). Taxonomy was assigned to ASVs using a Naive-Bayes approach implemented in the *scikit learn* Python library and the SILVA database (Yilmaz et al. 2014) using a QIIME 2 associated full-length 16S rRNA gene classifier (available online: https://docs.qiime2.org/2019.7/data-resources/#taxonomy-classifiers-for-use-with-q2-feature-classifier). The dataset was refined by removal of rare (<0.1% of mean sample depth; likely due to MiSeq (Illumina) between-run bleed-through) and mitochondrial ASVs, as well as those unclassified at the phylum level. Samples were rarefied to a sequencing depth of 2995 reads, a value which allowed to retain all samples from 60 meters. For further analysis, the ASVs assigned by SILVA to taxonomic groups of known nitrifiers (*Thaumarchaeota*, *Nitrosomonadaceae*, *Nitrosococcaceae*, *Nitrospinaceae* and *Nitrospirae*) were subset and their share in total 16S rRNA amplicon sequences scaled to total cell counts.

Representative sequences closely related to the nitrifier ASVs were collected from the NCBI ‘Nucleotide’ and ‘RefSeq Representative Genomes’ databases through comparison via BLAST (Pruitt et al. 2007) for the phylogenetic tree depicted in Figure B2. The accession codes for all previously published reference sequences used in the phylogenies are provided in a version of the bacterial tree without any collapsed nodes (Figure B12). For Figure B9 and Figure B10, sequences of operational taxonomic units affiliated with *Thaumarchaeota* and *Nitrospina*, respectively, identified by Kitzinger et al. from samples taken in the Gulf of Mexico were added (Kitzinger et al. 2019, 2020). For each tree, these sequences along with the ASVs from BB were aligned using MUSCLE (Edgar 2004) and maximum-likelihood phylogenies were constructed in MEGA7 (Kumar et al. 2016). Trees were then visualized in iTOL (Letunic and Bork 2016).

Quantitative PCRs

Quantitative PCR (qPCR) was used to measure the abundance of the ammonia monooxygenase subunit A gene (*amoA*). Using Primer Express 3.0.1 software (Applied Biosystems), *de novo* assays were developed to target representative sequences for each of the six oceanic phylotypes of archaeal *amoA* defined in reference (Sintes et al. 2016). Table B7 lists for each assay: designed primers, the accession code corresponding to the relevant phylotype representative, and the nucleotide sequence of the dsDNA (gBlock; Integrated DNA Technologies). qPCR reactions were carried out on a ViiA 7 real time PCR system with QuantStudio software (Applied Biosystems); cycling conditions were: an initiation/hold step of 50°C for 2 min then 95°C for 10 min, followed by 45 qPCR cycles of 95°C for 15 sec and 60°C for 1 min. Additionally, a melt curve for temperatures between 60°C and 95°C was run to determine any non-specific amplification. The 16-µL reactions included: 8 µL 1× Power SYBR Green PCR Master Mix (Applied Biosystems), 200 nM of each primer (IDT), 6.4 µg BSA (NEB), and 5µL of template (either time-series DNA or standard DNA). Ultrapure DNase/RNase-free water (Invitrogen) was used for no-template controls. A standard curve of 10^1–10^7 gene copies per reaction was used to determine gene copy numbers; dsDNA stocks were freshly quantified on a Qubit 4 Fluorometer using the 1× dsDNA HS Assay Kit (both from Invitrogen). The range of average qPCR efficiencies for the six assays as calculated from standards was 86–91%, as determined using LinRegPCR software (Ruijter et al. 2009). We also confirmed the specificity of each qPCR *amoA* assay to its intended *amoA* phylotype target by testing all combinations of primer sets and standards (Table B8). Due to limited DNA volume and since *amoA* phylotypes amoA-A3 to A6 were consistently much rarer than phylotypes amoA-A1 and amoA-A2 (based on DNA from the years 2015–2017), we did not run qPCR assays for these much rarer types in 2014.

Supplementary Discussion B1: The temporal distribution of the archaeal amoA phylotypes quantified by qPCR

Six phylotypes of archaeal *amoA* were quantified by qPCR in 60-meter BB samples. AmoA-A3, amoA-A4, amoA-A5 and amoA-A6 were measured in 2015, 2016 and 2017. Gene copies of amoA-A1 and amoA-A2 were measured additionally in 2014. The different phylotypes displayed very different quantitative and qualitative temporal distributions (Figure B3). AmoA-A1, the most abundant phylotype (up to 4.4×10^5 copies g_{sw}^{-1}; Figure B3A), decreased in copy numbers during major mixing events (winter mixing, intrusions), while it increased in number during each stratified period with maxima coinciding with periods of maximum nitrate increase, suggesting that it represented the overall dominant ammonia oxidizer as discussed in the main text. Its abundance was well described as a function of temperature (positive), dissolved oxygen and POC concentrations (negative; Table B1), reflecting the conditions at the end of stratified periods when nitrification tended to be strongest and amoA-A1 tended to be most abundant (Figure B3).

AmoA-A2 was the second most abundant phylotype (up to 1.1×10^4 copies g_{sw}^{-1}). Like amoA-A1, it has previously been associated with the surface ocean, whereas the remaining four phylotypes examined here have been associated with the deep ocean (Sintes et al. 2016). Interestingly, amoA-A2 displayed a distribution very similar to amoA-A6 and amoA-A3, which are associated with the deep oceanic realm (Sintes et al. 2016). With the exception of the year 2014, when only low amoA-A2 copy numbers were present exclusively during the stratified period, each of these phylotypes tended to appear at their highest numbers during the winter mixing period of each year (Figure B3B, E, F). This is reflected by the statistically significant and positive association of each of these phylotypes with dissolved oxygen concentration (Table B1). The sharp increases in copy numbers of *amoA* phylotypes A2, A3 and A6 coinciding with sharp salinity increases (shelf water intrusion events) in November 2016, March 2017 and December 2017 indicate that they may be brought to the BB bottom water from the Scotian Shelf by physical transport and mixing. Additionally, the growth of AOAs that are represented by these phylotypes may be favored by the conditions prevailing during the winter mixing period and they may represent ammonia oxidizers that are active in BB bottom waters during those times, but further research is necessary to establish this. The covariation of the surface-ocean associated amoA-A2 with the deep-ocean associated amoA-A6 and amoA-A3, respectively, is intriguing and further research may reveal why their appearance in BB bottom water is linked with the same mixing events.

AmoA-A4 displayed exceedingly low copy numbers (<2 copies g_{sw}^{-1}) and no clear temporal pattern (Figure B3D). AmoA-A5 was among the more abundant phylotypes (0–6.5×10^3 copies $g_{sw}^{-1)}$ but had no clear temporal distribution pattern (Figure B3E; Table B1).

Supplementary Discussion B2: The rate-increasing effect of warmer water from intrusion events

Based on our observations, the intrusion events during the time period 2014–2017 decreased nutrient concentrations and amoA-A1 copy number, but in no case did they deplete ammonium and/or the AOO community enough to significantly delay nitrification in their aftermath (Figure 3.2). This suggests that the mixing induced by intrusion events affected nitrification less than strong winter mixing. Following intrusion events, the associated temperature and oxygen increase may partly compensate for the small observed nitrifier biomass dilution by allowing for increased AO, NO and N remineralization rates. Both marine AOA and AOB have AO rate maxima at much higher temperatures (20–35°C; (Groeneweg et al. 1994; Ruijter et al. 2009; Qin et al. 2014) than occur in BB bottom water (0.6–5.9°C). The temperature range in BB bottom water is small during stratified periods (~1–4°C) with the largest increases associated with the intrusion events (0.5–2.3°C; **Error! Reference source not found.**). A very high Q_{10} value (Table B4) provided the best fit for the model, accounting for a strong nitrification rate increase after the intrusion events. The applied Q_{10} value is much higher than found in other AOA dominated, oligotrophic systems (Horak et al. 2013, 2018; Baer et al. 2014), but is similar to Q_{10} values observed in nutrient-rich parts of marine Narragansett Bay (Berounsky and Nixon 1990). This may suggest that high ammonium availability can lead to higher temperature-dependence of AO rates in AOA than has been observed in oligotrophic AOA (Horak et al. 2013, 2018; Qin et al. 2014; Baer et al. 2014).

Supplementary Discussion B3: Model-observation mismatches

Mismatches between model and observations can point to unknown influencing factors or levels of complexity not captured by the model. As described in the main discussion section, some of the smaller mismatches of the model with nitrate concentration data shown in Figure 3.3B were likely a result of attempting to model the entire four-year period using a fixed AO rate constant despite known kinetic differences between AOB and AOA. The largest model-data mismatch occurred in November 2015, when nitrate accumulation stopped and amoA-A1 abundance started to decrease, despite ~6 µmol kg_{sw}^{-1} ammonium still being present (Figure 3.3B,C). This observation was not captured by the model and may have been due to a combination of grazing (which is not represented in the model) and low prevailing oxygen concentrations (~50 µmol kg_{sw}^{-1}, decreasing further to the 4-year minimum of 11 µmol kg_{sw}^{-1}). Oxygen concentrations were overestimated by the model during this period, which may also be a consequence of stronger stratification in 2015 compared to other years. We hypothesize that low oxygen concentrations may have limited AO and caused AOO growth rates to fall below the level of grazing rates (Verhagen and Laanbroek 1992; Anderson et al. 2012; Qin et al. 2017). Once this threshold was crossed and oxygen concentration continued to decrease (as observed; Figure 3.2A), AOO growth could not exceed losses to grazing, leading to continued decrease until the system was reset by mixing. Identification and quantification of grazers as well as a more complex model that includes grazing would be required to explore this hypothesis further.

Supplementary Discussion B4: Statistical validation of conclusions using long-term BB time series data

The findings for the years 2014–2017 were further constrained in the context of the long-term BB time series, for which weekly measurements started in 1994 (temperature, salinity, nitrate, phosphate, silicate, chlorophyll *a*), 1999 (dissolved oxygen) or 2002 (ammonium, nitrite, POC, PON). Statistical tests (*SI Materials and Methods*) suggested an important role for mixing intensity on nitrification indicators in BB bottom water. The annual average nitrate:ammonium ratio correlated negatively with the annual averages (all at 60 m) of POC and dissolved oxygen concentrations, and positively with high silicate concentrations (Table B5). Rather than reflecting a direct connection of these parameters with nitrification, these factors may both co-vary with winter mixing intensity, reflecting the delaying effect of intense winter mixing on nitrification as demonstrated by the empirical results and model observations in the years 2014–17 (Figure 3.2C,D,E). Indeed, each of these factors was also correlated with minimum spiciness, which was used as a proxy for winter mixing intensity (Table B5). Quantification of mixing intensity is not straightforward, especially since winter mixing brings colder and fresher water to BB bottom water (Figure 3.1; Figure B1), therefore working approximately orthogonal to density. This is captured by spiciness, a parameter that is directly proportional to both temperature and salinity (Flament 2002; McDougall and Krzysik 2015). Annual spiciness minima appeared in the late phases of the winter mixing periods in each year 2014–17 due to mixing of low-temperature-low-salinity near-surface water into the bottom water (Figure 3.1A). Therefore, we used the minimum spiciness observed during annual winter mixing of each recorded year as a proxy for annual winter mixing intensity. Low intensity of winter mixing (indicated by less negative minimum spiciness) correlated significantly with low annual average O_2, POC and PON concentrations at 60 m, as well as high annual average nitrate:ammonium ratio, salinity, nitrate, and silicate concentrations (Table B5). The correlations of minimum spiciness with high nitrate concentrations and nitrate:ammonium ratios are consistent with a controlling influence of winter mixing on nitrification, with more intense mixing causing weaker nitrification.

Since the annual averages of POC and dissolved O_2 correlated positively, variations in annual O_2 are likely driven primarily by variations in mixing-induced reoxygenation and only secondarily by variations in remineralization. Winter mixing may also cause higher POC concentrations in the BB bottom water, explaining the correlation of POC with minimum spiciness. Measurements by Hargrave and Taguchi (Hargrave and Taguchi 1978a) suggested that winter destratification favored sedimentation to 60 m relative to shallower depths in BB. The same authors report a chlorophyll *a* maximum within sedimented material in January. While it is not clear that stronger winter mixing increases the positive effect of destratification on POC deposition at 60 m observed by Hargrave and Taguchi (Hargrave and Taguchi 1978a), this may provide an explanation for the correlation of intense winter mixing (low minimum spiciness) with increased POC concentrations observed here.

A multiple regression of weekly standard anomalies throughout the long-term time series suggested positive effects of temperature and negative effects of POC and oxygen concentrations on the nitrate:ammonium ratio (Table B6). The positive effect of temperature may reflect nitrification rate increase due to warmer temperatures (SI Discussion 2). As discussed above, low salinity and high dissolved oxygen and POC are probably caused primarily by high intensity winter mixing (Table B5). Hence, this test also suggests a negative influence of winter mixing on nitrification in BB (Table B6).

Supplementary Discussion B5: Broader relevance of the model-derived ammonia oxidation rates and underlying microbiology

In order to compare nitrification rates and the underlying nitrifier community observed in BB with other regions of the ocean, we estimated single-cell AO rates from the annual maximum modeled volumetric rates and the annual maximum observed *amoA* copies g_{SW}^{-1} (Figure 3.3). Given that *Nitrosopumilus* contain only one *amoA* copy per genome (Walker et al. 2010), we assumed that *amoA*-based rates equal rates per AOA cell. The estimated rates in the AOA-dominated years 2014 and 2016 then were 1.5 and 1.3 fmol NH_3 cell^{-1} d^{-1}, respectively. These values are within the range of cell-specific AO rates for AOA (1–8 fmol NH_3 cell^{-1} d^{-1}) measured in the Gulf of Mexico (Kitzinger et al. 2019, 2020). Further, the most abundant NOB ASVs found in BB (NOB-BB-ASVs 3–5) were phylogenetically related to NOB from the Gulf of Mexico based on their 16S rRNA gene sequences (Figure B10). Although the most abundant AOA ASVs found in the BB (AOA-BB-ASVs 2&3) formed a separate clade from Gulf-of-Mexico ASVs, they were still closely related (98–99% similarity) to those and other environmentally relevant *Nitrosopumilus* species (Figure B11). This suggests that microbial diversity and AO kinetics underlying the time series observations in BB are representative of nitrifiers in other parts of the ocean.

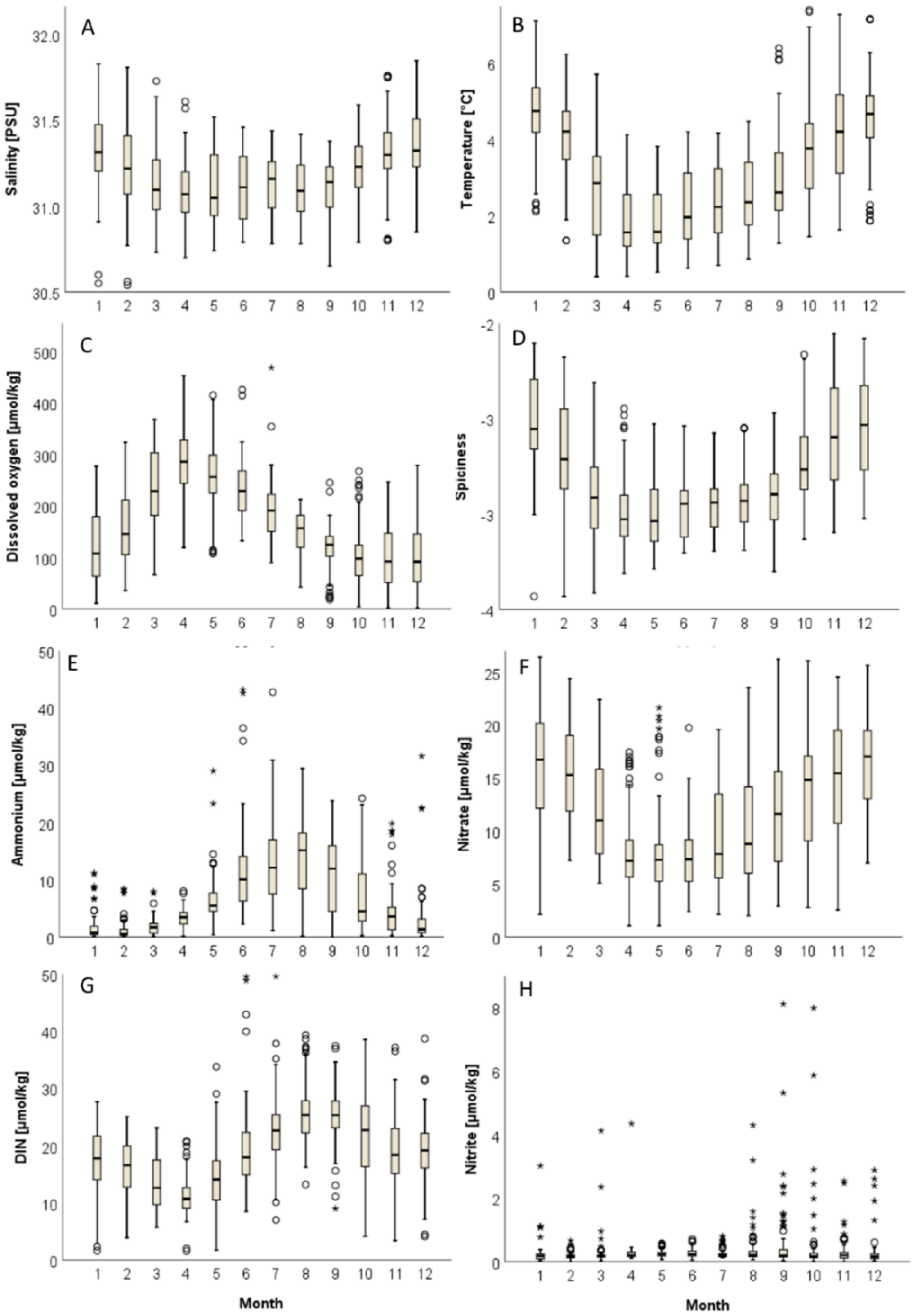

Figure B1. Monthly averages using weekly, long-term time series data at 60m BB until 2018, starting in 1994 (temperature, salinity, spiciness, nitrate), 1999 (dissolved oxygen) or 2002 (ammonium, nitrite, DIN).

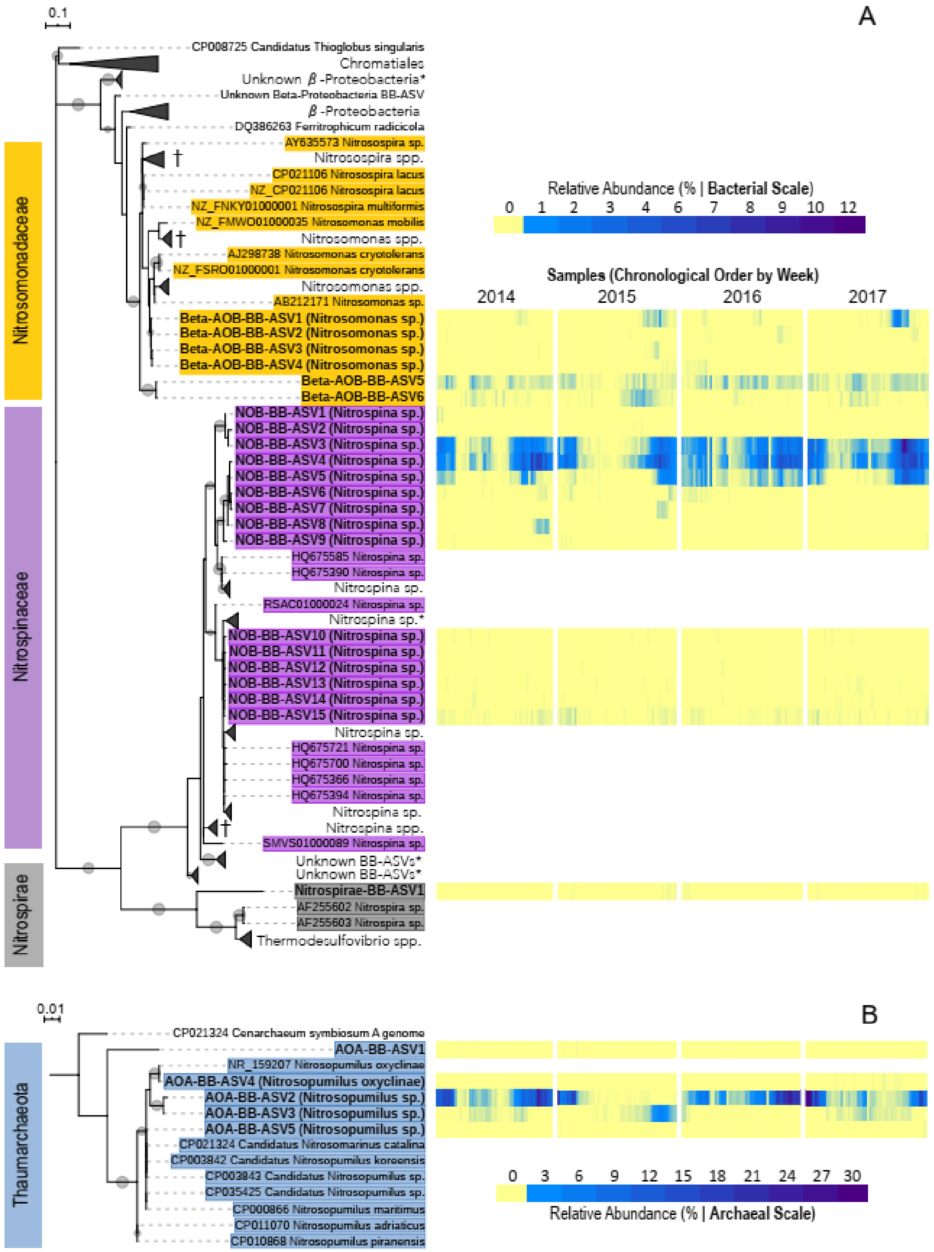

Figure B2. Phylogenetic maximum likelihood trees (1000 bootstraps) of A) bacterial and B) archaeal ASVs from 16S rRNA amplicon sequencing of the Bedford Basin bottom water community (bold) affiliated by SILVA with known nitrifier taxa, and their relative abundances in total 16S rRNA genes shown as heatmaps. Bedford Basin ASVs within collapsed branches (marked by *) were all quantitatively insignificant (≤0.2% in each sample) or blasting did not support their affiliation with known nitrifiers. Gray nodes indicate >80% bootstrap support. Collapsed nodes containing type species of a relevant AOB or NOB genus are marked with † and the full bacterial tree (A) can be seen in Figure B12. Relative ASV abundances are shown in weekly time steps interrupted at the end of each year due to missing samples.

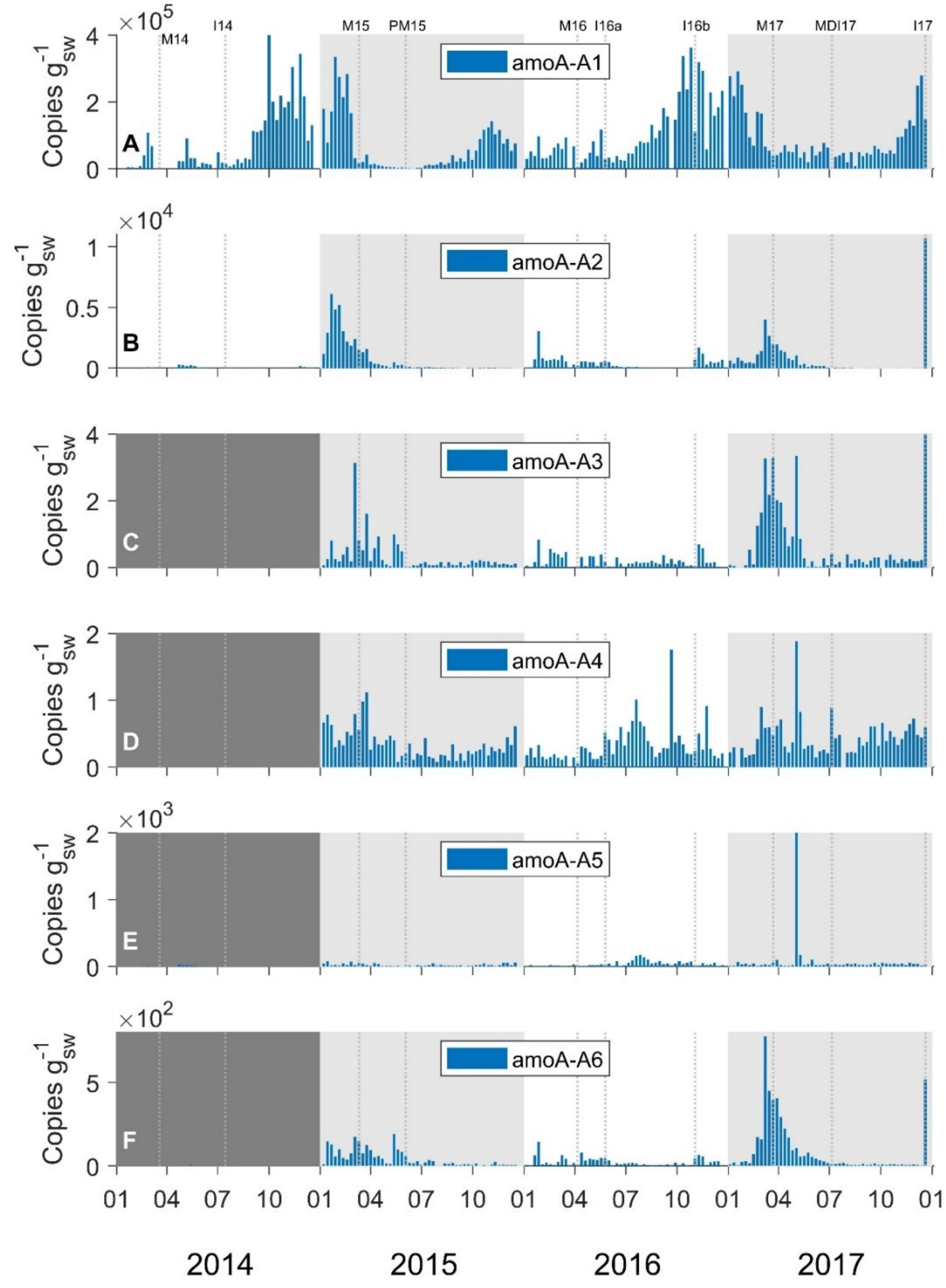

Figure B3. Temporal distribution of archaeal amoA phylotypes quantified by qPCR at 60 m in Bedford Basin, 2014–2017. A) amoA-A1; B) amoA-A2; C) amoA-A3; D) amoA-A4; E) amoA-A5; F) amoA-A6. Event numbers (“M”, “I”, “PM”, “MDI”) as in Figure 3.1.

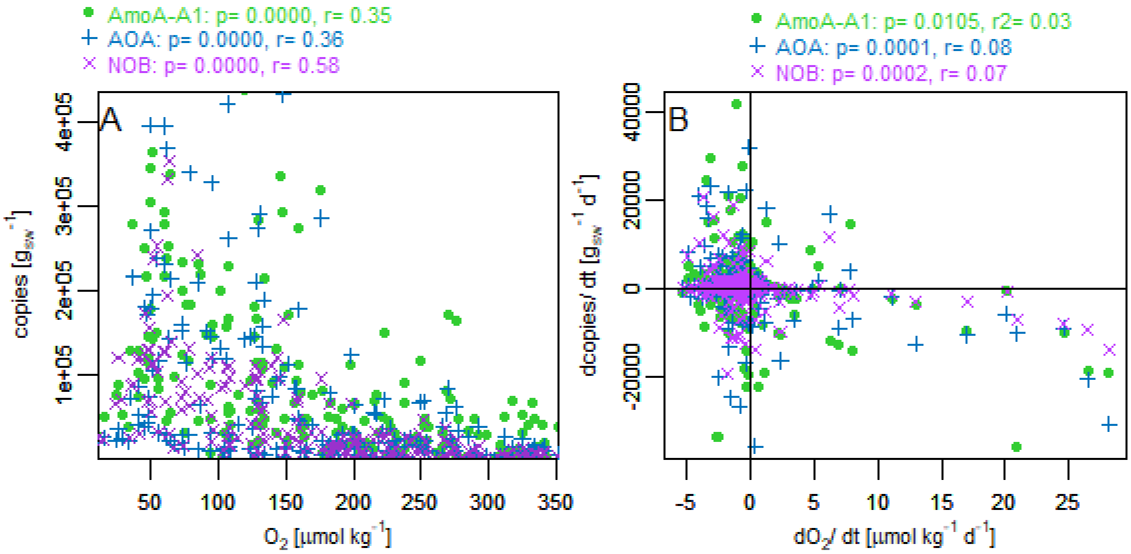

Figure B4. Concentrations (A) and time derivatives (B) of oxygen plotted against nitrifier abundances. Results from a Spearman's Rho correlation test (Table B1) are shown in the panel legends.

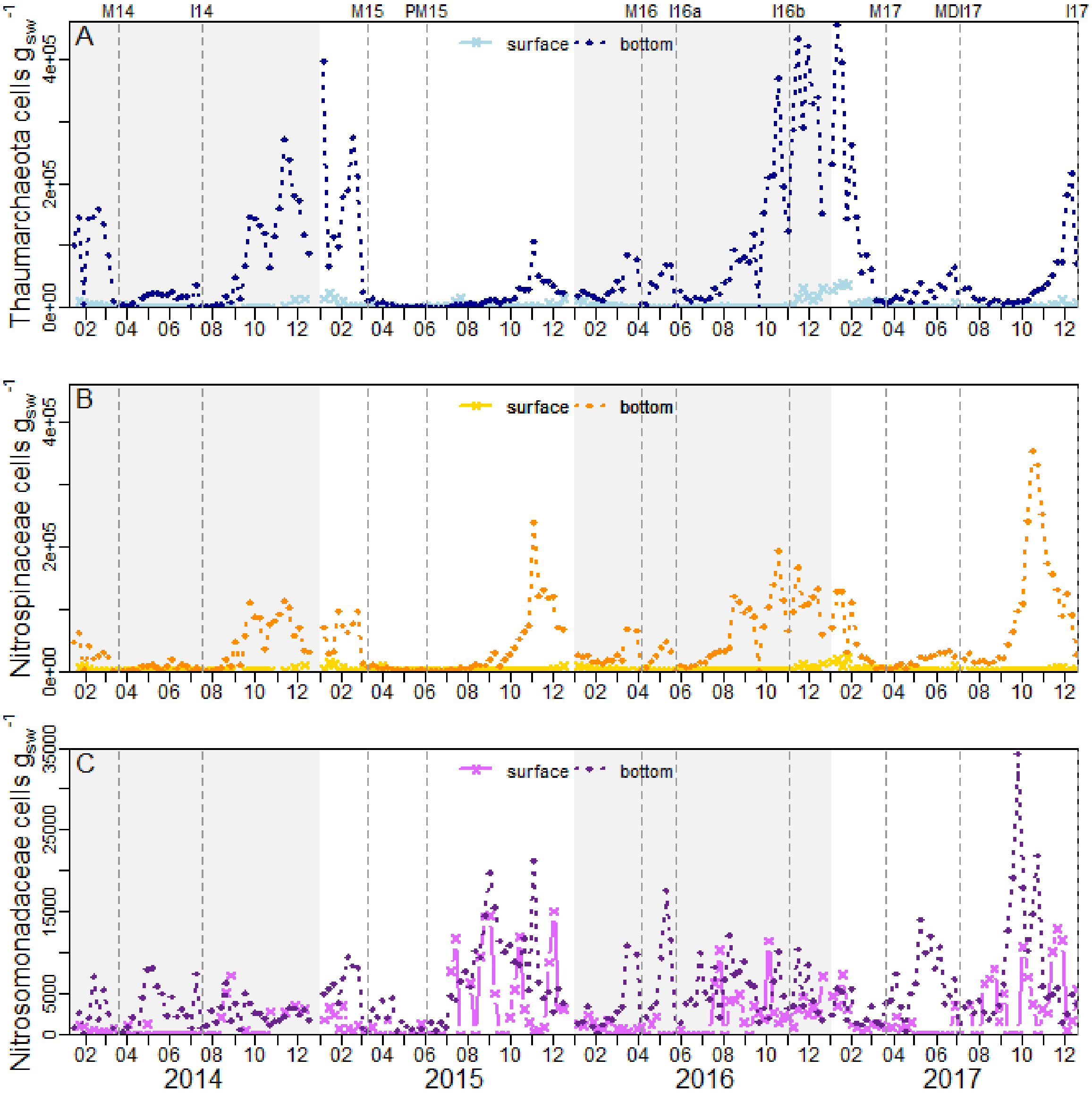

Figure B5. Time series of nitrifier abundance estimated based on the relative abundance of the relevant ASVs for each group at the surface (5 m) and in the bottom water (60 m) of Bedford Basin: A) *Thaumarchaeota* (AOA), B) *Nitrospinaceae* (NOB), C) *Nitrosomonadaceae* (AOB). Note the different scale for *Nitrosomonadaceae.* Event numbers (“M”, “I”, “PM”, “MDI”) as in Figure 3.1.

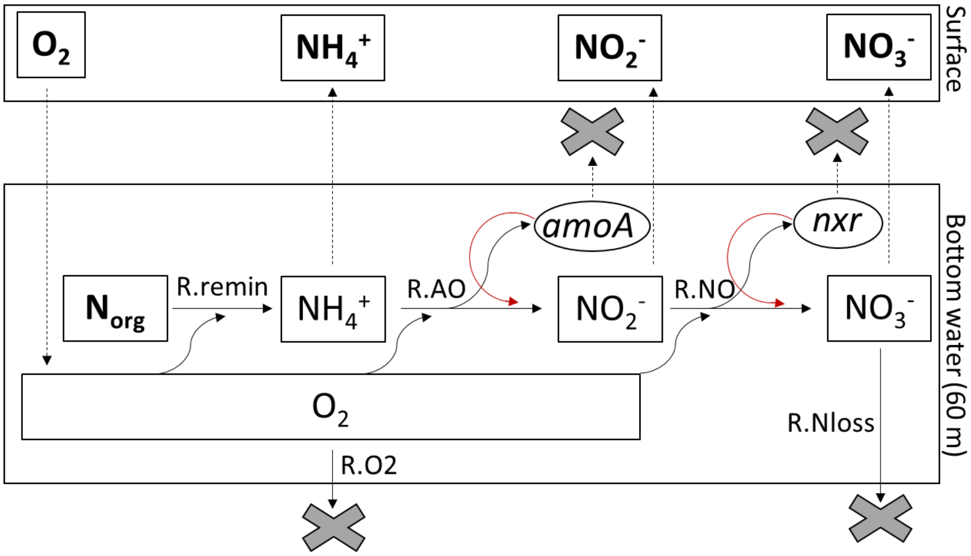

Figure B6. Network of biogeochemical reactions (solid arrows) and transport in and out of the 60-meter box of the model by physical mixing (dashed arrows). Directions of dashed arrows indicate the typical net flow of a given substance caused by mixing, which could be reversed in cases where the concentration gradient is reversed. As indicated by the red arrows, amoA and nxr increase reinforces the respective reactions catalyzed by them, AO and NO. Arrows toward 'X' indicate losses from the model. N_{org} (organic nitrogen) as well as all concentrations in the surface box are based on observations at 5 m depth (bold), the remaining variables in the 60-meter box are modeled. R.remin = remineralization rate; R.AO = ammonia oxidation rate; R.NO = nitrite oxidation rate; R.Nloss = N loss rate (= denitrification + assimilation); R.O2 = respiration rate.

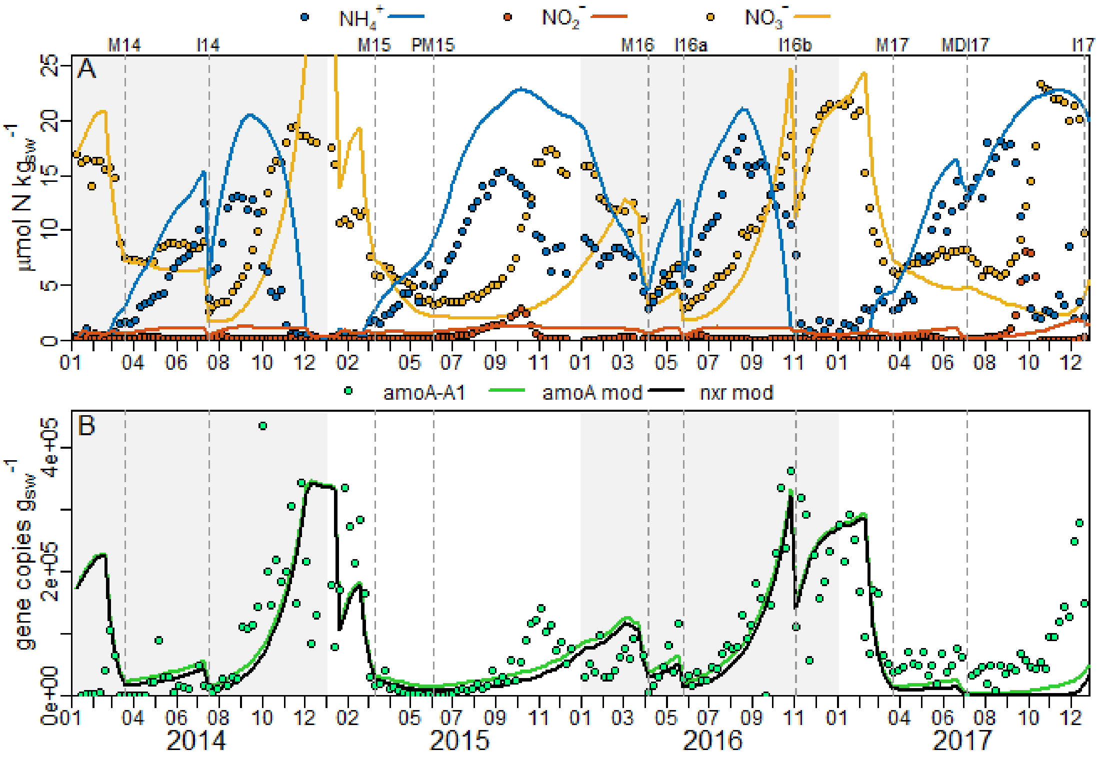

Figure B7. Time series of observed (scatter or bar) and modeled (lines: "mod") biogeochemical parameters at 60 m in Bedford Basin, 2014–2017, with modeled AO rate parameters adjusted to result in good fit to the observations in the year 2016 but otherwise identical to the model shown in Figure 3.3. A) Observed and modeled ammonium, nitrite and nitrate concentrations. B) AmoA-A1 (modeled and observed) and nxr (modeled) gene abundance. Event numbers ("M", "I", "PM", "MDI") as in Figure 3.1.

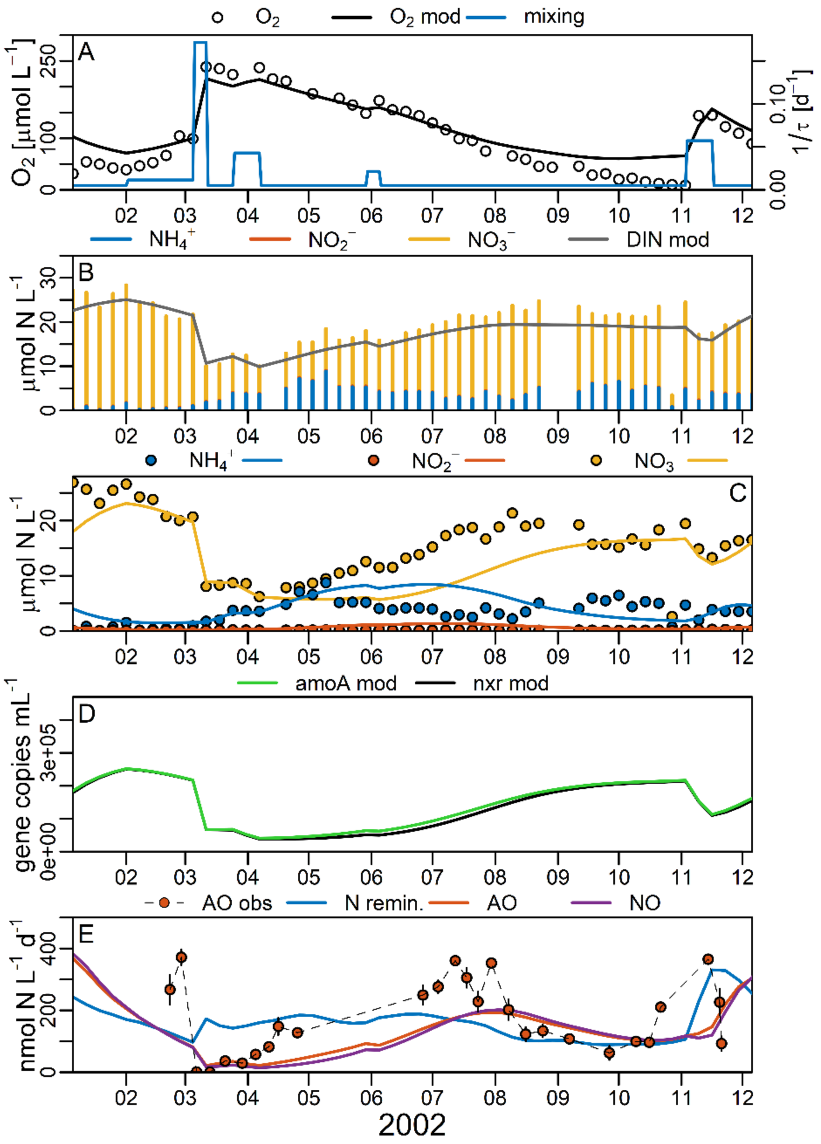

Figure B8. Model output for the year 2002 compared to empirical ammonia oxidation rates ("AO obs") from Punshon and Moore (Punshon and Moore 2004a). Scatter plots represent data, line plots represent model output. A) Oxygen concentrations and the inverse of residence time τ, describing the timescale of exchange of Bedford Basin bottom water with water from the basin surface or the shelf; B) DIN; C) ammonium, nitrite and nitrate; D) modeled amoA and nxr gene copy numbers; E) Modeled AO, NO and N remineralization rates as well as observed AO rates (Punshon and Moore 2004a). To ensure accurate comparability with rates from Punshon and Moore (Punshon and Moore 2004a), volumetric units were used in this model. Since POC data for 2002 were only available as of October 2002, this model is forced by a the weekly POC average 2014–2017 prior to October 2002. Note that two positive outliers (April 2nd, May 1st) were omitted from the oxygen data plotted in panel A, since the full water column profiles suggested that they most likely stemmed from methodological error.

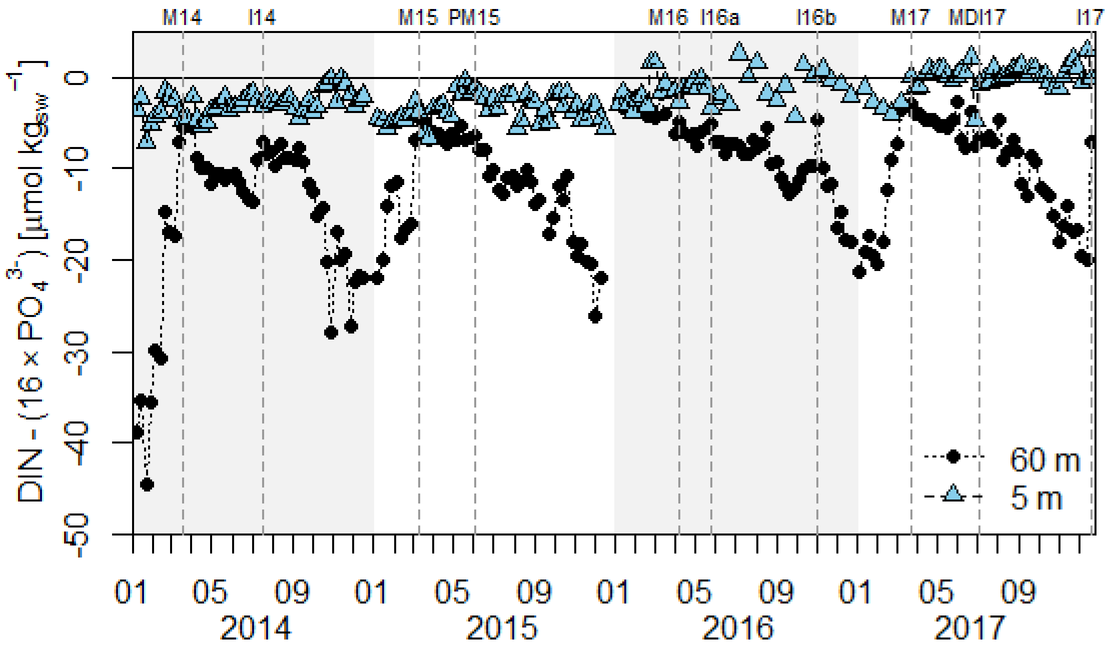

Figure B9. Observed difference between DIN and phosphate concentrations corrected for the Redfield Ratio (factor 16) in the BB near-surface water (5 m) and bottom water (60 m).

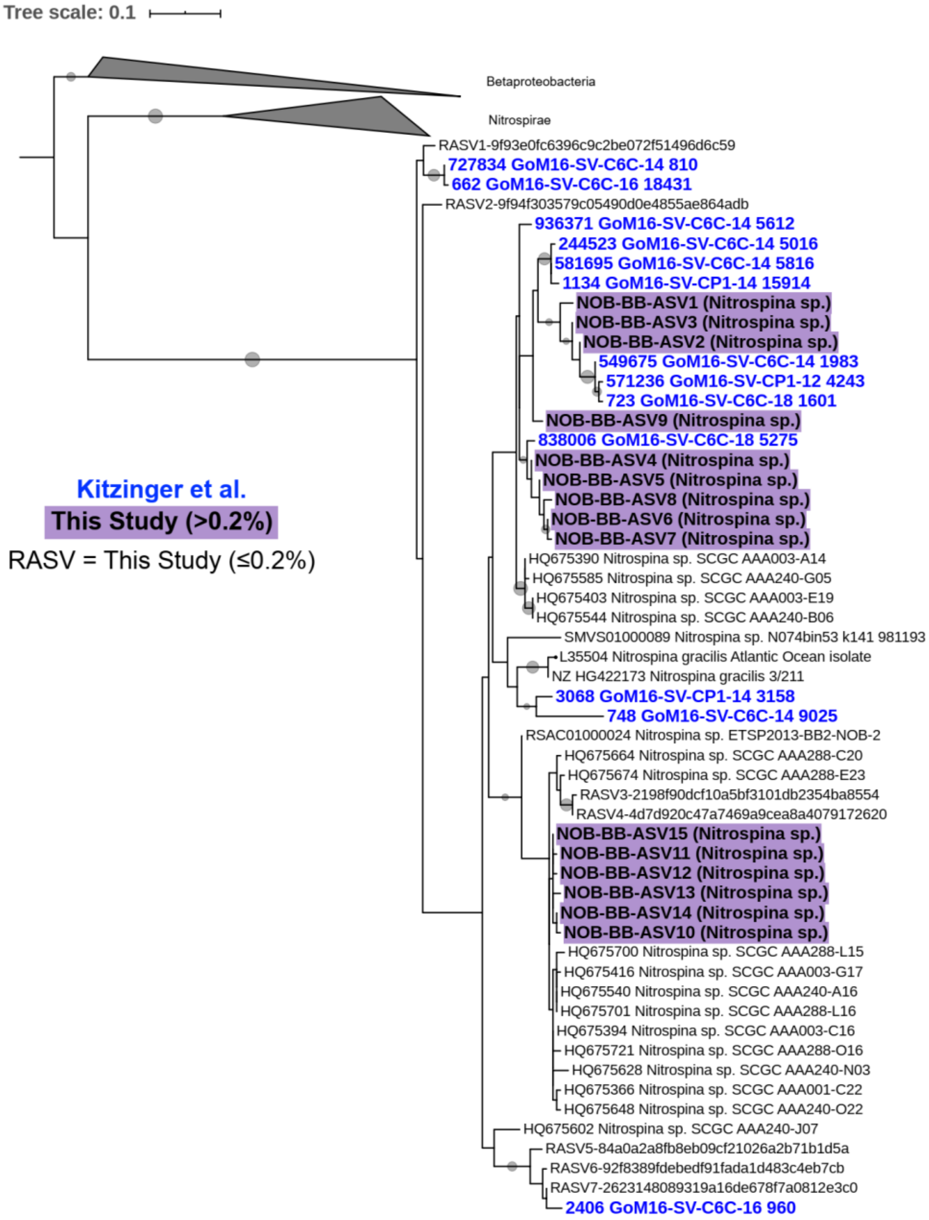

Figure B10. Phylogenetic Maximum Likelihood tree (1000 bootstraps) of *Nitrospina*-affiliated ASVs from this study, the reference sequences also used for the phylogenetic tree in Figure B2A and additional *Nitrospina*-affiliated reference sequences from the Gulf of Mexico, identified by Kitzinger et al. (Kitzinger et al. 2019, 2020). Kitzinger et al.'s sequences are shown in Table B9. Gray nodes indicate >50% bootstrap support.

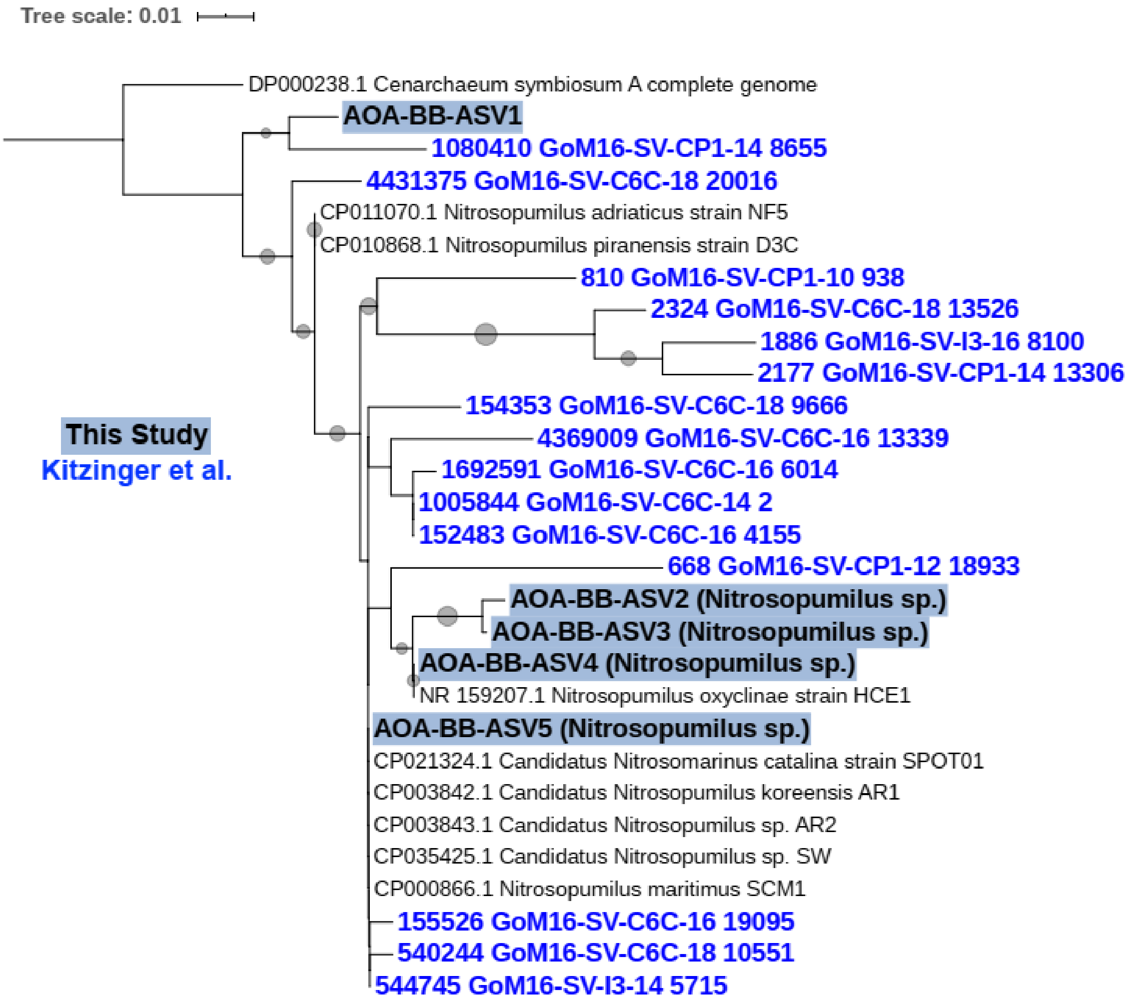

Figure B11. Phylogenetic Maximum Likelihood tree (1000 bootstraps) of *Thaumarchaeota*-affiliated ASVs from this study, the reference sequences also used for the phylogenetic tree in Figure B2B and additional *Thaumarchaeota*-affiliated reference sequences from the Gulf of Mexico, identified by Kitzinger et al. (Kitzinger et al. 2019, 2020). Kitzinger et al.'s sequences are shown in Table B9. Gray nodes indicate >50% bootstrap support.

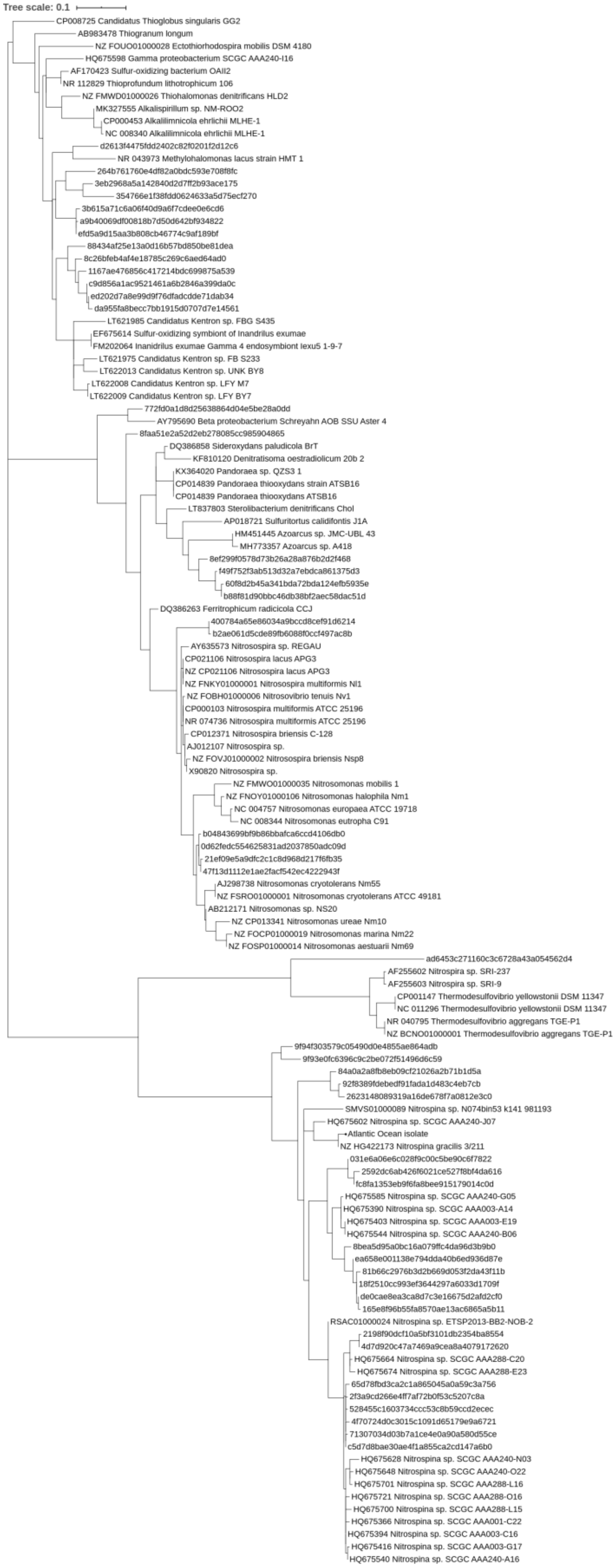
Tree scale: 0.1
CP008725 Candidatus Thioglobus singularis GG2
AB983478 Thiogranum longum
NZ FOUO01000028 Ectothiorhodospira mobilis DSM 4180
HQ675598 Gamma proteobacterium SCGC AAA240-I16
AF170423 Sulfur-oxidizing bacterium OAII2
NR 112829 Thioprofundum lithotrophicum 106
NZ FMWD01000026 Thiohalomonas denitrificans HLD2
MK327555 Alkalispirillum sp. NM-ROO2
CP000453 Alkalilimnicola ehrlichii MLHE-1
NC 008340 Alkalilimnicola ehrlichii MLHE-1
d2613f4475fdd2402c82f0201f2d12c6
NR 043973 Methylohalomonas lacus strain HMT 1
264b761760e4df82a0bdc593e708f8fc
3eb2968a5a142840d2d7ff2b93ace175
354766e1f38fdd0624633a5d75ecf270
3b615a71c6a06f40d9a6f7cdee0e6cd6
a9b40069df00818b7d50d642bf934822
efd5a9d15aa3b808cb46774c9af189bf
88434af25e13a0d16b57bd850be81dea
8c26bfeb4af4e18785c269c6aed64ad0
1167ae476856c417214bdc699875a539
c9d856a1ac9521461a6b2846a399da0c
ed202d7a8e99d9f76dfadcdde71dab34
da955fa8becc7bb1915d0707d7e14561
LT621985 Candidatus Kentron sp. FBG S435
EF675614 Sulfur-oxidizing symbiont of Inandrilus exumae
FM202064 Inanidrilus exumae Gamma 4 endosymbiont Iexu5 1-9-7
LT621975 Candidatus Kentron sp. FB S233
LT622013 Candidatus Kentron sp. UNK BY8
LT622008 Candidatus Kentron sp. LFY M7
LT622009 Candidatus Kentron sp. LFY BY7
772fd0a1d8d25638864d04e5be28a0dd
AY795690 Beta proteobacterium Schreyahn AOB SSU Aster 4
8faa51e2a52d2eb278085cc985904865
DQ386858 Sideroxydans paludicola BrT
KF810120 Denitratisoma oestradiolicum 20b 2
KX364020 Pandoraea sp. QZS3 1
CP014839 Pandoraea thiooxydans strain ATSB16
CP014839 Pandoraea thiooxydans ATSB16
LT837803 Sterolibacterium denitrificans Chol
AP018721 Sulfuritortus calidifontis J1A
HM451445 Azoarcus sp. JMC-UBL 43
MH773357 Azoarcus sp. A418
8ef299f0578d73b26a28a876b2d2f468
f49f752f3ab513d32a7ebdca861375d3
60f8d2b45a341bda72bda124efb5935e
b88f81d90bbc46db38bf2aec58dac51d
DQ386263 Ferritrophicum radicicola CCJ
400784a65e86034a9bccd8cef91d6214
b2ae061d5cde89fb6088f0ccf497ac8b
AY635573 Nitrosospira sp. REGAU
CP021106 Nitrosospira lacus APG3
NZ CP021106 Nitrosospira lacus APG3
NZ FNKY01000001 Nitrosospira multiformis Nl1
NZ FOBH01000006 Nitrosovibrio tenuis Nv1
CP000103 Nitrosospira multiformis ATCC 25196
NR 074736 Nitrosospira multiformis ATCC 25196
CP012371 Nitrosospira briensis C-128
AJ012107 Nitrosospira sp.
NZ FOVJ01000002 Nitrosospira briensis Nsp8
X90820 Nitrosospira sp.
NZ FMWO01000035 Nitrosomonas mobilis 1
NZ FNOY01000106 Nitrosomonas halophila Nm1
NC 004757 Nitrosomonas europaea ATCC 19718
NC 008344 Nitrosomonas eutropha C91
b04843699bf9b86bbafca6ccd4106db0
0d62fedc554625831ad2037850adc09d
21ef09e5a9dfc2c1c8d968d217f6fb35
47f13d1112e1ae2facf542ec4222943f
AJ298738 Nitrosomonas cryotolerans Nm55
NZ FSRO01000001 Nitrosomonas cryotolerans ATCC 49181
AB212171 Nitrosomonas sp. NS20
NZ CP013341 Nitrosomonas ureae Nm10
NZ FOCP01000019 Nitrosomonas marina Nm22
NZ FOSP01000014 Nitrosomonas aestuarii Nm69
ad6453c271160c3c6728a43a054562d4
AF255602 Nitrospira sp. SRI-237
AF255603 Nitrospira sp. SRI-9
CP001147 Thermodesulfovibrio yellowstonii DSM 11347
NC 011296 Thermodesulfovibrio yellowstonii DSM 11347
NR 040795 Thermodesulfovibrio aggregans TGE-P1
NZ BCNO01000001 Thermodesulfovibrio aggregans TGE-P1
9f94f303579c05490d0e4855ae864adb
9f93e0fc6396c9c2be072f51496d6c59
84a0a2a8fb8eb09cf21026a2b71b1d5a
92f8389fdebedf91fada1d483c4eb7cb
2623148089319a16de678f7a0812e3c0
SMVS01000089 Nitrospina sp. N074bin53 k141 981193
HQ675602 Nitrospina sp. SCGC AAA240-J07
Atlantic Ocean isolate
NZ HG422173 Nitrospina gracilis 3/211
031e6a06e6c028f9c00c5be90c6f7822
2592dc6ab426f6021ce527f8bf4da616
fc8fa1353eb9f6fa8bee915179014c0d
HQ675585 Nitrospina sp. SCGC AAA240-G05
HQ675390 Nitrospina sp. SCGC AAA003-A14
HQ675403 Nitrospina sp. SCGC AAA003-E19
HQ675544 Nitrospina sp. SCGC AAA240-B06
8bea5d95a0bc16a079ffc4da96d3b9b0
ea658e001138e794dda40b6ed936d87e
81b66c2976b3d2b669d053f2da43f11b
18f2510cc993ef3644297a6033d1709f
de0cae8ea3ca8d7c3e16675d2afd2cf0
165e8f96b55fa8570ae13ac6865a5b11
RSAC01000024 Nitrospina sp. ETSP2013-BB2-NOB-2
2198f90dcf10a5bf3101db2354ba8554
4d7d920c47a7469a9cea8a4079172620
HQ675664 Nitrospina sp. SCGC AAA288-C20
HQ675674 Nitrospina sp. SCGC AAA288-E23
65d78fbd3ca2c1a865045a0a59c3a756
2f3a9cd266e4ff7af72b0f53c5207c8a
528455c1603734ccc53c8b59ccd2ecec
4f70724d0c3015c1091d65179e9a6721
71307034d03b7a1ce4e0a90a580d55ce
c5d7d8bae30ae4f1a855ca2cd147a6b0
HQ675628 Nitrospina sp. SCGC AAA240-N03
HQ675648 Nitrospina sp. SCGC AAA240-O22
HQ675701 Nitrospina sp. SCGC AAA288-L16
HQ675721 Nitrospina sp. SCGC AAA288-O16
HQ675700 Nitrospina sp. SCGC AAA288-L15
HQ675366 Nitrospina sp. SCGC AAA001-C22
HQ675394 Nitrospina sp. SCGC AAA003-C16
HQ675416 Nitrospina sp. SCGC AAA003-G17
HQ675540 Nitrospina sp. SCGC AAA240-A16

Figure B12. Phylogenetic maximum likelihood tree (1000 bootstraps) of bacterial ASVs from 16S rRNA amplicon sequencing of the Bedford Basin bottom water community that were affiliated with known nitrifier taxa based on SILVA. Same as bacterial tree in Figure B2 without any collapsed clades to show the names of all used sequences from Bedford Basin and reference database.

Table B1. Multiple regression analyses with each amoA phylotype quantified by qPCR tested as a dependent variable against independent variables that may predict their presence in Bedford Basin bottom water. Significant parameters ($p<0.01$) are highlighted in bold font.

Dependent:	amoA-A1		amoA-A2		amoA-A3		amoA-A4		amoA-A5		amoA-A6	
	t value	Sign.	t value	Sign.	t value	Sign.	t value	Sign.	t value	Sign.	t value	Sign.
(Intercept)	-0.74	0.46	**-2.66**	**0.01**	**-3.49**	**6.00E-04**	-0.03	0.97	-0.27	0.79	-2.02	0.04
Temperature [°C]	**4.74**	**4.00E-06**	2.5	0.01	-1.6	0.11	0.72	0.47	-0.6	0.55	-0.69	0.49
Dissolved O_2 [µmol kg_{sw}^{-1}]	**-3.99**	**1.00E-04**	**4.31**	**3.00E-05**	**3.62**	**4.00E-04**	1.5	0.14	0.45	0.65	**4.91**	**2.00E-06**
NH_4^+ concentration [µmol kg_{sw}^{-1}]	-1.3	0.19	-1.89	0.06	-2.06	0.04	-0.19	0.85	-0.08	0.94	-2.05	0.04
POC concentration [µmol kg_{sw}^{-1}]	**-3.08**	**2.00E-03**	**-2.96**	**3.00E-03**	-1.57	0.12	-0.53	0.6	0.63	0.53	-2.18	0.03
Salinity [PSU]	0.81	0.42	**2.63**	**0.01**	**3.51**	**6.00E-04**	0.07	0.95	0.27	0.79	2.02	0.04
Multiple R^2	0.48		0.26		0.26		0.03		0.01		0.24	

Table B2. Model equations. sw = surface water; variable names, see Table B4.

$\frac{dO2}{dt} = -R.remin - 1.5 \times R.AO - 0.5 \times R.ON - R.O2 + \frac{1}{\tau} \times (O2.sw - O2)$
$\frac{dNH4}{dt} = rNC \times R.remin - R.AO + \frac{1}{\tau} \times (NH4.sw - NH4)$
$\frac{dNO2}{dt} = R.AO - R.NO + \frac{1}{\tau} \times (NO2.sw - NO2)$
$\frac{dNO3}{dt} = R.NO - R.Nloss + \frac{1}{\tau} \times (NO3.sw - NO3)$
$\frac{dAmoA}{dt} = R.AO + \frac{1}{\tau} \times (0 - AmoA)$
$\frac{dNxr}{dt} = R.NO + \frac{1}{\tau} \times (0 - Nxr)$

Table B3. Reaction terms used in the numerical box model. Modeled state variables are shown in bold.

$R.remin = k.remin \times (\exp(T) \times \ln(Q10_{remin})\ /10) \times POC \times \boldsymbol{O2}$
$R.AO = k.AO \times (\exp(T) \times \ln(Q10_{nitr})\ /10) \times \boldsymbol{AmoA} \times \boldsymbol{NH4} \times \frac{\boldsymbol{O2}}{K_s.O2.AO + \boldsymbol{O2}}$
$R.NO = k.NO \times (\exp(T) \times \ln(Q10_{nitr})\ /10) \times \boldsymbol{Nxr} \times \boldsymbol{NO2} \times \frac{\boldsymbol{O2}}{K_s.O2.NO + \boldsymbol{O2}}$
$R.Nloss = k.Nloss \times \boldsymbol{NO3}$
$R.O2 = k.sedi.o2 \times \boldsymbol{O2}$

Table B4. Parameter values used in the numerical box model.

Parameter	**Description**		**Value**	**Unit**	**Reference**
k.remin	rate constant for N remineralization		0.0002	kg μmol^{-1} d^{-1}	-
k.AO	rate constant for ammonia oxidation		0.0011	kg (gene copies)$^{-1}$ d^{-1}	-
k.NO	rate constant for nitrite oxidation		0.0091	kg (gene copies)$^{-1}$ d^{-1}	-
ks.O2.AO	Half-saturation constant for O_2 in AO		3	μmol kg$_{SW}^{-1}$	(Laanbroek and Gerards 1993; Martens-Habbena et al. 2009; Qin et al. 2017)
ks.O2.NO	Half-saturation constant for O_2 in NO		22	μmol kg$_{SW}^{-1}$	(Laanbroek and Gerards 1993)
k.Nloss	rate constant for N loss (denitrification, assimilation)		0.0014	d^{-1}	-
k.sedi.O2	rate constant for O_2 uptake by sediment/higher organisms		0.0014	d^{-1}	(Hargrave 1978b)
rNC	Redfield ratio for nitrogen/carbon		0.15	-	-
$Q10_{remin}$	Q_{10}-type temperature dependence affecting N remineralization		20	-	-
$Q10_{nitr}$	Q_{10}-type temperature dependence affecting ammonia and nitrite oxidation		20	-	-
τ	Residence time		194 (lowered by mixing)	d	(Burt et al. 2013)

Table B5. Results from Spearman's Rho, Kendall's Tau and Pearson's tests of the correlation between oceanographic parameters from the long-term Bedford Basin time series with i) the annual NO_3^-/NH_4^+, and ii) winter mixing proxied by the minimum spiciness during each annual winter mixing period. With the exception of the minimum spiciness during winter mixing, all parameters represent annual means from n tested years between 1994 and 2018. Results from the parametric Pearson's test are given if both tested parameters are normally distributed (Shapiro-Wilk test $p > 0.05$). Bold numbers highlight significance below the 5% level.

	annual (NO_3^-/NH_4^+) ratio (60 m)							Minimum spiciness during winter (60m)						
	Spearman			Kendall		Pearson		Spearman			Kendall		Pearson	
	n	r	p	r	p	r	p	n	r	p	r	p	r	p
Minimum spiciness during winter (60m)	15	**0.53**	**0.041**	0.37	0.173	Shapiro Wilk $p<0.05$								
annual (NO_3^-/NH_4^+) ratio (60 m)								15	**0.53**	**0.041**	0.37	0.173	Shapiro Wilk $p<0.05$	
Stratification [kg m^{-4}]	17	0.32	0.213	0.22	0.395			17	-0.04	0.874	-0.03	0.911	0.08	0.756
Dissolved O_2 (60 m) [µmol kg^{-1}]	17	**-0.59**	**0.012**	-0.41	0.101			17	**-0.52**	**0.034**	-0.37	0.147	**-0.53**	**0.029**
Nitrate (60 m) [µmol kg^{-1}]	17	**0.91**	**0.000**	**0.74**	**0.001**			18	**0.57**	**0.014**	0.40	0.101	**0.65**	**0.00**
Phosphate (60 m) [µmol kg^{-1}]	17	0.48	0.051	0.34	0.184			18	0.44	0.070	0.32	0.195	Shapiro Wilk $p<0.05$	
Salinity (60 m) [PSU]	17	0.30	0.244	0.18	0.498			19	**0.80**	**0.000**	**0.60**	**0.006**	**0.81**	**0.000**
Silicate (60 m) [µmol kg^{-1}]	17	**0.72**	**0.001**	**0.49**	**0.048**			18	**0.49**	**0.038**	0.35	0.159	**0.55**	**0.018**
Temperature (60 m) [°C]	17	0.41	0.103	0.31	0.228			19	0.12	0.637	0.06	0.794	0.17	0.474
Ammonium (60 m) [µmol kg^{-1}]	17	**-0.93**	**0.000**	**-0.81**	**0.000**			15	-0.44	0.098	-0.30	0.285	**-0.58**	**0.024**
Nitrite (60 m) [µmol kg^{-1}]	17	-0.33	0.191	-0.24	0.363			16	-0.47	0.068	-0.35	0.184	Shapiro Wilk $p<0.05$	
DIN (60 m) [µmol kg-1]	17	0.05	0.837	0.01	0.955			15	0.24	0.398	0.12	0.660	0.23	0.41
POC (60 m) [µmol kg^{-1}]	15	**-0.61**	**0.016**	-0.45	0.094			14	**-0.57**	**0.034**	-0.41	0.149	**-0.63**	**0.015**
PON (60 m) [µmol kg^{-1}]	15	-0.21	0.451	-0.14	0.612			14	**-0.53**	**0.049**	-0.41	0.149	**-0.53**	**0.050**
POC (5 m) [µmol kg^{-1}]	15	-0.32	0.243	-0.26	0.355			14	-0.11	0.714	-0.08	0.794	-0.21	0.465
PON (5 m) [µmol kg^{-1}]	15	-0.29	0.289	-0.24	0.393			14	-0.09	0.771	-0.03	0.911	-0.05	0.875
Chl a (5 m) [µg kg^{-1}]	17	-0.27	0.286	-0.21	0.428			18	-0.24	0.341	-0.18	0.484	-0.18	0.484
Sackville River discharge	16	0.24	0.368	0.15	0.579			17	-0.36	0.154	-0.26	0.317	-0.33	0.191

Table B6. Results from a multiple linear regression using weekly standard anomalies for each variable. The multiple R^2 of the regression was 0.25. Significant parameters ($p<0.01$) are highlighted in bold font.

Dependent	Independent	Estimate	Std error	t value	Significance
$NO_3^-/[NO_3^- + NH_4^+]$	(Intercept)	0.04	0.03	1.31	0.191
	dissolved O_2 [µmol kg_{SW}^{-1}]	**-0.33**	**0.03**	**-10.62**	**2.00E-16**
	Temperature [°C]	**0.22**	**0.03**	**7.62**	**7.76E-14**
	POC [µmol kg_{SW}^{-1}]	-0.08	0.03	-2.46	0.014
	Salinity [PSU]	**0.14**	**0.03**	**4.47**	**9.04E-06**

Table B7. Primer sets and dsDNA standards used to quantify archaeal amoA phylotypes. Primers and standards are written 5' to 3'. GenBank accession codes for larger reference sequences used to design primers and their standards are provided in parentheses.

Assay	**Forward Primer** **Name**: sequence	**Reverse Primer** **Name**: sequence	**dsDNA Standard** **Name** (reference sequence): nucleotides
amoA-A1	**amoA-A1-F:** GGCGGCGTACTGGTAGGA	**amoA-A1-R:** TGGGTCTGCTACTGTTATCAGGTTTA	**amoA-A1-STD (KJ807556):** TTCGTACACGGTATTTTCAGTATCGCAAACGTTGATGCTAATTGTAGGTGCATGTTATTACTTGACATTTACAGGCGTTCCAGGCACAGCGACGTACTACGCTCTAATTATGACAGTATACACATGGGTAGCAAAAGCCGCATGGTTTTCGCTAGGATATCCATATGACTTCATTGTAACTCCAGTTTGGCTTCCATCAGCAATGCTGTTGGACTTGGTCTACTGGGCGACAAAGAAGAACAAGCACTCCTTGATACTGTTTGGCGGCGTACTGGTAGGAATGTCTTTACCATTATTCAACATGGTAAACCTGATAACAGTAGCAGACCCACTAGAAACGGCATTCAAATA
amoA-A2	**amoA-A2-F:** GCGGAGTCTTAGTTGGAATGTCA	**amoA-A2-R:** GGGTCAGCCACTGTGATCAA	**amoA-A2-STD (KF727168):** ATCGTTTGTAGTATTCTCAATATCTCAAACACTTATGCTCACTGTAGGTGCGTGTTACTATCTCACCTTCACTGGAGTTCCAGGAACCGCAACGTATTATGCACTTATCATGACAGTCTACACTTGGATTGCAAAAGGTGCATGGTTCGCATTAGGTTACCCATATGACTTCATCGTTACACCAGTTTGGCTACCATCAGCAATGCTGTTGGATTTGGCGTACTGGGCAACAAAGAAGAATAAGCACTCTCTGATACTGTTCGGCGGAGTCTTAGTTGGAATGTCATTACCACTATTCAACATGGTCAATTTGATCACAGTGGCTGACCCACTAGAGACTGCATTCAAGTA

amoA-A3	**amoA-A3-F:** TGATGACGGTAGTCGGAGCTG	**amoA-A3-R:** AATACGCGCCTGTACCAGGAA	**amoA-A3-STD (KF727043.1):** ATCATTCGTAGTTTTCTCTATCGCCAACACTTTGATGACGGTAGTCGGAGCTGTGTATTACATTACATTTACGGGTGTTCCTGGTACAGGCGCGTATTACGGCTTAATAATGCAGGTCTATACATGGGTCGCTAAAGTTGCATGGTTTGCACTTGGTTATCCGGTGGATTTCATTGTTCATCCAATGTGGATTCCATCATGCATGTTGTTGGATTTGGCATATTGGGCTACGAAGAAGAATAAGCACTCGCTGATATTCTTTGGAGGAGTTTTGGTCGGTATGTCAATGCCGCTGTTCAATATGGTACAGCTGATGCTGATCGCCGATCCGCTAGAAACTGCATTCAAATA
Assay	**Forward Primer** **Name**: sequence	**Reverse Primer** **Name**: sequence	**dsDNA Standard** **Name** (reference sequence): nucleotides
amoA-A4	**amoA-A4-F:** CCTTGATGACAGTGGTAGGTGCT	**amoA-A4-R:** GCCATAATATGCGCCTGTGC	**amoA-A4-STD (KF727066.1):** ATCATTTGTAGTATTTTCCATAGCTAATACCTTGATGACAGTGGTAGGTGCTGTTTACTATATCACGTTTACAGGTGTTCCTGGCACAGGCGCATATTATGGCCTAATTATGCAAGTCTATACTTGGGTTGCTAAAGTTGCATGGTTTGCACTTGGCTATCCTGTGGATTTCATTGTTCATCCAATGTGGATTCCATCTTGTATGCTATTGGACTTGGCGTATTGGGCTACAAAGAAGAATAAGCACTCGCTGATATTCTTTGGTGGAGTTTTGGTTGGTATGTCAATGCCGCTGTTCAATATGGTACAGTTGATGTTGATCGCCGATCCGCTAGAAACTGCATTCAAGTA
amoA-A5	**amoA-A5-F:** TGACAGTCGTCGGAGCAGTC	**amoA-A5-R:** TTGGCGACCCAAGTATACACC	**amoA-A5-STD (KF727042):** TTCCTTTGTAGTTTTCTCCATTGCCAACACTCTCATGACAGTCGTCGGAGCAGTCTATTATATCACATTTACAGGCGTGCCTGGAACAGGCGCATATTATGGTTTAATTATGCAGGTGTATACTTGGGTCGCCAAAGTGGCATGGTTTGCACTTGGCTATCCTGCAGATTTCATCGTTCATCCAATGTGGATTCCATCATGCATGTTGTTGGATTTGGCATATTGGGCTACGAAGAAGAATAAGCACTCGCTGATATTCTTTGGTGGGGTTTTAGTTGGAATGTCAATGCCACTGTTCAATATGGTACAGTTGATGTTGATAGCAGATCCACTAGAAACTGCATTCAAGTA
amoA-A6	**amoA-A6-F:** TTGATGACTATTGTTGGTGCTGTG	**amoA-A6-R:** TCAGACCATAGTACGTTGCAGTACC	**amoA-A6-STD (KF727089):** ATCATTTGTCGTATTCTCAATTGCCAATACTTTGATGACTATTGTTGGTGCTGTGTATTATCTTACATTTACGGGCGTACCTGGTACTGCAACGTACTATGGTCTGATTATGCAAGTCTATACTTGGGTTGCAAAAGTTGCATGGTTTGCACTTGGCTATCCAGTAGATTTCATCGTTCATCCGATGTGGATTCCATCTTGTATGTTATTGGACTTGGCGTATTGGGCTACGAAGAAGAATAAGCACTCGCTGATATTCTTTGGAGGAGTTTTGGTCGGTATGTCAATGCCGCTGTTCAATATGGTACAGTTGATGTTGATCGCCGATCCGCTAGAAACTGCATTCAAGTA

Table B8. Target specificity of qPCR assays analyzed by cross-reaction test. F/R = Primers, STD = double stranded DNA standard, green = positive amplification. 10^7 copies of each standard were added to each reaction. With the ViiA7 and SYBR chemistry, 10^7 copies of amoA were typically detected after 14 cycles of DNA amplification. Detection at ≥31 cycles would equate to approximately ≤0.01% copies as false positives.

		Approximate Number of Cycles to Detection					
		dsDNA Standard Template					
		A1 STD	**A2 STD**	**A3 STD**	**A4 STD**	**A5 STD**	**A6 STD**
Assay / Primer Set	**A1 F/R**	14	–	–	–	–	–
	A2 F/R	32	14	–	–	–	–
	A3 F/R	–	–	14	36	–	–
	A4 F/R	–	–	35	14	–	–
	A5 F/R	–	–	–	–	16	–
	A6 F/R	34	34	34	36	36	14

Table B9. 16S rRNA gene sequences of OTUs affiliated with *Thaumarchaeota* and *Nitrospina* found in the Gulf of Mexico by Kitzinger et al. (Kitzinger et al. 2019, 2020). These sequences are used in Figure B10 and Figure B11, respectively. The raw sequences these OTUs were picked from were deposited by the authors of the original publication at NCBI under Bioproject PRJNA397176 and BioSample numbers SAMN07461114–SAMN07461122.

Thaumarchaeota
>1005844 GoM16-SV-C6C-14_2
AACCAGCACCTCAAGTGGTCAGGATGATTATTGGGCCTAAAGCATCCGTAGCCGGCTCTGTAAGTTTTCGGTTAAATCTGTACGCTCAACGTACAGGCTGCCGGGAATACTGCAAAGCTAGGGAGTGGGAGAGGTAGACGGTACTCGGTAGGAAGGGGTAAAATCCTTTGATCTATTGATGACCACCTGTGGCGAAGGCGGTCTACCAGAACACGTCCGACGGTGAGGGATGAAAGCTGGGGGAGCAAACCGG
>1080410 GoM16-SV-CP1-14_8655
AACCAGCACCTCAAGTGGTCAGGAGGATTATTGGGCCTAAAGCATCCGTAGCCGGCTCTGTAAGTTTTCGGTTAAATCTATGCGCTCAACGTATGGGCTGCCGAAAATACTGTAGAGATAGGGAGTGGGAGAGGTAGACGGTACTCGGTAGGAAGGGGTAAAATCCTTTGATCTATCGATGACCACCTGTGGCGAAGGCGGTCTACCAGAACACGTTCGACGGTGAGGGATGAAAGCTGGGGGAGCAAACCGG
>152483 GoM16-SV-C6C-16_4155
AACCAGCACCTCAAGTGGTCAGGATGATTATTGGGCCTAAAGCATCCGTAGCCGGCTCTGTAAGTTTTCGGTTAAATCTGTACGCTCAACGTACAGGCTGCCGGGAATACTGCAAAGCTAGGGAGTGGGAGAGGTAGACGGTACTCGGTAGGAAGGGGTAAAATCCTTTGATCTATTGATGACCACCTGTGGCGAAGGCGGTCTACCAGAACACGTCCGACGGTGAGGGATGAAAGCTGGGGAGCAAACCGG
>154353 GoM16-SV-C6C-18_9666
AACCAGCACCTCAAGTGGTCAGGATGATTATTGGGCCTAAAGCATCCGTAGCCGGCGCTATAAGTTTTCGGTTAAATCTGTACGCTCAACGTACAGGCTGCCGGGAATACTGTAGCGCTAGGGAGTGGGAGAGGTAGACGGTACTCGGTAGGAAGGGGTAAAATCCTTTGATCTATTGATGACCACCTGTGGCGAAGGCGGTCTACCAGAACACGTCCGACGGTGAGGGATGAAAGCTGGGGGAGCAAACCGG
>155526 GoM16-SV-C6C-16_19095
AACCAGCACCTCAAGTGGTCAGGATGATTATTGGGCCTAAAGCATCCGTAGCCGGCTCTGTAAGTTTTCGGTTAAATCTGTACGCTCAACGTACAGGCTGCCGGGAATACTGCAGAGCTAGGGAGTGGGAGAGGTAGACGGTACTTGGTAGGAAGGGGTAAAATCCTTTGATCTATTGATGACCACCTGTGGCGAAGGCGGTCTACCAGAACACGTCCGACGGTGAGGGATGAAAGCTGGGGGAGCAAACCGG
>1692591 GoM16-SV-C6C-16_6014
AACCAACACCTCAAGTGGTCAGGATGATTATTGGGCCTAAAGCATCCGTAGCCGGCTCTGTAAGTTTTCGGTTAAATCTGTACGCTCAACGTACAGGCTGCCGGGAATACTGCAAAGCTAGGGAGTGGGAGAGGTAGACGGTACTCGGTAGGAAGGG

GTAAAATCCTTTGATCTATTGATGACCACCTGTGGCGAAGGCGGTCTACCAGAACACGTCCGACGGTGAGGGATGAAAGCTGGGGGAGCAAACCGG
Thaumarchaeota
>4369009 GoM16-SV-C6C-16_13339
AACCTGCACCTCAAGTGGTCAGGATGTTTATTGGGCCTAAAGCATCCGTAGCCGGCGCTGTAAGTTTTCGGTTAAATCTGTACGCTCAACGTACAGGCTGCCGGGAATACTGCAAAGCTAGGGAGTGGGAGAGGTAGACGGTACTCGGTAGGAAGGGGTAAAATCCTTTGATCTATTGAGGACCACCTGTGGCGAAGGCGGTCTACCAGACCACGTCCGACGGTGAGGGATGAAAGCTGGGGGAGCAAACAGG
>4431375 GoM16-SV-C6C-18_20016
AACCAGCACCTCAAGTGGTCAGGATGATTATTGGGCCTAAAGCATCCGTAGCCTGCTTTGTAAGTTTTCGGTTAAATCTATACGCTCAACGTATGGGCTGCCGGGAATACTGCAAAGCTAGGGAGTGGGAGAGGTAGACGGTACTCGGTAGGAAGGGGTAAAATCCTTTGATCTATTGATGACCACCTGTGGCGAAGGCGGTCTACCAGAACACGTCCGACGGTGAGGGATGAAAGCTGGGGGAGCAAACCGG
>540244 GoM16-SV-C6C-18_10551
AACCAGCACCTCAAGTGGTCAGGATGATTATTGGGCCTAAAGCATCCGTAGCCGGCTCTGTAAGTTTTCGGTTAAATCTGTACGCTCAACGTACAGGCTGCTGGGAATACTGCAGAGCTAGGGAGTGGGAGAGGTAGACGGTACTCGGTAGGAAGGGGTAAAATCCTTTGATCTATTGATGACCACCTGTGCGAAGGCGGTCTACCAGAACACGTCCGACGGTGAGGGATGAAAGCTGGGGGAGCAAACCGG
>544745 GoM16-SV-I3-14_5715
AACCAGCACCTCAAGTGGTCAGGATGATTATTGGGCCTAAAGCATCCGTAGCCGGCTCTGTAAGTTTTCGGTTAAATCTGTACGCTCAACGTACAGGCTGCCGGGAATACTGCAGAGCTAGGAGTGGGAGAGGTAGACGGTACTCGGTAGGAAGGGGTAAAATCCTTTGATCTATTGATGACCACCTGTGGCGAAGGCGGTCTACCAGAACACGTCCGACGGTGAGGGATGAAAGCTGGGGGAGCAAACCGG
>New.CleanUp.ReferenceOTU1886 GoM16-SV-I3-16_8100
AACCAGCACCTCACTTGGTCAGGATGATTATTGGGCCTAAAGCATCCGTCGCCGGCTCTGTAAGTTTTCGGTTAAATCTGTACGCTCAACGTACAGGCTGCCGGGCCTCCGGCAGAGCTAGGGAGTGGGAGAGTTCTACGGTCCTCGGTAGGAAGGGGTAAAATCCTTTGATCTATTGATGACCACCTGTGGCGAAGGCGGTCTACCAGAACACGTCCGACGGTGAGGGAGGAAAGCTGGGGGAGCCCCCCGG
>New.CleanUp.ReferenceOTU2177 GoM16-SV-CP1-14_13306

AACCAGCACCTCCCGTGGTCAGGATGATTATTGGGCCTAAAGCATCCGTCGCCGGCTCTGTAAGTTTTCGGTTAAATCTGTACGCTCAACGTACAGGCTGCCGGGCATCCGGCAAAGCTAGGGAGTGGGAGAGGTCTCCGGTACTCGGTAGGAAGGGGTAAAATCCTTTGCTCTATTGATGACCACCTGTGGCGAAGGCGGTCTACCAGAACACGTCCGACGGTGAGGGAGGAAAGCTGGGGGAGCCCCCCGG
Thaumarchaeota
>New.CleanUp.ReferenceOTU2324 GoM16-SV-C6C-18_13526
AACCAGCACCTCAATTGGTCAGGATGATTATTGGGCCTAAAGCATCCGTCGCCGGCTCTGTAAGTTTTCGGTTAAATCTGTACGCTCAACGTACAGGATGCCGGGCATCCGGCAGAGCTAGGGAGTGGGAGAGGTATCCGGTACTCGGTAGGAAGGGGTAAAATCCTTTGATCTATTGATGACCACCTGTGGCGAAGGCGGTCTACCAGAACACGTCCGACGGTGAGGGAGGAAAGCTGGGGGAGCCACCCTG
>New.CleanUp.ReferenceOTU668 GoM16-SV-CP1-12_18933
AACCAGCACCTCAAGTGGTCAGGATGATTATTGGGCCTAAAGCATCCGTAGCCGGCTCTGTAAGGGGAAGGGAAAATCAGTACGCTCAACGTACAGGCTGCCGGGAATACTGCAGAGCCAGGGAGAGGGAGAGGTAGACGGTACTCGGTAGGAAGGGGTAAAATCCTTTGATCTATTGATGACAACCTGTGGCGAAGGCGGTCTACCAGAACACGTCCGACGGTGAGGGATGAAAGCTGGGGGAGCAAACCGG
>New.CleanUp.ReferenceOTU810 GoM16-SV-CP1-10_938
AACCAGCACCTCAAGTGGTCAGGATGATTATTGGGCCTAAAGCATCCGTAGCCGGCTCTGTAAGTTTTCGGTTAAATCTGTACGCTCAACGTACAGGCTGCCGGGAATACTGCAGAGCTAGGGAGTGGGAGAGGTCGCCGGTGCTCGGTAGCCCCCGGTAAAATCCTTTGATCTATTGATGACCACCTGTGGCGAAGGCGGTCTACCAGAACACGTCCGACGGTGAGGGATGAAAGCTGGGGGAGCAAACCCG
>244523 GoM16-SV-C6C-14_5016
TACGGAGGGGGCAAGCGTTGTTCGGAATCATTGGGCGTAAAGAGTATGTAGGCGGCTGAATAAGTCAGACGTGTAAGCCCACGGCTCAACCGTGGAATTGCGTTTGAAACTGTTTAGCTTGAGTGCAGAAGAGGAAAGCGGAATTCCCAGTGTAGCGGTGAAATGCATTGATATTGGGAAGAACACCGGTGGCGAAGGCGGCTTTCTGGTCTGCTACTGACGCTGAGATACGAAAGCCAGGGGAGCAAAGGGG
>549675 GoM16-SV-C6C-14_1983
TACGGAGGGGGCAAGCGTTGTTCGGAATCATTGGGCGTAAAGAGTATGTAGGCGGCTATTTAAGTCAGACGTGTAAGCCCACGGCTCAACCGTGGAATTGCGTTTGAAACTATTTAGCTTGAGTTCGGGAGAGGAAAGCGGAATTCCCAGTGTAGCGGTGAAATGCATTGATATTGGGAAGAACACCGGTGGCGAAGGCGGCTTTCTGGTCCGATACTGACGCTGAGATACGAAAGCCAGGGGAGCGAACGGG
Nitrospina
>571236 GoM16-SV-CP1-12_4243

TACGGAGGGGGCAGGCGTTGTTCGGAATCATTGGGCGTAAAGAGTATGTAGGCGGCTATTTAAGTCAGACGTGTAAGCCCACGGCTCAACCGTGGAATTGCGTTTGAAACTATTTAGCTTGAGTTCGGGAGAGGAAAGCGGAATTCCCAGTGTAGCGGTGAAATGCATTGATATTGGGAAGAACACCAGTGGCGAAGGCGGCTTTCTGGTCCGATACTGACGCTGAGATACGAAAGCCAGGGGAGCGAACGGG
Nitrospina
>581695 GoM16-SV-C6C-14_5816
TACGGAGGGGGCAAGCGTTGTTCGGAATCATTGGGCGTAAAGAGTATGTAGGCGGCTGGATAAGTCAGACGTGTAAGCCCACGGCTCAACCGTGGAATTGCGTTTGAAACTGTTTAGCTTGAGTGCAGAAGAGGAAAGCGGAATTCCCAGTGTAGCGGTGAAATGCATTGATATTGGGAAGAACACCGGTGGCGAAGGCGGCTTTCTGGTCTGCTACTGACGCTGAGATACGAAAGCCAGGGGAGCAAAGGGG
>727834 GoM16-SV-C6C-14_810
TACGGAGGGGGCAAGCGTTGTTCGGAATTATTGGGCGTAAAGAGTATGTAGGCGGTTAGGTAAGTCAGGCGTGTAAGCCCTCGGCTCAACCGAGGAATTGCGTTTGAAACTACCTAACTTGAGTACGAAAGAGGAAAGCGGAATTCCCAGTGTAGCGGTGAAATGCATTGATATTGGGAAGAACATCGGTGGCGAAGGCGGCTTTCTGGTTCGATACTGACGCTGAGATACGAAAGCCAGGGGAGCAAACGGG
>838006 GoM16-SV-C6C-18_5275
TACGGAGGGGGCAAGCGTTGTTCGGAATTATTGGGCGTAAAGAGTATGTAGGCGGCTGGATAAGTCAGACGTGTAAGCCCACGGCTCAACCGTGGAATTGCGTTTGAAACTATTCAGCTTGAGTGCAGGAGAGGAAGGCGGAATTCCCAGTGTAGCGGTGAAATGCATTGATATTGGGAAGAACACCGGTGGCGAAGGCGGCCTTCTGGTCTGTTACTGACGCTGAGATACGAAAGCCAGGGGAGCAAAGGGG
>936371 GoM16-SV-C6C-14_5612
TACGGAGGGGGCAAGCGTTGTTCGGAATTATTGGGCGTAAAGAGTATGTAGGCGGCTGGATAAGTCAGGTGTGTAAGCCCACGGCTCAACCGTGGAATTGCACTTGAAACTATTCAGCTTGAGTACAGGAGAGGAAAGCGGAATTCCCAGTGTAGCGGTGAAATGCATTGATATTGGGAAGAACACCGGTGGCGAAGGCGGCTTTCTGGTCTGTTACTGACGCTGAGATACGAAAGCCAGGGGAGCAAAGGGG
>New.CleanUp.ReferenceOTU1134 GoM16-SV-CP1-14_15914
TACGGAGGGGGCAAGCGTTGTTCGGAATCATTGGGCGTAAAGAGTATGTAGGCGGCTGGATAAGTCAGACGTGTAAGCCCACGGCTCAACCGTGGAATTGCGTTTGGAACTGTTTAGCTTGAGTGCAGAAGAGGAAAGCGGAATTCCCAGTGTAGCGGTGAAATGCATTGATATTGGGAAGAACACCGGTGGCGAAGGCGGCTTTCTGGTCTGCTACTGACGCTGAGATACGAAAGCCAGGGGAGCAAAGGGC
>New.CleanUp.ReferenceOTU2406 GoM16-SV-C6C-16_960

TACGGAGGGGGCAAGCGTTGTTCGGAATCATTGGGCGTAAAGAGTATGTAGGCGGTTAGATAAGTCAGGTGTGTAAGCCCAGGGCTCAACCTTGGAATTGCACTTGAAACTGTTTAACTTGAGTTCAGGAGAGGAAAGCGGAATTCCCAGTGTAGCGGTGAAATGCATTGATATTGGGAAGAACATCGGTGGCGAAGGCGGCTTTCTGGTCTGATACTGACGCTGAGATACGAAAGCCAGGGGAGCGAACGGG
Nitrospina
>New.CleanUp.ReferenceOTU3068 GoM16-SV-CP1-14_3158
TACGAAGGGGGCAAGCGTTGTTCGGAATCATTGGGCGTAAAGCGTATGTAGGCGGCCGAATAAGTCGGGCGTGCAAGCCCATGGCTCAACCATGGAATTGCGTTTGAAACTGTTCGGCTTGAGTGCAGGAGAGGAAGGCGGAATTCCCAGTGTAGCGGTGAAATGCGTTGATATTGGGAAGAACACCGGTGGCGAAGGCGGCCTTCTGGCCTGCTACTGACGCTGAGATACGAAAGCCAGGGGAGCGAACGGG
>New.CleanUp.ReferenceOTU662 GoM16-SV-C6C-16_18431
TACGGAGGGGGCAAGCGTTGTTCGGAATTATTGGGCGTAAAGAGTATGTAGGCGGTTAGGTAAGTCAGGCGTGTAAGCCCTCGGCTCAACCGAGGAATTGCGTTTGAAACTACCTACCTTGAGTACGAAAGAGGAAAGCGGAATTCCCAGTGTAGCGGTGAAATGCATTGATATTGGGAAGAACATCGGTGGCGAAGGCGGCTTTCTGGTTCGATACTGACGCTGAGATACGAAAGCCAGGGGAGCAAACGGG
>New.CleanUp.ReferenceOTU723 GoM16-SV-C6C-18_1601
TACGGAGGGGGCAAGCGTTGTTCGGAATCATTGGGCGTAAAGAGTATGTAGGCGGCTATTTAAGTCAGACGTGTAAGCCCACGGCTCAACCGTGGAATTGCGTTTGAAACTATTTAGCTTGAGTTCGGGAGAGGAAAGCGGAATTCCCAGTGTAGCGGTGAAATGCATTGATATTGGGAAGAACACCAGTGGCGAAGGCGGCTTTCTGGTCCGATACTGACGCTGAGATACGAAAGCCAGGGTAGCGAACGGG
>New.CleanUp.ReferenceOTU748 GoM16-SV-C6C-14_9025
TACGAAGGGGGCAAGCGTTGTTCGGAATCATTGGGCGTAAAGCGTATGTAGGCGGCTAGATAAGTCGGGCGTGCAAGCCCGCGGCTCAACCGCGGAATTGCGCTCGAAACTGTCTGGCTTGAGTGCAAGAGAGGGAAGCGGAATTCCCAGTGTAGCGGTGAAATGCGTTGATATTGGGAAGAACACCAGTGGCGAAGGCGGCTTTCTGGCTTGCAACTGACGCTGAGATACGAAAGCCAGGGGAGCGAACGGG

APPENDIX C: SUPPORTING INFORMATION TO CHAPTER 4

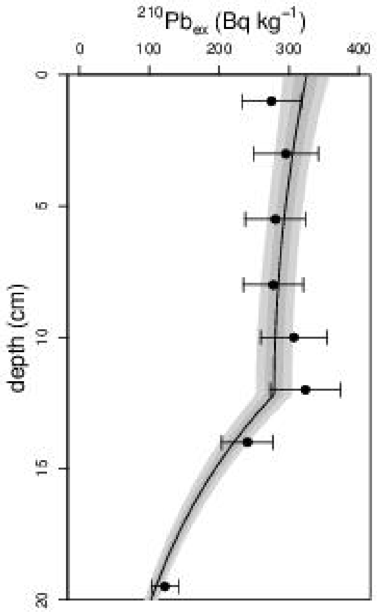

Figure C1. Excess ^{210}Pb distribution in Bedford Basin sediment (points). A 1D steady state reaction transport model was fit to the data to determine the bioturbation rate (D_b) and depth of bioturbation zone (D_b.L) (line). The model estimated $D_b = 9$ cm^2 year^{-1}, and D_b.L = 12 cm.

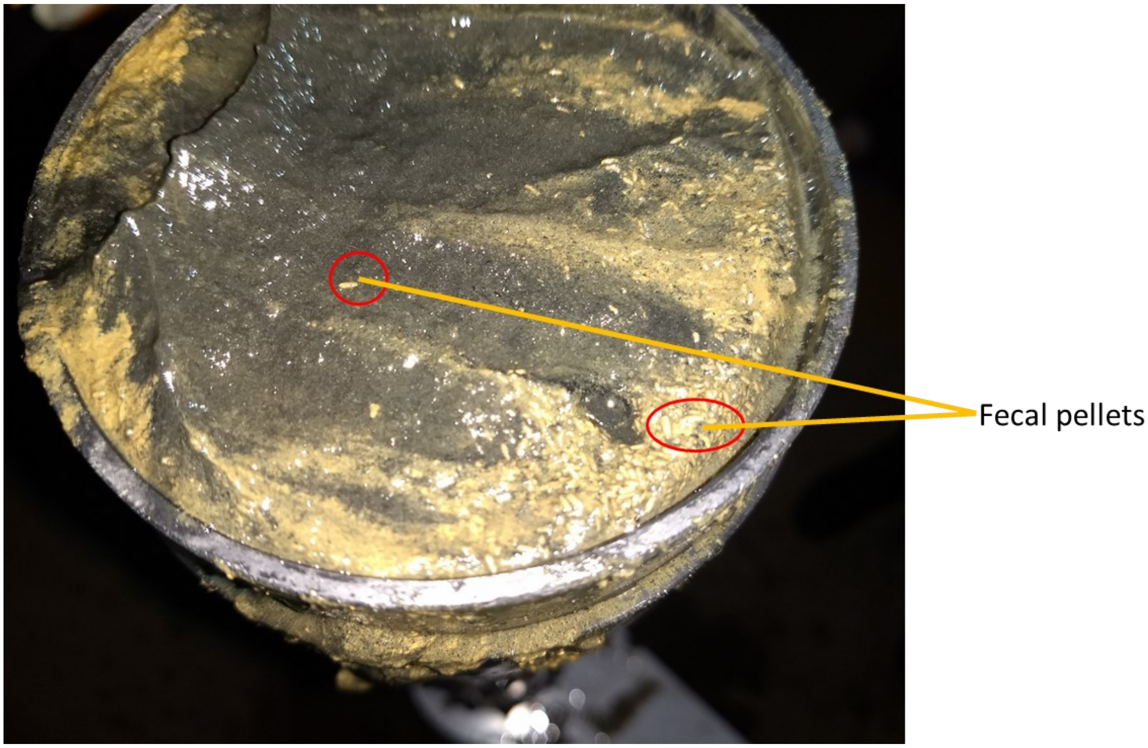

Figure C2. Rice grain shaped fecal pellets on the surface layers of recovered sediment cores from Bedford Basin.

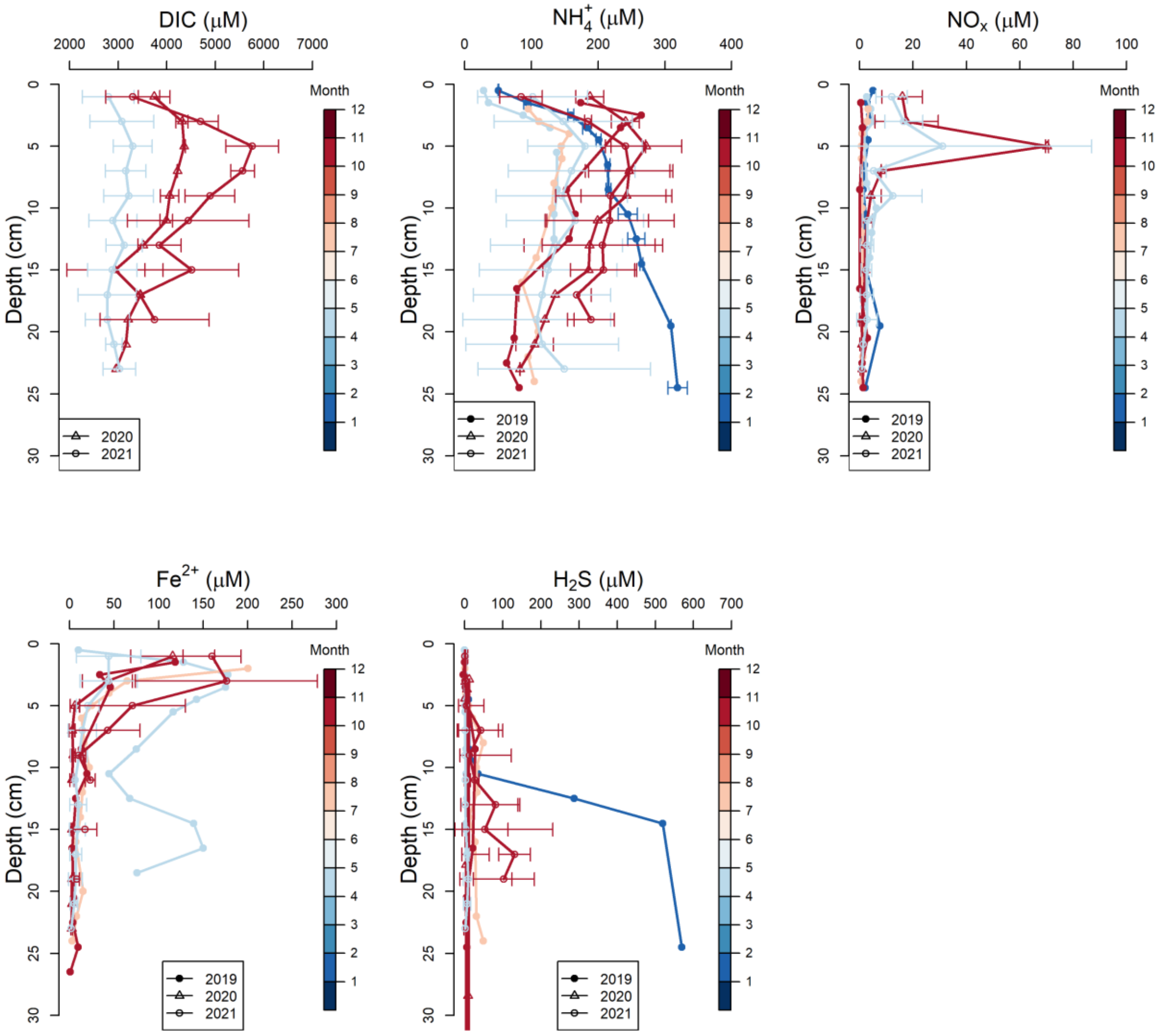

Figure C3. Seasonal sediment porewater profiles from Bedford Basin Compass Buoy station. The error bar represents standard deviation calculated from duplicate or triplicate cores. For symbols without error bar represents concentration measurement from one sediment core.

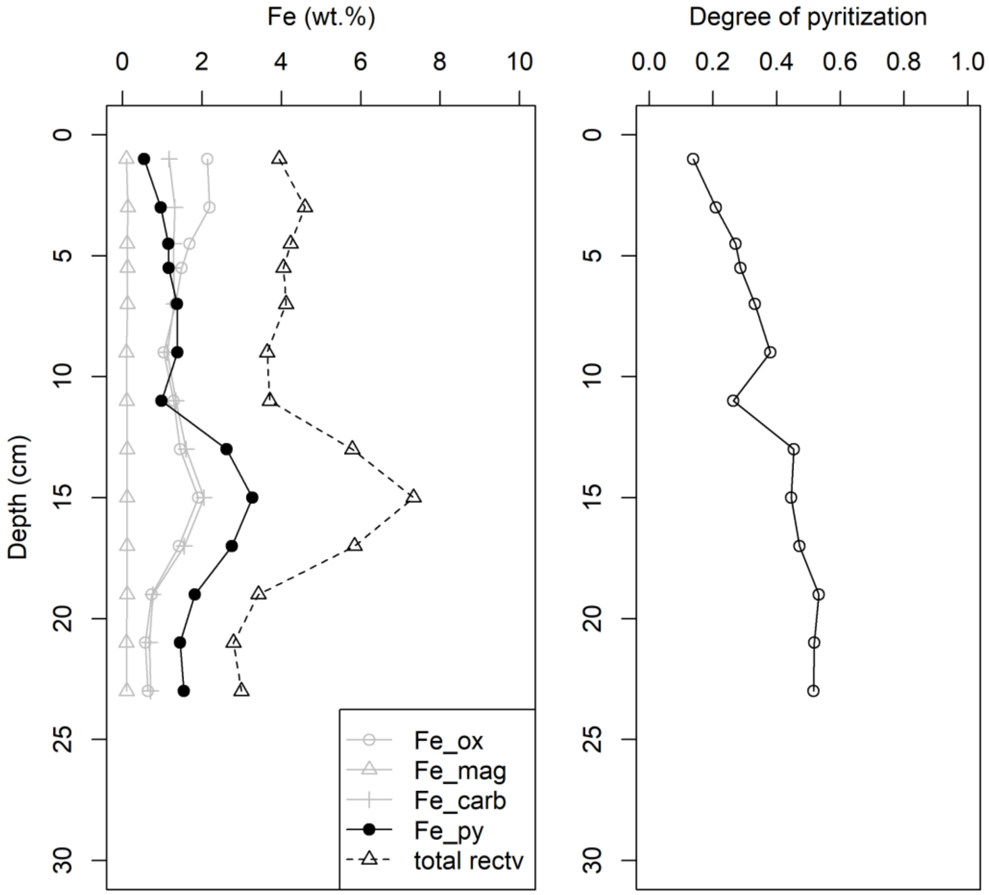

Figure C4. Measured solid iron data in the Bedford Basin sediment in May 2019.

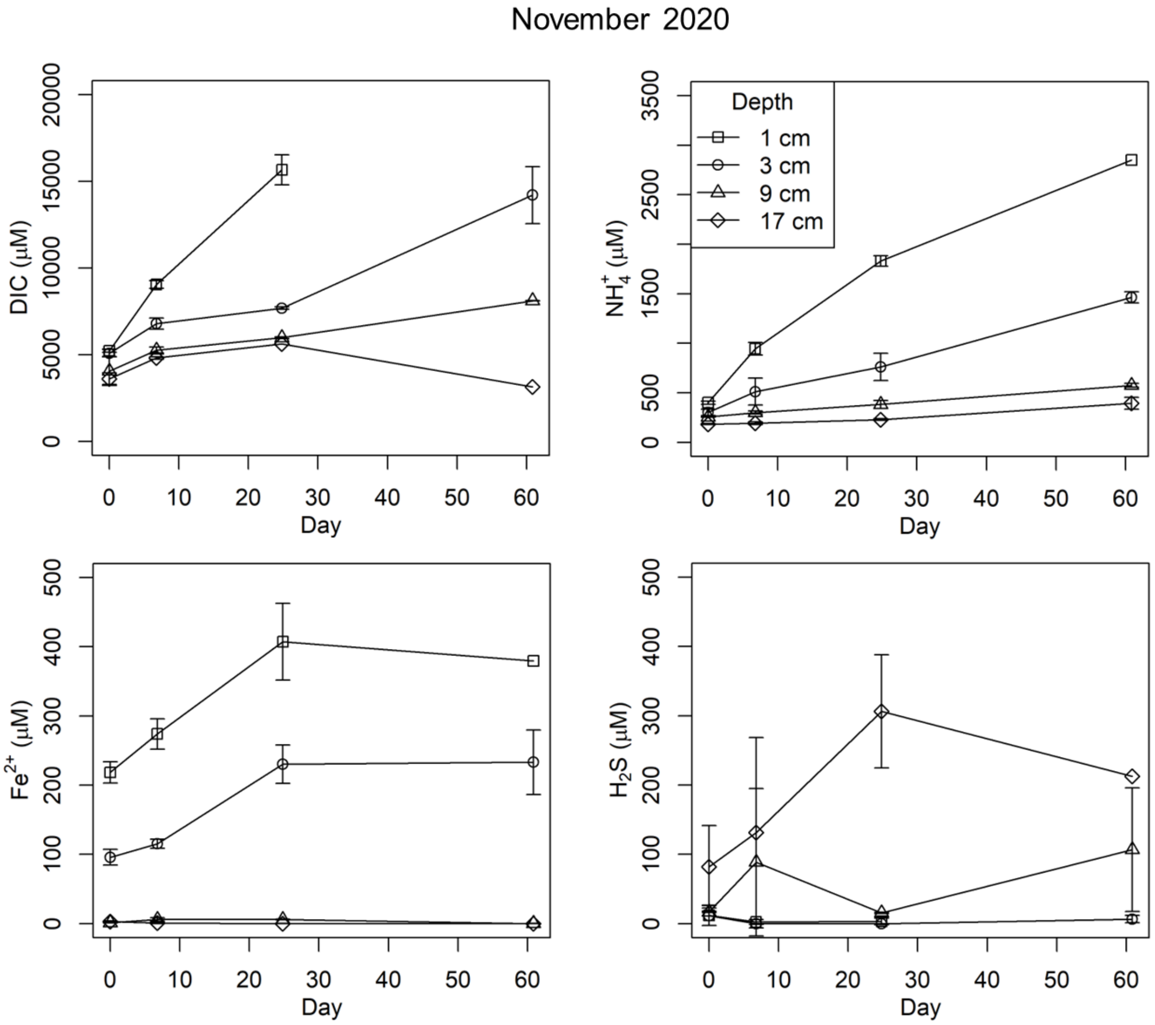

Figure C5. Sediment anoxic incubation data for DIC, ammonium, dissolved iron and hydrogen sulfide for November 2020 and May 2021 campaigns to Bedford Basin. The error bars represent standard deviation from duplicate samples. (contd. to next page)

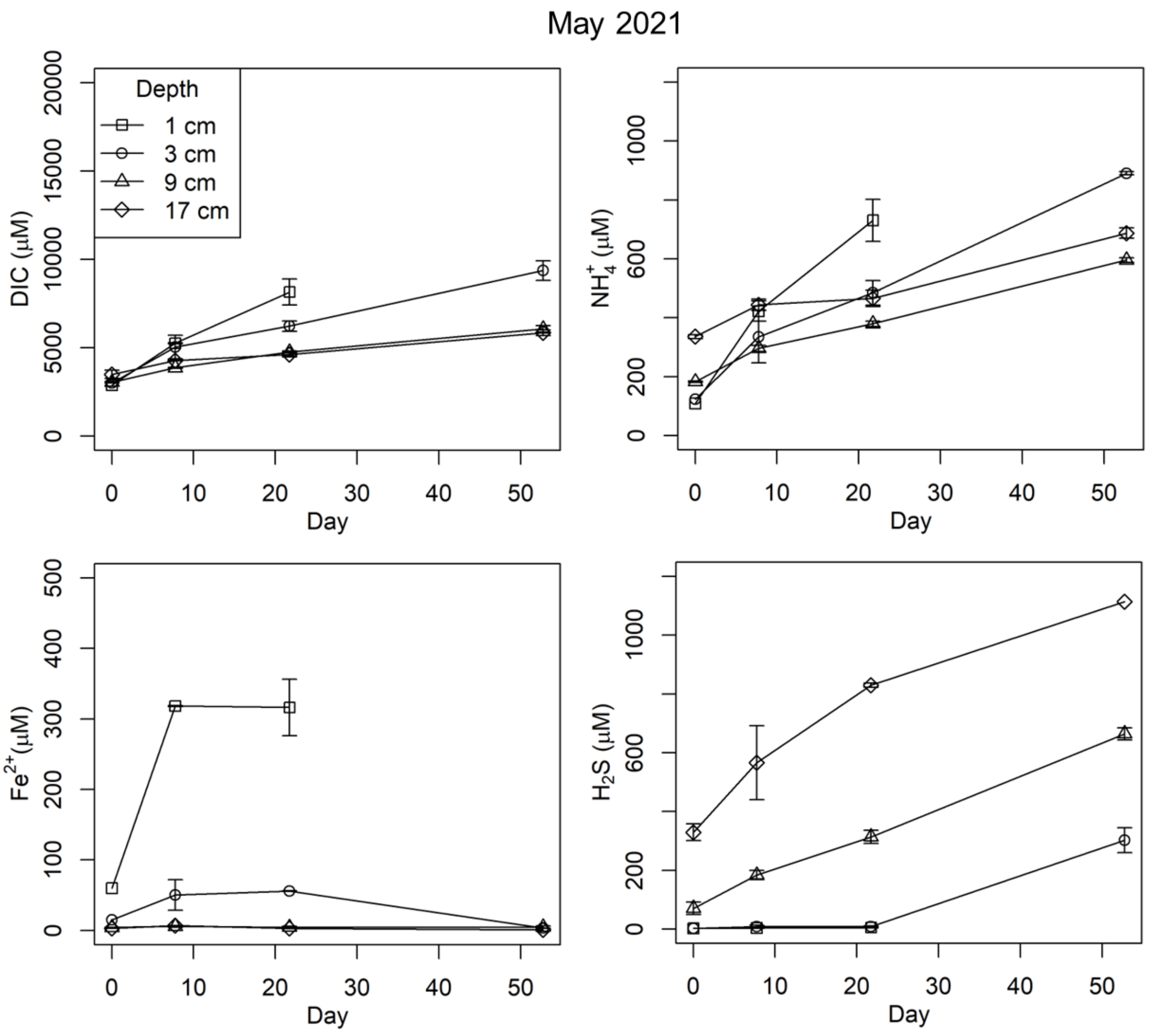

Figure C5: continued from last page.

Table C1. State variables and boundary condition (either fixed concentration or deposition flux) used in the reactive transport model.

Variable	Description	Value	Unit	Source
OM1	Highly reactive organic matter	280	µmol C cm^{-2} y^{-1}	1
OM2	Medium reactive organic matter	340	µmol C cm^{-2} y^{-1}	1
OM3	Low reactive organic matter	300	µmol C cm^{-2} y^{-1}	1
$Fe(OH)_3$	Highly reactive iron oxide	10	µmol Fe cm^{-2} y^{-1}	1
$Fe(OH)_3$.MR	Medium reactive iron oxide	30	µmol Fe cm^{-2} y^{-1}	1
$Fe(OH)_3$.LR	Low reactive iron oxide	20	µmol Fe cm^{-2} y^{-1}	1
MnO_2	High reactive Mn-oxide	7	µmol Mn cm^{-2} y^{-1}	1
MnO_2.MR	Medium reactive Mn oxide	7	µmol Mn cm^{-2} y^{-1}	1
FeS	Iron mono sulfide	0	µmol Fe cm^{-2} y^{-1}	2
FeS_2	Pyrite	0	µmol Fe cm^{-2} y^{-1}	2
O_2	Oxygen	0.170	mM	3
NH_4^+	Ammonium	0.0072	mM	3
NO_3^-	Nitrate	0.0122	mM	3
DIC	Dissolved inorganic carbon	2.2	mM	1
Fe^{2+}	Dissolved iron	0	mM	2
Mn^{2+}	Dissolved manganese	0	mM	2
SO_4^{2-}	Sulfate	28	mM	2
H_2S	Hydrogen sulfide	0	mM	2
CH_4	Methane	0	mM	2

$NO_{3}^{-}{}_{for}$	Intracellular nitrate in foraminifera	2	mM	1
$NO_{3}^{-}{}_{bac}$	Intracellular nitrate in bacteria	0	mM	1

1 = This study/model constrained.

2 = Assumed

3 = Bedford Basin Monitoring Program

Table C2. Modelled chemical reactions. Stoichiometry is balanced for modelled species.

Reactions	**Description**
Primary reactions: (Organic matter mineralization)	
$CH_2O(NH_3)_{rNC} + O_2 = HCO_3^- + (1\text{-}rNC)H^+ + rNC.NH_4^+$	Aerobic respiration
$CH_2O(NH_3)_{rNC} + 4/5\ NO_3 = HCO_3^- + 2/5\ N_2 + rNC.NH_4^+$	Denitrification
$CH_2O(NH_3)_{rNC} + 2MnO_2 = HCO_3^- + 2Mn^{2+} + rNC.NH_4^+$	Mn(IV) reduction
$CH_2O(NH_3)_{rNC} + 4Fe(OH)_3 = 4Fe^{2+} + HCO_3^-$	Fe(III) reduction
$CH_2O(NH_3)_{rNC} + 0.5SO_4 = HCO_3^- + 0.5H_2S + rNC.NH_4^+$	Sulfate reduction
$CH_2O(NH_3)_{rNC} = 0.5CH_4 + 0.5\ HCO_3^- + rNC.NH_4^+$	Methanogenesis
$CH_2O(NH_3)_{rNC} + 0.8\ NO_3.for = HCO_3^- + 0.4N_2 + rNC.\ NH_4^+$	Foraminiferal denitrification
Secondary reactions	
$NH_4^+ + 2O_2 = NO_3^- + H_2O + 2H^+$	Nitrification
$Fe^{2+} + 0.25O_2 = Fe(OH)_3$	Aerobic iron oxidation
$Fe^{2+} + 0.2NO_3 = Fe(OH)_3$	Anaerobic iron oxidation
$H_2S + 2O_2 = SO_4 + H_2O$	Aerobic sulfide oxidation
$Fe^{2+} + H_2S = FeS + 2H^+$	Iron monosulfide precipitation
$FeS + H_2S = FeS_2 + 2H^+$	Pyrite precipitation
$FeS + 2O_2 = Fe^{2+} + SO_4^{2-}$	Aerobic oxidation of FeS
$FeS_2 + 3.5O_2 = Fe^{2+} + 2SO_4^{2-}$	Aerobic oxidation of FeS_2

$Fe(OH)_3 + 0.125\ H_2S = 0.125\ SO_4^{2} + Fe^{2+}$	Fe.HR reduction by H_2S
$Fe(OH)_3.MR + 0.125\ H_2S = 0.125\ SO_4^{2-} + Fe^{2+}$	Fe.MR reduction by H_2S
$Fe(OH)_3.LR + 0.125\ H_2S = 0.125\ SO_4^{2-} + Fe^{2+}$	Fe.LR reduction by H_2S
$NO_3^{-}{}_{bac} + H_2S = NH_4^{+} + SO_4^{2-}$	DNRA
$H_2S + 2NO_3^{-}{}_{bac} = N_2 + SO_4^{2-}$	Chemoautotrophic denitrification
$NH_4^{+} + NO_3^{-}{}_{bac} = N_2$	Anammox
$CH_4 + SO_4^{2-} = H_2S$	Anaerobic methane oxidation
$Mn^{2+} + 0.5O_2 = MnO_2$	Aerobic oxidation of Mn^{2+}
$MnO_2 + 2Fe^{2+} = 2Fe(OH)_3 + Mn^{2+}$	Mn.HR reduction by Fe^{2+}
$MnO_2.MR + 2Fe^{2+} = 2Fe(OH)_3 + Mn^{2+}$	Mn.MR reduction by Fe^{2+}
$MnO_2 + 0.25H_2S = Mn^{2+} + 0.25SO_4^{2-}$	Mn.HR reduction by H_2S
$MnO_2.MR + 0.25H_2S = Mn^{2+} + 0.25SO_4^{2-}$	Mn.MR reduction by H_2S
$MnO_2.MR = \mathrm{k.MnO_2toMR} \times MnO_2$	Conversion from HR to MR
$Fe(OH)_3.MR = \mathrm{k.Fe(OH)_3toMR} \times Fe(OH)_3$	Conversion from HR to MR

Table C3. Modeled reaction terms. Reading key for most reactions: R.X.Y = reaction of X and Y, k.X.Y = rate constant for reaction of X and Y.

Remineralization reaction terms
$\mathrm{R.for.j} = \mathrm{kj} \times [\mathrm{OMj}] \times \frac{\mathrm{NO}_{3\,\mathrm{for}}^{-}}{\mathrm{Ks}_{\mathrm{for}} + [\mathrm{NO}_{3\,\mathrm{for}}^{-}]}$
$\mathrm{R.O_2.j} = \mathrm{kj} \times [\mathrm{OMj}] \times \frac{[\mathrm{O_2}]}{\mathrm{Ks}_{\mathrm{O_2}} + [\mathrm{O_2}]} \times \frac{\mathrm{Ks}_{\mathrm{for}}}{\mathrm{Ks}_{\mathrm{for}} + [\mathrm{NO}_{3\,\mathrm{for}}^{-}]}$
$\mathrm{R.NO_3^{-}.j} = \mathrm{kj} \times [\mathrm{OMj}] \times \frac{[\mathrm{NO_3^-}]}{\mathrm{Ks}_{\mathrm{NO_3^-}} + [\mathrm{NO_3^-}]} \times \frac{\mathrm{Ks}_{\mathrm{O_2}}}{\mathrm{Ks}_{\mathrm{O_2}} + [\mathrm{O_2}]} \times \frac{\mathrm{Ks}_{\mathrm{for}}}{\mathrm{Ks}_{\mathrm{for}} + [\mathrm{NO}_{3\,\mathrm{for}}^{-}]}$
$\mathrm{R.MnO_2.j} = \mathrm{kj} \times [\mathrm{OMj}] \times \frac{[\mathrm{MnO_2}]}{\mathrm{Ks}_{\mathrm{MnO_2}} + [\mathrm{MnO_2}]} \times \frac{\mathrm{Ks}_{\mathrm{NO_3^-}}}{\mathrm{Ks}_{\mathrm{NO_3^-}} + [\mathrm{NO_3^-}]} \times \frac{\mathrm{Ks}_{\mathrm{O_2}}}{\mathrm{Ks}_{\mathrm{O_2}} + [\mathrm{O_2}]}$ $\times \frac{\mathrm{Ks}_{\mathrm{for}}}{\mathrm{Ks}_{\mathrm{for}} + [\mathrm{NO}_{3\,\mathrm{for}}^{-}]}$
$\mathrm{R.Fe(OH)_3.j} = \mathrm{kj} \times [\mathrm{OMj}] \times \frac{[\mathrm{Fe(OH)_3}]}{\mathrm{Ks}_{\mathrm{Fe(OH)_3}} + [\mathrm{Fe(OH)_3}]} \times \frac{\mathrm{Ks}_{\mathrm{MnO_2}}}{\mathrm{Ks}_{\mathrm{MnO_2}} + [\mathrm{MnO_2}]}$ $\times \frac{\mathrm{Ks}_{\mathrm{NO_3^-}}}{\mathrm{Ks}_{\mathrm{NO_3^-}} + [\mathrm{NO_3^-}]} \times \frac{\mathrm{Ks}_{\mathrm{O_2}}}{\mathrm{Ks}_{\mathrm{O_2}} + [\mathrm{O_2}]} \times \frac{\mathrm{Ks}_{\mathrm{for}}}{\mathrm{Ks}_{\mathrm{for}} + [\mathrm{NO}_{3\,\mathrm{for}}^{-}]}$
$\mathrm{R.SO_4^{2-}.j} = \mathrm{kj} \times [\mathrm{OMj}] \times \frac{\mathrm{SO_4^{2-}}}{\mathrm{Ks}_{\mathrm{SO_4^{2-}}} + \mathrm{SO_4^{2-}}} \times \frac{\mathrm{Ks}_{\mathrm{Fe(OH)_3}}}{\mathrm{Ks}_{\mathrm{Fe(OH)_3}} + [\mathrm{Fe(OH)_3}]}$ $\times \frac{\mathrm{Ks}_{\mathrm{MnO_2}}}{\mathrm{Ks}_{\mathrm{MnO_2}} + [\mathrm{MnO_2}]} \times \frac{\mathrm{Ks}_{\mathrm{NO_3^-}}}{\mathrm{Ks}_{\mathrm{NO_3^-}} + [\mathrm{NO_3^-}]} \times \frac{\mathrm{Ks}_{\mathrm{O_2}}}{\mathrm{Ks}_{\mathrm{O_2}} + [\mathrm{O_2}]}$ $\times \frac{\mathrm{Ks}_{\mathrm{for}}}{\mathrm{Ks}_{\mathrm{for}} + [\mathrm{NO}_{3\,\mathrm{for}}^{-}]}$
$\mathrm{R.CH_4.j} = \mathrm{kj} \times [\mathrm{OMj}] \times \frac{\mathrm{Ks}_{\mathrm{SO_4^{2-}}}}{\mathrm{Ks}_{\mathrm{SO_4^{2-}}} + [\mathrm{SO_4^{2-}}]} \times \frac{\mathrm{Ks}_{\mathrm{Fe(OH)_3}}}{\mathrm{Ks}_{\mathrm{Fe(OH)_3}} + [\mathrm{Fe(OH)_3}]}$ $\times \frac{\mathrm{Ks}_{\mathrm{MnO_2}}}{\mathrm{Ks}_{\mathrm{MnO_2}} + [\mathrm{MnO_2}]} \times \frac{\mathrm{Ks}_{\mathrm{NO_3^-}}}{\mathrm{Ks}_{\mathrm{NO_3^-}} + [\mathrm{NO_3^-}]} \times \frac{\mathrm{Ks}_{\mathrm{O_2}}}{\mathrm{Ks}_{\mathrm{O_2}} + [\mathrm{O_2}]}$ $\times \frac{\mathrm{Ks}_{\mathrm{for}}}{\mathrm{Ks}_{\mathrm{for}} + [\mathrm{NO}_{3\,\mathrm{for}}^{-}]}$
Secondary reaction terms
$\mathrm{R.nox} = \mathrm{k.nox} \times [\mathrm{NH_4^+}] \times [\mathrm{O_2}]$
$\mathrm{R.Fe^{2+}.O_2} = \mathrm{k.Fe^{2+}.o2} \times [\mathrm{Fe^{2+}}] \times [\mathrm{O_2}]$

$\mathrm{R.\,Fe^{2+}.\,NO_3^-} = \mathrm{k.\,Fe^{2+}.\,NO_3^-} \times [\mathrm{Fe^{2+}}] \times [\mathrm{NO_3^-}]$
$\mathrm{R.\,H_2Sox} = \mathrm{k.\,H2Sox} \times [\mathrm{H_2S}] \times [\mathrm{O_2}]$
$\mathrm{R.\,Fe^{2+}.\,H_2S} = \mathrm{k.\,Fe2.\,H_2S} \times [\mathrm{Fe^{2+}}] \times [\mathrm{H_2S}]$
$\mathrm{R.\,FeS.\,H_2S} = \mathrm{k.\,FeS.\,H_2S} \times [\mathrm{FeS}] \times [\mathrm{H_2S}]$
$\mathrm{R.\,FeS.\,O_2} = \mathrm{k.\,FeS.\,O_2} \times [\mathrm{FeS}] \times [\mathrm{O_2}]$
$\mathrm{R.\,FeS_2.\,O_2} = \mathrm{k.\,FeS2.\,O_2} \times [\mathrm{FeS_2}] \times [\mathrm{O_2}]$
$\mathrm{R.\,Fe(OH)_3.\,H_2S} = \mathrm{k.\,Fe(OH)_3.\,h2s} \times [\mathrm{Fe(OH)_3}] \times [\mathrm{H_2S}]$
$\mathrm{R.\,Fe(OH)_3.\,MR.\,H_2S} = \mathrm{k.\,Fe(OH)_3.\,H_2S} \times [\mathrm{Fe(OH)_3.\,MR}] \times [\mathrm{H_2S}]$
$\mathrm{R.\,Fe(OH)_3.\,LR.\,H_2S} = \mathrm{k.\,Fe(OH)_3.\,H_2S} \times [\mathrm{Fe(OH)_3.\,LR}] \times [\mathrm{H_2S}]$
$\mathrm{R.\,NO^-_{3.bac}} = \mathrm{k.\,dnra} \times [\mathrm{H_2S}] \times [\mathrm{NO^-_{3.bac}}]$
$\mathrm{R.\,Cdenit} = \mathrm{k.\,Cdenit} \times [\mathrm{H_2S}] \times [\mathrm{NO^-_{3.bac}}]$
$\mathrm{R.\,ana.\,bac} = \mathrm{k.\,ana.\,bac} \times [\mathrm{NH_4^+}] \times [\mathrm{NO^-_{3.bac}}]$
$\mathrm{R.\,CH_4.\,SO_4^{2-}} = \mathrm{k.\,CH_4.\,SO_4^{2-}} \times [\mathrm{SO_4^{2-}}] \times [\mathrm{CH_4}]$
$\mathrm{R.\,Mn^{2+}.\,O_2} = \mathrm{k.\,Mn2.\,O_2} \times [\mathrm{Mn^{2+}}] \times [\mathrm{O_2}]$
$\mathrm{R.\,MnO_2.\,Fe^{2+}} = \mathrm{k.\,MnO_2.\,Fe^{2+}} \times [\mathrm{MnO_2}] \times [\mathrm{Fe^{2+}}]$
$\mathrm{R.\,MnO_2.\,MR.\,Fe^{2+}} = \mathrm{k.\,MnO_2.\,MR.\,Fe^{2+}} \times [\mathrm{MnO_2.\,MR}] \times [\mathrm{Fe^{2+}}]$
$\mathrm{R.\,MnO_2.\,H_2S} = \mathrm{k.\,MnO_2.\,H_2S} \times [\mathrm{MnO_2}] \times [\mathrm{H_2S}]$
$\mathrm{R.\,MnO_2.\,MR.\,H_2S} = \mathrm{k.\,MnO_2.\,MR.\,H_2S} \times [\mathrm{MnO_2.\,MR}] \times [\mathrm{H_2S}]$
$\mathrm{R.\,MnO_2toMR} = \mathrm{k.\,MnO_2toMR} \times [\mathrm{MnO_2}]$
$\mathrm{R.\,Fe(OH)_3toMR} = \mathrm{k.\,Fe(OH)_3toMR} \times [\mathrm{Fe(OH)_3}]$

Table C4. Modeled differential equations.

$tran$ = appropriate transport terms for solids or solutes (Section 4.3.5)

$\frac{\mathrm{dOMj}}{\mathrm{dt}} = \mathrm{tran} - (\mathrm{R.for.j} + \mathrm{R.O_2.j} + \mathrm{R.NO_3^-.j} + \mathrm{R.MnO2.j} + \mathrm{R.Fe(OH)_3.j} + \mathrm{R.SO_4^{2-}.j} + \mathrm{R.CH4.j})$
$\frac{\mathrm{dO_2}}{\mathrm{dt}} = \mathrm{tran} - \left(\frac{1-\varphi}{\varphi}\right)(\mathrm{R.O_2.j} + 3.5 \times \mathrm{R.FeS_2.O_2} + 2 \times \mathrm{R.FeS.O_2}) - 2 \times \mathrm{R.nox} - 0.25 \times \mathrm{R.Fe^{2+}.O_2} - 2 \times \mathrm{R.H_2Sox} - 0.5 \times \mathrm{R.Mn2.O_2} + \alpha \times ([\mathrm{O_2.w}] - [\mathrm{O_2}])$
$\frac{\mathrm{dNO_3^-}}{\mathrm{dt}} = \mathrm{tran} - \left(\frac{1-\varphi}{\varphi}\right) \times \frac{4}{5} \times (\mathrm{R.NO_3^-.j}) + \mathrm{R.nox} - 0.2 \times \mathrm{R.Fe^{2+}.NO_3^-} + \alpha \times ([\mathrm{NO_3^-.w}] - [\mathrm{NO_3^-}])$
$\frac{\mathrm{dNH_4^+}}{\mathrm{dt}} = \mathrm{tran} - \left(\frac{1-\varphi}{\varphi}\right) \times (\mathrm{rNC.j} \times \mathrm{R.for.j} + \mathrm{rNC.j} \times \mathrm{R.O_2.j} + \mathrm{rNC.j} \times \mathrm{R.NO_3^-.j} + \mathrm{rNC.j} \times \mathrm{R.MnO2.j} + \mathrm{rNC.j} \times \mathrm{R.Fe(OH)_3.j} + \mathrm{rNC.j} \times \mathrm{R.SO_4^{2-}.j} + \mathrm{rNC.j} \times \mathrm{R.CH_4.j}) - \mathrm{R.nox} + \mathrm{R.NO_{3.bac}^-} - \mathrm{R.ana.bac} + \alpha \times ([\mathrm{NH_4^+.w}] - [\mathrm{NH_4^+}])$
$\frac{\mathrm{dFe(OH)_3}}{\mathrm{dt}} = \mathrm{tran} - 4 * (\mathrm{R.Fe(OH)_3.j}) + \left(\frac{\varphi}{1-\varphi}\right) \times (\mathrm{R.Fe^{2+}.O_2} + \mathrm{R.Fe^{2+}.NO_3^-}) - \mathrm{R.Fe(OH)_3.H_2S} + 2 * \mathrm{R.MnO_2.Fe^{2+}} + 2 * \mathrm{R.MnO_2.MR.Fe^{2+}} - \mathrm{R.Fe(OH)_3toMR}$
$\frac{\mathrm{dFe(OH)_3.MR}}{\mathrm{dt}} = \mathrm{tran} - \mathrm{R.Fe(OH)_3.MR.h2s} + \mathrm{R.Fe(OH)_3toMR}$
$\frac{\mathrm{dFe(OH)_3.LR}}{\mathrm{dt}} = \mathrm{tran} - \mathrm{R.Fe(OH)_3.LR.H_2S}$
$\frac{\mathrm{dFe^{2+}}}{\mathrm{dt}} = \mathrm{tran} - 4 \times \left(\frac{1-\varphi}{\varphi}\right) \times (\mathrm{R.Fe(OH)_3.j}) - \mathrm{R.Fe^{2+}.O_2} - \mathrm{R.Fe^{2+}.NO_3^-} - \mathrm{R.Fe^{2+}.H_2S} + \left(\frac{1-\varphi}{\varphi}\right) \times (\mathrm{R.FeS.O_2} + \mathrm{R.FeS_2.O_2} + \mathrm{R.Fe(OH)_3.H_2S} + \mathrm{R.Fe(OH)_3.MR.H_2S} + \mathrm{R.Fe(OH)_3.LR.H_2S} - 2 \times \mathrm{R.MnO_2.Fe^{2+}} - 2 \times \mathrm{R.MnO_2.MR.Fe^{2+}}) + \alpha/4 \times (0 - [\mathrm{Fe^{2+}}])$

$$\frac{\mathrm{dFeS}}{\mathrm{dt}} = \mathrm{tran} + \left(\frac{\varphi}{1-\varphi}\right) * \mathrm{R.Fe^{2+}.H_2S} - \mathrm{R.FeS.H_2S} - \mathrm{R.FeS.O_2}$$
$$\frac{\mathrm{dFeS_2}}{\mathrm{dt}} = \mathrm{tran} + \mathrm{R.FeS.H_2S} - \mathrm{R.FeS_2.O_2}$$
$$\begin{aligned} \frac{\mathrm{dSO_4^{2-}}}{\mathrm{dt}} = \mathrm{tran} &- \left(\frac{1-\varphi}{\varphi}\right) \times (\mathrm{R.SO_4^{2-}.j}) + \mathrm{R.H_2Sox} + 2 \times \left(\frac{1-\varphi}{\varphi}\right) \times \mathrm{R.FeS_2.o2} \\ &+ 0.125 \times \left(\frac{1-\varphi}{\varphi}\right) \times (\mathrm{R.Fe(OH)_3.H_2S} + \mathrm{R.Fe(OH)_3.MR.H_2S} \\ &+ \mathrm{R.Fe(OH)_3.LR.H_2S}) + 0.25 \times \left(\frac{1-\varphi}{\varphi}\right) (\mathrm{R.MnO_2.H_2S} \\ &+ \mathrm{R.MnO_2.MR.H_2S}) + \mathrm{R.NO^-_{3.bac}} + \mathrm{R.Cdenit} - \mathrm{R.CH_4.SO_4^{2-}} \\ &+ \alpha \times ([\mathrm{SO_4^{2-}.w}] - [\mathrm{SO_4^{2-}}]) \end{aligned}$$
$$\begin{aligned} \frac{\mathrm{dH_2S}}{\mathrm{dt}} = \mathrm{tran} &- 0.5 \times \left(\frac{1-\varphi}{\varphi}\right) \times (\mathrm{R.SO_4^{2-}.j}) - \mathrm{R.H_2Sox} - 2 \times \mathrm{R.Fe^{2+}.H_2S} \\ &- 0.125 \times \left(\frac{1-\varphi}{\varphi}\right) \\ &\times (\mathrm{R.Fe(OH)_3.H_2S} + \mathrm{R.Fe(OH)_3.MR.h2s} + \mathrm{R.Fe(OH)_3.LR.h2s}) \\ &- \left(\frac{1-\varphi}{\varphi}\right) \times \mathrm{R.FeS.H_2S} - 0.25 \times \left(\frac{1-\varphi}{\varphi}\right) \times (\mathrm{R.MnO_2.H_2S} \\ &+ \mathrm{R.MnO_2.MR.h2s}) - \mathrm{R.NO^-_{3.bac}} - \mathrm{R.Cdenit} + \mathrm{R.CH_4.SO_4^{2-}} \\ &+ \alpha \times ([\mathrm{H_2S.w}] - [\mathrm{H_2S}]) \end{aligned}$$
$$\begin{aligned} \frac{\mathrm{dNO^-_{3.bac}}}{\mathrm{dt}} = \mathrm{tran} &+ \gamma(z) \times (\mathrm{NO^-_{3.bac.0}} - \mathrm{NO^-_{3.bac}}) - \mathrm{R.NO^-_{3.bac}} - 2 \times \mathrm{R.Cdenit} \\ &- \mathrm{R.ana.bac} \end{aligned}$$
$$\frac{\mathrm{dNO^-_{3\,for}}}{\mathrm{dt}} = \mathrm{tran} + \gamma(z) \times (\mathrm{NO^-_{3\,for.0}} - \mathrm{NO^-_{3\,for}}) - 0.8 \times \left(\frac{1-\varphi}{\varphi}\right) \times (\mathrm{R.for.j})$$
$$\frac{\mathrm{dCH_4}}{\mathrm{dt}} = \mathrm{tran} - 0.5 \times \left(\frac{1-\varphi}{\varphi}\right) \times (\mathrm{R.CH_4.j}) - \mathrm{R.CH_4.SO_4^{2-}} + \alpha \times ([\mathrm{CH_4.w}] - [\mathrm{CH_4}])$$
$$\begin{aligned} \frac{\mathrm{dMnO_2}}{\mathrm{dt}} = \mathrm{tran} &- 2 \times (\mathrm{R.MnO_2.1} + \mathrm{R.MnO_2.2} + \mathrm{R.MnO_2.3}) \\ &+ \left(\frac{\varphi}{1-\varphi}\right) \times \mathrm{R.Mn^{2+}.O_2} - \mathrm{R.MnO_2.Fe2} - \mathrm{R.MnO_2.H_2S} \\ &- \mathrm{R.MnO_2toMR} \end{aligned}$$

$$\frac{\mathrm{dMnO_2.MR}}{\mathrm{dt}} = \mathrm{tran} - \mathrm{R.MnO_2.MR.Fe^{2+}} - \mathrm{R.MnO_2.MR.H_2S} + \mathrm{R.MnO_2toMR}$$

$$\frac{\mathrm{dMn^{2+}}}{\mathrm{dt}} = \mathrm{tran} + 2 \times \left(\frac{1-\varphi}{\varphi}\right) \times (\mathrm{R.MnO_2.j}) - \mathrm{R.Mn^{2+}.O_2} + \left(\frac{1-\varphi}{\varphi}\right) \times (\mathrm{R.MnO_2.Fe^{2+}} + \mathrm{R.MnO_2.MR.Fe^{2+}} + \mathrm{R.MnO_2.H_2S} + \mathrm{R.MnO_2.MR.H_2S}) + \alpha \times (0 - [\mathrm{Mn^{2+}}])$$

Table C5. Model parameter values.

Parameter	Description	Value	Unit	Source
temp	Temperature	5	degree C	1
S	Salinity	31	psu	1
J.OM1	Flux of OM1 pool	360	μmol C cm^{-2} yr^{-1}	1
J.OM2	Flux of OM2 pool	30	μmol C cm^{-2} yr^{-1}	1
J.OM3	Flux of OM3 pool	300	μmol C cm^{-2} yr^{-1}	1
k1	OM1 decay constant	8	Yr^{-1}	1
k2	OM2 decay constant	0.1	Yr^{-1}	1
k3	OM3 decay constant	0.002	Yr^{-1}	1
J.Fe	Flux of HR Fe-oxide	10	μmol Fe cm^{-2} yr^{-1}	1
J.Fe.MR	Flux of MR Fe-oxide	30	μmol Fe cm^{-2} yr^{-1}	1
J.Fe.LR	Flux of LR Fe-oxide	20	μmol Fe cm^{-2} yr^{-1}	1
J.MnO$_2$	Flux of HR Mn-oxide	13.6/2	μmol Mn cm^{-2} yr^{-1}	1

J.MnO$_2$.MR	Flux of MR Mn-oxide	13.6/2	μmol Mn cm^{-2} yr^{-1}	1
k.nox	Rate constant for aerobic oxidation of ammonium	1e4	mmol^{-1} L yr^{-1}	2
k.Fe^{2+}.O$_2$	Rate constant for aerobic oxidation of Fe(II)	5e6	mmol^{-1} L yr^{-1}	3
k.Fe^{2+}.NO$_3^-$	Rate constant for anaerobic oxidation of Fe(II)	1e2	mmol^{-1} L yr^{-1}	4
k.H$_2$Sox	Rate constant for aerobic oxidation of H$_2$S	1e2	mmol^{-1} L yr^{-1}	3
k.Fe^{2+}.H$_2$S	Rate constant for FeS precipitation	1e5	mmol^{-1} L yr^{-1}	5
k.FeS.H$_2$S	Rate constant for pyrite (FeS$_2$) precipitation	1e2	mmol^{-1} L yr^{-1}	6
k.FeS.O$_2$	Rate constant for aerobic oxidation of FeS	1e3	mmol^{-1} L yr^{-1}	3
k.FeS$_2$.O$_2$	Rate constant for aerobic oxidation of FeS$_2$	8e2	mmol^{-1} L yr^{-1}	1
k.Fe(OH)$_3$.H$_2$S	Rate constant for Fe.HR reduction by H$_2$S	1e2	mmol^{-1} L yr^{-1}	7

k.Fe(OH)$_3$.MR.H$_2$S	Rate constant for Fe.MR reduction by H$_2$S	1	mmol^{-1} L yr^{-1}	7
k.Fe(OH)$_3$.LR.H$_2$S	Rate constant for Fe.LR reduction by H$_2$S	0.0001	mmol^{-1} L yr^{-1}	7
k.dnra	Rate constant for DNRA	0	mmol^{-1} L yr^{-1}	1
k.Cdenit	Rate constant for chemoautotrophic denitrification	0	mmol^{-1} L yr^{-1}	1
k.ana.bac	Rate constant for bacterial anamox	0	mmol^{-1} L yr^{-1}	1
k.CH$_4$.SO$_4^{2-}$	Rate constant for anerobic oxidation of CH$_4$	1e4	mmol^{-1} L yr^{-1}	6
k.Mn^{2+}.O$_2$	Rate constant for aerobic oxidation of Mn(II)	5e3	mmol^{-1} L yr^{-1}	3
k.MnO$_2$.Fe^{2+}	Rate constant for Mn(IV).HR reduction by Fe(II)	1e4	mmol^{-1} L yr^{-1}	8
k.MnO$_2$.MR.Fe^{2+}	Rate constant for Mn(IV).MR reduction by Fe(II)	1e2	mmol^{-1} L yr^{-1}	8
k.MnO$_2$.H$_2$S	Rate constant for Mn(IV).HR reduction by H$_2$S	1e2	mmol^{-1} L yr^{-1}	8
k.MnO$_2$.MR.H$_2$S	Rate constant for Mn(IV).MR reduction by H$_2$S	1	mmol^{-1} L yr^{-1}	8

k.MnO$_2$toMR	Rate constant for Mn(IV).HR aging to Mn(IV).MR	1.7	yr^{-1}	5
k.Fe(OH)$_3$toMR	Rate constant for Fe(III).HR aging to Fe(III).MR	0.7	yr^{-1}	5
Ks$_{O2}$	Half saturation constant for O_2 for OM degradation	0.001	mM	1
Ks$_{for}$	Half saturation constant for nitrate in foraminiferal denitrification of OM degradation	0.2	mM	1
Ks$_{NO3-}$	Half saturation constant for nitrate for OM degradation	0.001	mM	1
Ks.$_{MnO2}$	Half saturation constant for Mn(IV) for OM degradation	0.1	Wt%	1
Ks.$_{Fe(OH)3}$	Half saturation constant for Fe(III) for OM degradation	0.6	Wt%	1
Ks.$_{SO42-}$	Half saturation constant for SO_4^{2-} for OM degradation	1	mM	1
O_2.w	Bottom water oxygen concentration	0.107	mM	1
NO_3^-.w	Bottom water nitrate concentration	0.0137	mM	1

$NH_4^+.w$	Bottom water ammonium concentration	0.0012	mM	1
$SO_4^{2-}.w$	Bottom water sulfate concentration	28	mM	1
$Fe^{2+}.w$	Bottom water Fe^{2+} concentration	0	mM	1
$H_2S.w$	Bottom water sulfide concentration	0	mM	1
$NO_3^-{}_{for.0}$	Intracellular foraminiferal nitrate concentration at surface	2	mM	9
$NO_3^-{}_{bac.0}$	Intracellular bacterial nitrate concentration at surface	Bottom water value	mM	1
rNC.1	N/C for OM1	1/6.6		1
rNC.2	N/C for OM2	1/8		1
rNC.3	N/C for OM3	1/10		1
ps	Sediment density	2.65	g cm^{-3}	
w	Sedimentation rate	0.25	cm yr^{-1}	1
Db.max	Max bioturbation	9	cm^2 yr^{-1}	1
Db.L	Depth of bioturbation zone	12	cm	1
α.max	Max bioirrigation coeff.	10	yr^{-1}	1
xL.a	Active depth of bioirrigation	30	cm	1
xb.g	Attenuation	1		1

γ.max	Max. bacterial/foram transport coefficient	4	yr^{-1}	1
xL.g	Depth of bac/foram activity	5	cm	1
Por.0	Porosity at sediment surface	0.97		1
Por.inf	Porosity in compacted sediment	0.9		1
x.att	Porosity attenuation	2		1

1 = this study. 2 = (Bohlen et al. 2012); 3 = (Van Cappellen and Wang 1996); 4 = (Dhakar and Burdige 1996); 5 = (Berg et al. 2003); 6 = (Dale et al. 2009); 7 = (Canfield et al. 1992); 8 = (Dale et al. 2015); 9 = (Dale et al. 2016).

Table C6. Detailed results from Foraminiferal abundances and experiments.

Sediment depth (cm)	0-1		1-2		2-3		3-4		4-5		Total
Size fraction	>125 µm	63-125 µm	>125 µm	63-125 µm	>125 µm	63-125 µm	>125 µm	63-125 µm	>125 µm	63-125 µm	
Nov-2020											
Abundance (ind cm^{-2})											
Stainforthia fusiformis	11.5	303.4	8.6	29.8	11.3	55.5	4.1	26.6	5.2	17.6	473.6
Elphidium albiumbilicatum	6.3	2	3.2	2.3	1.4	1.4	0.2	1.4	0.7	2.3	21
Other species	0.2	0	0	0	0.5	0	0.2	0	0	0	0.9
Population density (ind cm^{-3})											
Stainforthia fusiformis	11.7	307.2	9.2	32	16	78.7	3.4	22.5	5.3	17.8	503.8
Elphidium albiumbilicatum	6.4	2.1	3.4	2.4	1.9	1.9	0.2	1.1	0.7	2.3	22.4
Other species	0.2	0	0	0	0.6	0	0.2	0	0	0	1.1
Species percentage (%)											
Stainforthia fusiformis	63.8	99.3	73.1	93	86.2	97.6	90	95.2	88.5	88.6	95.6
Elphidium albiumbilicatum	35	0.7	26.9	7	10.3	2.4	5	4.8	11.5	11.4	4.2
Other species	1.3	0	0	0	3.4	0	5	0	0	0	0.2
All species abundance (ind cm^{-2})	18.1	305.4	11.7	32.1	13.1	56.9	4.5	28	5.9	19.9	495.5
All species population density (ind cm^{-3})	18.3	309.3	12.6	34.4	18.6	80.6	3.8	23.6	5.9	20.1	527.3
Split	0.0625	0.03125	0.03125	0.03125	0.0625	0.03125	0.0625	0.03125	0.0625	0.03125	
Sample volume (cm^{3})	70	70	66	66	50	50	84	84	70	70	
Total foraminiferal denitrification rate (mmol m^{-2} day^{-1})	0.008	0.212	0.006	0.021	0.008	0.039	0.003	0.019	0.004	0.012	0.332

Total foraminiferal nitrate storage (µmol l^{-1} of sediment)		23.91		3.09		7.1		1.94		1.73	
May-2021											
Abundance (ind cm^{-2})											
Stainforthia fusiformis	5.5	51.6	6.7	50.6	7.2	30.2	6.1	26.2	6.1	10.8	201
Elphidium albiumbilicatum	1.2	1.5	0	1.4	3.4	2.7	3.3	4.1	5.6	7.7	30.8
Other species	0.6	0	0	0	0.9	0	0	0	0	0	1.5
Population density (ind cm^{-3})											
Stainforthia fusiformis	5.6	52.2	9.1	68.9	6.9	29	7	29.9	6.2	11	225.8
Elphidium albiumbilicatum	1.2	1.5	0	1.8	3.2	2.6	3.7	4.6	5.7	7.8	32.3
Other species	0.6	0	0	0	0.9	0	0	0	0	0	1.4
Species percentage (%)											
Stainforthia fusiformis	75.6	97.2	100	97.4	62.7	91.8	65.1	86.6	51.9	58.5	86.2
Elphidium albiumbilicatum	16.9	2.8	0	2.6	29.4	8.2	34.9	13.4	48.1	41.5	13.2
Other species	7.6	0	0	0	7.8	0	0	0	0	0	0.6
All species abundance (ind cm^{-2})	7.3	53	6.7	51.9	11.5	33	9.4	30.2	11.7	18.5	233.2
All species population density (ind cm^{-3})	7.4	53.7	9.1	70.8	11	31.6	10.7	34.6	11.9	18.7	259.5
Split	1	0.125	0.3784	0.0625	0.0625	0.0313	0.125	0.0313	0.0625	0.0313	
Sample volume (cm^3)	70	70	52	52	74	74	62	62	70	70	
Total foraminiferal denitrification rate (mmol m^{-2} day^{-1})	0.004	0.036	0.005	0.035	0.005	0.021	0.004	0.018	0.004	0.008	0.141
Total foraminiferal nitrate storage (µmol l^{-1} of sediment)	4.34		5.85		2.69				1.29		

APPENDIX D: COPYRIGHT AGREEMENTS

For Chapter 2:

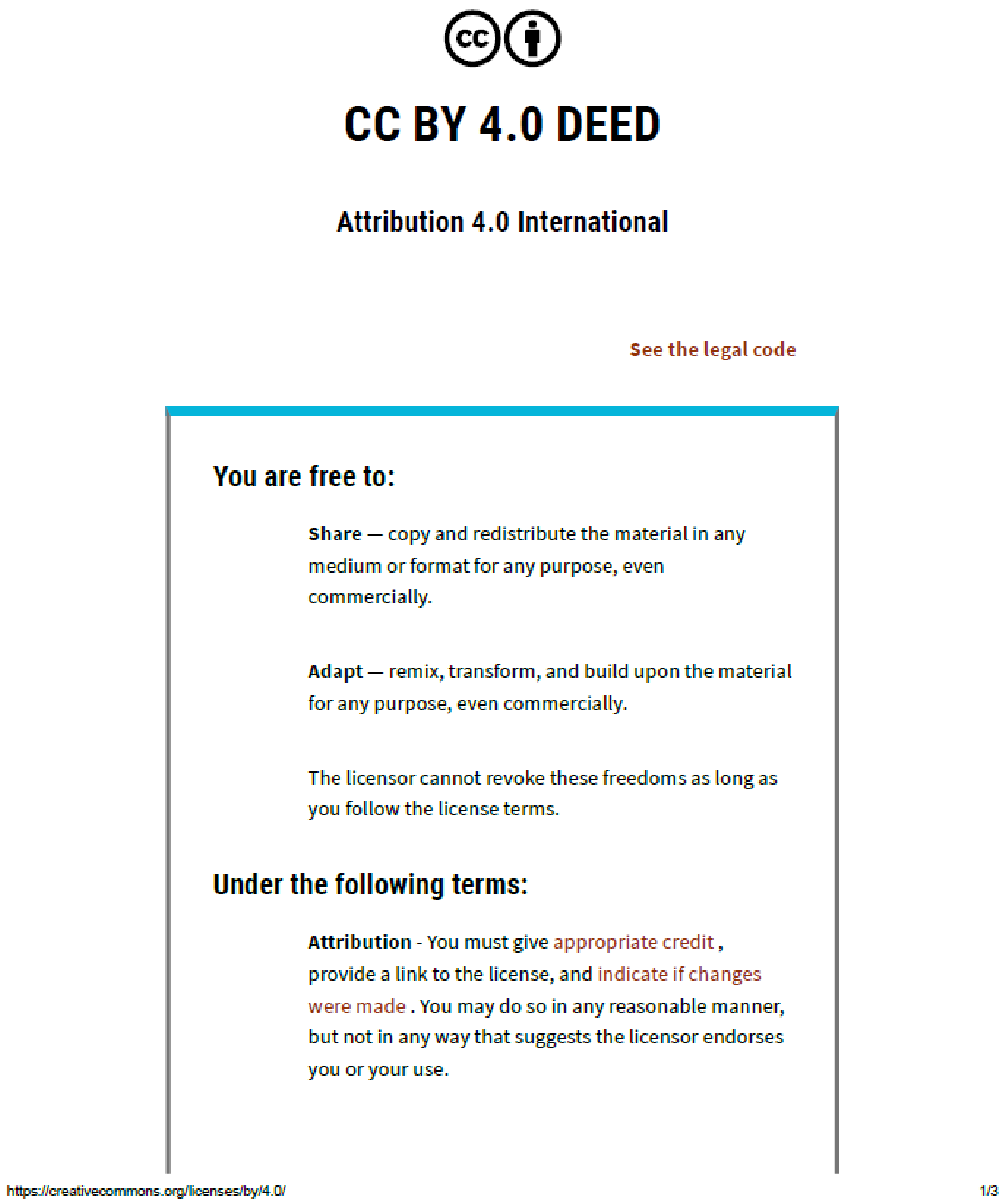

CC BY 4.0 DEED

Attribution 4.0 International

See the legal code

You are free to:

Share — copy and redistribute the material in any medium or format for any purpose, even commercially.

Adapt — remix, transform, and build upon the material for any purpose, even commercially.

The licensor cannot revoke these freedoms as long as you follow the license terms.

Under the following terms:

Attribution - You must give appropriate credit , provide a link to the license, and indicate if changes were made . You may do so in any reasonable manner, but not in any way that suggests the licensor endorses you or your use.

https://creativecommons.org/licenses/by/4.0/ 1/3

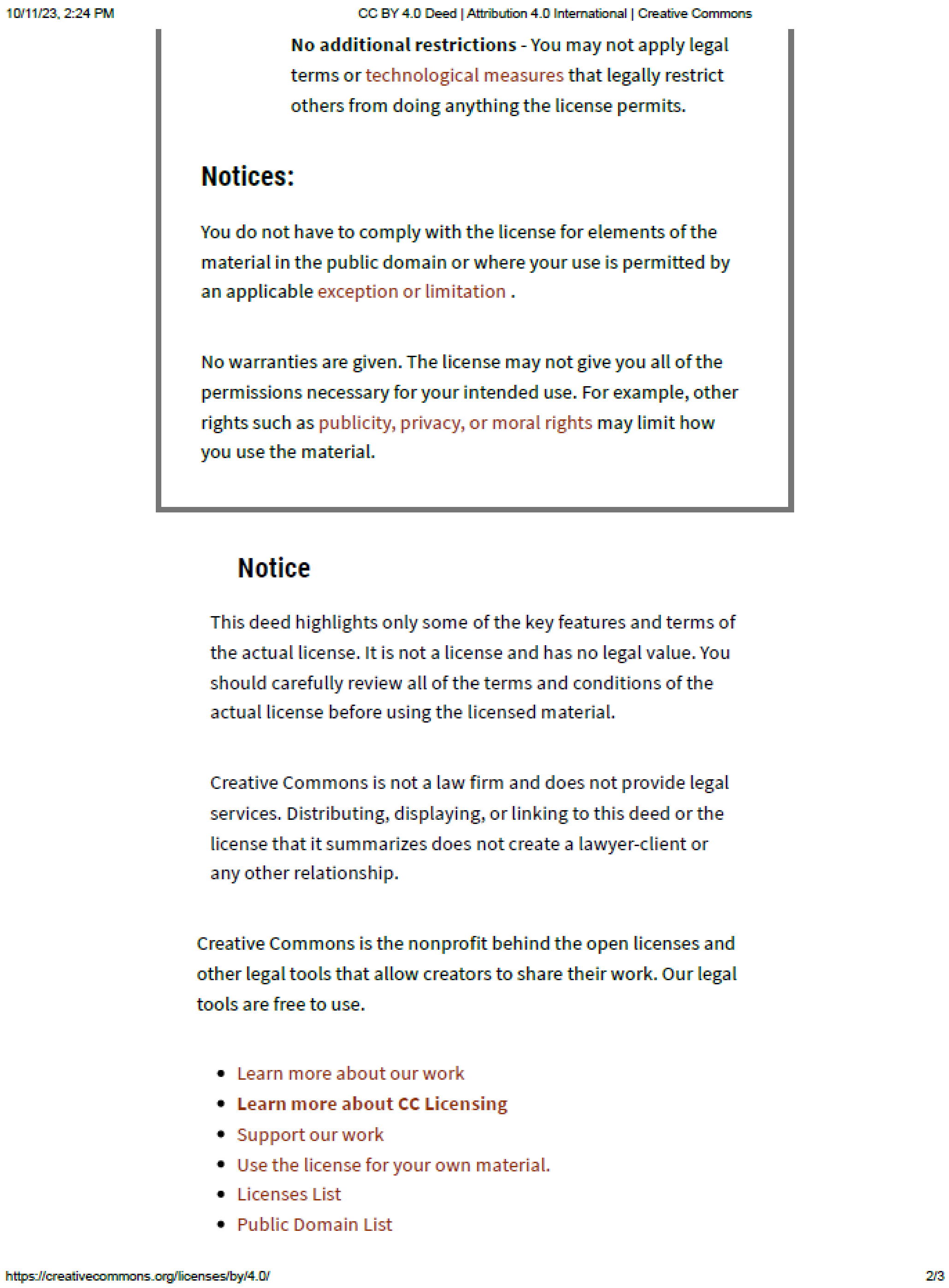

No additional restrictions - You may not apply legal terms or technological measures that legally restrict others from doing anything the license permits.

Notices:

You do not have to comply with the license for elements of the material in the public domain or where your use is permitted by an applicable exception or limitation .

No warranties are given. The license may not give you all of the permissions necessary for your intended use. For example, other rights such as publicity, privacy, or moral rights may limit how you use the material.

Notice

This deed highlights only some of the key features and terms of the actual license. It is not a license and has no legal value. You should carefully review all of the terms and conditions of the actual license before using the licensed material.

Creative Commons is not a law firm and does not provide legal services. Distributing, displaying, or linking to this deed or the license that it summarizes does not create a lawyer-client or any other relationship.

Creative Commons is the nonprofit behind the open licenses and other legal tools that allow creators to share their work. Our legal tools are free to use.

- Learn more about our work
- **Learn more about CC Licensing**
- Support our work
- Use the license for your own material.
- Licenses List
- Public Domain List

For Chapter 3:

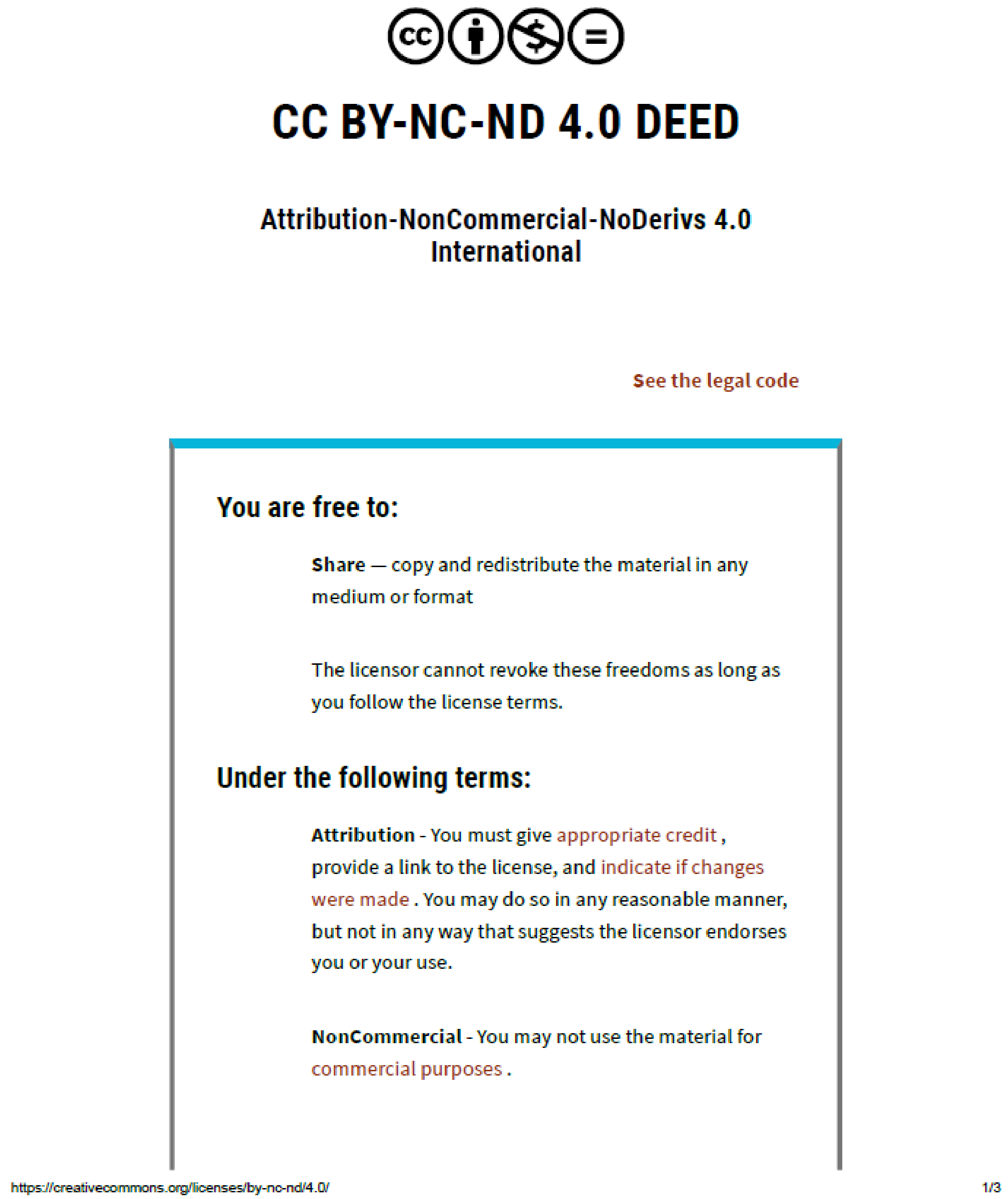

CC BY-NC-ND 4.0 DEED

Attribution-NonCommercial-NoDerivs 4.0 International

See the legal code

You are free to:

Share — copy and redistribute the material in any medium or format

The licensor cannot revoke these freedoms as long as you follow the license terms.

Under the following terms:

Attribution - You must give appropriate credit , provide a link to the license, and indicate if changes were made . You may do so in any reasonable manner, but not in any way that suggests the licensor endorses you or your use.

NonCommercial - You may not use the material for commercial purposes .

https://creativecommons.org/licenses/by-nc-nd/4.0/ 1/3

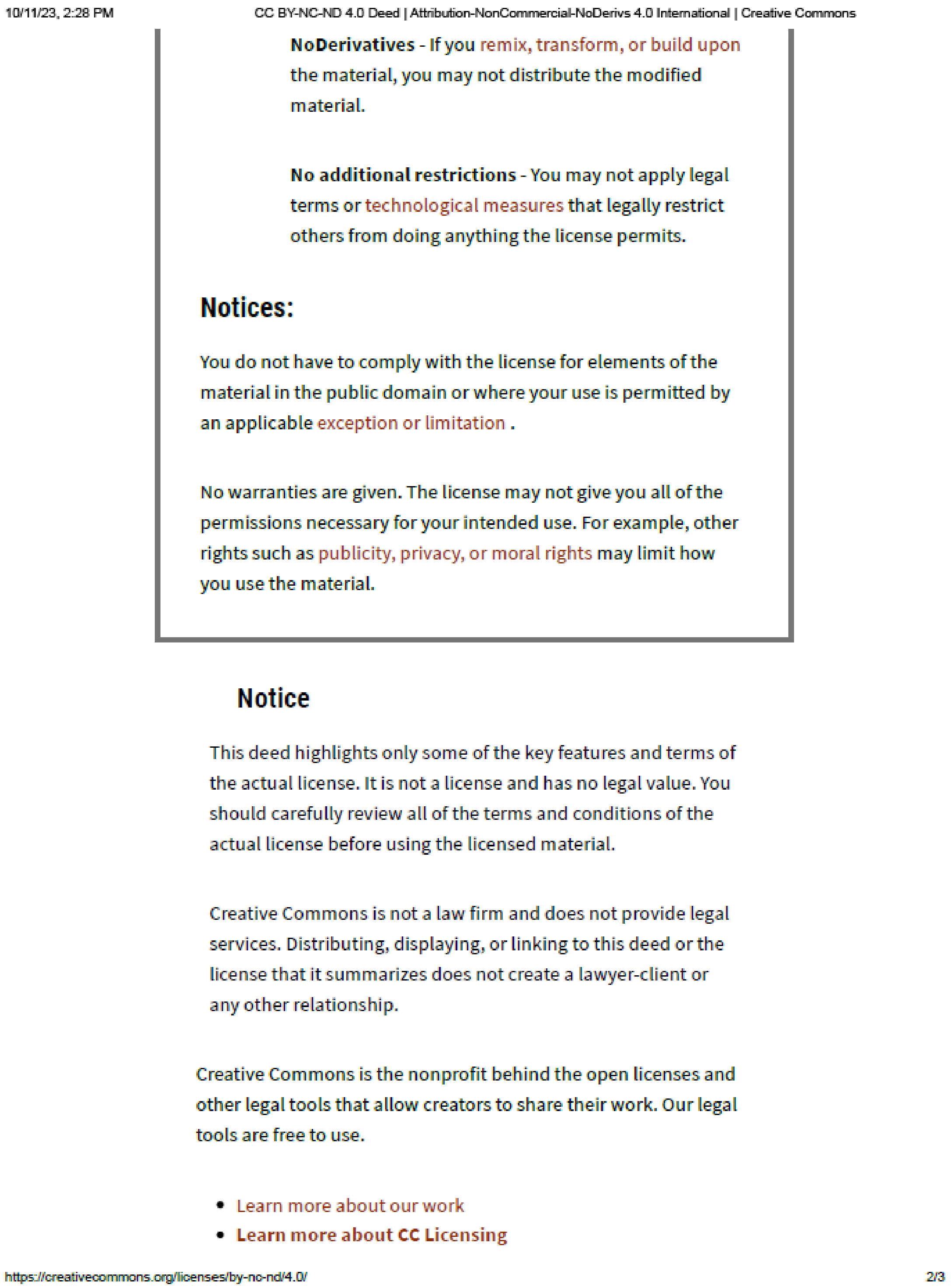

10/11/23, 2:28 PM CC BY-NC-ND 4.0 Deed | Attribution-NonCommercial-NoDerivs 4.0 International | Creative Commons

NoDerivatives - If you remix, transform, or build upon the material, you may not distribute the modified material.

No additional restrictions - You may not apply legal terms or technological measures that legally restrict others from doing anything the license permits.

Notices:

You do not have to comply with the license for elements of the material in the public domain or where your use is permitted by an applicable exception or limitation .

No warranties are given. The license may not give you all of the permissions necessary for your intended use. For example, other rights such as publicity, privacy, or moral rights may limit how you use the material.

Notice

This deed highlights only some of the key features and terms of the actual license. It is not a license and has no legal value. You should carefully review all of the terms and conditions of the actual license before using the licensed material.

Creative Commons is not a law firm and does not provide legal services. Distributing, displaying, or linking to this deed or the license that it summarizes does not create a lawyer-client or any other relationship.

Creative Commons is the nonprofit behind the open licenses and other legal tools that allow creators to share their work. Our legal tools are free to use.

- Learn more about our work
- **Learn more about CC Licensing**

https://creativecommons.org/licenses/by-nc-nd/4.0/ 2/3